

Solar Thermoelectrics for Small Scale Power Generation

By

Reja Amatya

B.S. Smith College, Northampton, MA (2005)

S.M. Massachusetts Institute of Technology, Cambridge, MA (2008)

Submitted to the

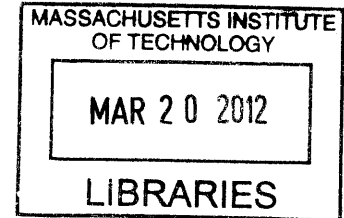
Department of Electrical Engineering and Computer Science
in partial fulfillment of the requirements for the degree of

Doctor of Philosophy

at the

Massachusetts Institute of Technology

February 2012



© 2012 Massachusetts Institute of Technology

All rights reserved.

Signature of Author _____

Department of Electrical Engineering and Computer Science

January 13, 2012

Certified by _____

Rajeev J. Ram

Professor of Electrical Engineering

Thesis Supervisor

Accepted by _____

Leslie A. Kolodziejcki

Professor of Electrical Engineering

Chair, Committee on Graduate Students

Solar Thermoelectrics for Small Scale Power Generation

by
Reja Amatya

Submitted to the
Department of Electrical Engineering and Computer Science on

January 13, 2012

in Partial Fulfillment of the Requirements for the Degree of
Doctor of Philosophy in Electrical Engineering and Computer Science

ABSTRACT

In the past two decades, there has been a surge in the research of new thermoelectric (TE) materials, driven partly by the need for clean and sustainable power generation technology. Utilizing the Seebeck effect, the thermoelectric devices can be used as heat engines to convert heat into electricity. With no moving parts, the generators are considered highly reliable with low maintenance, which is essential for decentralized power source. With nearly 1.6 billion people living without basic electricity, the need for a small scale power generation is there. Through this work, we show that the solar thermoelectric generators (STEGs) using cheap parabolic concentrators with high ZT modules can be a viable and a cost-effective alternative to solar photovoltaics for distributed power generation. The maximum conversion efficiency of 3% has been achieved for a STEG under AM 1.5G conditions with commodity thermoelectric module. The generator was able to produce a peak output power of 11 W_p with an inexpensive parabolic solar concentrator which can be found in developing countries being used as solar cookers. The output power is the highest achieved value for concentrated solar thermoelectrics and it is comparable to photovoltaic modules that are deployed in these rural communities. Based on a heat transfer model developed during this work, various system parameters were analyzed for maximizing the performance. An optimized thermoelectric module design with a slight aspect ratio variation for the TE legs have been identified that can increase the efficiency by 28%.

Another parameter for system improvement that has been considered is the use of novel TE material. Issues of earth-abundance, material scarcity and cost have been taken into consideration for new material. These are important considerations for a technology that can have a potential cost-effective large scale deployment. A robust, high temperature thermoelectric material characterization tool (Z -meter) has been

developed with proper radiation suppression (20x below black body radiation) and low system parasitics (41.6% lower electrical contact parasitic than previous published results). We investigated novel metal-semiconductor superlattice structures ((Hf,Zr)N/ScN) using the Z-meter setup. Low thermal conductivities (2.5-5 W/m.K) have been measured for temperature range of 300-650 K. The Seebeck coefficient of 132 $\mu\text{V/K}$ was measured at 830 K, which is comparable to the state-of-the-art SiGe at similar temperature.

Thesis Supervisor: Rajeev J. Ram

Title: Professor (EECS), Associate Director, Research Laboratory of Electronics (RLE)

Acknowledgement

I would like to thank Prof. Rajeev Ram, my research advisor who has supported me throughout my thesis with his patience and knowledge whilst allowing and encouraging me to work in my own way.

The group members of POE have been an integral part of my MIT life; without them this journey would not have been as exciting and fun. Kevin Lee and Jason Orcutt have especially been there for me throughout my time at MIT. I thank both of them for their support not just for technical discussions and help with experiments but for being who they are around the lab and making it a great place to work. Among the previous group members: Harry Lee, Peter Mayer, Tom Liptay and Joe Summers were great individuals that I came to know in this lab and were also inspirational for their work ethics and dedication. Parthiban Santhanam has been a great mind to work around. His passion for knowledge is admirable and it was great to have him around to bounce ideas. I would also like to thank group members: Shireen Goh (trying her best to keep a disordered lab in order as our EHS representative), William Lo, Karan Mehta and Charles. I would like to thank Prof. Vladimir Bulovic and Prof. Gang Chen for their guidance and support during the thesis preparation and for being in my committee.

A major portion of this work would not have taken place without One Earth Designs. I would like to thank Scot Frank, Catlin Powers and Amy Qian for their tremendous support during all the trips to China. I would also like to thank my collaborators: Prof. Ali Shakouri (UCSC, Purdue), Jeremy Schroeder (Purdue), Robert Wortman (Purdue), Prof. Timothy Sands (Purdue) and Dr. Gehong Zeng (UCSB) for the work on new thermoelectric material.

Beyond MIT, I would like to thank my friends and family for supporting me, particularly my husband for always being there. I would like to dedicate this work to my mom and maa (the strong women in my life).

Table of Contents

1. Introduction	23
1.1 Solar engineering in developing countries	26
1.1.1 Photovoltaics	26
1.1.2 Concentrated photovoltaics	28
1.1.3 Hybrid systems	28
1.1.4 Solar thermal	29
1.1.5 Others	30
1.2 Solar Thermoelectrics.....	33
1.2.1 Thermoelectricity	33
1.2.1.1 Basic principle.....	34
1.2.1.2 Thermoelectric applications	37
1.2.1.3 Thermoelectric material	38
1.2.2 Solar concentration.....	39
1.2.3 Selective surface.....	43
1.2.4 Heat sink.....	47
1.3 Previous work.....	48
1.4 Thesis preview.....	51
2. Solar Thermoelectric Generator	53
2.1 Thermodynamic model.....	54
2.2 System validation	62
2.3 Design methodology.....	65
2.3.1 Selective surface.....	65
2.3.2 Material property: ZT	69
2.3.3 Heat sink (thermal impedance).....	71
2.3.3.1 Air convection	75

2.3.3.2	Forced water convection	76
2.3.3.3	Natural water convection.....	80
2.3.4	Hot side absorber design	85
2.4	Generator assembly	94
2.5	Transient simulation	98
2.6	Conclusion.....	102
3.	Field Trial and Demonstration.....	105
3.1	Methodology for field testing.....	106
3.2	Trial locations.....	108
3.3	Field trials.....	111
3.3.1	STEG performance with the local cookers.....	114
3.3.2	Tracking	117
3.3.3	STEG performance with cooking stoves.....	119
3.3.4	Feedback from STEG users.....	121
3.4	Conclusion.....	127
4.	Module Design and Optimization	129
4.1	Module variables	129
4.2	Optimization of the aspect ratio	133
4.3	Conclusion.....	137
5.	Novel Thermoelectric Material Study	141
5.1	ZT vs. crustal abundance	146
5.2	High ZT material	151
5.2.1.	Skutterudite	151
5.2.2.	Clathrate	152
5.2.3.	Zintl phase.....	153
5.2.4.	TAGS/LAST	154
5.3	Earth-abundant TE material	154
5.3.1.	Half-Heusler	154

5.3.2.	Oxide	155
5.3.3.	Silicide.....	156
5.4	Guidelines for good thermoelectrics	157
5.5	Metal-Semiconductor superlattice.....	160
5.6	Z-meter	163
5.6.1.	Experimental setup	164
5.6.2.	Measurement parameters.....	167
5.6.3.	Thermal radiation suppression	171
5.6.4.	System validation	173
5.7	New TE material measurement	179
5.8	Conclusion.....	188
6.	Economic Model	191
6.1	System cost.....	192
6.2	LCOE cost model	193
6.2.1	Cost analysis using new TE material.....	197
6.2.2	Impact of dual (hybrid) use of STEG on cost.....	198
6.3	Conclusion.....	199
7.	Conclusions and Future work	201
7.1	Summary	201
7.2	Future work	207
Appendix 1:	Properties of fluids.....	211
Appendix 2a:	Survey Questionnaire I	213
Appendix 2b:	Survey Questionnaire II.....	219
Appendix 3:	MATLAB codes	221
Bibliography	243

List of Tables

Table 1: Comparison for various lighting sources (http://www.lutw.org)	24
Table 2: Common target groups for rural electrification.....	24
Table 3: Different villages in Western China where OED is working.....	25
Table 4: Comparison for various electricity generating systems ^{[20, 25],[31],[32-35]}	32
Table 5: Comparison at room temperature of the thermoelectric properties of metal, semiconductor and insulators	35
Table 6: Various applications of thermoelectrics in power generation and cooling	38
Table 7: Comparison for various concentrators ^[69-74]	42
Table 8: Comparison for various selective surfaces ^[78-80, 83-86]	46
Table 9: Heat transfer coefficients for various heat sinks ^[39]	48
Table 10: Saturation temperature for some common liquids (lower than water's saturation temperature of 100°C)	82
Table 11: Summary of different heat sink options for STEG.....	85
Table 12: Commercial TEG module specifications (company data sheet)	96
Table 13: Electrical – thermal equivalent parameters for SPICE.....	100
Table 14: Current options for lighting in many rural communities.....	110
Table 15: Thermal power available at the focal spot for local solar cookers in various locations.....	112
Table 16: Results from preliminary test conducted on STEG.....	113
Table 17: Energy and capacitance for different fuel source.....	120
Table 18: comparison between PV and STEG (input from families using both).....	128
Table 19: High <i>ZT</i> thermoelectric material	144
Table 20: Summary of previous <i>Z</i> -meter measurement for TE characterization	166
Table 21: Samples used for system validation	174
Table 22: <i>Z</i> -meter measurement showing progressive improvement for metal-semiconductor sample...	187
Table 23: Cost break down for solar thermoelectric generator	192

Table 24: Material cost for STEG	193
Table 25: Price of electricity for an STEG using various thermoelectric materials compared to PV	197
Table 26: Price of raw material for thermoelectrics [Ref. www.metalprices.com , April 2009]	198
Table 26: Lighting options for a rural community not connected to grid	207

List of Figures

Figure 1: Conceptual representation of solar thermophotovoltaics (www.gcep.stanford.edu)	29
Figure 2: Charge distribution in a thermoelectric material due to temperature gradient causes potential difference. In the n-type material, electrons move from hot to cold side. Similarly, in the p-type material, holes move towards the cold side.....	34
Figure 3: Thermoelectric module with more than one couple of n- and p-type legs connected electrically in series between ceramic substrate.....	35
Figure 4: Normalized output power vs. efficiency for a TEG with varied load resistance (R_L) for different ZT values	37
Figure 5: ZT for n- and p-type materials at difference temperature range ^[53]	39
Figure 6: Geometry of a parabolic collector showing small acceptance angle and focal spot.....	40
Figure 7: Geometry of a compound parabolic collector showing a large acceptance angle	41
Figure 8: SK-14 solar cooker (popular in South Asia; designed in Germany); concrete solar cooker (popular in Western China).....	43
Figure 9: Solar spectrum and blackbody radiation at different temperature. AM0 is the extraterrestrial spectrum, AM1.5G is the irradiance on 37° tilted surface, and AM1.5 is the direct normal spectral irradiance (Ref. www.rredc.nrel.gov)	44
Figure 10: Reflectance data for the selective surface using metal-dielectric set (AlN/SS).....	45
Figure 11: The system efficiency vs. the hot side temperature, showing large radiation loss at high temperature. Radiation loss can be suppressed by changing the emissivity (ϵ). Parameters used for the plot: $ZT = 0.5$, $T_c = 30^\circ\text{C}$, convective heat transfer (h) = $5\text{W/m}^2\text{K}$, absorber area = 0.06m^2 , system's thermal impedance = 0.1K/W	47
Figure 12: Previous experiments for STEG shown with system efficiency and output electrical power ...	50
Figure 13: (a) A solar thermoelectric generator showing the concentrator and the heat sink (air cooled); (b) Water convection heat sink scheme is used in this STEG.....	54
Figure 14: Dependence of radiative loss on the hot side absorber temperature given by the Stefan-Boltzmann law; radiative loss can be suppressed by using low emissivity material	55

Figure 15: Schematic of the enclosure holding the thermoelectric generator, a Fresnel lens is used in this prototype to increase the thermal flux.....	57
Figure 16: (a) Schematic for a STEG showing heat flow through the generator and various temperatures at different interfaces; (b) thermal circuit equivalent for the STEG system showing various paths for heat flow	58
Figure 17: Schematic for a TEG showing loss within the leg which is mostly joule heating; conductive path through the generator is also path for heat leak.....	59
Figure 18: Theoretical simulation for Bi_2Te_3 showing module ZT and system efficiency: Without any parasitic, maximum system efficiency of 4% can be achieved at 70x suns. The model is verified with an experiment at 66x and 40x suns intensity. Parasitics are included in the theory to represent the commercial module	63
Figure 19: Output power from STEG at 66x suns with variable load resistance; open circles are experimental data with solid line as the modeling result	64
Figure 20: ZT vs. temperature for $\text{MAM-Bi}_2\text{Te}_3$ (o – measured data provided by Marlow Inc, -- quadratic fit).....	64
Figure 21: Effect of emissivity on system efficiency for Bi_2Te_3 based STEG at different solar concentration	66
Figure 22: Optical properties of a commercial selective surface compared to a black painted surface ($\epsilon \sim 0.9$) and a white ceramic plate. Blackbody radiations at different temperatures are shown (dotted lines). The peak for 200-300°C body is in the mid IR range (4-5 μm)	68
Figure 23: Optical transmission properties of different thickness coating for the selective surface.....	68
Figure 24: Difference in the overall output power for the STEG for different absorber surface coating that has various absorbance and emissivity (theoretical modeling shown with solid lines)	69
Figure 25: Dependence of STEG efficiency on the figure-of-merit for a TE material at different solar concentration. The darkest line indicates the Z value achievable today at various temperature ranges (2e-3 K^{-1}). Bi_2Te_3 at room temperature has $Z \sim 2.5\text{e-}3 \text{ K}^{-1}$, whereas with temperature > 400 K, it decreases to 1e-3 K^{-1}	70
Figure 26: System performance for different TE material system	70
Figure 27: Performance curve of a commercial Bi_2Te_3 module (TG12-6L) at different cold side temperature.....	72
Figure 28: Theoretical estimates for system efficiency with different heat sinks	73
Figure 29: Measure bar experiment to determine the heat transfer coefficient for various heat sinks.....	74

Figure 30: Natural convection heat sink with splayed fins for larger area (Cool Innovations Inc.)	75
Figure 31: Temperature dependent heat transfer coefficient for (a) natural and (b) forced air convection	76
Figure 32: Temperature dependent heat transfer coefficient for forced water convection.....	77
Figure 33: (a) Cold loop as a heat sink for a TEG using cold plate; (b) Setup schematic to measure the heat transfer coefficient for cold loop	78
Figure 34: (a) The pump efficiency for a solar DC-pump depends on the input electrical power; (b) The heat transfer coefficient for the cold plate heat sink using forced convection also depends on the flowrate; at low electrical power (< 3W), the flow rate was very small to be accurately measured with the flow meter.....	79
Figure 35: Flowrate and temperature drop across the thermoelectric module for various thermal inputs for the self-powered cooling loop	79
Figure 36: Boiling curve for water showing different stages from natural (free) convection, nucleate boiling, transition boiling to film boiling ^[116]	81
Figure 37: Temperature dependent heat transfer coefficient for natural water convection.....	82
Figure 38: Measured heat transfer coefficient for various heat sinks.....	84
Figure 39: (a) A TEG module in between a thermal absorber and a heat sink; (b) Open circuit voltage measurement for a TEG module with and without an extra layer in the front acting as a thermal absorber using the solar simulator setup	86
Figure 40: Open circuit voltage measurement for the STEG (with and without an absorber) using a solar cooker.....	87
Figure 41: Hot-side absorber design for consideration (a) flat-plate; (b) cylindrical design	87
Figure 42: Finite-element simulation (COMSOL) showing snapshots of temperature field for different absorber heights (d = 0 (a), 2 cm (b), 6 cm (c), 8cm (d)) for t = 5 minutes, and t = 10 minutes; and air flow under the hot side absorber (streamline velocity profile is shown here).....	92
Figure 43: Maximum hot-side temperature vs. absorber height (d) (for t = 10 minutes) for a constant input flux	93
Figure 44: Temperature drop across the TEG module varies as the thermal impedance of the hot side absorber is changed for different input heat flux; fixed heat sink thermal impedance based on natural air convection was used for this analysis (1 K/W).....	93
Figure 45: STEG prototype using natural water convection scheme for heat sink with four commercial Bi ₂ Te ₃ modules.....	96
Figure 46: Clamping force for STEG assembly.....	97

Figure 47: Circuit schematic for (a) battery charging with STEG using a charge controller; (b) battery discharging across a load.....	98
Figure 48: (a) cold side water temperature over time reaching pasteurization point (65°C); (b) output electrical power for STEG measured across a fixed load resistor with an input thermal power of 230 W.....	99
Figure 49: STEG system schematic used in SPICE to do transient modeling (all temperature dependent parameters: TE material parameters and heat transfer coefficients are represented by voltage controlled current sources inside the model: shown here as variable resistors).....	100
Figure 50: Seebeck voltage modeled as a temperature-controlled voltage source in series with the internal resistance of the module.....	101
Figure 51: (a) Measured output electrical power and transient simulation results; (b) cold side water temperature measured by a thermocouple with SPICE model results (dark lines) for 130 W and 230 W thermal inputs.....	101
Figure 52: (a) Electrical appliances used by nomadic and agricultural communities; (b) average hour of electricity use and monthly electricity bill for different communities	109
Figure 53: Lighting sources available in the summer settlement for nomadic community; a small percentage of families in the agricultural village (~10%) also used PV system for lighting	110
Figure 54: (a) concrete-based mirror reflector and (b) metal reflector solar cooker, locally available in China	111
Figure 55: Testing for STEG in (a) Mairi, China; (b) Tianzhu, China; (c) Ping ‘an, China	112
Figure 56: Uneven heating of the absorber at the focal spot of the local solar cooker causes burning at the hot spot.....	114
Figure 57: Output power for STEG measured across a load resistor (16 Ω) for different hours of a day (solar irradiance measured at the beginning of the experiments with a flux meter).....	115
Figure 58: Comparison of the transient simulation with the measured field data.....	116
Figure 59: Effect of cloud coverage on the output power (average power of 6.5 W was measured even under such condition).....	117
Figure 60: Azimuth angle variation in (a) winter and (b) summer at the northern hemisphere [www.solarplot.info]	118
Figure 61: Decrease in power during manual tracking as the sun moves away from the focal spot causing decrease in the input intensity and temperatures; power level increases as the cooker’s position is changed every 10-15 minutes	118
Figure 62: Traditional cooking stove used in Qinghai region (metal body)	119

Figure 63: Output power from the STEG using waste heat from the cooking stove.....	119
Figure 64: Using latent heat from the cooking stove to generate electricity even after the fire is out and no more fuel is added	120
Figure 65: STEG being tested with the cooking stove during a cloudy day as the stove was being used for meal preparation.....	121
Figure 66: Frequency of use of STEG by six families surveyed over four months	121
Figure 67: (a) # of hours STEG used to charge a battery; (b) # of hours STEG used for cell phone charging and lighting.....	123
Figure 68: STEG being tested in one of the homes in an agricultural village of Gangta.....	124
Figure 69: STEG being tested by family # 2 in Gangta	124
Figure 70: STEG being tested in high grassland village of Serjia using metal reflector cooker.....	125
Figure 71: STEG being tested with: (a) solar cooker and (b) mud cooking stove	126
Figure 72: A 5 W LED bulb lighting a tent in the nomadic village of Serjia in the evening (fire from the stove was used for lighting before the installation of the STEG).....	126
Figure 73: STEG being used by a family in the nomadic village (Serjia).....	127
Figure 74: Spreading resistance increasing as the fill factor is decreased (in this case by decreasing the cross-section area of the TE leg) ($L_{ceramic} = 0.75$ mm, $\kappa_{ceramic} = 20$ W/m.K)	130
Figure 75: TEG module schematic showing n- and p-type legs with ceramic substrate at the top and bottom	132
Figure 76: (a) STEG system efficiency vs. TE leg thickness; (b) efficiency vs. fill factor achieved here by changing the cross section area of the TE leg.....	132
Figure 77: System efficiency for different aspect ratio modules achieved in the bench-top prototype design	133
Figure 78: 3-dimensional plot showing maximum system efficiency for various leg thicknesses and module fill factors	134
Figure 79: System efficiency at various solar irradiance with the optical concentration $\sim 10x$ for the module with different TE leg geometry than the commercial Bi_2Te_3 module	134
Figure 80: A top-down view of the system efficiency vs. TE leg thickness and the fill factor (shading: dark $\sim 0\%$ efficiency, lightest $\sim 3.3\%$ efficiency), with the total TE volume used for different thickness and fill factors.....	135
Figure 81: System efficiency for optimized module and commercial module using same amount of TE material.....	136

Figure 82: Improved system performance achieved with the best research grade selective surface and ideal conditions (no module parasitics).....	137
Figure 83: ZT for MgSiSn – Sb doped taken from Ref. [132]	138
Figure 84: Performance of a new material (MgSiSn) module compared to Bi ₂ Te ₃ -based modules	138
Figure 85: Comparison of various energy generation sources such as heat engines with thermoelectric efficiency at different ZT and temperature range [Adapted from [161]].....	146
Figure 86: Solar (a) and crustal (b) abundance of elements according to their atomic number [Adapted from [165, 166]]	147
Figure 87: Price data collected from USGS and metalprice.com (*USGS report includes material purity for the price data; e.g. 99.6% purity for Antimony price).....	148
Figure 88: Price (\$/kg) vs. crustal abundance [Adapted from [167] (2009-2010 prices)].....	149
Figure 89: ZT vs. crustal abundance for bulk thermoelectric materials	151
Figure 90: Yb ₁₄ MnSb ₁₁ – crystal structure (www. thermoelectrics.caltech.edu/thermoelectrics/index.html)	152
Figure 91: Clathrate structure showing open framework (dark dots), with guest atoms in between [150]	153
Figure 92: Half-Heusler crystal structure (http://cst-www.nrl.navy.mil/lattice/struck/c1_b.html)	155
Figure 93: Na _x Co ₂ O ₄ - crystal structure (http://physicsworld.com/cws/article/news/17531)	156
Figure 94: MnSi – crystal structure (Nowotny-chimney ladder) ^[223]	157
Figure 95: Pictorial depiction of electron filtering in metal-semiconductor superlattice structure with phonon scattering at the interface.....	161
Figure 96: Theoretical estimation for ZT vs. conduction band edge for ZrN/ScN ^[233] ; Theoretical estimation for ZT for 6 nm HfN/ 6 nm ScN multilayer structures with different conduction band offset	162
Figure 97: Z-meter schematic showing a picture of the vacuum chamber within which the measure bar setup is held for high temperature experiments.....	165
Figure 98: Schematic of a Z-meter setup inside a vacuum chamber.....	167
Figure 99: Strain gauge on top of the Z-meter ensures low and reproducible thermal and electrical contact parasitics.....	167
Figure 100: Thermal equivalent circuit showing interface resistances and heat flow through the sample to the measure bar.....	168
Figure 101: (a) Active load for electrical resistivity and power measurement with current input setup, (b) Active load using low resistance power FET circuitry	170

Figure 102: Matched load resistance (\circ , \bullet) vs. thickness of MAM-Bi₂Te₃ samples to evaluate dry metal-metal contact parasitic, with a linear fit (----, ····) for power FET active load system and current source setup170

Figure 103: Equivalent electrical circuit depicting TE sample and system parasitics at maximum power condition with load matching171

Figure 104: Schematic for radiation error calculation from the measure bar due to the heater172

Figure 105: Radiated power measured for copper (\circ) and gold-plated (\bullet) measure bars at different heater temperatures and under different gap (z) conditions follow close to the theoretical prediction (solid lines)173

Figure 106: Seebeck coefficient and thermal conductivity measurement for n-type SiGe (JPL)175

Figure 107: ZT measurement for the n-type ErAs: InGaAlAs using the Z-meter in comparison to published result ^[43]176

Figure 108: (a) Thermal conductivity estimation for the TE sample in the case of no radiation suppression, compared to thermal conductivity measured with 3ω method ^[43]; (b) The measured thermal conductivity data vs. data from 3ω measurement ^[43]176

Figure 109: Seebeck coefficient (\circ) and electrical conductivity (\blacklozenge) measurement for the n-type ErAs: InGaAlAs sample177

Figure 110: (a) Efficiency and (b) power density measurement data (\circ) with theoretical estimations for different system parasitics at an average temperature of 614 K (- - - $R_{\text{parasitic}} = 0 \Omega$, — $R_{\text{parasitic}} = 3 \text{ m}\Omega$, ··· $R_{\text{parasitic}} = 5 \text{ m}\Omega$, — — $R_{\text{parasitic}} = 10 \text{ m}\Omega$)178

Figure 111: Generated power density for ErAs sample at different temperature gradient and average temperature increasing from 350 K to 575 K (Power density vs. temperature gradient is shown in the inset).....179

Figure 112: Bulk-laminate superlattice sample preparation order180

Figure 113: (Hf, Zr) N and ScN superlattice structure with 12 nm periodicity180

Figure 114: Samples (CuBond21) with gold shorts along the thickness of the superlattice structure181

Figure 115: Seebeck coefficient measurement for CuBond21 sample.....181

Figure 116: Polished nitride sample with visibly less gold shortenings between TE layers.....182

Figure 117: Modified Z-meter setup to decrease the temperature gradient across the TE sample182

Figure 118: Seebeck coefficient measured for the nitride superlattice structure183

Figure 119: Measured matched load resistance at various average temperatures.....184

Figure 120: HfN/ScN superlattice structure (120 μm thick sample).....184

Figure 121: Measured Seebeck coefficient (a) and thermal conductivity (b) for CuBond36 sample	185
Figure 122: Thermoelectric parameters for different earth-abundant TE materials in comparison to nitride samples measured in this research.....	189
Figure 123: Solar irradiation for different hours in a day over a year (location: Xining, China) [Ref. HOMER simulation: solar radiation data set provided by US NREL and NASA's Surface Solar Energy database].....	195
Figure 124: Solar flux dependence for the system efficiency for Bi ₂ Te ₃ and silicide material is shown. The total number of hours within a year for certain flux radiation is also shown as a histogram	196
Figure 125: Electricity cost variation for STEG using different module <i>ZT</i> ; as the module <i>ZT</i> increases, the system efficiency also increases which leads to lower electricity price; in order to achieve grid parity, the required module <i>ZT</i> for thermoelectrics is > 2	208
Figure 126: Y-form generator design from BSST Inc. that has lower	209
Figure 127: Survey result for lighting option during summer in Gajia village	215
Figure 128: Survey result for lighting option during summer in Serjia village	216
Figure 129: Survey result for (a) average monthly electricity bill; and (b) average electricity use (hours)	216

Chapter 1

Introduction

According to the World Bank's 2010 development report, 1.6 billion people living in developing countries have no access to electricity. Most of them live in South Asia (706 million) and sub-Saharan Africa (547 million), where they lack access to centrally produced electricity. As a result, the people in these regions rely heavily on inefficient sources of energy. A common source of power for cooking and heating is the wood burning stove, which has only 10% thermal efficiency, and for light is the kerosene lamp, which is 150 times less efficient than an incandescent light bulb. These dramatic inefficiencies for energy production and consumption in the developing world cost its resident as much money or in some cases even more than an affluent resident in the United States ^[1]. Due to rough terrain and uneven population distribution, central electricity production and transmission often becomes a difficult and expensive option. In such cases, "distributed generation" can be an ideal choice. In order to develop an efficient off-grid technology for electricity production in these remote regions, one would need to harness the natural resources readily available. Fortunately, these regions lie near the equator where the solar irradiance is high (1900 kW hr/m² yearly average) ^[2]. In this thesis, we have explored appropriate off-grid technology based on solar thermal energy for electricity production in the developing world utilizing solid-state thermoelectrics.

Even within developing countries, the need and demand for energy can vary from location to location. It is important to understand the energy usage of the community to address the generation issue. The availability of a small-scale distributed power generation can bring a number of benefits to a community:

1. reduced dependency on fossil fuel such as coal, kerosene and diesel
2. reduced dependency of wood, and time saving from fuel gathering
3. electricity generation in areas not served by the grid

In most industrial developed countries, electricity has become a basic necessity. In developing communities, electricity can play a vital role in improving the quality of life by providing residential lighting, power for communication systems such as televisions, radios, and cell phones and, can open doors for economic development in the community (water pumps for better irrigation systems, motors for

food processing mills and small craft industries) [3]. Consider the lighting application: a relatively cheap (< \$3) white light emitting diode (LED) can operate at 75 lumens for less than 2 W electrical power, whereas a candle or a single wick kerosene lamp gives less than 10 lumens of brightness (Table 1) [4, 5]. The highest efficiency white LED is claimed by Philips Lighting Co., with luminous efficacy of 115 lm/W. The cost of these high efficiency LEDs in bulk quantity (1,000+) is \$5. A small-scale power generator can be used in rural locations for powering a radio, or charging a cell phone (power requirement: 3-5 W at 12 VDC). It can also be used in a remote health center for vaccine refrigeration (power requirement: 7-12 W at 12 VDC) or for survey equipment support such as GPS system and data collection.

Lamp Type	Kerosene	Incandescent	Compact Fluorescent	W-LED
<i>Efficiency (Lumens/watt)</i>	0.03	5 - 18	30 - 79	25 - 50
<i>Rated Life (Hours)</i>	Supply of kerosene	1000	6500 - 15,000	50,000
<i>Durability</i>	Fragile and dangerous	Very fragile	Very fragile	Durable
<i>Power Consumption</i>	0.04 - 0.06 liters/hour	~ 5 W	~ 4 W	1 W
<i>\$ After 50,000 hours</i>	1251	175	75	20

Table 1: Comparison for various lighting sources (<http://www.lutw.org>)

Within a rural community, apart from the aforementioned basic needs for electricity, different beneficiaries can utilize the energy to fulfill different needs as shown in Table 2 [6].

Beneficiary	Energy need	Potential cost and consideration
<i>Farmer</i>	Water pump for irrigation, food processing	Reduce work-hours leading to reduced employment, social system restructuring
<i>Student</i>	Lighting for studying	
<i>Householder</i>	Lighting for housework, radio or television	Social system restructuring, reduce household work-hours
<i>Small business owner</i>	Lighting, small motors/machines for business	Market restructuring
<i>Regional administrators</i>	Health care, schools, street lighting, water purification	

Table 2: Common target groups for rural electrification

For this thesis, we worked closely with the communities in rural Western China. In order to assess the needs for the target group to understand the system requirement for power generation, we worked with a

non-profit organization - One Earth Designs Inc. Founded in 2007, the organization has various developmental projects ranging from water purification to the design and deployment of portable solar cookers in rural communities in Qinghai Province in Western China. **Table 3** lists some of the villages where OED is working; also listed at the bottom are 3 villages surveyed for this research. Within the province, nearly 100,000 households do not have electricity ^[7]. This accounts for nearly 20% of total rural households. The average net household annual income in the province is less than \$1300 ^[8]. The rural population can be divided into two categories based on life-style: agricultural and nomadic. Most agricultural villages have become grid connected in the past ten years. The heavily subsidized grid electricity cost in the province is 0.30–0.45 Yuan/kWh (~ 4.5–7 cents/kWh) ^[9]. However, many rural villages routinely experience unreliable power supply. Nomadic villagers travel for four-five months during summer season to high pasture land where there is no electricity. The cost of extension of the grid to a remote location can be as high as ~ \$3.50 kWh⁻¹ ^[8]. For such communities, distributed power generation can be a very reliable source of clean energy.

Village	Household	People per household	Current fuel source for cooking/heating	Electricity availability	Electricity usage
Mairi (agricultural)	51	5-7	Wood, dung, solar (cookers)	Grid	Lighting, cell phone, and television
Sitaj Gou (agricultural)	63	2-4	Dung	Grid	Lighting, cell phone, and television
Normgo (nomadic)	105	4-5	Dung, fossil fuel (motorcycle oil)	Solar (PV) - few	Lighting, cell phone
Awuju (agricultural)	42	3-4	Dung, fossil fuel (motorcycle oil)	Grid (intermittent)	Only ~ 30 minutes at night
*Gajia (nomadic)	100	4-5	Dung, petroleum products	Solar (PV) - few	Lighting, cell phone charging
*Serjia (nomadic)	27	3-5	Dung	Solar (PV) - few	Lighting, cell phone charging
*Gangta (agricultural)	38	3-5	Dung, wood	Grid	Lighting, cell phone, television

Table 3: Different villages in Western China where OED is working

*villages where survey and field trials were done for this research

The need for electricity in most of these remote places is dominated by lighting application. As mentioned earlier, the total electrical output power necessary to reliably light a bulb or charge a cell phone is less

than 10 W. A generator capable of supplying 10-20 W of electrical power can be enough for a single household for their basic electricity need. In this thesis, we have worked on designing and building a portable power generation system utilizing available solar cookers and solid-state thermoelectrics for thermal-to-electrical energy conversion.

In the next section, we will introduce some of the prominent solar based technologies used for electricity generation such as photovoltaics (PV) and solar thermal. The concept of solar thermoelectrics will be introduced in Section 1.2. Brief descriptions of different components of a solar thermoelectric system will be presented in this section. Previous work on solar thermoelectrics will be discussed in Section 1.3, with the thesis preview at the end of the chapter.

1.1 Solar engineering in developing countries

Solar energy has been used previously in different systems for both large (> 1 kW) and small scale (< 100 W) electricity generation. Apart from providing energy for electricity, solar energy is also widely used in developing countries for applications such as solar cookers and solar water heaters. Solar cookers provide thermal energy for cooking purposes and solar heaters are used for heating water and homes. More details on the solar cooker technology will be discussed in Section 1.2.2. In the following section, a comparative study for various electricity generation schemes using solar energy and other sources is presented.

1.1.1 Photovoltaics

One of the most prominent solar technologies for remote electricity generation is photovoltaics (PV). Silicon based solar panels have been leading the field of rural electrification for more than three decades. However, given the large number of people who do not have access to electricity, the use of solar energy for electricity generation is minimal. Due to relative low module cost ($\sim \$2$ - $3/W$), amorphous silicon (a-Si) and multi-crystalline silicon photovoltaic panels have been deployed in many parts of the world by governments, private companies as well as non-profit organizations and International Charities like Isofoton, Selco India, Light Up The World Foundation, SOLUZ, the Solar Electric Light Fund and SolarAid. PV offers the freedom from fuel prices with the additional benefits of low maintenance costs and high reliability – both essential for the developing world environment ^[10]. Many international organizations (United Nations, World Bank, International Energy Agency, International Finance Corporations, and Global Environmental Facility) and multi-national companies such as BP Solar and General Electric (GE) do not have a business model for distributing solar panels in developing countries,

and they rely heavily on donor-funds and government subsidies for supporting the electrification programs in these regions. Non-profit organizations such as Selco India, SOLUZ and LUTW have taken advantage of a micro-credit finance system to offer their products (individual solar home systems – SHS) to people in rural areas who cannot afford to pay the upfront cost of solar panels. In Bangladesh, Grameen Bank has financed 400 PV installations with 8% interest rate for 2 years, with 25% down payment requirement. Similarly, Genesis in Guatemala provides 3-year loan at 15% interest rate for PV installation^[11]. At relatively high interest rate ranging from 5-15%, the total cost of the system over a long period of time (3-5 years) adds up to make it a very expensive power generation option. For example, a 5 W solar panel from LUTW cost more than \$50. The price for a system including 2 LEDs, a charge controller, a 5 W solar panel and a lead acid battery is \$217. With micro-finance, people can pay back in small portions (~ \$5-10 /monthly) over a long period of time, and the idea being this monthly payment can be similar to what they would be paying for lighting with inefficient sources. Since early 2000, more than 50 MW (total) of PV has been installed annually in developing countries with the growth rate of 6-10%. It is estimated that more than 2 million individual solar photovoltaic systems are presently installed in rural areas worldwide^[12]. Mainly due to high module cost, the single-crystalline silicon panels have a marginal share in the developing countries' market. Single-crystalline silicon has the highest efficiency (15-19%) for a non-concentrating commercial system, but the module cost is expensive (1.5x) compared to amorphous silicon or multi-crystalline (7-15%). For any electricity generation system, the levelized cost of electricity (LCOE) is generally the ultimate comparison metric. The LCOE depends on performance, system cost and ongoing operation and maintenance over the lifetime of a system. Lower conversion efficiency of a-Si PV means that the LCOE is higher than that for single-crystalline PV (35 cents/kWh vs. 20 cents/kWh). However, the larger distribution share of a-Si PV in the developing countries indicate that more than LCOE, the steep up-front system cost is a bigger market barrier. For the cost modeling of the generator in this research, both the system cost (\$/W) and the LCOE (cents/kWh) are considered and described in Chapter 6.

Recently, thin-film photovoltaics have emerged as a growing technology in the western developed countries with more than 1 GW yearly module production using mostly Cadmium Telluride solar cells at 11% efficiency^[13]. Thin-film a-Si PV also has efficiency in the range of 10-12%. Thin-film technology indicates lower system cost by cutting the amount of semiconductor material used in the solar panel, thus giving the LCOE ~ 14 cents/kWh^[14]. However, stability and performance degradation have been the main issues for thin-film a-Si PV, where the degradation is caused by light-induced metastable changes in the properties of hydrogenated amorphous silicon^[15]. Even though, bulk silicon PV is a mature technology for distributed generation compared to new thin-film technology, the overall power cost in

developing countries is very expensive (\$10/Watt); there might be other options, which have cheaper upfront cost than PV.

1.1.2 Concentrated photovoltaics

Another emerging solar technology is the concentrated photovoltaics (CPV), which offer very high efficiency (~ 38%) (SolFocus Inc.) not achieved with commercial silicon PV panels (7-19%). A highly efficient solar concentrator (~ 80%), with sophisticated tracking system can focus solar intensity equivalent to 500x suns (1x sun = 1000 W/m²) on a multi junction solar cell (III-V material system) to achieve high conversion efficiency. The solar cells in such concentrated systems have to be cooled very well in order to keep their temperature within the operating regime. The cooling mechanism adds to a large upfront cost to the system. The smallest commercial concentrated PV is in the range of 1 kW generation scale. The overall electricity cost for high concentration PV can be lower than that for a flat-plate silicon PV as less expensive semiconductor material is required. A solar collector is less expensive than an equivalent area of the solar cell. A US based company (Sunrgi LLC) had claimed in 2008 to have CPV that can provide electricity at the wholesale price of 5 cents/kWh which is nearly equivalent to the wholesale electricity price for fossil fuel. However, it has not been available in the market yet. The current pricing for CPV is ~ 25 cents/kWh (similar to the non-concentrated silicon PV pricing). The high pricing has been attributed to the small scale of projects. From the economic perspective, usage of CPV for electricity generation is cost effective only for medium or large scale generation (greater than 5kW)^[16, 17]. This might not be a feasible solution in developing countries for small remote communities or single households for power generation of less than 1 kW.

The use of rare-earth materials or toxic compounds in photovoltaic modules can be an unattractive feature for the power generation system. The extensive recycling and toxic material handling program at the end of the lifetime of the module can add extra cost to the system. Thin-film PV cells have either rare-earth materials such as tellurium or toxic elements such as cadmium, CPV cells have arsenic (III-V cells). This can make thin film PV and CPV unattractive for power generation applications. Apart from high cost and material issues, PV is seasonal and without the possibility of hybrid use, i.e. they cannot be used during cloudy/rainy days or during night times with other energy sources. We have to look for solutions other than photovoltaics.

1.1.3 Hybrid systems

A hybrid system of PV and thermoelectric generator (TEG) has been explored, where the solar cell is the primary electricity generator and TEG is used for waste heat conversion^[18-20]. This is an expensive

solution for energy generation as the cost includes both PV and TEG; furthermore the TEG is used well outside the optimal (high) temperature range. Another technology that has evolved in the energy sector utilizing solar thermal energy is the solar thermophotovoltaics (TPV). Unlike photovoltaics, this system utilizes thermal radiation. The main components of the system are: solar absorber, selective emitter and photovoltaic cell (Figure 1). The solar absorber is heated by the concentrated sunlight. The selective emitter behind the absorber re-radiates at particular wavelength range depending on its temperature. The photovoltaic cell is optimized to work at these wavelengths by choosing the material with correct band gap. The theoretical efficiency for an ideal concentrated solar thermophotovoltaics can be as high as 80-85% [21, 22]. The system efficiency depends on the solar concentration ratio and the band gap of the solar cell. Practical systems with thermal and optical losses have been demonstrated with system efficiencies of 10-16% [18-20, 23, 24]. Most of the materials used for thermophotovoltaics have band gap around 0.5-2 eV [20]. Efficient thermal radiation from the emitter in this range requires emitter temperature to be above 2000 K. High solar concentration (more than 500x) is necessary to get to such temperature regime. This puts constraints in the solar collector design; either the area has to be large to increase the concentration ratio or expensive optics and tracking systems have to be utilized to achieve desired temperature for the emitter. Often times, rare-earth oxide ceramics (Ytterbium, Erbium etc.), or expensive metals such as tungsten are used for the selective emitter to re-radiate at the desired wavelength for photovoltaics.

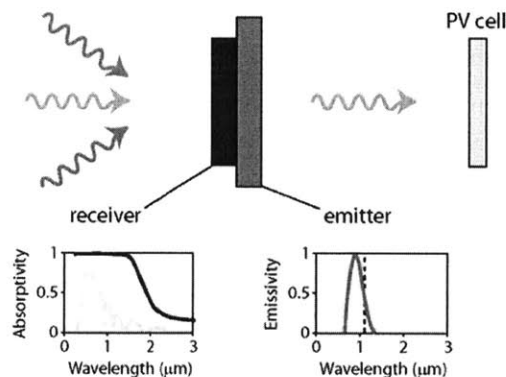


Figure 1: Conceptual representation of solar thermophotovoltaics (www.gcep.stanford.edu)

1.1.4 Solar thermal

The other options for power generation involve utilizing solar thermal energy. Depending on the generation scale, people have looked at various technologies: Solar heat engines, solar thermophotovoltaics or solar thermoelectrics. For large scale systems (greater than 5 kW), it has been proven to be significantly cheaper to use the energy from the sun to drive a mechanical heat engine such as Brayton or Stirling engine [25] (solar-thermal-mechanical-electrical conversion). The efficiency of the

heat engine decreases dramatically when they are miniaturized as the thermal losses become significant [25]. Thermal insulation between the heating wall and the cooling wall becomes difficult due to large surface area per unit volume as the device is scaled down [26]. The friction force for the piston and the displacer also becomes significant as the output power decreases [26]. Heat engines can give high conversion efficiencies: 27% efficient at 1,100 K for a Stirling engine and 14.6% efficient at 1,300 K for a Brayton engine with solar concentration for a 5 kW generation [25]. For a smaller generation scale (1 kW), the conversion efficiency for a Stirling engine is only 5.5% [27]. The size of the solar collector for concentration also depends on the desired output power. For a 5 kW system, the dish size is approximately 5.5 meters in diameter [28]. Similarly for a 10 kW system, the dish size is 10 meters [28]. Such large systems are not appropriate for residential applications due to excess land usage. Another system for electricity generation is a solar tower that concentrates sunlight using reflectors (heliostat) to heat the working fluid for heat engines. These have been implemented in countries such as Spain for electricity generation. They are large scale mega watt range power plants. The heat engines have a large number of moving parts that can make them unreliable and have significant maintenance cost. Thus, this might not be a suitable option for distributed electricity generation in developing countries.

Lastly, solar thermoelectrics also utilizes solar thermal energy for direct electricity generation by taking advantage of the temperature gradient across a solid-state semiconductor. Unlike photovoltaics whose efficiency decreases with the rise in module or cell temperature, the performance of a thermoelectric generator increases with higher temperature. At this generation scale of 10-20 W for single household type applications, we have designed and built a solar thermoelectric system based on solid-state thermoelectric generation. Such a system can be a cost effective and a viable option for direct conversion of solar thermal energy to electricity, providing an alternative to PV for remote electrification. A thermoelectric generator has the potential of hybrid operation with solar energy during the day time and other heat sources such as conventional cooking stove for night time utilization and non-sunny days. Even though the overall conversion efficiency for TEG is low, with higher temperature, the efficiency rises and we have looked into ways for increasing the temperature and overall output power performance of the generator through various loss-suppression designs, module redesigning and new material exploration. **Table 4** lists all the options for electricity generation using solar energy, showing maximum efficiencies and generation scales where they work the best.

1.1.5 Others

For completeness, other popular non-solar off-grid power generation sources in developing countries were also studied, namely: diesel generators and micro-hydro power plants. People, who can afford to pay

a large upfront cost, buy diesel generators, which burn petroleum products. The price fluctuation and scarcity of fossil fuels in remote locations is the biggest disadvantage for diesel generator. Even though the rated lifetime of the engine can be more than 20,000 hours, due to many moving parts within the machine, constant maintenance is required. The levelized electricity cost of using a diesel generator is ~\$1/kWh^[8]. Micro-hydro power generators (~ 5 kW) can be an efficient option for small communities with proper resources i.e. high volume of water flow. The efficiency and electricity price depends on resources such as water flow and head between intake and power house. For generation less than 1 kW, the electricity cost is more than \$5 per watt with the LCOE ~ 40 cents/kWh^[29], which makes it an expensive option for smaller scale approaches. Due to moving parts in the machinery, the maintenance cost is high. Other small-scale options such as hand-cranked dynamos have been commercially available as electricity generator for LED lights or radios. Although it relies on human power and not on any feedstock or weather, the technology is considered labor-intensive, and many times customers do not find it an appealing way to generate power. Village Tech Solutions' bicycle-powered generator (30-50 W) in Nepal was unsuccessful when it was found that there were cultural barriers to pedaling. People did not like pedaling for a long time (30 minutes – 1 hour) continuously. Especially village women did not feel comfortable in the position of pedaling^[30].

Technology		Generation scale	Efficiency (max)	Temperature (K)	Electricity Price (LCOE: \$/kWh) (US market)	Comment
Solar photovoltaic (PV)	Single-crystalline Si	5 – 300 W	24.7%	313 (max)	0.20	UNSW
			19%			SunPower ^[13]
	Single-crystalline Si	50 kW	27.6%		0.15	Amonix ^[13]
	Concentrated: Fresnel lens					(utility scale)
	Multi-crystalline Si	5-300 W	20%		0.25	Commercial modules ~ 10-15%
	Amorphous Si	5-300 W	15%		0.35	Commercial module ~ 7-10%
	Multi-junction		40.7%			Spectrolab
	Thin Film		19.9%			NREL ^[13]
	(a-Si)	> 30 kW	12%		0.14	United Solar (Commercial-12%)
			16%		0.15	Fist Solar (Commercial-11%)
				(utility scale)		
	Concentrated PV	100 kW – 50 MW	38%	328 (max)	0.25	SolFocus Inc.
Concentrated	Parabolic trough	> 1 MW	16%		0.15	
Solar thermal	Dish Stirling	150 kW	31.25%	900-1100	0.12	Sandia Nat. Lab
	Solar tower	> 1 MW	17%	700-1000	0.13	
	Brayton engine	> 5 kW	15%	1300		
Thermophotovoltaic (TPV)			16%	> 1000		
Solar thermoelectric (STEG)			4.6%	500		

Table 4: Comparison for various electricity generating systems^{[20, 25],[31],[32-35]}

1.2 Solar Thermoelectrics

The concept of the conversion of sunlight to electricity utilizing solid-state thermoelectric devices is the basis for solar thermoelectrics. Thermoelectric devices can offer a low-cost thermal micro-power system for remote communities without grid option. Our objective was to develop a thermoelectric system specifically designed for thermal-to-electrical power conversion that is simple and inexpensive enough to be used by the poorest communities. Direct or concentrated sunlight can be used to provide the input thermal energy. In most cases, the efficiency of a thermoelectric system increases with the rise in temperature. Concentration systems can provide large heat flux for high temperature with relatively small area coverage. A solar thermoelectric generator (STEG) employing light concentrators and modules with high figure-of-merit thermoelectric materials are an attractive alternative to solar photovoltaic for small-scale power applications. With an optimized heat sink, a thermoelectric generator can be utilized with a solar concentrator to produce relatively small but zero-marginal cost electrical power. The main concepts of solar thermoelectrics: thermoelectricity, solar concentration, selective surface and heat sinks are introduced here.

1.2.1 Thermoelectricity

Thermoelectricity is based on the Seebeck effect ^[36], according to which, a temperature variation across a material can give rise to an electrostatic potential difference ^[36]. Charged electrons/holes for n/p-type material move away from the hot side towards the cold side (**Figure 2**). When this temperature-induced voltage is applied across a resistive load, useful electric power is generated.

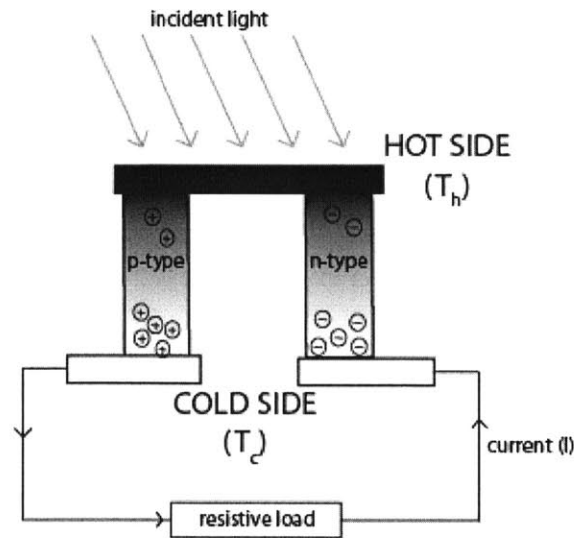


Figure 2: Charge distribution in a thermoelectric material due to temperature gradient causes potential difference. In the n-type material, electrons move from hot to cold side. Similarly, in the p-type material, holes move towards the cold side.

1.2.1.1 Basic principle

The Seebeck effect can be understood as the entropy transported per unit charge of a material ^[37]. When a temperature gradient is applied across a material, free carriers diffuse from the hot to cold side creating density variation. In thermoelectric (TE) material, as these carriers are charged (holes/electrons), the density variation leads to a voltage difference between the hot and cold sides. In semiconductor, both electron and hole contribute to the Seebeck effect but with opposite signs. Thus, in order to have a large Seebeck effect, the TE material should have a majority charge carrier contributing to the voltage gradient.

The magnitude of the thermoelectric emf (ΔV) is directly proportional to the temperature variation (ΔT) across the element, and the Seebeck coefficient (S). The relationship defined by the Seebeck effect is given by $S = -\frac{\Delta V}{\Delta T}$. The temperature gradient across a thermoelectric material for a given heat flux is

governed by the material's thermal conductivity (κ). When the temperature induced voltage is applied across a resistive load, useful electrical power is generated which depends on the electrical conductivity (σ) of the material and the load itself. Thermoelectric materials are characterized with a figure-of-merit: $ZT = (S^2 \sigma) T / \kappa$, where T is the average material temperature ^[36]. In order to have high ZT , the

□□□□□ñ□□□□□□□□□□□□□□□□

(similar to glass or wood). Due to very low electrical conductivity, insulators are not good thermoelectric materials. Metals are also not good thermoelectric materials due to low Seebeck coefficients and high

thermal conductivities. Typically, semiconductors and semi-metals such as Bismuth Telluride, Lead Telluride and Silicon Germanium (SiGe) are used as thermoelectric materials. **Table 5** summarizes typical values for thermoelectric properties for metal, semiconductor and insulator ^[38].

Metals	Semiconductors	Insulator
$S \sim 5 \times 10^{-6} \text{ V/K}$	$S \sim 200 \times 10^{-6} \text{ V/K}$	$S \sim 1000 \times 10^{-6} \text{ V/K}$
$\sigma \sim 10^8 \Omega^{-1}\text{m}^{-1}$	$\sigma \sim 10^5 \Omega^{-1}\text{m}^{-1}$	$\sigma \sim 10^{-10} \Omega^{-1}\text{m}^{-1}$
$\kappa \sim 10\text{-}1000 \text{ W/m K}$	$\kappa \sim 1\text{-}100 \text{ W/m K}$	$\kappa \sim 0.1\text{-}1 \text{ W/m K}$
$ZT \sim 10^{-3}$	$ZT \sim 0.1\text{-}1.5$	$ZT \sim 10^{-14}$

Table 5: Comparison at room temperature of the thermoelectric properties of metal, semiconductor and insulators

A thermoelectric generator (TEG) module is made from n- and p-type materials, connected electrically in series and thermally in parallel (**Figure 3**). The temperature gradient across the legs causes the charges to move from the hot side to the cold side. This leads to the voltage build up, which drives a current (I) through the resistive load when it is connected as shown in **Figure 2**. More than one couple is used in a commercial generator to increase the output voltage, since the Seebeck coefficient for most of the thermoelectric materials are in the range of hundreds of micro-volt per Kelvin. There are various other factors, apart from the number of couples that determine the generator design such as the thermal impedance of the heat sink, the resistive load, the geometry of thermoelectric element (area/thickness), and the total module area. These parameters have been considered for the generator design for the distributed power application and are described in Chapter 2.

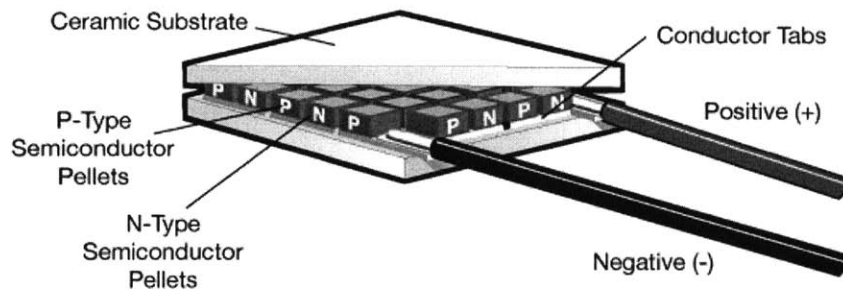


Figure 3: Thermoelectric module with more than one couple of n- and p-type legs connected electrically in series between ceramic substrate

The TEG can be optimized for either the maximum efficiency or the maximum power. The mode of operation depends on factors such as the quality of fuel used for the heat flux (economic consideration). For a high quality premium fuel, the operation is towards achieving maximum efficiency ^[39, 40]. On the other hand, for applications where the heat source could be considered unlimited or free, maximizing the

output power becomes the optimizing criteria. The conversion efficiency (η_{TEG}) for a TEG for the maximum output power is given by Equation 1 [36, 39], where T_h is the hot side temperature, T_c is the cold side temperature and η_c is the Carnot efficiency ($= (T_h - T_c)/T_h$).

$$\eta_{TEG} = \frac{\Delta T}{2T_h - \Delta T/2 + 2(T_h + T_c)/ZT} = \eta_c \frac{1}{2 - \eta_c/2 + 4/ZT_h} \quad (1)$$

The maximum power is achieved when the load resistance (R_L) is equal to the internal resistance (R_{int}) of the TEG. The maximum power ($P_{gen,P}$) at the matched load condition is given by

$$P_{gen,P} = \frac{(T_h - T_c)^2 S^2}{4R_{int}} \quad (2)$$

For the maximum efficiency, the optimized load resistance varies from the total internal resistance of the TEG by a factor $x \left(= \left(1 + Z \left(\frac{T_h + T_c}{2} \right) \right)^{1/2} \right)$ [39]. The efficiency in such a case is given by:

$$\eta = \left(\frac{T_h - T_c}{T_h} \right) \left[\frac{x - 1}{x + \frac{T_c}{T_h}} \right] \quad (3)$$

The maximum power versus maximum efficiency behavior is shown in **Figure 4**. To generate the following curves, $T_h = 300^\circ\text{C}$, $T_c = 30^\circ\text{C}$, and R_L is varied between 0 to 100 Ω . Typical values for a TEG module is used to obtain the output power and efficiency where $S = 0.05$ V/K, $R_{int} = 3$ Ω , and thermal impedance = 1.5 K/W giving $ZT \sim 0.5$. With infinite ZT curve, it is evident that the highest power would be at reduced efficiency. For typical ZT values ~ 1 , the points of the highest output power and the highest efficiency are relatively close.

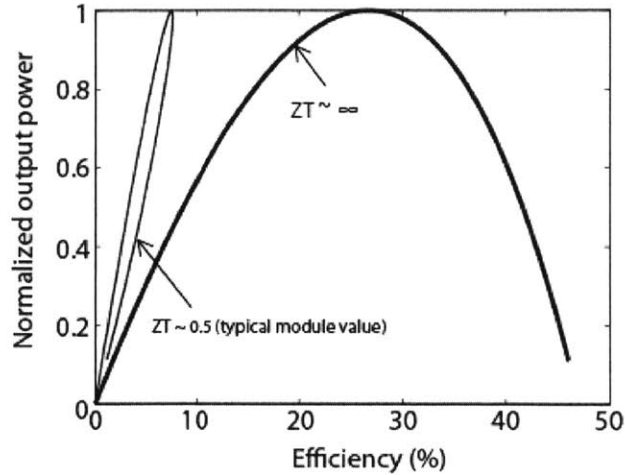


Figure 4: Normalized output power vs. efficiency for a TEG with varied load resistance (R_L) for different ZT values

For this particular application of electricity generation, we looked into getting the maximum output power from a given TEG module for a low quality free heat flux source. Performance and design curves will be discussed in detail in Chapter 2.

1.2.1.2 Thermoelectric applications

Primarily, thermoelectrics were used for deep space exploration as power generators: radioisotope thermoelectric generator (RTG) since the 1960s. For the Apollo and Voyager missions, thermoelectric materials were used for the power supply (~ 350 W). Thermoelectrics are still powering spacecrafts such as Cassini launched more than a decade ago. These applications exemplify the reliability for thermoelectrics, which have no moving parts, thus there is virtually no maintenance required for these generators. The conversion efficiency for these RTGs is in the range of 7-10%, mainly due to high operating temperature of nearly 1000 K provided by the radioactive isotope at the core of the RTG. The commercial development of the technology for terrestrial low temperature application has been hampered by relatively small efficiency (~ 3 -5%) for bulk thermoelectric material.

In the last two decades, the field of thermoelectrics has seen a growth in research interest due to the advancement in material properties ^[41-48] and also due to the need for alternative energy sources rather than the fossil fuel. Even though, the conversion efficiency for thermoelectrics are lower compared to all other energy generation processes such as diesel generators, nuclear reactors, photovoltaics, steam engines etc., there are some niche market areas where thermoelectrics have been able to show huge potential. After space programs, thermoelectric systems have been designed to operate within automobiles or naval vessels for energy harvesting or cooling purposes. The use of thermoelectrics for waste heat

recovery in vehicles can improve the fuel economy by 5% [49]. Waste heat recovery in large industrial settings (aluminum smelters) [50] and body powered electronics utilizing thermoelectrics [51] are some of the recent applications for power generation (Table 6). Thermoelectric commodity market has been dominated by cooling applications, i.e. thermoelectric coolers (TEC). These devices are used for cooling many electronics such as lasers, detectors, sensors etc. Luxury items such as compact refrigerator, automotive climate control car seats are few other applications of thermoelectrics. In this thesis, we have explored the potential of thermoelectrics as a viable option of small-scale portable power generation for remote off-grid communities. With the benefits of no noise, no moving parts, and low maintenance, a thermoelectric (TE) generator, can be an attractive alternative power source for such application.

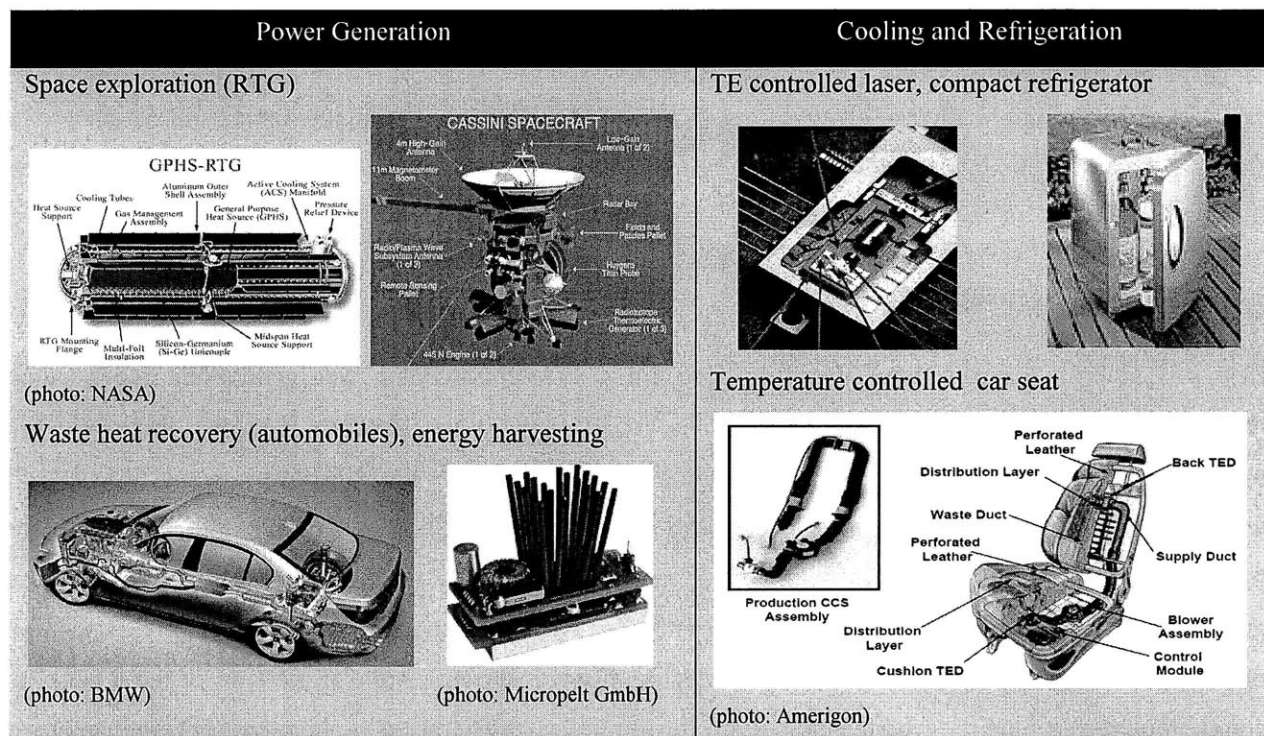


Table 6: Various applications of thermoelectrics in power generation and cooling

1.2.1.3 Thermoelectric material

Commercial thermoelectric modules are made from n- and p-type Bismuth Telluride. It is a well-studied bulk thermoelectric material, which has shown good thermoelectric properties ($ZT \sim 1$) at low temperature range ($T_{avg} \sim 300-400$ K) with module efficiency up to 5% [52]. Figure 5 shows some of the other advanced thermoelectric materials that have been studied and well characterized at different temperature ranges [53]. Among bulk materials, Bi_2Te_3 is the most common material at low temperature (300-400 K), followed by Lead Telluride with $ZT < 1$ at 400-600 K. Similarly at higher temperature ($>$

800 K), Silicon Germanium (SiGe) has been used for large scale space application. Depending on the solar intensity, concentration factor, and system thermal impedance, the temperature at the hot side of the TEG can vary. For the application of small-scale power generation, the interesting temperature regime is within 300-500 K. We started with system design and implementation using Bi_2Te_3 modules to show the system performance. At hot side temperatures above 500 K, materials other than Bi_2Te_3 have to be explored, due to its degrading performance (Figure 5). Other novel TE materials were studied during this research for optimization and will be discussed in detail in Chapter 5.

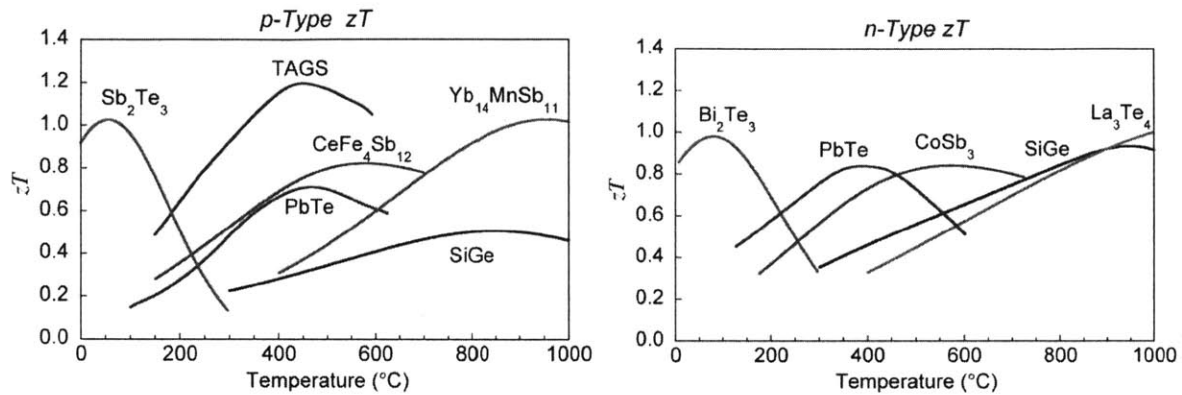


Figure 5: ZT for n- and p-type materials at difference temperature range ^[53]

As mentioned in the case of PV, the material issue in terms of availability and toxicity is also present for thermoelectrics. Tellurium used in many thermoelectric materials is a rare-earth element. In terms of material usage, a non-concentrating PV module using silicon gives ~ 0.2 watt per gram of silicon. For thin film PV, the material usage is ~ 14 watts per gram of tellurium ^[54]. For a commercial thermoelectric module, currently this number is ~ 0.35 watt per gram of bismuth and ~ 0.55 watt per gram of tellurium ^[55]. The annual tellurium production is only ~ 170 -200 tons (USGS data). For a potential high volume thermoelectric application such as rural electrification, rare material usage will play a critical role, not only in terms of material scarcity but also due to price fluctuation caused by it. Novel materials such as oxides (Cobalt, Lanthanum) ^[56, 57] and silicides (Magnesium, Manganese) ^[58, 59] are currently being explored by multiple research groups as potential useful thermoelectric materials due to their abundance and benign nature. In this thesis, we have researched the earth-abundance and thermoelectric behavior of various materials. Thermal and electrical characterizations for novel materials have been explored and will be presented in Chapter 5.

1.2.2 Solar concentration

In solar thermoelectrics, an important component is the solar collector for heating the thermoelectric material. Flat-plate solar collectors (concentration ratio $C = 1$) have been studied with thermoelectrics [31, 35]. Here we have looked at optical concentrators to increase the heat flux and thus the performance of the generator. Solar concentrators have been widely studied in various engineering fields [60-63]. They range from complex systems such as using optical fibers [25] to simple geometric shapes such as parabolic dish reflectors. A concave dish reflector and semi-cylindrical trough are examples of concentrating solar collector. A system with a Fresnel lens is based on refraction, and mirrors use the principle of reflection for concentration. Many simple designs such as parabolic reflectors are based on optical imaging, where the sunlight is reflected to a focal point to increase the intensity at that particular spot (absorber) (Figure 6). The parabolic troughs used for solar thermal power plants are based on this design. Due to single reflection, the acceptance angle is relatively small and a tracking system is needed in this kind of solar collector to get efficiencies above 70% [64]. The concentration ratio and subsequently the maximum achievable temperature at the absorber depend on the size of the collector.

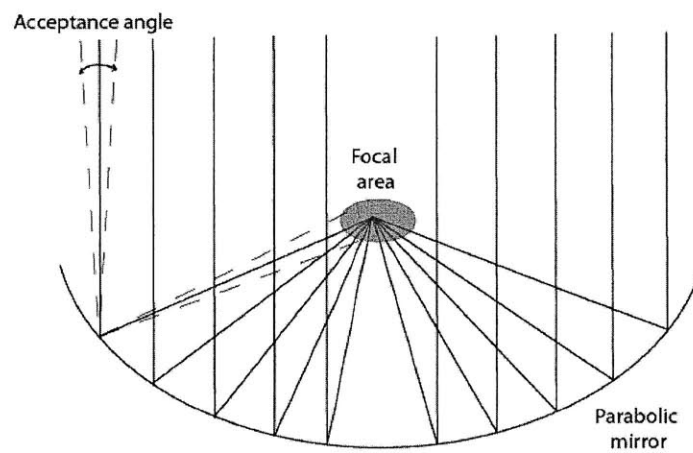


Figure 6: Geometry of a parabolic collector showing small acceptance angle and focal spot

Another technique for designing the concentrator is non-imaging optics, which has led to very efficient solar collectors (more than 80%) [65]. A compound parabolic collector (CPC) (Figure 7) is an example of non-imaging concentrator where the incident radiation within a wide range of angles can be reflected to the absorber at the bottom of the collector via multiple reflections [66, 67]. For a given acceptance angle, the concentration ratio of such a compound parabolic collector can be a factor of two or four more than other conventional solar collectors (trough, parabolic dish, lens, reflecting mirrors etc.), but a large reflector area is required. A combination of a parabolic mirror, a secondary reflective mirror and a CPC (optical rod) can give very high concentration (500x) (SoIFocus Inc.) [65]. There is a trade-off between the concentration ratio and the acceptance angle. If the acceptance angle is decreased, a tracking system is

required to maintain the high concentration ratio ^[68]. The relationship between the concentration ratio (C) and the half acceptance angle (θ_c) is given by ^[69]:

$$C_{(ideal_2_dim)} = \frac{1}{\sin \theta_c} \quad (4)$$

$$C_{(ideal_3_dim)} = \frac{1}{\sin^2 \theta_c} \quad (5)$$

In a CPC, the large acceptance angle allows for concentration without a tracking system. This system can concentrate solar energy even on cloudy days as diffused light can be focused into the absorber. However, the concentration for a large angle such as 70° is very small $\sim 2x$. To increase the concentration, the acceptance angle has to be decreased. The shape of the collector will be narrower and as the acceptance angle decreases, the need for tracking increases.

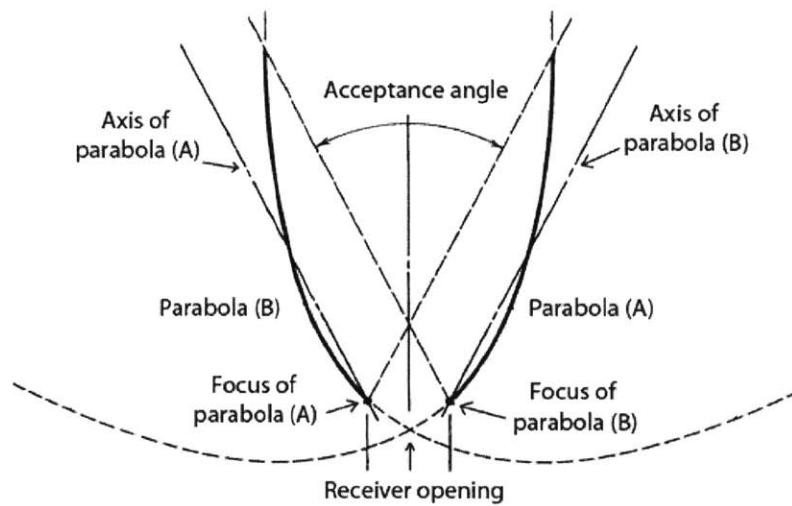


Figure 7: Geometry of a compound parabolic collector showing a large acceptance angle

The half acceptance angle of the sun is $\sim 1/4^\circ$, thus, the maximum concentration achieved from an ideal three-dimensional concentrator is $\sim 45,000$. The second law of thermodynamics limits the highest possible ideal absorber temperature to the sun's temperature at 6000 K ^[69]. Similarly for a two-dimensional concentrator (cylindrical, trough-like) the highest concentration is 213, with absorber temperature limited to 1570 K ^[69]. **Table 7** summarizes the properties of different types of solar concentrators.

	Concentration	Acceptance angle	Tracking	Efficiency	Cost (\$/m ²)
Paraboloidal dish	$1/4 C_{(ideal_2_dim)}$	1-7 °	Two-axis	65-70%	50-300
Trough/Cylindrical	$1/4 C_{(ideal_2_dim)}$	1 °	Single-axis	55-60%	150-300
Heliostat (Fresnel reflector)	$1/6 C_{(ideal_2_dim)}$	35 °	Single-axis	75%	170
Compound Parabolic Concentrator (CPC)	$C_{(ideal_2_dim)}$	~ 70 °	$C < 5$ (no tracking required) Two axis tracking for higher concentration	> 80%	

Table 7: Comparison for various concentrators ^[69-74]

A metal reflector can be a cheap source of concentrated solar energy in developing countries. These reflectors can be of various sizes and configurations. They can be easily mass produced and can be made portable ^[25]. Solar cookers used in many developing countries are a good example of such a concentrator technology (Figure 8). Widely deployed solar cookers such as the SK-14 solar concentrators (1.5 m² area) deliver approximately 600 W of thermal power to a 28 cm diameter focal spot (irradiance ~ 10x suns). According to an international organization involved in distributing solar cookers (<http://solarcookers.org>), there are more than 3 million cookers used worldwide, mostly in rural parts of China, India and African sub-continent. People in more than 90 countries use solar cookers that are distributed or sold by hundreds of NGOs working in the field. The cooker design varies from box-style cooker to parabolic shape. The large number of solar cookers in many rural locations of the developing nations makes the concept of solar thermoelectrics utilizing solar collector appealing in both application scope and economics. Thermoelectric generators using such solar concentrators offer the reliability of solid-state systems with low maintenance costs.

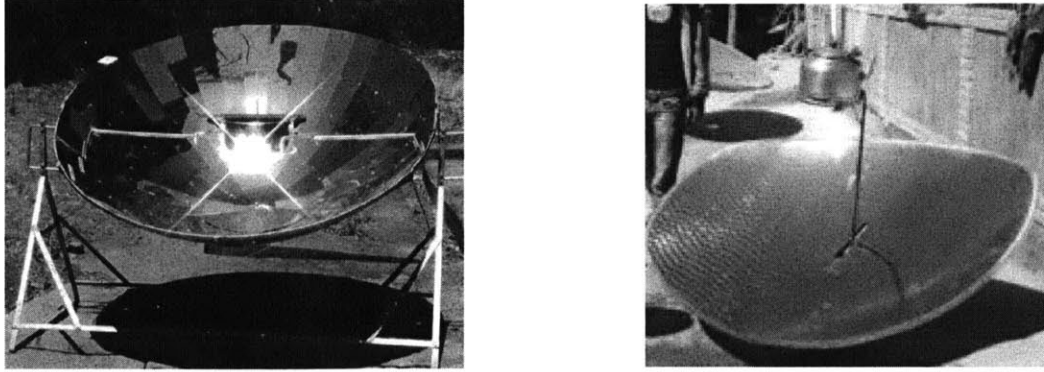


Figure 8: SK-14 solar cooker (popular in South Asia; designed in Germany); concrete solar cooker (popular in Western China)

For this work, the STEG system is compatible with manual pointing as the electrical tracking systems add to the cost and an additional electrical power (5-7 W) is needed for tracking circuit board. The concentrator cost can increase by 30-40% with a two-dimensional electrical tracking device (\$72 vs. \$100 for metal reflector cooker with and without tracker). The overall thermal input power can increase by only 20-25% with automatic tracking versus manual tracking done every 15-20 minutes (as shown in Chapter 3). Relatively cheaper mechanical tracking systems can add reliability issues and increase maintenance cost due to lots of moving parts. Manual tracking is feasible for small scale systems as has been demonstrated by the solar cooker application. For the simplest electrical application such as battery charging, the time can be sufficiently short (less than 20 minutes for 300 mAh rechargeable AA battery at nominal voltage of 1.5 V) ^[75] such that efficient, and reliable charging can occur without strict requirements on tracking. Successful system level implementation of STEG has been demonstrated with these local concentrators. The system trials are described in Chapter 3.

1.2.3 Selective surface

A solar concentrator directs the sunlight on to a fixed focal spot. The hot side for a thermoelectric generator placed at this spot heats up as it absorbs the concentrated sun light. A “selective surface” on the hot side of the generator has high (> 90%) absorbance from 300 – 1000 nm ^[76]. This allows the hot side to absorb most of the incident solar energy. The concept of selective surface has been tested with other solar related application, namely in solar water heaters. The ‘black paint’ layer on top of the absorber allows most of the solar energy (within the visible spectrum) to be absorbed while reducing re-radiation of thermal energy from the hot surface. The solar spectrum is mainly between 300 nm and 2.5 μm , while the blackbody spectrum at a temperature below 600 K is almost exclusively at wavelengths longer than 3 μm as shown in **Figure 9**. The emissivity of the selective surface layer is wavelength dependent: with high

absorbance in the visible spectrum and low emissivity at the longer thermal radiation wavelength, such that radiation loss is minimized.

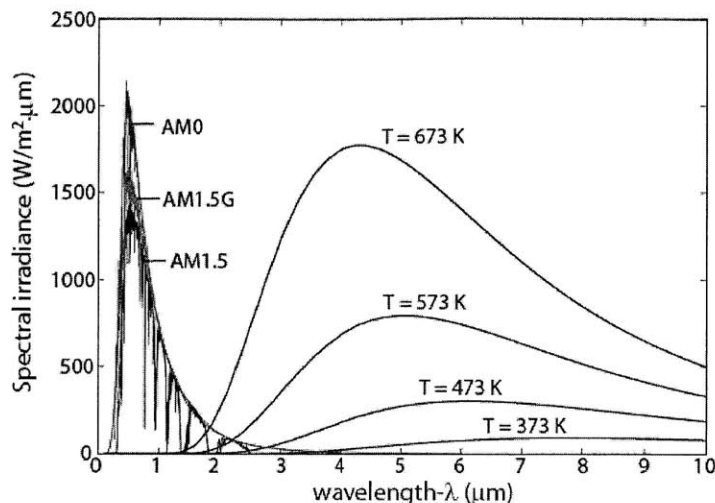


Figure 9: Solar spectrum and blackbody radiation at different temperature. AM0 is the extraterrestrial spectrum, AM1.5G is the irradiance on 37° tilted surface, and AM1.5 is the direct normal spectral irradiance (Ref. www.nrel.gov)

Here, the spectral radiance i.e. the energy per unit time per unit surface area of emitting surface per unit solid angle per unit wavelength is given by Planck's law [77]:

$$I'(\lambda, T) = \frac{2\pi hc^2}{\lambda^5} \frac{1}{e^{\frac{hc}{\lambda k_B T}} - 1} \quad (6)$$

The constants are: Planck constant (h) = 6.62×10^{-34} Js, speed of light (c) = 2.99×10^8 m/s, and Boltzmann constant (k_B) = 1.38×10^{-23} J/K

Black chrome, a material composition of nano-particles of chromium and chromium oxide has been used as selective surface for water heating applications. The absorbance at the visible wavelength is 0.92 and IR emittance at wavelengths greater than 2 μm is less than 0.1 [78]. The highest solar performance for a selective surface is reported for a metal-nitride dielectric set of stainless steel and aluminum nitride (AlN) cermet with absorbance of 0.96 and emittance of 0.05 (Figure 10) [79]. With appropriate selective surfaces most of the solar energy (UV, visible and IR) incident on the generator contributes towards raising the hot side temperature. A fraction of this thermal energy is converted to electrical energy by the thermoelectric module via the Seebeck effect.

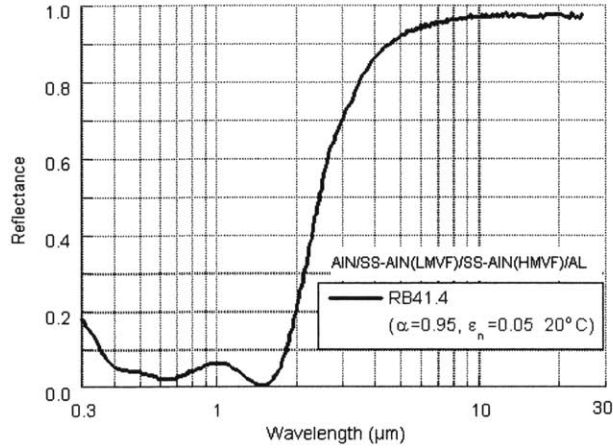


Figure 10: Reflectance data for the selective surface using metal-dielectric set (AlN/SS)

Apart from the metal-oxide and nitride structures, photonic crystals, distributed Bragg reflector (DBR) and metal gratings can also be used as frequency selective surfaces (FSS) ^[80, 81]. Photonic crystals and DBR structures are being developed primarily for solar cells as light trapping layers to increase their efficiency. The overall efficiency increases by 24% with DBR and 1D grating structure, and similarly, the efficiency increases by 26.3% with a six-period triangular photonic crystal ^[80]. FSS are also used in the thermophotovoltaic system, where the thermal emitter needs to have wavelength selectivity quality such that it can emit certain wavelength corresponding to the TPV cell's band gap ^[81, 82]. Ideally, the thermal emitter would have high emissivity above the band gap and low emissivity below the band gap. A 3-D tungsten photonic crystal has shown selectivity behavior with high absorbance (80-85%) at wavelengths 1.5-1.9 μm ^[82]. The absorbance goes below 0.05 for higher wavelengths. Best commercial and research grade selective surfaces are listed in **Table 8**.

Selective coatings	Absorber (300-900nm)	Emittance (> 2 μm)
Black Chrome	0.92	0.1
TiN-TiAlN	0.9-0.94	0.1 (@ 400°C)
Mo-Al ₂ O ₃ (Cermet)	0.954	0.107 (@ 300°C)
SS-AlN	0.96	0.05 (@ 20°C)
Ni-NiO (Commercial grade)	0.94	0.13-0.15
Mixed metal carbide	0.93	0.1 (@ 300°C)
Photonic Crystal	0.96 (peak @ 550 nm)	
DBR+grating	0.92 (peak @ 500 nm)	
Silicone polymer with proprietary oxide pigment (Commercial – Solkote)	0.88-0.94	0.2-0.4

Table 8: Comparison for various selective surfaces ^[78-80, 83-86]

Efficient conversion of thermal radiation to electrical power requires the solar energy be captured efficiently by the thermoelectric module via the solar collector and the selective surface at the absorber. There is a natural design trade-off for STEG: the TEG works optimally at a higher hot side temperature, however the hot side absorber becomes less efficient as the temperature increases – since the hot side will then radiate the energy away from the module (**Figure 11**). Optimization requires determination of optimal operating temperature and maximizing the module performance at this operating temperature. Using the selective surface, the thermal radiation loss from the surface of the generator can be decreased. The heat transfer within the system with various losses from the hot side and their suppression mechanism will be described in the system analysis in Chapter 2.

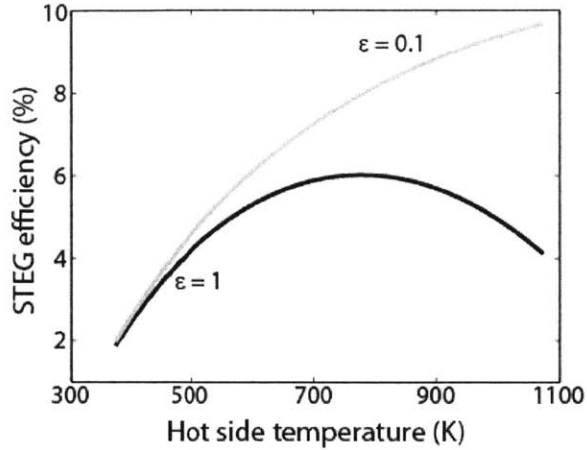


Figure 11: The system efficiency vs. the hot side temperature, showing large radiation loss at high temperature. Radiation loss can be suppressed by changing the emissivity (ϵ). Parameters used for the plot: $ZT = 0.5$, $T_c = 30^\circ\text{C}$, convective heat transfer (h) = $5\text{W/m}^2\text{K}$, absorber area = 0.06m^2 , system's thermal impedance = 0.1K/W

1.2.4 Heat sink

Efficient power conversion requires that a large temperature difference (ΔT) be maintained across the thermoelectric module. The amount of thermal power that can be pushed through a TE module depends on the cold side heat exchanger. Efficient heat transfer is required in order to maintain relatively low cold side temperature. Otherwise the system performance can be limited by the heat exchanger where the cold side temperature for the generator is closer to the hot side temperature rather than the heat sink temperature (i.e. the ambient temperature). The most effective heat transfer from the generator to the surrounding for terrestrial application is via convection, given by Newton's law of cooling.

$$Q = h\Delta TA_{hs} \quad (7)$$

Here, Q is the thermal power extracted from the cold side, h is the heat transfer coefficient, A_{hs} is the area of the heat sink and ΔT is the temperature difference between the surface and the ambient. During convection, the heat transfer from the cold side depends on many things: the working fluid (liquid or air), flow rate (natural or forced fluid flow) and area of the heat sink. Convection is mainly due to two processes: one is where the heat is carried away by a fluid whose motion is due to it being heated (natural convection) and the second is where a moving fluid carries away heat as it passes along the hot surface (forced convection). Typical values for the heat transfer coefficient for different types of heat exchange mechanism are listed in **Table 9**. The natural convection process has a relatively low heat transfer coefficient as the fluid motion is slower compared to forced convection. Natural convection does provide low-cost opportunity since the fluid does not have to be pushed using external energy (fan or pump). Pool

boiling is another example of heat extraction from the surface, which utilizes energy transfer via phase change of the liquid. Nucleate boiling has a higher heat transfer coefficient than the natural convection. Pool boiling using water can support a 10-100x higher heat transfer than natural convection but requires raising the cold side temperature to its boiling point. There is a growing research focused on achieving high boiling critical heat flux for efficient heat transfer and reduction of fluid saturation temperature using nano-particle surfaces ^[58, 87] or nanofluids (colloidal nanoparticles in homogenous fluid) ^[88]. Different schemes such as natural (air/water) and forced (air/water) convection were examined experimentally and tested under solar illumination for the thermoelectric generator system and are described in Chapter 4. The effects of thermal interface between the thermoelectric module and the hot/cold side are important factors for good heat transfer and can vastly influence the overall system efficiency.

Heat sinks	Heat transfer coefficient (h) (W/cm ² /K)
Natural convection	0.0005
Natural convection (water)	0.01
Forced convection	0.004
Forced convection (water)	0.6
Pool boiling (water)	2
Microchannel heat sink	20

Table 9: Heat transfer coefficients for various heat sinks ^[39]

1.3 Previous work

The first concept for solar thermoelectrics was tested in 1922 by Coblenz for measuring infrared radiation from stars ^[31]. The thermoelectric efficiency for a copper-constantan couple for that experiment was only 0.008%. The crucial limitation for efficiency in that setup was the low material thermoelectric properties. Since then, great advances have been made to increase TE materials' ZT values. Most earlier experimental results for solar based thermoelectric systems ^[31, 75, 89-94] have shown low efficiencies (< 1%) and low output power, primarily due to small material ZT (< 0.4) and low solar concentration. For the concentrated solar thermoelectric systems, the highest measured efficiency till date is 3.35% using a unicouple of $ZT = 0.4$ and solar concentration of 48x suns ^[31]. The measured output power for the single couple was 0.156 W. For a flat-plate system, Telkes in the same publication showed result of only 0.63% efficiency with the same material (ZnSb p-type element and Bi₂Te₃ n-type element: $ZT \sim 0.3$). The goal for solar thermoelectrics after this result has been to achieve higher efficiency and or achieve larger useful

output power for practical applications. Recently, utilizing thermal concentration, efficiency of 4.6% was measured for a flat-panel solar thermoelectric system with a unicouple structure of bismuth-antimony-telluride ($ZT \sim 1.4$)^[35]. The total output power from the single couple structure was less than 50 mW. The high efficiency is attributed to large ZT material as well as convection loss suppression by doing the experiment in vacuum condition. The noted high efficiency was achieved by keeping the cold side temperature at 20°C using a thermoelectric cooler. This system efficiency does not include power for active cooling. With higher cold side temperature ($> 60^\circ\text{C}$), the efficiency of the couple drops to $< 3.5\%$ due to lower temperature gradient. Two of the highest performances for solar thermoelectrics have been recorded for single couple structures. Single TE module or multiple modules incorporating systems have shown smaller efficiencies^[95, 96]. One of the key reason being the difference in the material ZT and module ZT , which is explained in detail in Chapter 2. Primarily due to thermal and electrical parasitic in a module, its performance is worst than a single couple structure. Previous system level work on solar thermoelectrics have been directed towards minor applications such as operating TE coolers, and for non-terrestrial applications such as near-earth space satellites^[75, 97, 98]. **Figure 12** summarizes the previous published experimental results for different solar thermoelectrics not including the space-based application systems. Results from this work are also presented for comparison^[99]. At module level, the maximum efficiency of 3% with an output power of 1.8 W was achieved for concentrated solar thermoelectrics using solar simulator. Higher electrical power (11 W) has been achieved for a solar thermoelectric generator using solar cooker with infield trials. In order to achieve higher output electrical power, TEG modules have to be used instead of a single TE couple structure. As the modules are integrated for larger output power, the system efficiency decreases due to added loss from system parasitics (both electrical and thermal). The desirable section to be in the electrical power vs. efficiency plot is the upper right most corner. We have looked at various aspects of the system design to increase the performance, both in efficiency and output power.

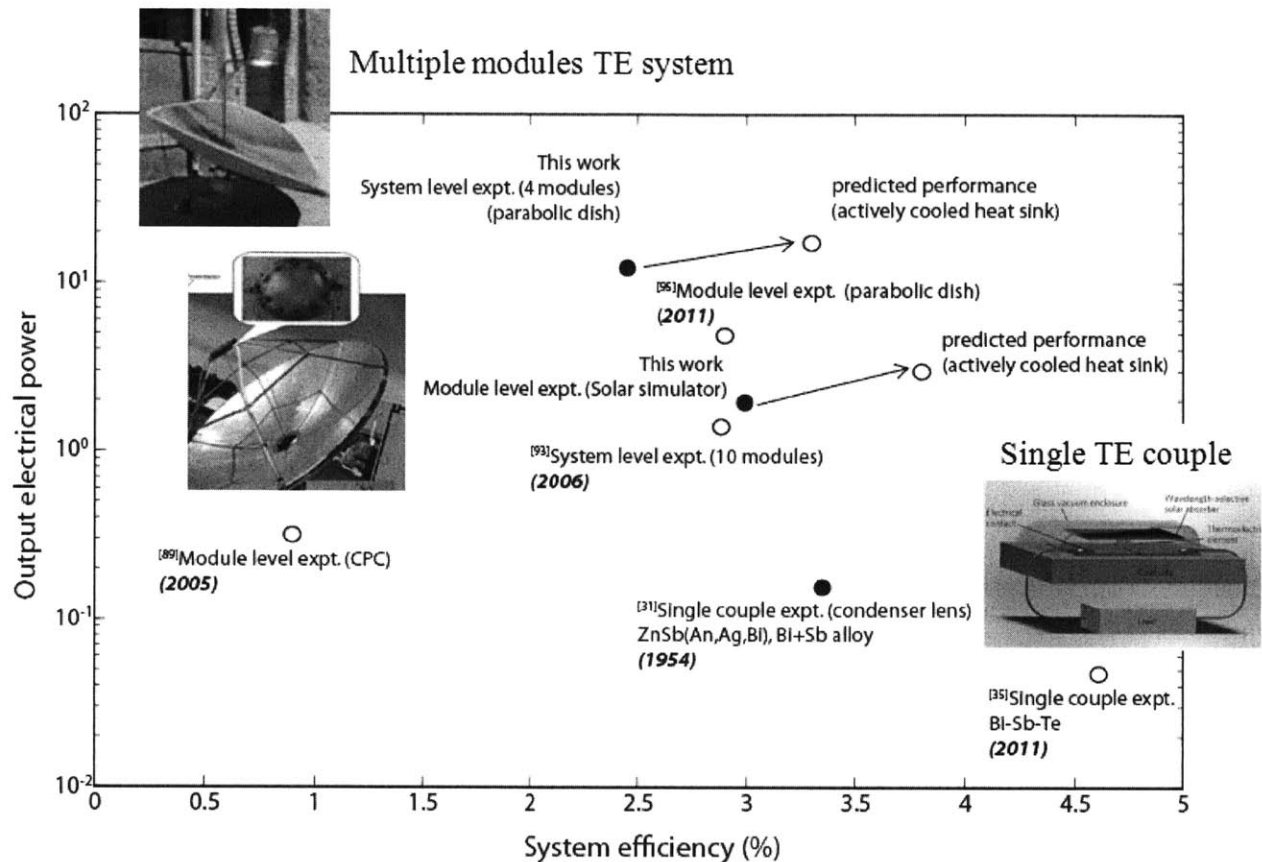


Figure 12: Previous experiments for STEG shown with system efficiency and output electrical power

- – system efficiency for actively cooled system (without including power consumption for heat sink)
- – total system efficiency for natural convection heat sink

Complementing this experimental effort has been a history of solar thermoelectrics modeling. In the early 80's along with space application, interest was growing for solar thermoelectric for terrestrial application. Rowe analyzed a high concentration STEG predicting a potential performance of more than 12% for a silicon germanium based system with 2000x solar concentration ^[100]. A recently published model estimated a maximum system efficiency of 35% for a flat-plate solar thermoelectric system ^[101]. The significant gap between this theory and prior experiments results from a fundamental inconsistency in the published treatment of hot side heat transfer resulting in hot side temperature of 900 K without solar concentration ^[101]. In fact for a module using Bi_2Te_3 material (same material used in the reference) with natural air convection, the heat flux at low solar concentration using flat-plate concentrator results in relatively low hot side temperature (320 K). Also, the commercial thermoelectric modules have relatively low ZT ($= 0.25-0.6$) compared to material values (Bi_2Te_3 : $ZT \sim 1$), mostly due to thermal and electrical parasitics. Although not the dominant error, the electrical parasitics were not considered in the 35%

estimate ^[101]. Many heat transfer modeling analysis for solar thermoelectrics had been done for flat—plate solar incidence and has been incomplete with various assumptions such as temperature independent parameters, constant cold side temperature, constant temperature gradient, no contact parasitics and temperature independent heat transfer coefficients ^[102, 103]. In the past year, there have been more modeling related publications that address one or more of the above assumptions ^[104-107], but none of the analysis address all the problems of simplified modeling. We independently developed complete steady state and transient models to analyze the solar thermoelectric generator performance at system level, including parasitics to model TE modules.

1.4 Thesis preview

In this thesis, we have developed a modular TEG system that can move from daylight applications to nighttime (cooking stoves) applications. One significant aspect of this ‘dual-use’ approach is that the DC power supplied by the solar thermoelectric generator can utilize much of the infrastructure of solar photovoltaic (or other TEG based) systems. The wirings, batteries, charge controllers and inverters for traditional PV installations (roughly 30% of the cost for residential solar in the US) can all be used at night using a small-scale thermoelectric generator. An economic model has been developed to study the cost of electricity generation for an STEG and compare it to other power generation mechanisms. This ‘dual-use’ aspect of the STEG design can help improve the overall output power performance of the system as well as cut cost.

Chapter 2 will describe the thermodynamic analysis of the STEG with theoretical modeling and experimental verification. Both bench-top and large-scale system level modeling and experimental results will be presented and analyzed in this section. Theoretical analysis and optimization for system efficiency is shown by changing various parameters such as the selective surface, TE material and concentration ratio. Heat sink optimization is one of the crucial system design parameter to increase the efficiency. We have looked at the heat transfer properties and analyzed the STEG system performance with various heat sinks in Chapter 2. The potential of co-generation (heat and electricity) is provided by water convection mechanism at the cold side, where the rejected heat can be utilized for water pasteurization.

Integral part of the research has been to understand the system’s need from the application perspective. System level implementation results and field trials are discussed in Chapter 3. The dual-use aspect of the STEG, i.e. utilization with solar cookers and cooking stoves, which came as a feedback result from the field trials are discussed and analyzed in this chapter.

In order to achieve higher performance from solar thermoelectrics, we looked at two different aspects: module redesign and use of novel TE materials. In Chapter 4, the system optimization is achieved by changing the TEG module design. The parameters that were varied are the geometric aspect ratio of the TE legs (i.e. the cross section area and the leg thickness). Higher system efficiency is possible with the optimized modules using same TE material (Bi_2Te_3).

TE materials with higher ZT values can dramatically increase the performance of STEGs. We have looked at novel materials with the potential of high thermoelectric properties. Chapter 5 will look at these materials and introduce a characterization technique (both electrical and thermal) for high temperature measurement developed within the course of this work.

A simple economic model was developed to understand the market feasibility of the current system and is described in Chapter 6.

Lastly, we will present and discuss general conclusions of the research work and future prospect of this technology in Chapter 7.

Chapter 2

Solar Thermoelectric Generator

Historically, thermoelectrics have been used primarily for deep-space exploration and waste heat recovery. We explored the potential of thermoelectrics with solar energy for small-scale electricity generation using a solar thermoelectric generator (STEG) (Figure 13). A solar collector (parabolic reflector) directs the sun light on to a fixed focal spot. The hot side for a thermoelectric generator placed at this spot heats up as it absorbs the concentrated sun light. A “selective surface” on the hot side of the module has high ($> 90\%$) absorbance within the visible wavelengths^[76]. This allows the hot side to absorb most of the incident solar energy. With appropriate selective surfaces most of the solar energy (UV, visible and IR) incident on the generator contributes towards raising the hot side temperature. A fraction of this thermal energy is converted to electrical energy by the thermoelectric module via the Seebeck effect.

STEGs using cheap parabolic concentrators with high ZT modules can be a cost-effective alternative to solar photovoltaics for micro-power generation. A thermodynamic model was developed for predicting the thermal-to-electrical conversion efficiency for the generator. A bench-top experimental setup (Figure 15) was used to validate the thermodynamic model. With solar concentration of 66x suns, a system efficiency of 3% was measured for a commercial Bi_2Te_3 module with the output power of 1.8 W. For a TEG module (i.e. not a single TE couple structure) this performance with concentrated solar energy is the highest efficiency to our knowledge. With module optimization and by using novel thermoelectric materials, higher conversion efficiencies can be achieved for a STEG.

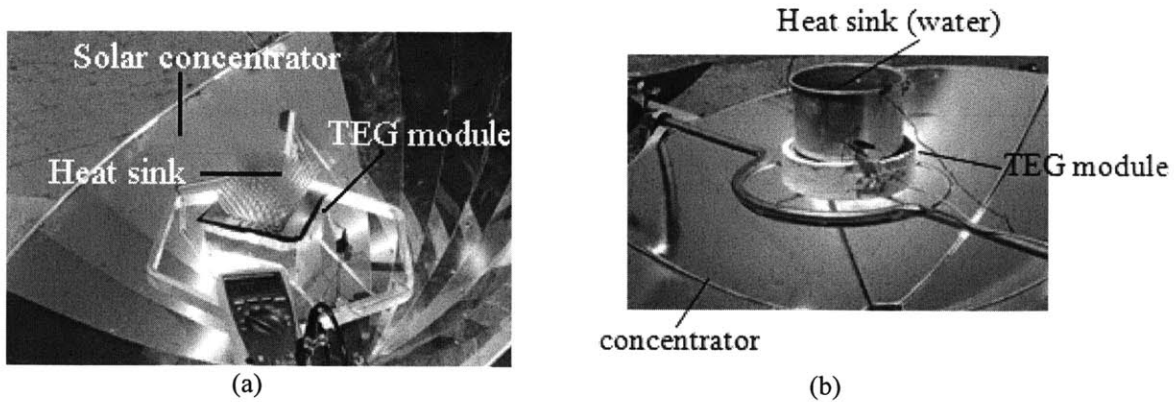


Figure 13: (a) A solar thermoelectric generator showing the concentrator and the heat sink (air cooled); (b) Water convection heat sink scheme is used in this STEG

Section 2.1 presents the analysis of the generator system based on heat transfer and energy balance to calculate the system efficiency. Different loss mechanisms for the system are discussed with possible solutions to suppress these losses. A bench-top prototype and the experimental results are shown in Section 2.2 for validation. Section 2.3 presents results from the theoretical analysis for the system performance and its dependence on various parameters such as selective surface, heat sink, TE figure-of-merit, and hot-side absorber design. Large scale (four modules) system was build in the lab to test with available solar concentrators (solar cookers) and to generate useful output power (Section 2.4); transient simulation for this system is discussed in Section 2.5.

2.1 Thermodynamic model

A thermodynamic analysis based on energy balance and heat transfer allows us to predict the system efficiency (η_{sys}) for the STEG. The energy loss in the system can be categorized into two parts: loss at the hot side absorber and loss in the thermoelectric module. The absorber efficiency (η_{ρ}) is defined by how well the solar flux can be guided into the thermoelectric module. As mentioned in Chapter 1, a common parabolic reflector such as a concrete solar cooker can concentrate ~ 10 - 20 x suns (= optical concentration = area of the reflector/area of the focal spot) on the focal spot whose area is equivalent to 20-30 cm diameter circle. We take the concentrated sunlight as the initial input to the generator. For all our analysis, we vary the input solar irradiance to show the STEG performance dependence on the input thermal flux and to represent the solar flux variation over a day. The efficiency for the hot side absorber is given by

$\eta_Q = \frac{Q_h}{\phi_i A}$, where Q_h is the total thermal power into the TEG, ϕ_i is the total input flux hitting the focal spot of the concentrator (= optical concentration (C_{opt}) x solar flux (q_i)) and A is the area of the STEG absorber. The losses degrading the hot side efficiency are convective and radiative losses. As the input flux increases, if everything else in the system is kept constant, the hot side temperature rises. With the increase in temperature, both convective and radiative loss increases; mostly the radiative loss which is dependent on the hot side temperature by the Stefan-Boltzmann law (Figure 14). Thus, the efficiency of the hot side absorber decreases with increasing temperature.

$$P(\text{radiative}) = \varepsilon \sigma_{sb} A T_h^4 \quad (8)$$

Here, ε is emissivity of the surface, σ_{sb} is the Stefan-Boltzmann constant and T_h is the absorber temperature

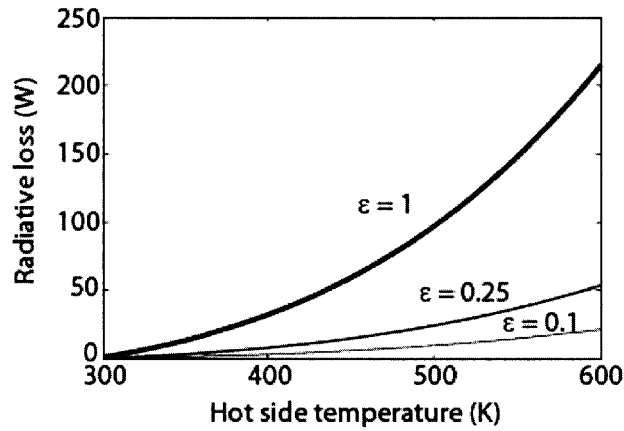


Figure 14: Dependence of radiative loss on the hot side absorber temperature given by the Stefan-Boltzmann law; radiative loss can be suppressed by using low emissivity material

The TEG module efficiency (η_{TEG}) depends on the thermoelectric material and the module design. It is

given by $\eta_{TEG} = \frac{P}{Q_h}$; where P is the total electrical power generated which depends on material properties

such as the Seebeck coefficient (S), the electrical conductivity (σ) and the thermal conductivity (κ). For maximum power, the module efficiency can also be expressed by Equation 9, where T_h is the hot side temperature, T_c is the cold side temperature and ΔT is the temperature gradient across the module. ZT_{module} is the figure-of-merit of the TE module which depends on the material parameters and the module parasitics as described later in this section.

$$\eta_{TEG} = \frac{\Delta T}{2T_h - \Delta T / 2 + 2(T_h + T_c) / ZT_{module}} \quad (9)$$

The module efficiency increases with the rise in temperature if the material parameters are considered as temperature independent values. The total system efficiency for the STEG is given by $\eta_{sys} = \eta_{TEG} \eta_Q$. As mentioned before, the absorber efficiency decreases with the rise in temperature, but the TEG efficiency increases. Thus, there is an optimal input flux (and an optimal hot side temperature) for which the system efficiency is maximum. More on the optimum efficiency will be discussed later in this section.

For the theoretical modeling, the following assumptions were made:

- The hot side absorber area with the selective surface coating is equal to the focal area of the optical system.
- Radiation loss from the hot side to the ambient is considered in the model. Any radiation loss from the hot side to the cold side is negligible (< 1% of the input thermal power). The low loss is due to small emissivity between the hot and the cold side ($\epsilon_{hc} = \frac{1}{1/\epsilon_h + 1/\epsilon_c - 1} < 0.05$: heat transfer between two parallel surfaces^[107]).
- Any heat loss from the side walls of the thermoelectric elements is neglected in the model. Conduction through the TE leg is the main path for heat transfer to the cold side. Convection through air between the hot and the cold side is also considered for the heat transfer in this model as a parasitic path.
- The temperature and the heat flux in the TE leg do not vary over the cross-section area.
- The material properties are only a function of temperature and not position.

The key features of this model are as follows:

- Temperature dependent material parameters (S , κ , and σ) are considered for the analysis to fully model the STEG system.
- Electrical and thermal contact resistances as well as ceramic wafer's thermal conductance are included in the model to define a TEG module.
- Instead of a fixed cold side temperature, the solution is based on temperature dependent heat transfer coefficient of the heat sink. In order to have a fixed cold side temperature, many times external resources are needed such as having a thermoelectric cooler or a fan. The input power for maintaining the cold side temperature is often not included in the system efficiency calculations as discussed in Chapter 1.

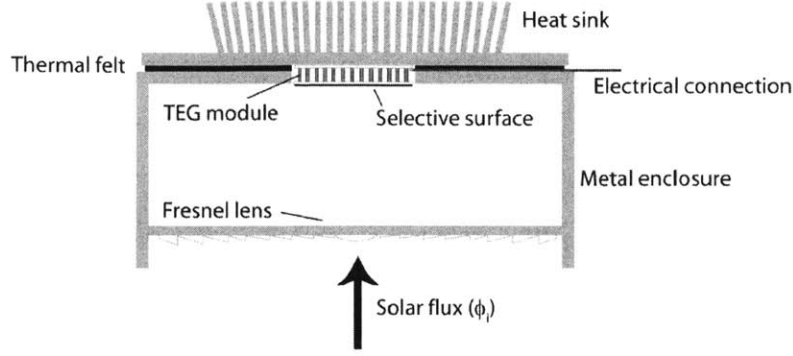


Figure 15: Schematic of the enclosure holding the thermoelectric generator, a Fresnel lens is used in this prototype to increase the thermal flux

In general, the convective loss at the hot side absorber can be reduced by introducing suppression mechanisms such as multiple glass panels and dead air between the glass and the hot side. In the bench-top experimental setup (Figure 15); the concentrated light hits the generator from below. An enclosure with a Fresnel lens traps the warm air near the hot surface. This trapped air suppresses convective loss at the hot side. The transmission coefficient for the lens (0.90) was included in the analysis. For radiative loss suppression, the hot side of the module was coated with the selective surface consisting of silicone polymer as a binder with an oxide pigment^[76]. The selective surface has a large absorbance (0.88-0.94) for the visible wavelengths (300-900 nm) and low emissivity (0.2-0.4) at wavelengths above 2 μm ^[76]. More details on the particular selective surface used for the system and its performance will be discussed in the next section.

The STEG performance was modeled using mature thermoelectric material such as micro-alloy Bi_2Te_3 . Other materials working at different temperature ranges will be explored in Section 2.3. Commercial thermoelectric modules have relatively low effective ZT ($= 0.25 - 0.6$) compared to material ZT (Bi_2Te_3 : $ZT \sim 1$), mostly due to thermal and electrical parasitics. Material ZT is given by $ZT_{\text{material}} = \left(\frac{S^2}{K_{TE} R_{TE}} \right) T$,

where S is the Seebeck coefficient, R_{TE} is the electrical resistance and K_{TE} is the thermal conductance for a thermoelectric material. Module ZT can be formulated as $ZT_{\text{module}} = \left(\frac{S^2}{(K_{TE} + K_{\text{parasitic}})(R_{TE} + R_{\text{parasitic}})} \right) T$,

where $R_{\text{parasitic}}$ and $K_{\text{parasitic}}$ are the electrical and thermal parasitics. It can be seen from the above relationships that the module ZT is less than the material ZT due to parasitics. For a STEG, the conversion efficiency is determined by the module ZT rather than the material ZT as given in Equation 9.

For the theoretical simulation of the generator, a set of equations (10-20) representing heat transfer and energy balance within the STEG was self consistently solved for temperatures at various interfaces. The TEG is modeled as a one-dimensional system in which the energy flux through the generator is conserved. The input solar flux (ϕ_i) is the only independent variable in the simulation. The cold side heat transfer coefficient (h) is set by the convection scheme of the heat sink, which limits the cold side temperature for the generator (T_c). The thermal impedance of the module and the cold side heat transfer coefficient set the hot side temperature for different input energy flux. Depending on the temperature of the module, the generator efficiency is calculated.

Figure 16 shows the schematic for a STEG with the heat flow path through the generator and different loss paths. Interfaces at the hot side absorber and the cold side (heat sink) are shown in the figure to emphasize the temperature gradient created due to interface parasitics.

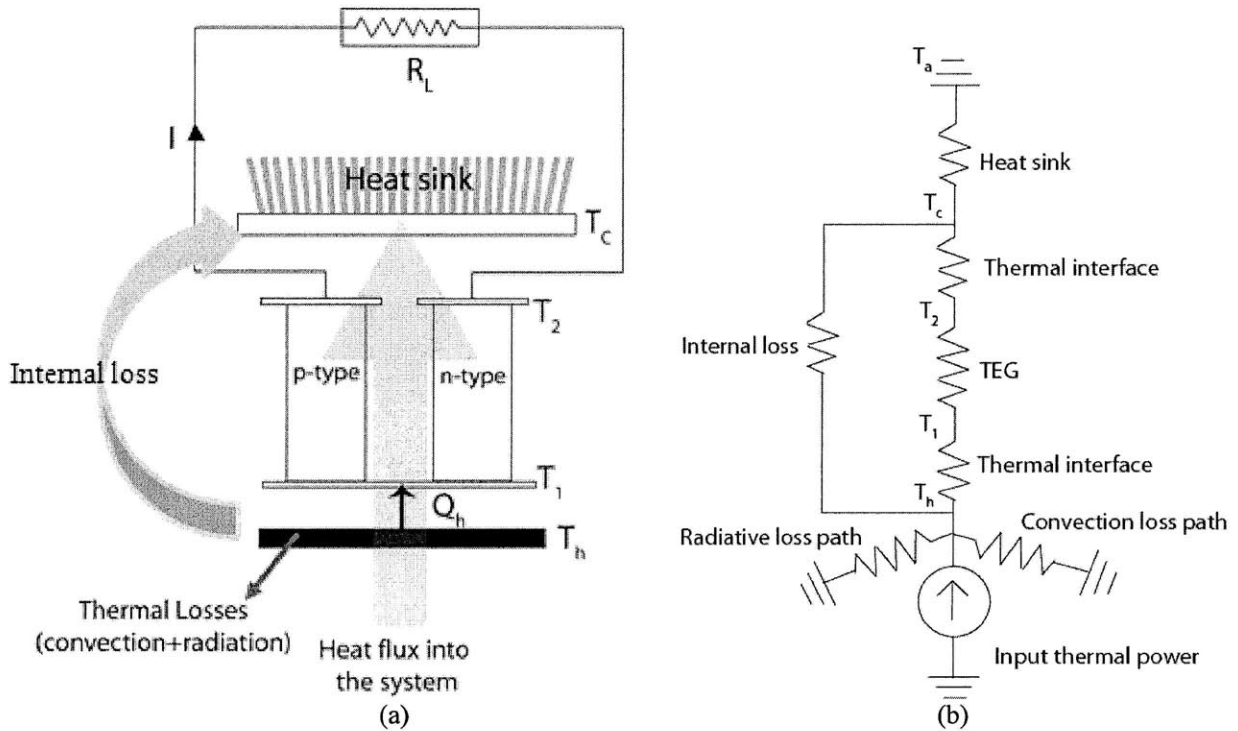


Figure 16: (a) Schematic for a STEG showing heat flow through the generator and various temperatures at different interfaces; (b) thermal circuit equivalent for the STEG system showing various paths for heat flow

The convective and radiative losses at the hot side depend on the hot side temperature and are related to the input thermal power by:

$$Q_h = \tau\alpha\phi_i A - k_1(T_h - T_a)A - k_2(T_h^4 - T_a^4)A - k_{air}(T_h - T_c) \quad (10)$$

Here, τ is the transmission coefficient for the optical system (i.e. the acrylic Fresnel lens in the case of the prototype shown in **Figure 15**), α is the optical absorbance for the hot side absorber given by the selective surface, k_1 is the convective heat transfer coefficient, k_2 is the radiative heat transfer coefficient, A is the absorber area and T_a is the ambient temperature. The final term in the expression is the thermal loss due to air in between the hot and the cold side as the internal loss of the module where k_{air} is the heat transfer coefficient for air. T_1 and T_2 are the temperatures across the TE material. Variations in these temperatures from T_h and T_c are due to the thermal parasitics which are captured in the model as k_h and k_c – hot side and cold side thermal conductance. The thermal resistance is mainly due to the interface between the absorber and the TEG module. This resistance depends on the surface finishing, applied pressure between the surfaces as well as the thermal conductance of any thermal cement or paste used in between. A_{module} is the area of the TEG module. The thermal power at the hot side is given by Fourier’s Law in its one dimensional form as:

$$Q_h = \frac{k_h(T_h - T_1)}{A_{module}} \quad (11)$$

The total heat transported from the hot side of the TE elements can be separated into contributions from the Seebeck effect, thermal conductance and Joule heating as shown in Equation 12 (**Figure 17**). K is the thermal conductance and R is the resistance of the module which incorporates both the TE material parameters as well as the module parasitics. I is the electrical current through the TEG across a load resistance (R_L).

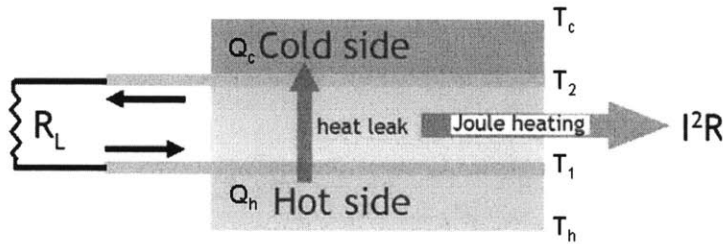


Figure 17: Schematic for a TEG showing loss within the leg which is mostly joule heating; conductive path through the generator is also path for heat leak

$$Q_h = ST_1I + K(T_1 - T_2) - \frac{I^2R}{2} \quad (12)$$

Similarly, the total heat at the cold side is given by Equation 13.

$$Q_c = ST_2 I + K(T_1 - T_2) + \frac{I^2 R}{2} \quad (13)$$

The total electrical power generated by the TEG is then given by:

$$P = Q_h - Q_c = S(T_1 - T_2)I - I^2 R = I^2 R_L \quad (14)$$

For maximum power, the condition of load matching is applied, according to which the load resistance (R_L) is equal to the internal resistance of the TEG (R).

$$I = \frac{S(T_1 - T_2)}{2R} \quad (15)$$

For a TEG module, the Seebeck coefficient is given by:

$$S = (S_p - S_n)N \quad (16)$$

Here, the subscripts p and n are for p- and n-type TE legs and N is the total number of couples in a module. In module designing, the number of couples is generally determined by the output voltage requirement and the area constraint.

The module thermal conductance is given by:

$$K = \left(\frac{\kappa_p A_p}{l_p} + \frac{\kappa_n A_n}{l_n} \right) N + K_{parasitic} \quad (17)$$

And, the electrical resistance of the module is given by:

$$R = \left(\frac{l_p}{\sigma_p A_p} + \frac{l_n}{\sigma_n A_n} \right) N + R_{parasitic} \quad (18)$$

The heat transfer to the cold side (heat sink) is given by Equations 19 and 20. A_{hs} is the area of the heat sink.

$$Q_c = \frac{k_c (T_2 - T_c)}{A_{module}} \quad (19)$$

$$Q_c = hA_{hs} (T_c - T_a) \quad (20)$$

Within the simulation, the TE material properties namely the Seebeck coefficient, the thermal conductivity and the electrical conductivity are taken as temperature dependent parameters. The convective heat transfer coefficients at the hot side absorber and the heat sink are also taken as temperature dependent parameters. For different prototypes, various convection options were explored to optimize the system performance. Temperature dependent heat transfer coefficients for natural air convection, forced air convection and natural water convection are used appropriately in the model. The coefficients are taken from various correlations used in fluid dynamics as described below.

The key variables that define a convective heat transfer coefficient are Reynolds number, Nusselt number, Prandtl number and Rayleigh number. The Reynolds number characterizes the influence of inertial and

viscous forces in a fluid problem, and it is expressed as $Re \equiv \frac{\rho u x}{\mu} = \frac{u x}{\nu}$. Here, ρ is the fluid density

(kg/m^3), μ is the dynamic viscosity (kg/m.s), x is the characteristic length (m), u is the velocity (m/s), and ν is the kinematic viscosity (m^2/s). This dimensionless parameter indicates whether the flow is laminar or turbulent. The flow is laminar for $Re \leq 5 \times 10^5$ and turbulent for $Re \geq 5 \times 10^5$ [108]. The Nusselt number is

defined as $Nu_x = \frac{hx}{k}$. It is the ratio of convection for fluid in motion to conduction for motionless fluid

layer. In this expression, k is the conductivity of the fluid (W/m.K), and h is the heat transfer coefficient ($\text{W/m}^2.\text{K}$). The Prandtl number represents the relative effectiveness of molecular transport of momentum

and energy within the thermal boundary layers, and it is defined as $Pr \equiv \frac{\nu}{\alpha} = \frac{\text{kinematic viscosity}}{\text{thermal diffusivity}} = \frac{\mu c_p}{k}$.

Here, α is the thermal diffusivity (m^2/s), and c_p is the specific heat capacity at constant pressure (J/kg.K).

The average Prandtl number for air over the temperature range of 280-350 K is 0.7091 [108]. Lastly, the

Rayleigh number is defined as $Ra \equiv \frac{g\beta(T_{surface} - T_{\infty})x^3}{\alpha\nu}$. This dimensionless parameter characterizes the

importance of buoyant forces relative to viscous forces. Here, g is the acceleration due to gravity (m/s^2), β is the coefficient of thermal expansion ($1/\text{K}$), and, T_{bulk} is the bulk fluid temperature (K). Knowing these four parameters, the heat transfer coefficient can be extracted for different flow conditions.

For laminar flow (natural convection) in a uniform wall-heat flux plane surface, the following empirical relation for Nusselt number holds true [108, 109].

$$Nu_x = \frac{hx}{k} = 0.630 \left(\frac{Ra \times Pr}{4 + 9\sqrt{Pr} + 10Pr} \right)^{1/5} \quad (21)$$

$$\text{Thus, } h = \frac{0.630 \left(\frac{\text{Ra} \times \text{Pr}}{4 + 9\sqrt{\text{Pr}} + 10\text{Pr}} \right)^{1/5}}{x} k \quad (22)$$

Similarly, for turbulent boundary condition over plane surfaces ($5 \times 10^5 \leq \text{Re}$), the Nusselt number is given by ^[108, 109] (Sieder-Tate correlation):

$$\text{Nu}_x = \frac{hx}{k} = 0.023 \text{Re}^{0.8} \text{Pr}^{1/3} \left(\frac{\mu_{\text{bulk}}}{\mu_{\text{surface}}} \right)^{0.14} \quad (23)$$

For forced convection, we used the heat transfer coefficient relation as:

$$h = \frac{\text{Nu}_x k}{x} = \frac{0.023 \text{Re}^{0.8} \text{Pr}^{1/3} \left(\frac{\mu_{\text{bulk}}}{\mu_{\text{surface}}} \right)^{0.14}}{x} k \quad (24)$$

The characteristic lengths are given by the dimensions of the absorber area and the heat sink. For natural convection, the velocity is driven by buoyancy. For forced convection, a uniform air velocity was considered between conservative estimates (1 mph) to an average daily wind speed of the particular location for field trials (5-10 mph). Fluid (air and water) properties were taken as temperature dependent parameters (Appendix 1), and they were evaluated at the film temperature which is the average of the surface and the surrounding bulk temperature.

A bench-top experimental setup was used to verify the theoretical analysis as described in the next section. Results from the simulations are discussed in Section 2.3 to identify key parameters affecting the system performance.

2.2 System validation

Experiments were conducted using a prototype built in the lab (**Figure 15**) with a Newport solar simulator (2" x 2" beam size – Max. output power ~ 60 W). A commercial MAM-Bi₂Te₃ TEG module was used for the STEG (Marlow TG12-4L) with a module *ZT* in the range of 0.4-0.6 and the material *ZT* of 0.6-0.9 ^[110]. A heat sink based on natural air convection was used at the cold side of the generator which was rated for low thermal impedance in the order of 0.99 K/W. A commercial selective surface ($\alpha = 0.94$ and $\varepsilon = 0.22$) was directly painted on the top ceramic layer of the commercial TEG module as there was no extra hot side absorber in this setup. A Fresnel lens was used between the output of the solar simulator

and the thermoelectric module in order to increase the optical concentration at the hot side of the TEG. The transmission coefficient of the lens (0.90) was included in the efficiency calculation. For the highest efficiency, the average input thermal flux onto the hot side of the generator was 66x suns (1 sun = 1000 W/m² corresponding to AM1.5G condition) as measured with a thermopile sensor. A conversion efficiency of 3% with an output electrical power of 1.8 W was measured for the prototype (Figure 18, Figure 19). The generator was connected to a power MOSFET based variable resistance for load matching and maximum power measurement. The theoretical model overestimated the system efficiency based on Bi₂Te₃ material properties alone (dotted lines in Figure 18). An electrical parasitic of 1.5 Ω and thermal resistance of 0.35 K/W along with Bi₂Te₃ material parameters were used to model the system and match the experimental results. The electrical parasitic originates from multiple metal/solder connections for the TE legs and wires. The thermal parasitic is due to the interfaces at the TE leg connections, ceramic wafers at the hot and the cold side, as well as the interface between the module and the heat sink. The system parasitic was the fitting parameter used for the theoretical modeling.

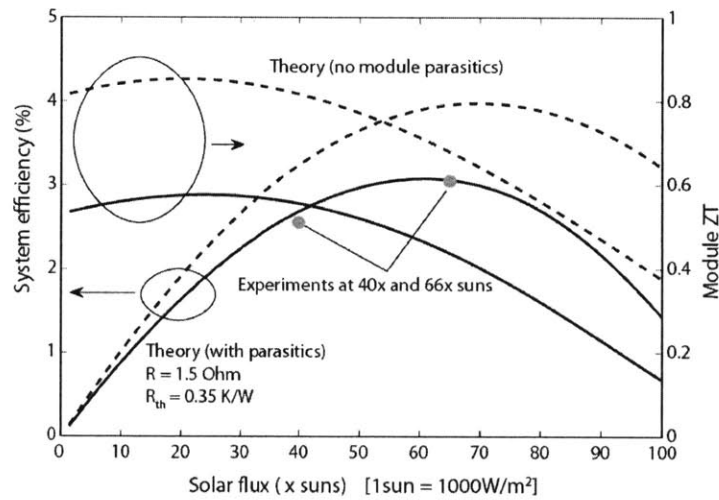


Figure 18: Theoretical simulation for Bi₂Te₃ showing module ZT and system efficiency: Without any parasitic, maximum system efficiency of 4% can be achieved at 70x suns. The model is verified with an experiment at 66x and 40x suns intensity. Parasitics are included in the theory to represent the commercial module

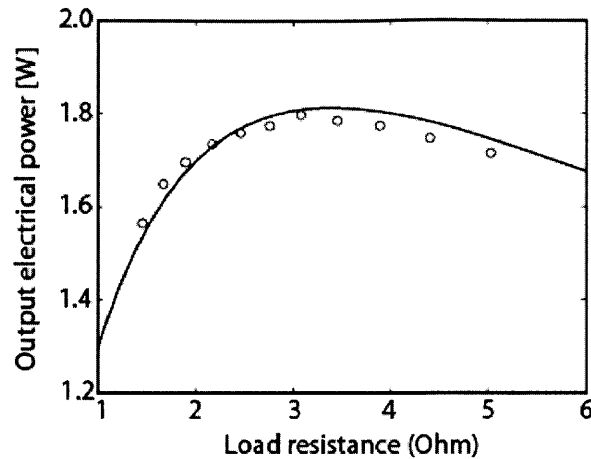


Figure 19: Output power from STEG at 66x suns with variable load resistance; open circles are experimental data with solid line as the modeling result

As the solar concentration is increased, the overall temperature of the system increases. The efficiency peak seen in Figure 18 is mainly due to the tradeoff between the TE material performance and the overall module performance. We mentioned earlier, the TE efficiency increases with temperature (Equation 9). However, the material for consideration here: Bi_2Te_3 's ZT degrades after average temperature range of 300-350 K (Figure 20). At higher temperature, for Bi_2Te_3 , the Seebeck coefficient decreases and the thermal conductivity increases^[11].

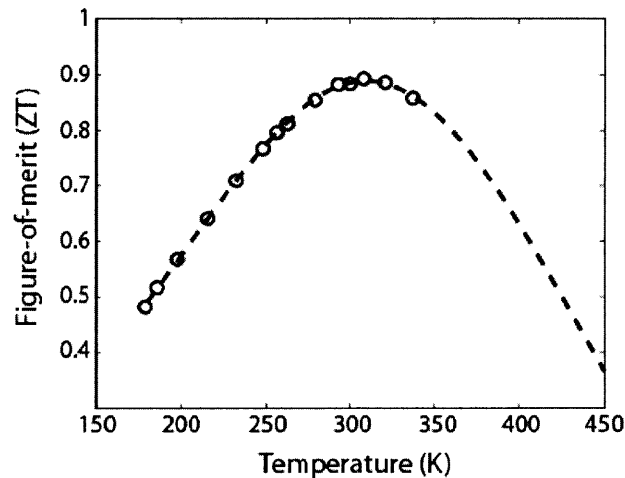


Figure 20: ZT vs. temperature for MAM- Bi_2Te_3 (o – measured data provided by Marlow Inc, -- quadratic fit)

Experimentally measured system efficiency and the output power for the STEG agree with the thermodynamic model presented above. However, we can see that even with greater solar concentration and with no module parasitics the system efficiency with commercial grade Bi_2Te_3 is limited to 4% for the given setup. In order to realize higher efficiencies we must consider materials with high ZT at higher

temperatures or look at system redesigning, namely module optimization. In the next section, we look at various parameters to understand how they affect the system performance such that we can do optimization to gain maximum output from the STEG.

2.3 Design methodology

Here we analyze individual parameters and see how each affect the system efficiency for maximum output power. We use the same model as described in the previous section for all our theoretical analysis with few assumptions for simplicity whenever necessary. In general, as the optical concentration is increased, the overall temperature of the system increases which helps improving the TEG efficiency unless it is limited by the material properties.

2.3.1 Selective surface

The selective surface allows for near optimal absorption of the incident solar radiation while minimizing the radiative heat loss from the hot side absorber. State-of-art and research grade selective surfaces were discussed in Chapter 1. Here we look at the dependence of system performance with different selective surface properties, namely emissivity. The characteristics of the selective surface used for the STEG prototype are also discussed here.

Figure 11 in Chapter 1 used a very simplistic model to show the dependence of the STEG efficiency on the hot side temperature and the emissivity. As the hot side temperature increase, the efficiency decreases due to rise in the radiative loss. At temperature > 1000 K, with emissivity change from 0.1 to 1, the system efficiency can go down from 10% to 5%. Meanwhile at lower absorber temperature < 550 K, the drop in efficiency is less than 1% for the same emissivity variation; indicating the importance of low emissivity for high temperature application where radiation losses are critical. Here, we have analyzed the effect of selective surface on Bi_2Te_3 based modules using the theoretical model described in the previous section with temperature dependent material parameters. For simplicity, we consider an ideal TEG module without thermal and electrical parasitic to focus on the best performance of the STEG. The theoretical estimates for the system efficiency with three different emissivity values ($\epsilon = 0.05, 0.2,$ and 0.9) are shown in **Figure 21**.

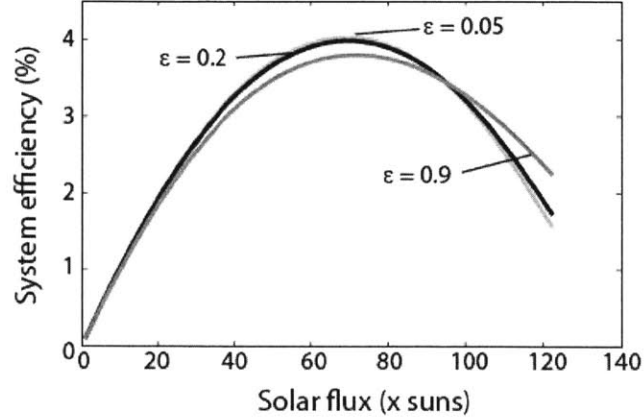


Figure 21: Effect of emissivity on system efficiency for Bi_2Te_3 based STEG at different solar concentration

At solar concentrations below 80x suns, we see higher emissivity value giving lower system performance due to higher radiation loss at $\varepsilon = 0.9$. However, the effect is relatively small (less than 0.5% change in the overall system efficiency), and this is due to the high optical concentration. In the previous section, we

defined the hot side absorber efficiency as $\eta_Q = \frac{Q_h}{\phi_i A}$.

Replacing Q_h with Equation 10, we get the efficiency as:

$$\eta_Q = \frac{\tau\alpha\phi_i A - k_1(T_h - T_a)A - k_2(T_h^4 - T_a^4)A - k_{air}(T_h - T_c)}{\phi_i A} \quad (25)$$

To easily show the dependence on the radiative term, we ignore the convection loss factors here and represent the radiation heat transfer coefficient as $k_2 = \varepsilon\sigma_{sb}$. Then,

$$\eta_Q = \frac{\tau\alpha(C_{opt}q_i)A - k_2(T_h^4 - T_a^4)A}{C_{opt}q_i A} = \tau\alpha - \frac{\varepsilon\sigma_{sb}(T_h^4 - T_a^4)}{C_{opt}q_i} \quad (26)$$

As the optical concentration (C_{opt}) increases, the second term for the efficiency decreases. Within the concentration range (40-80x suns) where the system efficiency for STEG peaks, the variation due to emissivity change is relatively small. Also, the radiation loss itself is low within the temperature ranges < 550 K to make a significant effect. This is one of the primary reasons that concentrated solar thermoelectrics can have smaller emissivity variation effect, where as for flat-plate solar thermoelectrics, slight emissivity variation can have a huge impact on the system efficiency ^[35].

In **Figure 21**, at higher solar fluxes ($> 100x$ suns), it seems lower emissivity value actually gives lower system efficiency which is counter intuitive. But this lower system performance is due to degrading ZT value for Bi_2Te_3 at higher temperature. With higher solar fluxes and higher emissivity, the radiation loss increases and the overall temperature of the system is slightly lower than that with low emissivity coating. As the average temperature is lower, the material ZT (**Figure 20**) within this temperature range is actually higher which causes this apparent switch in the trend of the efficiency versus the emissivity. If the material parameters were temperature independent, then the dependence according to **Figure 11** would be true. For Bi_2Te_3 based STEG systems where the hot side absorber temperature is less than 550 K, the selective surface with emissivity of 0.05 vs. 0.2 does not make a dramatic difference. The overall system efficiency is primarily controlled by the TE module efficiency and the convective losses at the absorber side are larger than the radiative loss.

The optical transmission properties of an inexpensive commercial selective surface were tested and compared with black (non-glossy) paint. The absorbance and the emissivity for the selective surface used for the system were measured using a spectrophotometer (Perkin Elmer UV/VIS Lambda 950: 300 nm - 2 μm) and a Fourier Transform Infrared (FTIR) spectroscopy measurement setup (2-5 μm). At lower wavelengths ($< 2 \mu\text{m}$), the transmission and the reflectance coefficients for the sample were measured with a broadband light source (pre-aligned tungsten-halogen and deuterium source) and a built-in photo-detector at room temperature. For the FTIR measurement, the emissivity was calculated at an elevated temperature (150°C). The FTIR measurements were done on two samples of identical areas, one with a known emissivity (Black chrome: $\epsilon = 0.12$) and another one with the selective surface coating. By measuring the radiative power for both surfaces, the unknown emissivity can be calculated for the coating. The results are shown in **Figure 22**. The absorbance for a black-painted surface remains flat (~ 0.92) across the wavelength range of 300-2000 nm. For the selective surface, there is a wavelength dependent emissivity, with absorbance value of 0.94 across the solar spectrum (300-1100 nm). At higher wavelength ($> 4 \mu\text{m}$) where the thermal radiation due to the hot absorber matters, an emissivity of 0.22 was calculated from the FTIR measurement. There is a small overlap window between the spectrometer and the FTIR measurement around 1.9 μm showing similar absorption data for the same sample. These values of absorbance and emittance for the selective surface were used in the theoretical modeling.

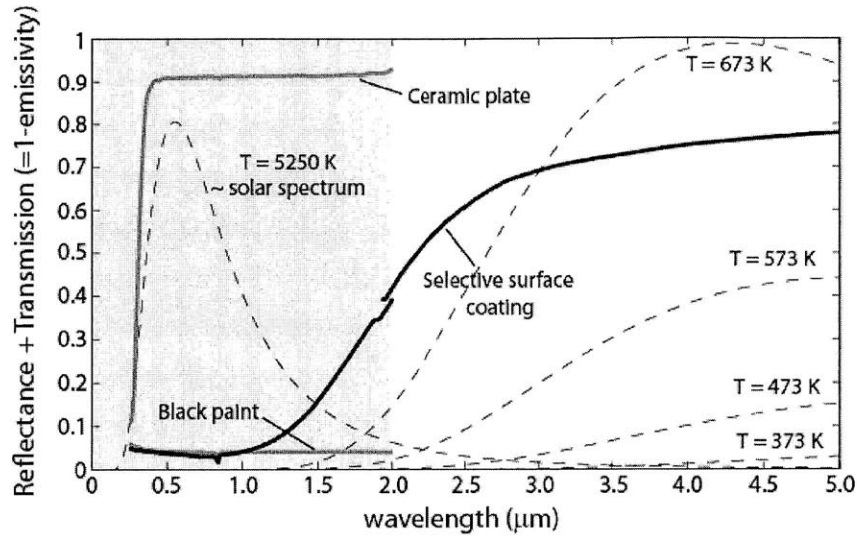


Figure 22: Optical properties of a commercial selective surface compared to a black painted surface ($\epsilon \sim 0.9$) and a white ceramic plate. Blackbody radiations at different temperatures are shown (dotted lines). The peak for 200-300°C body is in the mid IR range (4-5 μm)

The emissivity dependence on the coating thickness for the selective surface was also studied with the spectrometer test setup (Figure 23). On average, there was less than 10% difference in the optical transmission properties for the selective surface paint within the spectrometer's wavelength range for coating thickness ranging from 7-16 μm . We tried to maintain similar coating thicknesses for different STEG prototypes by using the same volume to area ratio when spray painting it on the absorber.

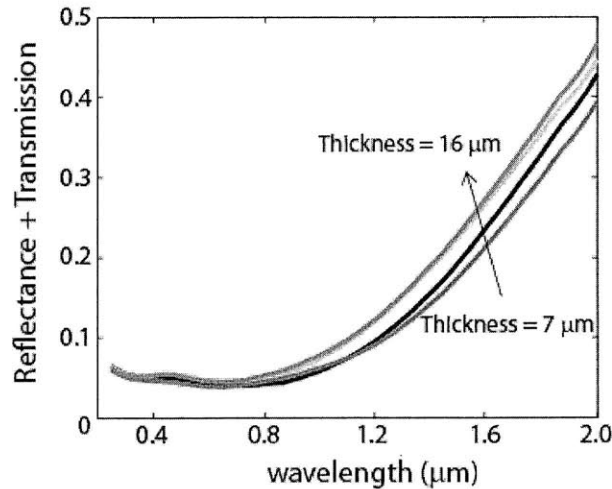


Figure 23: Optical transmission properties of different thickness coating for the selective surface

Even at relatively low hot side temperature ($< 500 \text{ K}$), the selective surface coating did perform better than the ordinary black paint. An increment in the overall output power by nearly 8% was measured

(Figure 24). The increase in power was mostly due to the difference in the absorbance and the emissivity of the absorber surfaces.

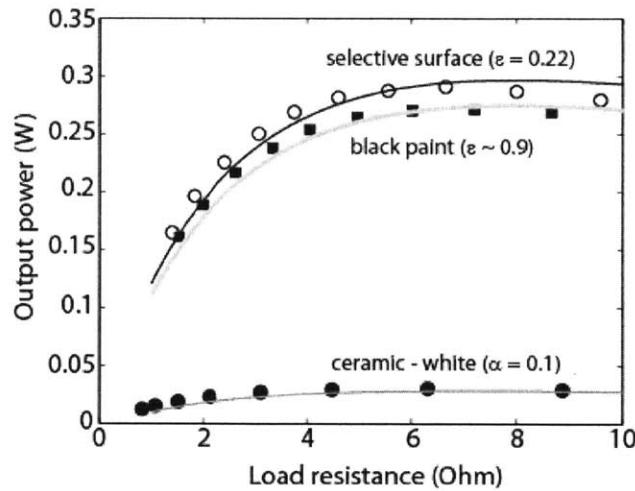


Figure 24: Difference in the overall output power for the STEG for different absorber surface coating that has various absorbance and emissivity (theoretical modeling shown with solid lines)

For the concentrated solar thermoelectric generator, the emissivity of the absorber surface and its effect on the system performance were studied. Unlike a flat-plate system, the absorber emissivity has relatively smaller effect on the system efficiency within the temperature ranges where the concentrated solar thermoelectrics is utilized. The radiative losses do increase with higher temperature, but the material properties degrade faster to reduce the efficiency at such temperature range.

2.3.2 Material property: ZT

Initially we showed the system efficiency for a STEG with Bi_2Te_3 modules. The efficiency for an ideal generator (no parasitic) with the given system design for this material was limited to 4% due to material properties within the temperature range. We present the modeling results for various other TE materials for the same system configuration as well as show the dependence on the figure-of-merit.

To show the influence of the figure-of-merit, we take the material properties to be temperature independent for simplicity. We used different Seebeck coefficients (130-300 $\mu\text{V}/\text{K}$) to change the effective Z as shown in Figure 25. Unlike an actual material, Z does not change with temperature in this analysis, and the increment in the system efficiency with larger Z can be explained by higher TEG efficiency (Equation 9).

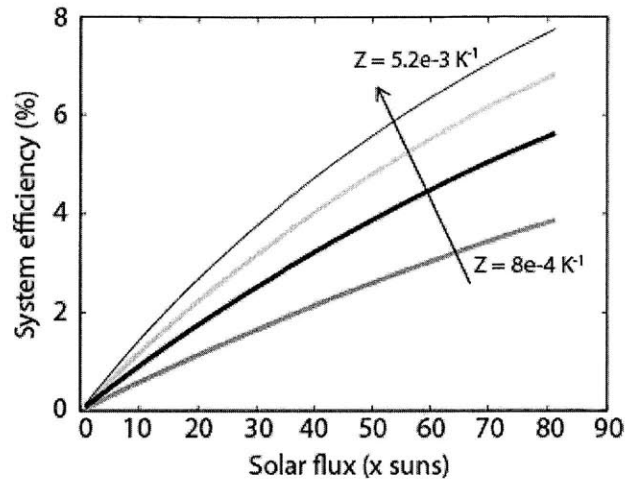


Figure 25: Dependence of STEG efficiency on the figure-of-merit for a TE material at different solar concentration. The darkest line indicates the Z value achievable today at various temperature ranges ($2e-3 K^{-1}$). Bi_2Te_3 at room temperature has $Z \sim 2.5e-3 K^{-1}$, whereas with temperature $> 400 K$, it decreases to $1e-3 K^{-1}$

We also analyzed the system to predict performance with some other state-of-art TE materials. Here, we show the results for PbTe and SiGe (Figure 26). Again, an ideal system without any module parasitic was considered.

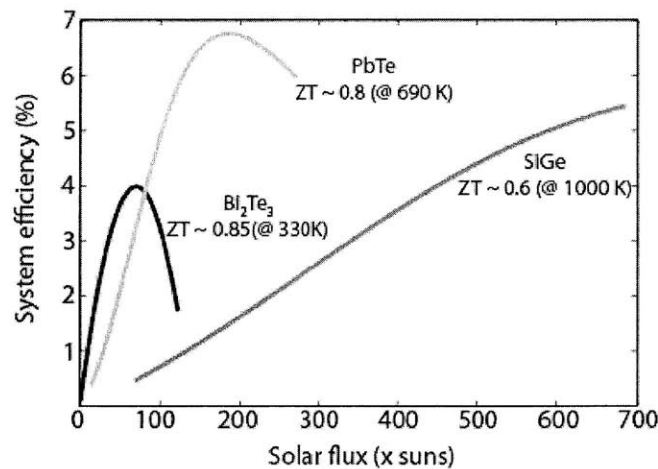


Figure 26: System performance for different TE material system

Between PbTe and Bi_2Te_3 , the ZT values for the material are close to 1. The increase in the system efficiency for PbTe is due to larger overall operating temperature at higher concentration. According to Equation 9, for the same Z value, if the material can operate at a higher temperature, its TEG efficiency will be larger. Similarly, for SiGe, even though its ZT is lower than that of Bi_2Te_3 , the peak efficiency can be higher mainly due to the fact that it can operate at very high temperature ($> 1000 K$). This dependence of higher temperature and efficiency will be explored more in Chapter 5, where we discuss novel TE

materials. From this analysis, we can conclude that the operating temperature and the available solar concentration will determine what type of material is optimal for the STEG. With the available solar cookers, we are working with an optical concentration $\sim 10\text{-}20\times$ suns, and the operating temperature regime of 350-450 K. Bi_2Te_3 is the only material currently available in commercial TEG modules and it does have the highest ZT at the average temperature range of 350 K. For a larger scale system prototype we used commercial Bi_2Te_3 modules. However, at the highest solar intensity, the hot side temperature of the STEG does go beyond the rated 550 K which can destroy the module. More on the performance of the large-scale STEG with commercial modules is discussed later in this chapter.

2.3.3 Heat sink (thermal impedance)

In a solar thermoelectric generator, the solar energy heats the hot side of a thermoelectric module through the absorber. A small percentage of the thermal energy is converted to electrical energy via the Seebeck effect. Most of the heat is transferred across the module through conduction. Eventually the heat at the cold side of the module is dissipated in the surrounding. The cold side temperature of the generator is determined by the thermal flux through the module and the heat transfer properties of the heat sink. In a thermoelectric generator, maintaining a large temperature gradient ($\Delta T \sim 150\text{--}200$ K) between the hot and the cold side of a module is necessary to get useful electric power across a load. It is critical to have a good heat sink that can affectively remove heat from the cold side of the module to maintain a large temperature gradient for a given input thermal power. Many times, the system performance can be drastically reduced by the poor performance of the heat sink rather than the module. In such cases, where the heat sink is not able to extract excess heat efficiently, the cold side's temperature rises, causing a smaller temperature gradient across the module, which results in low output power. Heat transfer from the cold side to the ambient can be through two mechanisms: convection and radiation. Radiation is an effective cooling mechanism for high temperature RTG in space, but in the case of solar thermoelectrics, the cold side is generally at low temperature ($\sim 300\text{-}350$ K). Thus, radiative heat loss from the cold side is minimal. Convection is the most efficient way of extracting heat from the cold side of the generator. There are various ways convection can occur: natural air/water convection or forced air/water convection. Air convection allows for direct heat transfer from the heat sink to the ambient. In the case of water cooling loops and heat pipes, the convection mechanism simply removes heat from the source to another location. Unless the reservoir is infinite, such mechanisms require additional heat exchangers to dissipate heat into the environment. Pool boiling is another mechanism of convection which is based on phase change from liquid to vapor. These heat transfer processes can be characterized with a heat transfer coefficient (h) which tells us how much thermal energy can be extracted via convection (Table 9). In a

STEG, high system efficiency can be achieved when the thermal impedance of the heat sink is small i.e. the total temperature drop across the heat sink for a given thermal power is small. This allows the cold side to remain near the ambient temperature. In a one-dimensional heat flow approximation, the thermal impedance for a heat sink is given by $R_{th} = 1/(h.A_{hs})$, where A_{hs} is the area of the heat sink. Any kind of natural convection (air or water) will have relatively high thermal impedance due to small h value. Thermal impedance for such natural convection based system can be decreased by increasing the overall area of the heat sink. For applications such as STEG, there is a physical limit to the size of the generator that is useful with a solar concentrator (area of the solar cooker: 1.5 m^2 , focal spot size $\sim 20 \text{ cm}$). The cost and the overall weight of the system are also important. As for the heat transfer coefficient, the forced convection systems have larger h than natural convection. However, the price for a forced convection system can be an added complexity/cost to the system as well as many times there is an external electrical power requirement (fan, pumps etc.).

The primary limitation of a heat sink can be seen through module performance degradation as the cold side temperature is increased. System performance curves for a commercial Bi_2Te_3 module shows that the output power of a module can be cut to half when the cold side temperature is changed from 50°C to 100°C (Figure 27).

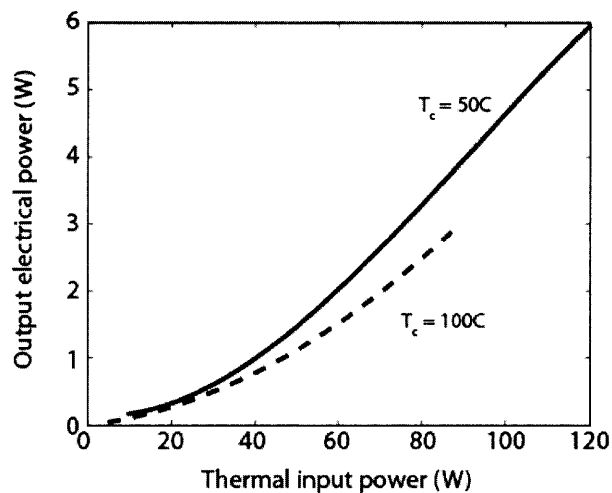


Figure 27: Performance curve of a commercial Bi_2Te_3 module (TG12-6L) at different cold side temperature

Most commercial TEG modules have operating hot side temperature range of $230\text{-}250^\circ\text{C}$. Beyond this temperature, the module fails due to melting of the electrical contacts at the TE leg connections. As the cold side temperature is increased, the hot side temperature quickly reaches this operating point for a lower input thermal power since the thermal impedance of the module changes very slightly. For the module considered here, the hot side temperature quickly reaches 230°C for less than 100 W thermal

input, giving an output power of $< 3\text{ W}$ when the cold side temperature is 100°C . Whereas 100 W input thermal power gives $\sim 4.5\text{ W}$ output power with the cold side maintained at 50°C . The hot side temperature in this case will be less than 200°C .

Even though higher system efficiency can be achieved with lower cold side temperature, in order to maintain such temperatures, the required heat transfer coefficient for a heat sink can be enormous. Again, looking at the module discussed above, in order to maintain the cold side temperature of 50°C , with the hot side of 230°C for the maximum output power, the thermal impedance of the heat sink has to be very low $\sim 0.2\text{ K/W}$. For comparison, the best natural air convection heat sinks (with elaborate fin structures) only have impedance in the range of 1 K/W . To achieve thermal impedance of 0.2 K/W , the required heat transfer coefficient will be approximately $3125\text{ W/m}^2\text{ K}$ (if the heat sink area is kept equal to the area of the module). Such high heat transfer coefficient can only be achieved with forced water convection. Using pump and water cooled loop for the heat sink adds to the complexity of the system as well as requires additional electrical power. Furthermore, there will be need for expensive heat exchangers to dump heat from water to the ambient in order to keep the water temperature low. Ultimately, it will be limited by the thermal impedance of this heat exchanger. The overall benefit of maintaining low cold side temperature at the heat sink can be negative to the system cost and total useful output power of the STEG. Apart from these pros and cons, there may be some general cogeneration benefits of using some of the heat sink options compared to others. We will discuss them individually as we look at different heat transfer options. **Figure 28** shows the theoretical estimates of the system efficiency with different heat sinks; thermal impedance of the heat sink was varied in this analysis. The ideal module parameters were used in the modeling.

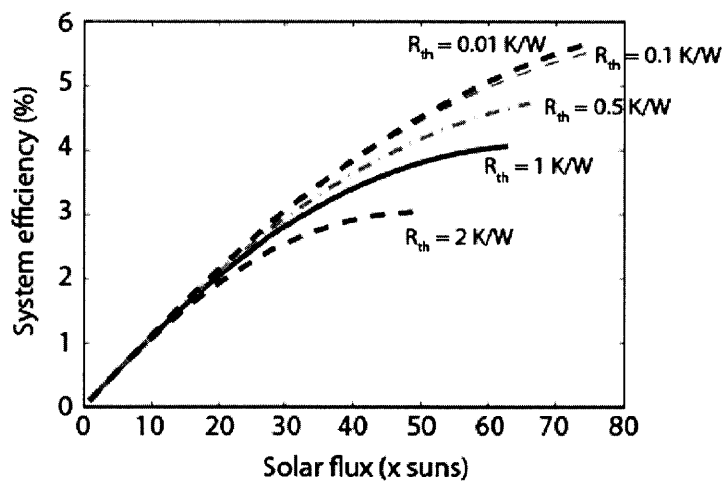


Figure 28: Theoretical estimates for system efficiency with different heat sinks

As the thermal impedance of the heat sink decreases, the cold side temperature will be closer to the ambient temperature. For a given input thermal power, the efficiency of the TEG module will be higher when the cold side temperature is small (**Figure 27**). Beyond 0.1 K/W, the difference in efficiency is very small as the cold side temperature is pinned to the ambient temperature. As mentioned before, the best natural air convection heat sinks have thermal impedance in the range of 1 K/W, and this is achieved by using extensive splayed fin structure to increase the area, which makes it very expensive. Different heat sink options are discussed below with their pros and cons to identify the best match for the STEG system.

The heat transfer coefficients for various heat sinks were measured independently in the lab. A setup including a measure bar, a heater and thermocouples (**Figure 29**) was used to estimate the heat transfer coefficient for different heat sinks. The heat sink was placed on top of a measure bar with thermocouples for temperature measurement. The total energy flux through the heat sink is equivalent to the heat flux through the measure bar. Errors due to convection and radiation were reduced by using thick insulator around the measure bar and by doing the experiment at relatively low temperature (< 390 K).

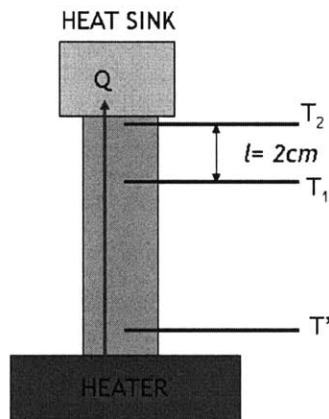


Figure 29: Measure bar experiment to determine the heat transfer coefficient for various heat sinks

The thermal interface between the heat sink and the measure bar plays an important role in determining the heat transfer coefficient. Using a liquid metal eutectic such as gallium-tin, very low interface resistance ($0.05 \text{ Kcm}^2/\text{W}$) was achieved between the heat sink and the measure bar to give accurate heat transfer coefficient. The results are compiled in **Figure 38** at the end of this section. Different thermal interfaces (thermal grease, dry metal-metal interface and liquid metal) between the copper bar and the heat sinks were tested as well. The thermal parasitic at the interface depends on many factors such as surface finishing, clamping force and thermal conductivity of the interface material. A study by Ritzer et al. ^[112] showed the thermal interface junction quality for various interface materials such as silicon based grease, graphite sheet, and dry metal-metal contact, and the influence of clamping force, surface

contamination and surface roughness. An interesting result from the study showed a human hair contaminating the interface can reduce the junction quality to about half of the typical value. Thus, one has to be very careful in dealing with the thermal interfaces in these TEG assemblies, and they were one of the larger unknown factors during experiments.

2.3.3.1 Air convection

The simplest of convection mechanism is the natural air convection, which relies on air flow due to buoyancy. The overall system complexity is minimized with a natural air convection based heat sink when compared to systems with forced convection requiring fans or pumps. However, compared to all other options, natural air convection has the lowest heat transfer coefficient, which can limit the performance of the system. As mentioned earlier, the total thermal impedance of the heat sink can be decreased by increasing the area of the heat sink. Highly efficient natural convection heat sink with splayed-circular fin structure (**Figure 30**) can have low thermal impedance ~ 1 K/W. The flow patterns for different fin arrangements and the geometry determine the heat transfer performance of the heat sink. According to Ref. [113], the fluid flow (known as deflection flow) around the splayed circular pin fins causes an improved airflow mixing and heat transfer performance. On the other hand, such deflection flow does not occur in flat plate fin structures. Such splayed heat sink was used in the preliminary bench-top prototype system to get 3% efficient STEG. Temperature gradient of ~ 140 K was maintained across the thermoelectric module, with the heat sink temperature at 64°C (measured at the base of the fins).



Figure 30: Natural convection heat sink with splayed fins for larger area (Cool Innovations Inc.)

High cost for such specialized forged pin heat sinks may be disadvantageous for the system (\$100), considering the end use for STEG is for remote electrification. Cheaper extruded or bonded plate-fin structured heat sinks have higher thermal impedance ~ 5 - 10 K/W, which will lower the system performance of the generator (**Figure 28**). The smallest thermal impedance (~ 0.75 K/W) specified for a commercial extruded fin heat sink was with 18 cm fin length, and a bulky weight of 2.5 kg.

Forced air convection could provide slightly better heat transfer option than the natural air convection. However, the addition of a fan at the heat sink could negate the benefit of higher heat transfer by the need for additional electricity to run the fan. Low input power fans do not provide large air flows that can make a substantial change in the heat transfer coefficient (Figure 31). Electric fans requiring less than 1 W power have airflow rates of 15 CFM \sim 2 mph or less. The heat transfer coefficient depends on the surface temperature as well as the velocity of air in the surrounding. Based on Equations 22 and 24, Figure 31 shows the temperature dependent heat transfer coefficients for natural and forced air convection. In order to achieve a thermal impedance of 0.5 K/W, even with forced air convection ($h \sim 20 \text{ W/m}^2 \text{ K}$), the required area of the heat sink is $> 100x A_{\text{module}}$.

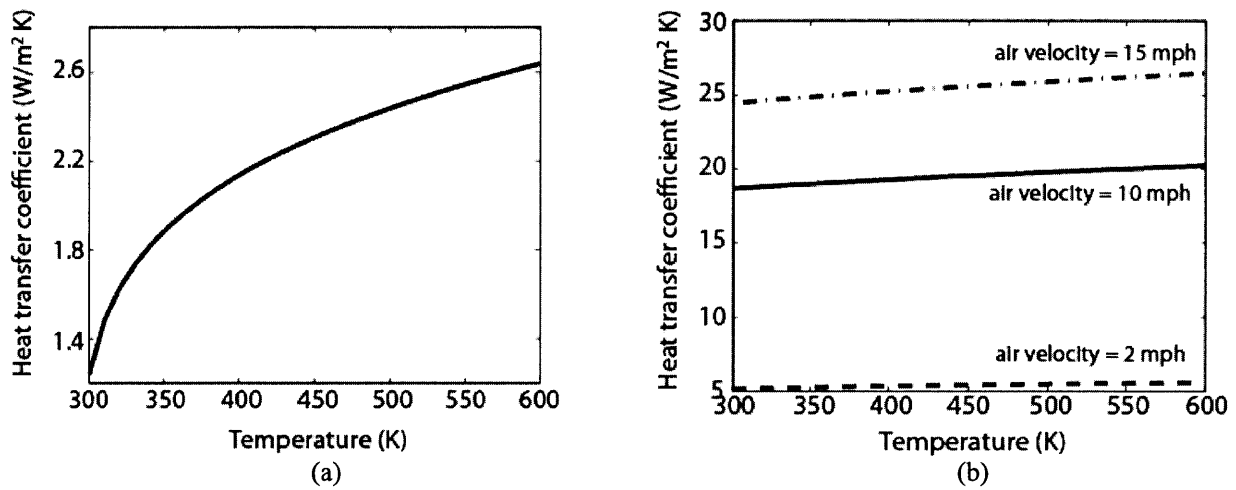


Figure 31: Temperature dependent heat transfer coefficient for (a) natural and (b) forced air convection

Studying the utilization pattern of the solar cookers in Western China, most people boil water for 2-4 hours during a day. Some slow cooking recipes can take up to 5 hours. The concentrator is not used for the rest of the day. Times when the cooker is not being used (3-4 hours), the solar thermoelectric generators with natural convection based heat sinks can help families with extra power generation. In terms of cogeneration benefits, natural air convection system does not provide any cogeneration option for the people during power generation as the heat is lost to ambient.

2.3.3.2 Forced water convection

Forced water convection can have 2-3 orders of magnitude higher heat transfer coefficient than natural air convection. The heat transfer coefficient for such convection mechanism depends on many variables such as hydraulic resistance, liquid pressure, flow rate and water temperature (Figure 32). As mentioned earlier, there can be natural and forced water convection. Natural convection occurs in still water due to

difference in densities of hot and cold liquid. For example if we have a pot of water on top of the generator, the heat transfer from the TEG to water is due to natural convection. Due to large specific heat capacity (4186 J/kg), water can hold thermal energy for a long time. The final heat transfer in such case will be between the top water surface/pot surface and the ambient air. Water temperature rises due to thermal input and can eventually boil. We will describe this phenomenon in detail in the next section. The forced convection is achieved by using external force to push the liquid such that as it moves across the hot surface, the heat is transfer to the liquid. Based on Equation 24 (Sieder-Tate correlation), the heat transfer coefficient for various water flow rate is shown in **Figure 32**. With the heat transfer coefficient of $1000 \text{ W/m}^2 \text{ K}$, the required heat sink area to achieve the thermal impedance of 0.5 K/W is $2.2x A_{\text{module}}$.

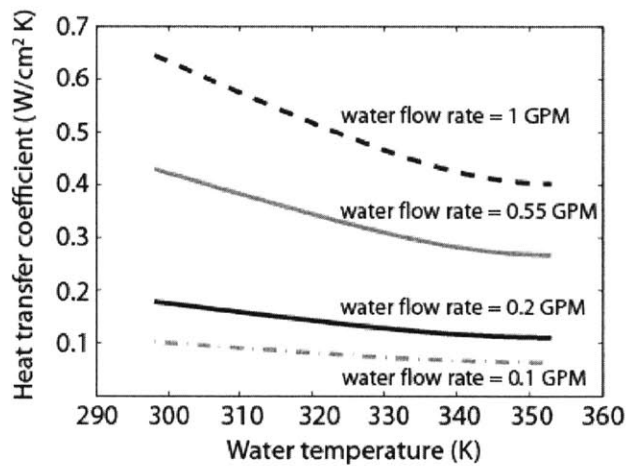


Figure 32: Temperature dependent heat transfer coefficient for forced water convection

A heat sink utilizing forced convection generally consists of an electric pump, a heat exchanger, a radiator and a reservoir (**Figure 33 a**). The pump needs electrical input current, which can be powered by the TEG in the case of solar thermoelectrics.

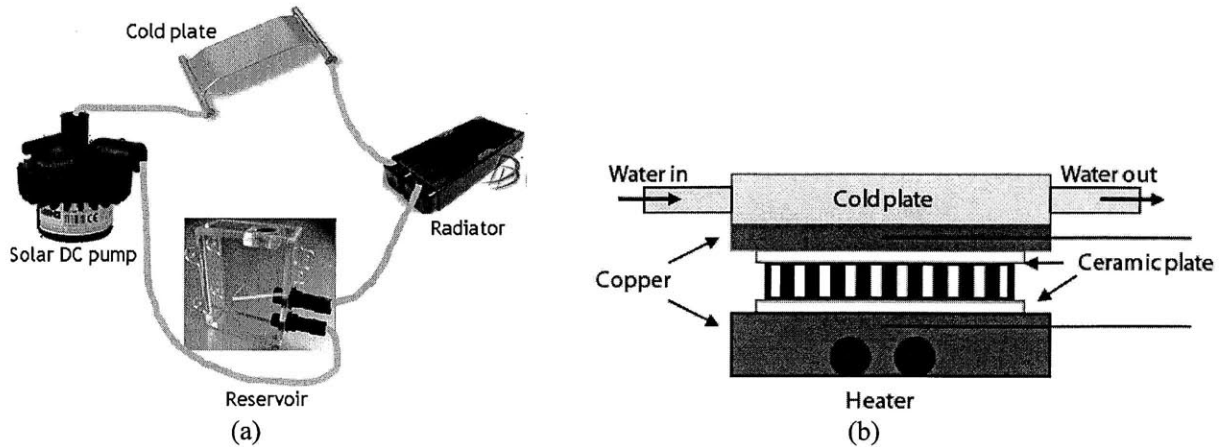


Figure 33: (a) Cold loop as a heat sink for a TEG using cold plate; (b) Setup schematic to measure the heat transfer coefficient for cold loop

As a proof-of-concept, a prototype for such a self-starting cooling loop was built in the lab using a solar DC pump (Figure 33). The dc-pump can start at low input power (2-3 W) with electrical-to-hydraulic efficiency of $\sim 5\%$ (Figure 34 a). The hydraulic power was estimated using the measured flowrate and the fluid pressure in the loop (i.e. power = flowrate x pressure gradient). There is a trade-off between power consumption of the pump and the overall pressure/flow rate which determines the heat transfer coefficient. In this loop, as the electrical input power to the solar pump is increased, the pump efficiency (electrical-mechanical conversion) increases, the flow rate increases which results in higher heat transfer coefficient (Figure 34 b). At 0.36 gallon per minute (GPM), the pump efficiency was 12%. The heat transfer coefficient was measured to be $1.26 \text{ W/cm}^2 \text{ K}$. The measured heat transfer coefficient was very high compared to the typical heat transfer due to forced water convection ($h \sim 0.2 \text{ W/cm}^2 \text{ K}$). This can be attributed to the use of a customized cold plate as the heat exchanger in the loop which has the heat transfer properties similar to that of micro-channels ($h \sim 20 \text{ W/cm}^2 \text{ K}$). The ultra-high performance copper cold plate (Lytron Inc. CP25) with internal crisscrossed fin mesh provides a large heat transfer between the cold junction and the heat sink. At 1 GPM flow rate, the thermal resistance for the heat sink can reach 0.02 K/W , which corresponds to the heat transfer coefficient of $3 \text{ W/cm}^2 \text{ K}$. In order to reach such critical flow rate ($> 1 \text{ GPM}$), the input electrical power to the pump has to be greater than 15 W in this setup.

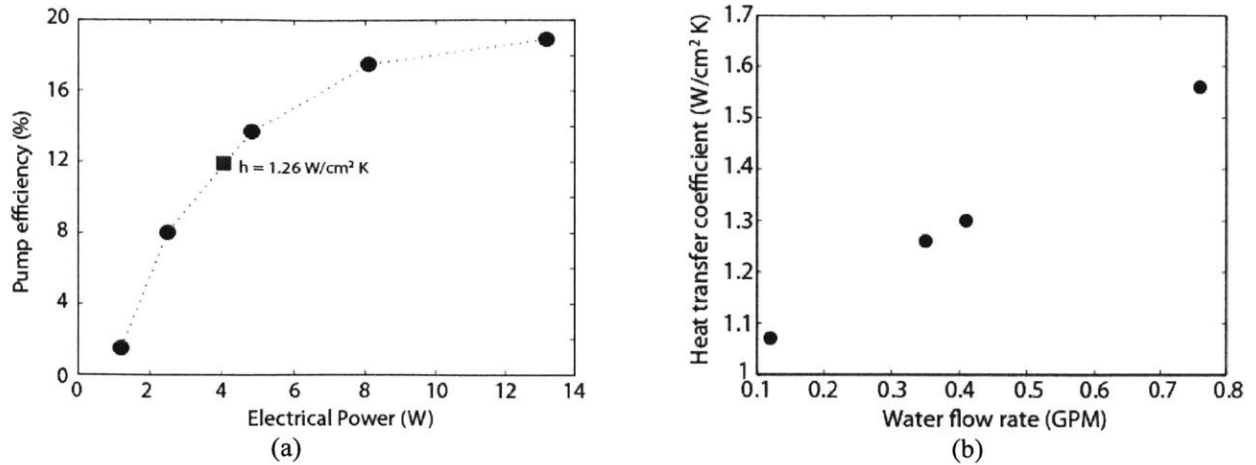


Figure 34: (a) The pump efficiency for a solar DC-pump depends on the input electrical power; (b) The heat transfer coefficient for the cold plate heat sink using forced convection also depends on the flowrate; at low electrical power ($< 3\text{W}$), the flow rate was very small to be accurately measured with the flow meter

A DC-DC converter was used in this setup to provide a 12 V constant input to the solar pump. The conversion efficiency of the DC-DC converter was 85%. A TEG module provided the input power for the converter. In this setup, resistive heaters were used to provide thermal input to the TEG and the heat exchanger (cold plate) was placed on the cold side of the module to create a temperature gradient (Figure 33 a). Flow rate and the temperature gradient for various input thermal power of the heater are shown in Figure 35.

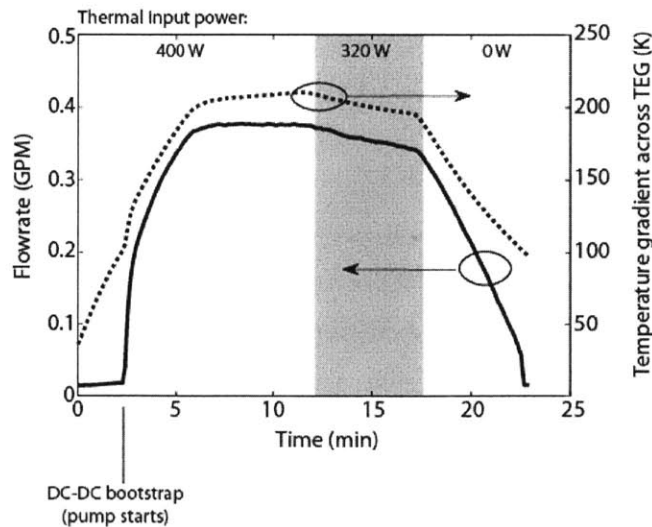


Figure 35: Flowrate and temperature drop across the thermoelectric module for various thermal inputs for the self-powered cooling loop

Even with a low flow rate (0.1 GPM), the measured heat transfer coefficient was nearly three orders of magnitude larger than the natural air convection system. This suggests the possibility of same or lower thermal impedance without the use of large area bulky heat sinks. As mentioned earlier, the high heat transfer coefficient in this setup was mainly due to the micro-channel structures in the cold plate. The primary disadvantage of using such a heat exchanger at the cold side is the high cost (\$200+) and the added system complexity which could prohibit using such heat sink system with the STEG.

A potential advantage of using this kind of water cooling loop for the cold side could be cogeneration of water heating and circulation for household chores (bathing, washing and cleaning) along with electricity generation. Depending on the flow rate and the system size, comfortable water temperature of 330-350 K could be maintained at the cold side. For a home circulation system, the water flow rates can be relatively small (50 liter/hour \sim 0.22 GPM ^[114]). However, the hydraulic resistance corresponding to such flow rates for a home water circulation system is large enough such that the pump requires an electric power in the range of 50-100 W ^[114]. Small solar DC-powered pumps as used in the prototype here are primarily for small flow applications such as gardening, water fountains etc. The output power from the STEG will be barely enough to run a small pump at low flowrate, which does not have many useful applications in the rural settings. From the cogeneration aspect, water temperature at the cold side will be maintained at higher value $> 60^{\circ}\text{C}$, which does not benefit the overall system efficiency.

2.3.3.3 Natural water convection

Another option for heat sink to be used with solar thermoelectrics is pool boiling. This phase change mechanism using liquid convection system has high heat transfer coefficient as it is a two-phase process. Nucleated pool boiling has the heat transfer coefficient in the range of 1-2 W/cm² K, which is comparable to the heat transfer achieved using the expensive cold plate heat exchanger with forced water convection. However, there is no external electrical power required for pool boiling which can boost the overall system efficiency for a STEG. The heat transfer coefficient for pool boiling can be enhanced by providing a large surface area for water boiling. A commercial product called “metafoam” has porous copper foam with large specific surface area. The heat transfer coefficient for pool boiling was measured to be 1.4-1.5 W/cm² K.

Pool boiling can be advantageous for people not only as the heat sink for thermoelectrics but also for water purification purposes. Currently one of the major utilization of solar cookers in rural China is for boiling water. Boiling water is one of the oldest and the easiest means of water purification. Most disease-causing microorganisms cannot survive at temperatures beyond 55°C. If the water is boiled at 100°C for

one minute, Hepatitis A virus is inactivated [115]. Longer time is taken for water disinfection if the temperature is lower. Pasteurization is done by heating water at 65°C for 5-7 minutes [115]. The cold side of the TEG generator can be the bottom of a pot such that the heat rejected from the module can be used for boiling. Thus, pool boiling can be a very good fit for the solar thermoelectrics application as a heat sink.

The primary limitation and concern associated with pool boiling is the high thermal flux requirement and the relatively large cold side temperature (100°C). The boiling curve for water (Figure 36) shows the total amount of thermal flux needed to reach a fully developed nucleated boiling stage which is an order of magnitude larger compared to the natural convection regime. The critical heat flux (CHF) is also a limitation for nucleate boiling, after which the transition boiling occurs, which is less efficient heat transfer mechanism than the nucleate boiling. In film boiling, a thin air film forms in between the surface and the liquid which acts as the insulating barrier for heat transfer. The transition from natural convection to nucleate boiling occurs when the temperature of water is couple of centigrade above the saturation temperature (100°C). With such high cold side temperature, Bi₂Te₃ based TEG module efficiency and the output power will decrease dramatically (Figure 27). For the STEG system using Bi₂Te₃ modules, pool boiling at the cold side is not the most ideal solution.

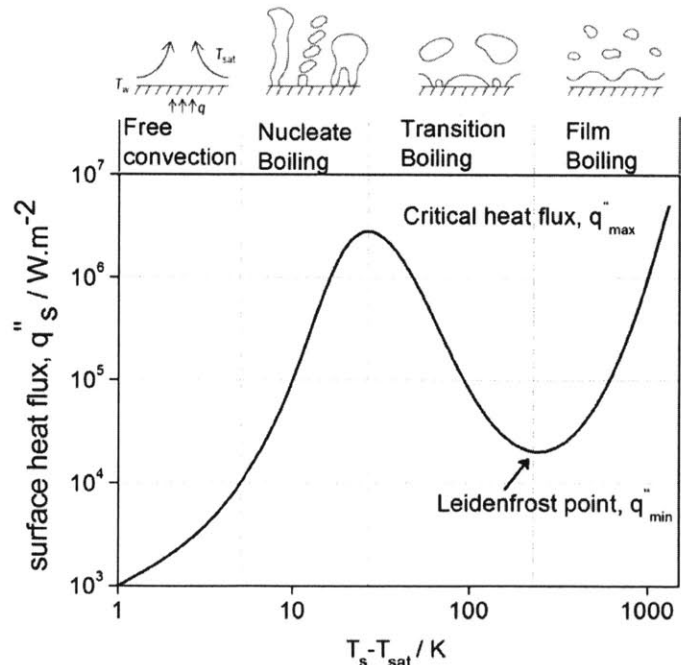


Figure 36: Boiling curve for water showing different stages from natural (free) convection, nucleate boiling, transition boiling to film boiling [116]

Using different fluids, the saturation temperature can be lowered such that efficient heat transfer can occur at lower cold side temperature. **Table 10** lists some of the common liquids which have saturation temperature lower than that of water at 1 atmospheric pressure. Among the listed liquids, some are extremely flammable (acetone), some are considered highly toxic in gaseous state (bromine) and some are health hazards (benzene, chloroform).

Liquid	Boiling point (saturation temperature) (@ 1 atm)
Acetone	50°C
Alcohol (ethanol)	78°C
Alcohol (methanol)	66°C
Benzene	80°C
Bromine	59°C
Chloroform	62°C

Table 10: Saturation temperature for some common liquids (lower than water’s saturation temperature of 100°C)

Taking advantage of the large thermal capacitance of water during heating process may be beneficial for STEG use. Maintaining the water temperature below 70°C for several minutes could provide solution for both the STEG and water purification application. We can utilize the relatively larger natural convection heat transfer coefficient (**Figure 37**) during water heating, and then take the generator off the solar cooker once the water reaches 70°C. The pasteurized water at the cold side can be exchanged with fresh cold water, and electricity generation cycle can continue.

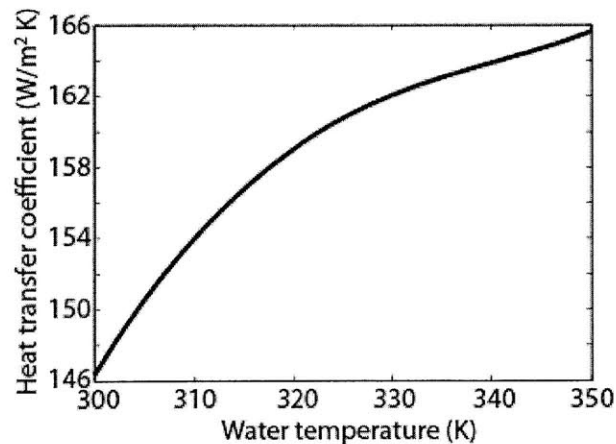


Figure 37: Temperature dependent heat transfer coefficient for natural water convection

Another available option for a heat sink using natural liquid convection is through the thermosiphon effect ^[117]. Thermosiphon is a method of passive natural water convection which has been used in many solar water heater applications in developing countries. The principle for thermosiphon is based on difference in buoyancy and pressure of cold and hot liquid which allows the circulation within a closed or open loop. As the liquid gets hot, it becomes less dense and more buoyant than the colder liquid. The flow is maintained due to this difference in buoyancy. No external pump is required for the water loop. The flow rate of water depends on the hydraulic resistance of the loop. Higher liquid flow rate increases the heat transfer coefficient as shown in the case of forced convection. In thermosiphon, flow rates up to 50 liters per hour and small thermal impedance of 0.55 K/W can be achieved with commercial designs for home water circulation ^[114]. The water temperature for residential heating is usually maintained at 350-360 K. Similar to the boiling water application, the advantage of using this technology is the additional benefit of heated water for household use along with electricity generation without any mechanical pump requirement. Apart from the system complexity, the disadvantage of using such system comes from area usage. Thermosiphon based water heating systems discussed in Ref. [114] are generally roof-top systems with area coverage of $\sim 1-2 \text{ m}^2$. For distributed generation scale, the area of the solar concentrators is of such order. With smaller thermosiphon system, the overall hydraulic resistance can increase causing lower flowrate and lower heat transfer coefficient. For the distributed power generation utilizing available solar concentrators, this heat sink option only adds complexity without any significant increase in the system performance, as the cold side temperature will be $\sim 70^\circ\text{C}$.

The measured heat transfer coefficients for different heat sinks are summarized in **Figure 38**. Data using a commercial water chiller with the cold plate is also shown for the reference. Even though, this option has the highest heat transfer coefficient, it is not a viable solution as the chiller requires a large input electrical power ($\sim 12 \text{ A}$, 115 Vac). Apart from pool boiling, the high heat transfer coefficient ($> 1 \text{ W/cm}^2 \text{ K}$) was achieved by using the micro-channeled cold plate for forced water convection. Regular air convection and natural water convection are orders of magnitude lower in performance.

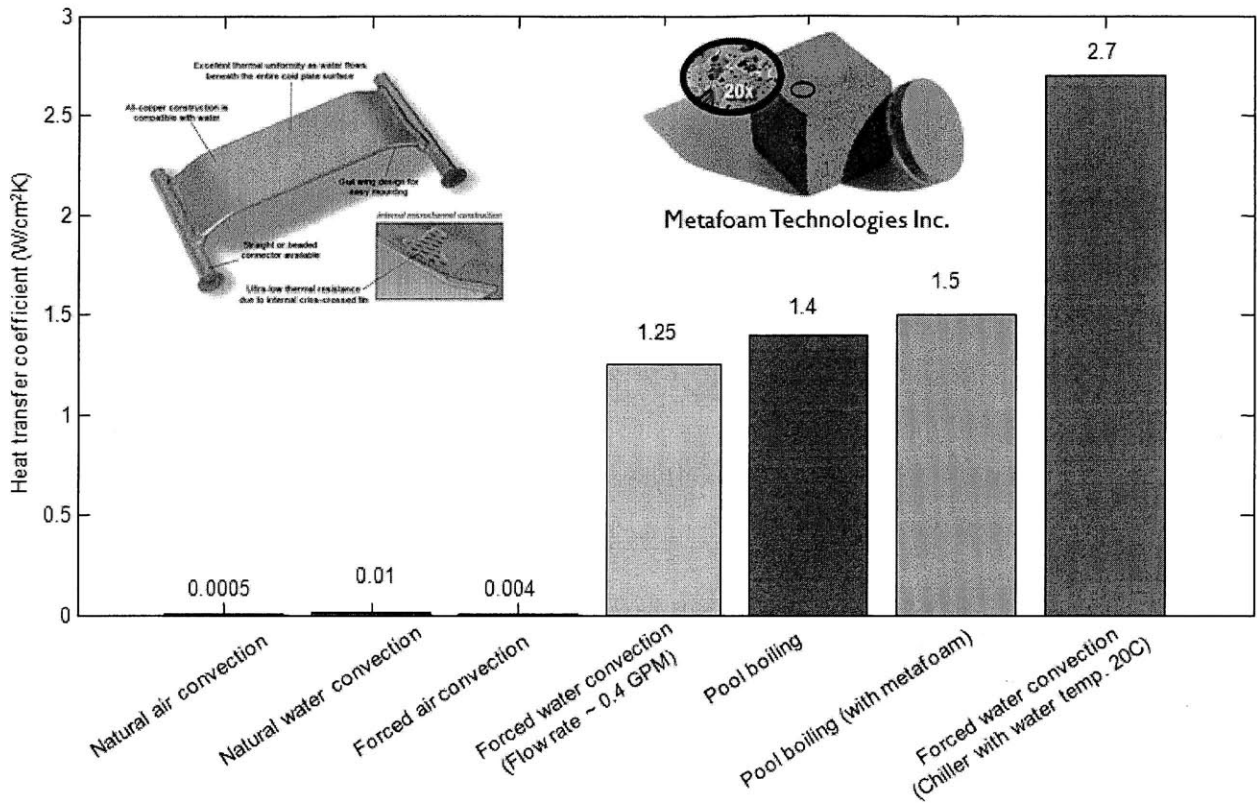


Figure 38: Measured heat transfer coefficient for various heat sinks.

Table 11 summarizes the pros and cons for different heat sinks considered in this study indicating that the heat transfer coefficient is not the only criteria for choosing a heat sink. Apart from the forced water convection, the heat sink temperatures for all other option are similar. If forced water convection is to be used with cogeneration aspect, then the necessary cold side temperature will again be similar to 60-80°C requirement for home heating water.

Heat transfer mechanism	Heat transfer coefficient (W/cm ² K)	Cold side temperature (°C)	Cost	Self-powered	Comment
Natural air convection	~ 0.0005	~ 60-80 °C	\$\$\$ (\$100)	Yes	Simple integration
Forced air convection	~ 0.002-0.004	~ 40-70 °C	\$\$	No (fan)	
Pool boiling	~ 1.5	>100 °C	\$	Yes	High cold side temperature, high heat flux requirement
Natural water convection (heating water)	~ 0.015	~ 70-80 °C	\$	Yes	Need to change water after reaching pasteurization temperature
Natural water convection (Thermosiphon)	~ 0.02	~ 70 °C	\$\$	Yes	System complexity, large area requirement
Forced water convection	~ 0.1-0.5	~ 20-50 °C	\$\$	No (water pump)	System complexity
Forced water convection (micro-channel/chiller)	~ 2.5	20 °C	\$\$\$ (\$200)	No (water chiller)	System complexity

Table 11: Summary of different heat sink options for STEG

With cogeneration of hot water, the STEG system can have dual benefit. However, limiting the cold side temperature for Bi₂Te₃ module closer to the ambient temperature for maximum output power is challenging. With heating water at the cold side to pasteurization point, the temperature can be limited to moderate 70-80°C; at the same time STEG can be incorporated with the local solar cooker for a full day operation.

2.3.4 Hot side absorber design

One of the assumptions in the theoretical model was that the hot side absorber area was equal to the focal area of the optical concentrator. In the case of the bench-top prototype, the Fresnel lens placement was such that its focal area was equal to the area of the TEG module. The hot side ceramic for the TEG was the absorber with the selective surface coating. In the case of parabolic solar concentrators, the focal area spot size is ~ 20-30 cm in diameter. The optical concentration at this focal spot is only ~ 10-20x suns. If

the entire focal spot is covered directly with the TEG modules, the concentration will not be high enough to achieve a large hot side temperature (180-230°C). Secondary optical concentration using a Fresnel lens is also not possible due to the fact that the incoming sunlight at the focus is not parallel as in the case of the solar simulator. Thus, a hot side absorber must be designed such that it can help in “thermal concentration” to increase the solar flux through the TEG module. Thermal concentration can simply be defined as the ratio of the area of the absorber to the area of the TEG module. The absorber collects the solar power and transfers it through the TEG module to the heat sink (**Figure 39 a**). In the STEG system, the absorber is a piece of metal attached to the front of the TEG module. Aluminum was chosen for the absorber due to its low density (light weight) and good thermal conductivity (250 W/m.K). The addition of an absorber will immediately decrease the system performance in the case of constant input thermal power, mainly because of an additional interface between the TEG module and the hot side. Due to this parasitic thermal resistance, there will be a temperature drop across the interface which will lower the actual hot side temperature of the TE module. 17.5% drop in the open circuit voltage was measured for the bench-top prototype with and without an extra absorber layer under the solar simulator (**Figure 39 b**). A thin layer of thermal grease (Omega Silicon grease: $\kappa \sim 2.3$ W/m.K) was used in between the absorber and the TEG to improve the interface. The drop in the open circuit voltage directly corresponds to lower temperature gradient across the TEG, which results in lower efficiency.

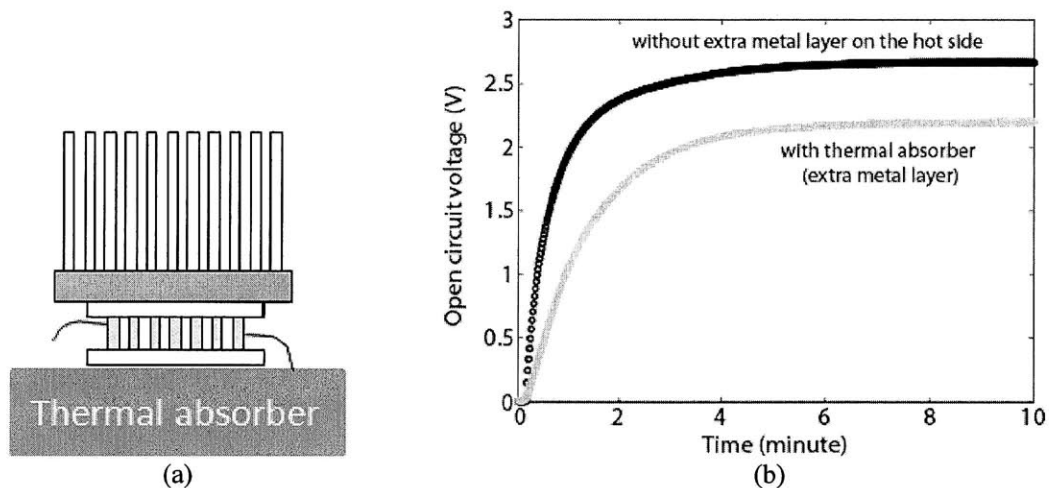


Figure 39: (a) A TEG module in between a thermal absorber and a heat sink; (b) Open circuit voltage measurement for a TEG module with and without an extra layer in the front acting as a thermal absorber using the solar simulator setup

As mentioned earlier, the hot-side absorber is needed to increase the input thermal power to the STEG when using with a solar cooker. Even with the added thermal interface due to the absorber and convection

losses around it, there was improvement in the system performance (34% increment in the open circuit voltage measurement) primarily due to a larger input thermal power (Figure 40). The experiments were conducted within an hour of each other using a metal reflector solar cooker. Similar environmental conditions are assumed for comparison. The increase in the open circuit voltage can be attributed to the higher input thermal power collected by the absorber at the focus of the solar cooker. Without the absorber, only a fraction (\sim area of the module/focal area = 0.21) of the concentrated light will hit the thermoelectric generator. The temperature of the heat sink will also increase as the concentrated light hits it directly if there is no absorber, causing decrease in the overall performance.

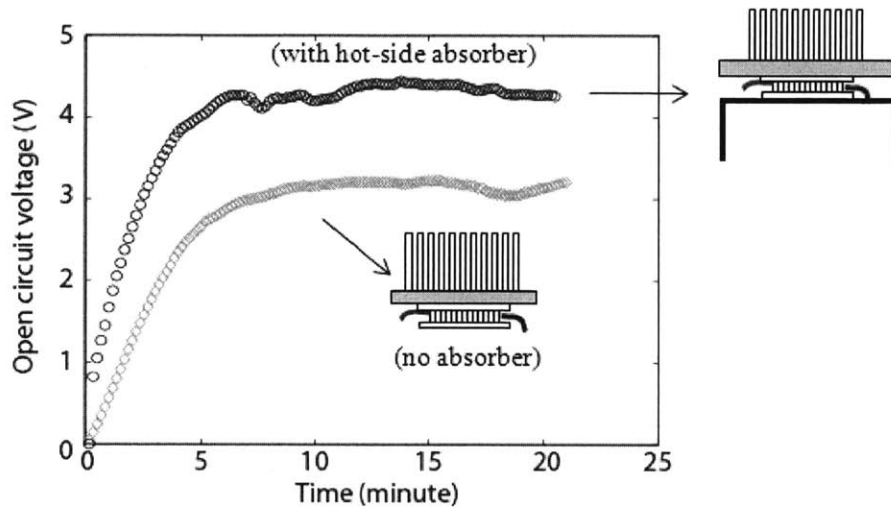


Figure 40: Open circuit voltage measurement for the STEG (with and without an absorber) using a solar cooker

In the bench-top prototype, the convection loss at the hot side was highly suppressed by creating a dead air layer closer to the TEG module with an enclosure. A similar strategy was used for the hot side absorber design. Rather than a flat-plate absorber, a cylindrical design was used to suppress the convective loss underneath the hot surface by confining hot air (Figure 41).

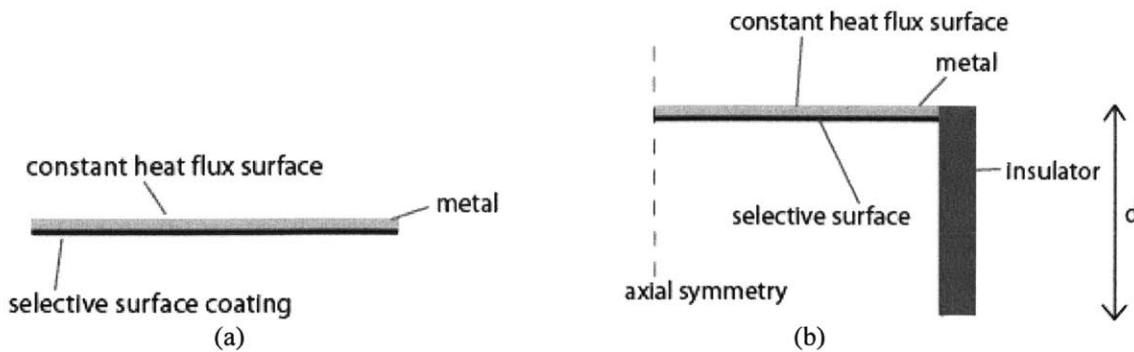
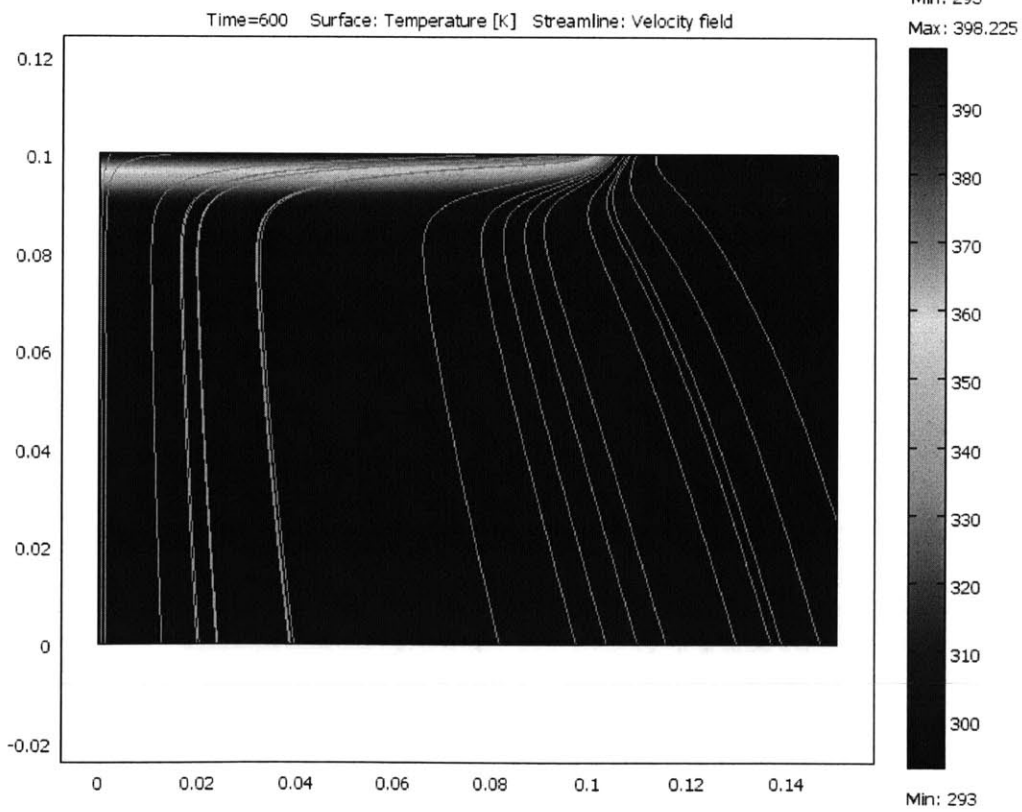
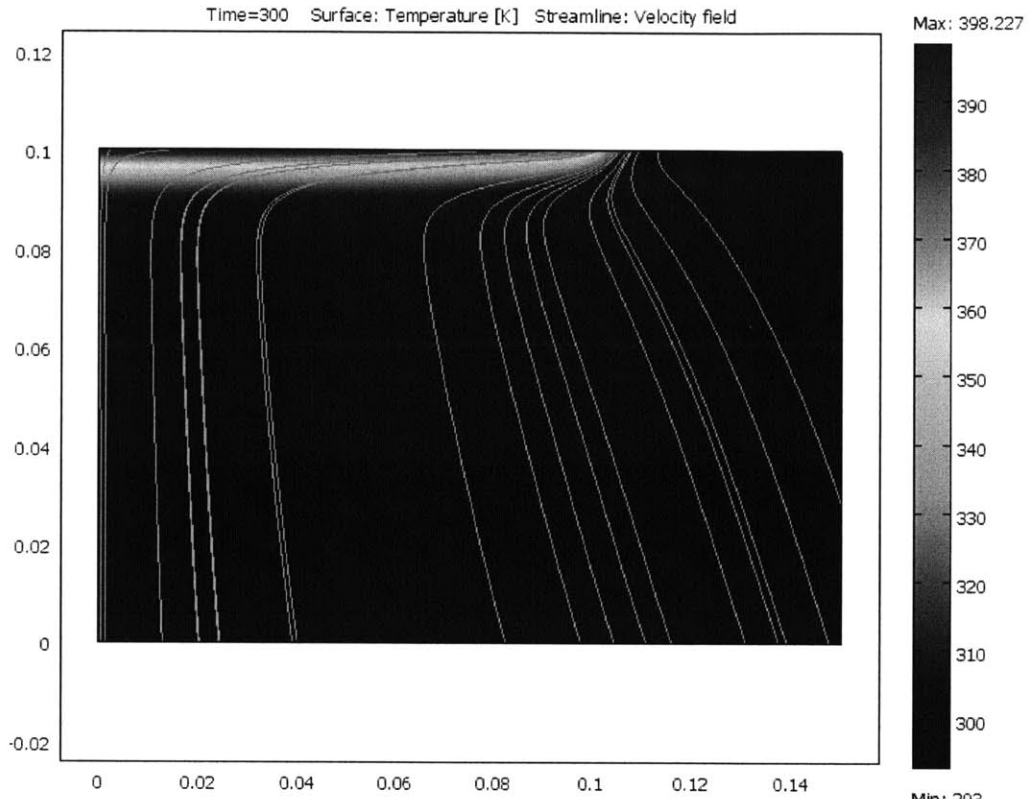
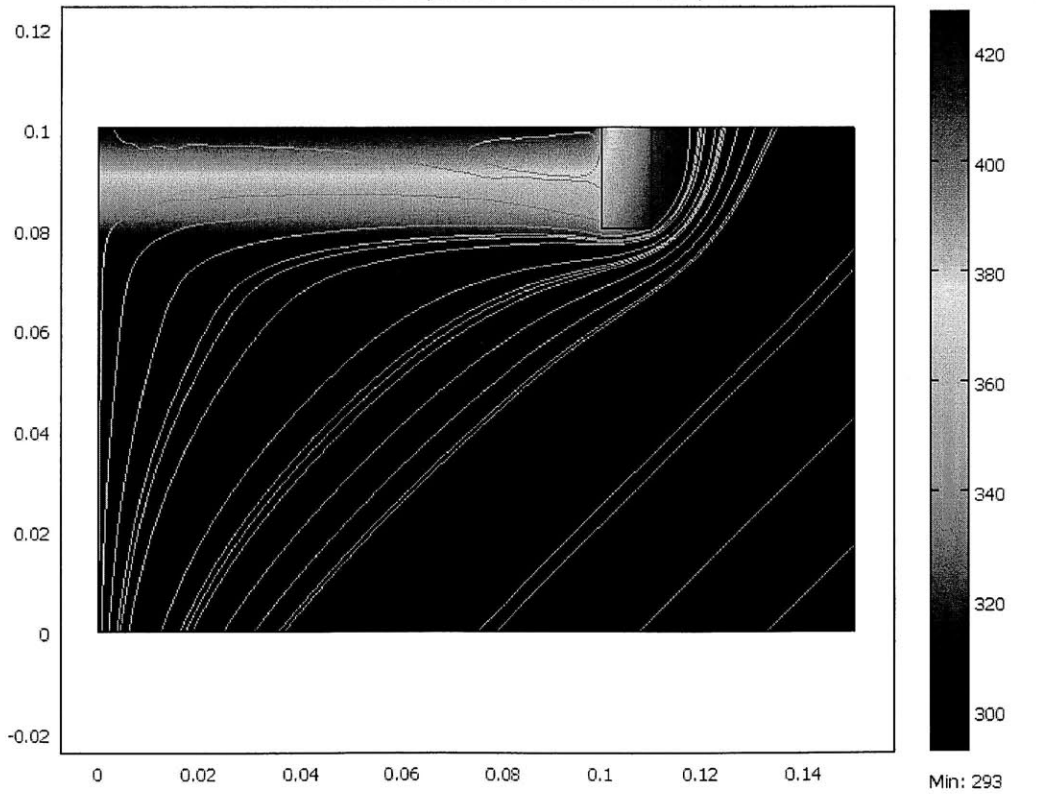
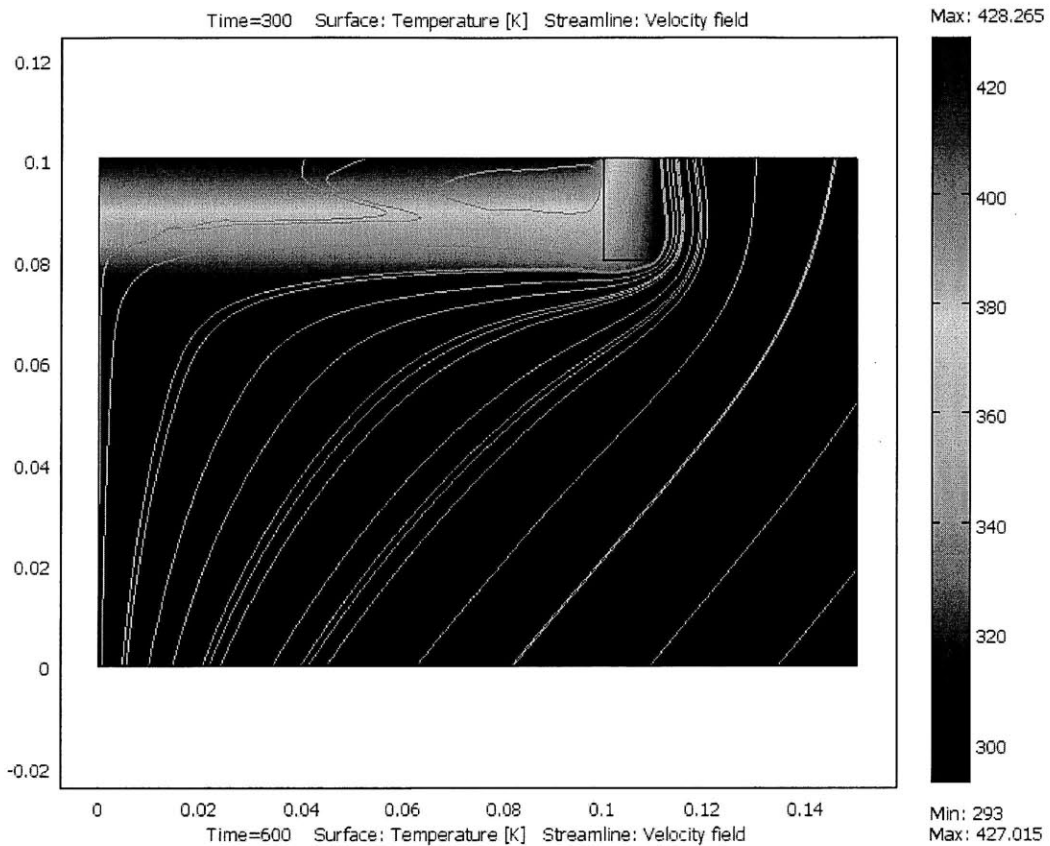


Figure 41: Hot-side absorber design for consideration (a) flat-plate; (b) cylindrical design

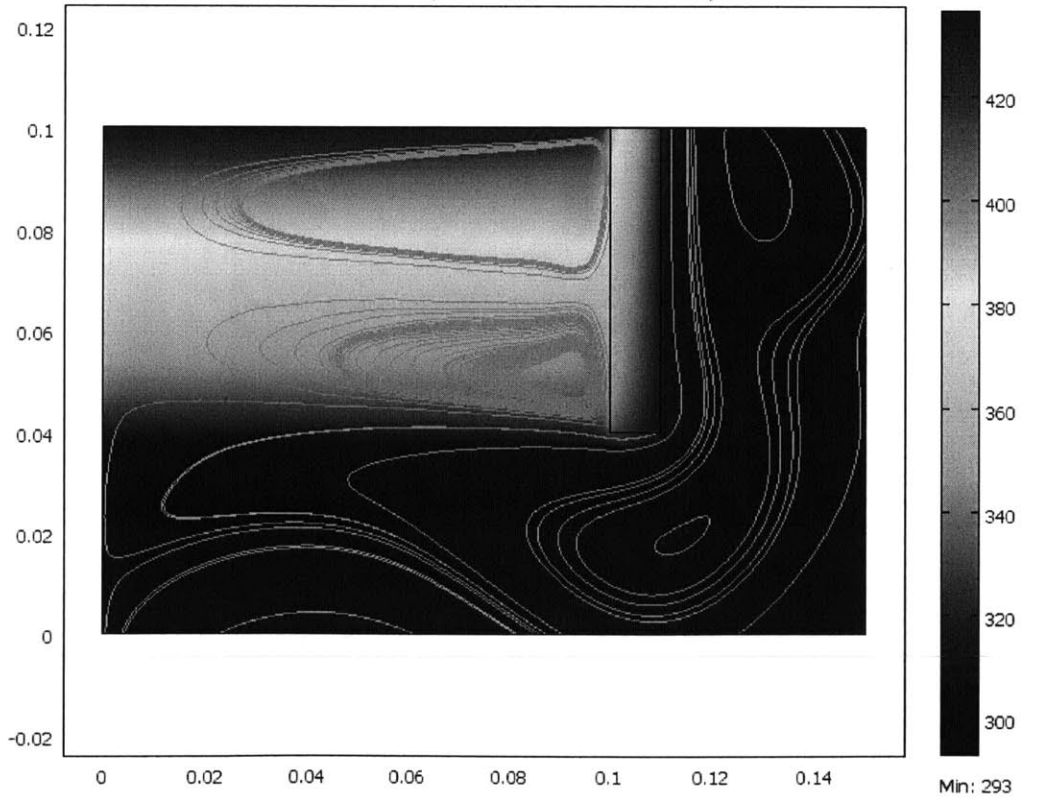
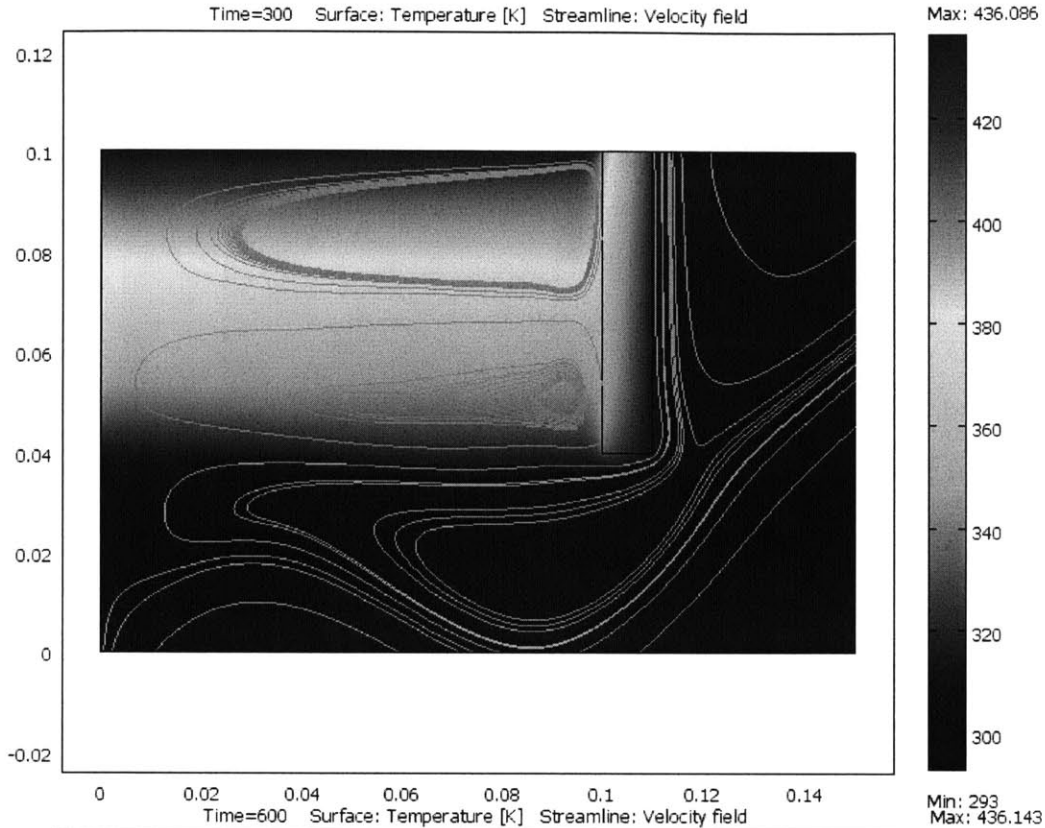
The vertical walls of the cylinder can create a dead air space between the hot side and the ambient such that the heat transfer due to convection can be minimized. A finite element analysis (COMSOL) was done to show the temperature variation for the hot side with cylindrically enclosed absorbers of different wall heights under a constant input heat flux (Figure 42). A thick (0.40”) industrial grade insulator (Pyrogel XT: $\kappa = 0.035 \text{ W/m.K}$) was used around the vertical wall to suppress convection loss. With a constant heat flux (800 W/m^2) at the metal surface, the finite element analysis solved for conduction, convection and radiation heat transfer. For the boundary conditions, axial symmetry was used on one side as shown in Figure 41 (b). Air convection around the absorber determines the final temperature. On the edges of the simulation space, air temperature of 298 K was taken as the boundary condition. Results from the transient simulations for two different times ($t = 5$ minutes and $t = 10$ minutes) are presented here to show the development of air flow over time. The buoyancy-driven flow induces recirculation zones within the enclosure. These recirculation zones are clearly seen in the streamline plot of the velocity field (dark lines). As the wall height (d) is increased, the overall convection loss from the outer exposed surface increases due to larger surface area exposure. The temperature variation for the hot side for different absorber designs (Figure 43) is due to air convection loss around the absorber. The optimum height for maximum absorber temperature was determined to be 6 cm.



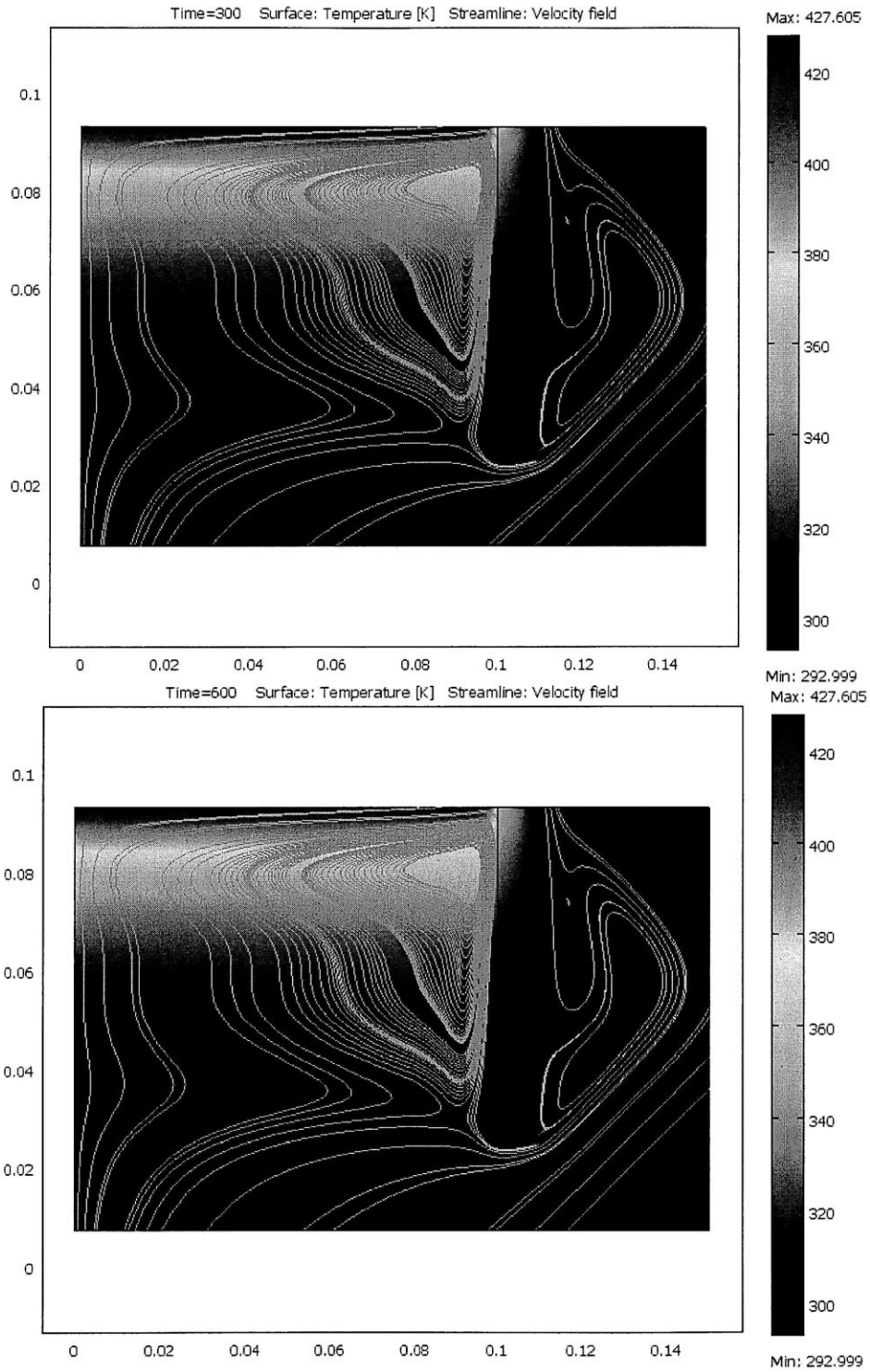
(a)



(b)
90



(c)



(d)

Figure 42: Finite-element simulation (COMSOL) showing snapshots of temperature field for different absorber heights ($d = 0$ (a), 2 cm (b), 6 cm (c), 8cm (d)) for $t = 5$ minutes, and $t = 10$ minutes; and air flow under the hot side absorber (streamline velocity profile is shown here)

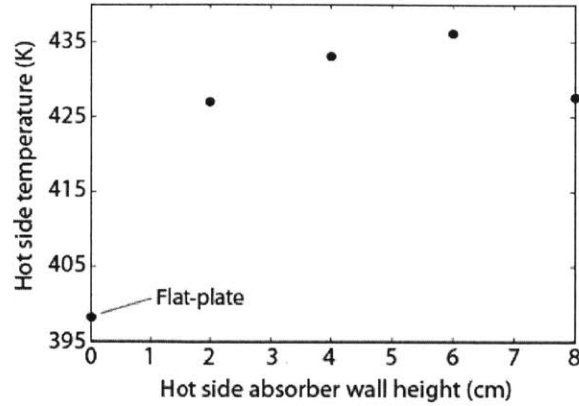


Figure 43: Maximum hot-side temperature vs. absorber height (d) (for $t = 10$ minutes) for a constant input flux

With a relatively large exposure area for convection loss, the side walls have to be well insulated in order to minimize the loss even for a small airflow around the hot side ($h \sim 5 \text{ W/m}^2\text{K}$). **Figure 44** shows the dependence of the temperature gradient across the TEG on the thermal impedance of the hot side absorber, where the impedance is defined as the thermal resistance for the convective heat loss path. A simple thermal equivalent circuit of the system as shown in **Figure 16** (b) was used to model this dependence. In this analysis, temperature independent TE properties were considered, i.e. a single thermal resistance defined the TEG module. Larger thermal impedance for the hot side absorber means higher resistance for the heat flow through convection to the environment such that most of the heat would flow through the TEG contributing to useful output power.

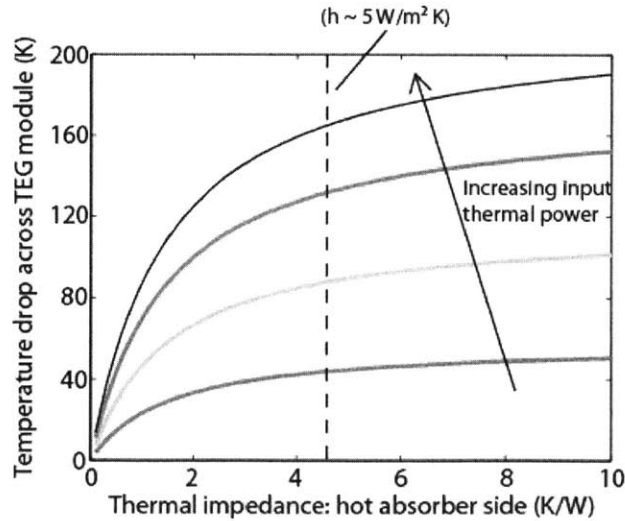


Figure 44: Temperature drop across the TEG module varies as the thermal impedance of the hot side absorber is changed for different input heat flux; fixed heat sink thermal impedance based on natural air convection was used for this analysis (1 K/W)

The convective heat transfer from the absorber has to be highly suppressed to realize a large temperature gradient across the TEG module such that higher efficiency can be obtained. For a commercial Bi_2Te_3 module, the maximum output power is achieved when the temperature gradient across the module is $\sim 180\text{-}200$ K, with the cold side temperature of 50°C . From **Figure 44**, it is evident that the temperature gradient drops drastically as the thermal impedance of the hot side absorber decreases. For the concentrated solar thermoelectrics, it is critical to suppress the convection loss by properly designing the hot side absorber. Using a vacuum system is an option that can completely eliminate the convection loss at the hot side. However, for the application of distributed power generation for rural setting, the usage of glass and maintenance of vacuum can add unwanted cost and decrease the robustness of the system. We chose to work with industrial grade insulators (thermal conductivity ~ 35 mW/m.K) around the hot side absorber to decrease the convection loss. The system used in the field trials is discussed next.

2.4 Generator assembly

A prototype with water convection based heat sink and a hot side absorber was designed and built to be used with local solar cookers. Four commercial TEG modules (TG -12-6) were used in the generator in series to achieve useful power > 10 W. The objective of the system was to provide 2-3 hours of lighting with 2-5 W LED lamps, and 2-3 hours of cell phone charging capabilities at 3 W. This would require total energy generation of approximately 40 Wh and storage per day. With a daily average of 6 hours of generation time with solar cooker, the output power should be 6.7 W. During the early hours of a day and late afternoon, the solar irradiance is lower. To compensate for this variation in power, it was estimated that a peak power of 10 W would be necessary to result in this average power, accounting for the inefficiency in the charging system. With higher cold side temperature from water heating, the performance of the generator will be lower than the factory specification. Modules with maximum power of 20 W were chosen to provide the necessary power for the STEG application. One of the criteria for choosing the modules was based on thermal impedance. Higher module thermal impedance indicates larger temperature gradients for a given thermal input power. However, one has to be careful about choosing the impedance for a given heat sink condition. With higher cold side temperature (than the ideal operating point), a larger thermal impedance indicates higher hot side temperature as well. For commercial modules, there is a limit ($230\text{-}250^\circ\text{C}$) beyond which permanent damage can occur. Also, higher thermal impedance for the module adds to the overall resistance in the path of heat flow through the absorber, TEG module and the heat sink. Depending on how well convection is suppressed at the absorber side, the total

resistance through the generator could become comparable to the convection loss path. Commercial modules for consideration are listed in Table 12. Modules from Marlow Inc. were chosen due to their high material quality (better module ZT compared to Hi-Z modules). Laboratory tests between two commercial Marlow products (part number: TG-12-4 and TG-12-6) gave higher output power from the later module for similar input thermal conditions. Even though TG-12-4 has higher thermal impedance due to smaller aspect ratio, the internal resistance of the module is also larger than that for TG-12-6 (6Ω vs. 4Ω). TG-12-4 module may have higher open circuit voltage due to a larger temperature gradient, but the current across a matched load will be reduced. The optimum between the thermal impedance and the internal resistance of a TEG module for maximum performance will be discussed in Chapter 4 during module redesigning. The difference in the total areas for the two modules also affects the system performance. For a fixed input thermal flux condition, less thermal power is going through a smaller area module. The larger thermal impedance for TG-12-4 also causes the module to reach the maximum hot side operating temperature for lower input thermal power, and causes quicker failure at the hot side. The bulk cost for TG-12-6 was also slightly lower than the cost for TG-12-4. Thus, TG-12-6 was chosen for the prototype generator. In Chapter 4, we will discuss in detail the optimization of the module design for maximum power by changing the TE leg geometry.

TEG module	Hot side (°C)	Cold side (°C)	Heat flow through the module (W)	Thermal resistance (K/W)	Comment
Hi-Z (19 W)	230	30	~ 536	0.37	Modules do not come with ceramic wafers for electrical isolation; Lower TE material quality (low module ZT < 0.35)
Hi-Z (9 W)	230	30	~ 220 (2 modules: 440)	0.64 (2 modules: 0.32)	Same as previous
TEHP1-12656-0.8 (10 W)	230	50	~ 240 (2 modules: 480)	0.75 (2 modules: 0.375)	
Marlow TG-12-4 (3.5 W)	230	50	~ 75 (4 modules: 300)	2.21 (4 modules: 0.55)	With higher cold side temperature, input flux ~ 220 W will be enough to get hot side temperature beyond 230°C
Marlow TG-12-6 (5 W)	230	50	~ 105 (4 modules: 420)	1.47 (4 modules: 0.36)	

Table 12: Commercial TEG module specifications (company data sheet)

The schematic of the generator is shown in **Figure 45**. We expected slightly lower efficiency for this prototype compared to the bench-top primarily due to an additional thermal interface at the hot side absorber and increased convection loss around it.

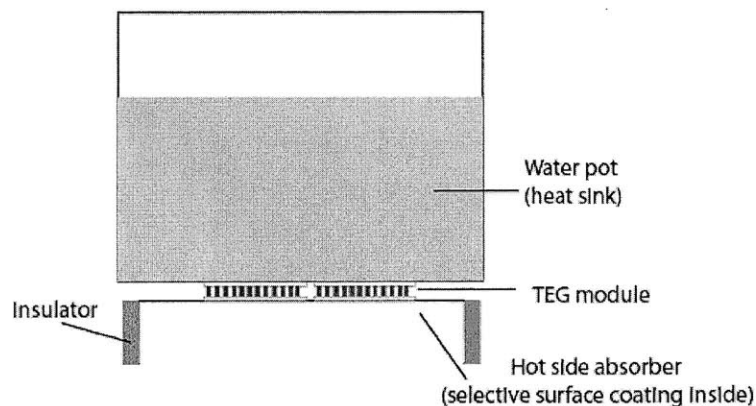


Figure 45: STEG prototype using natural water convection scheme for heat sink with four commercial Bi_2Te_3 modules

In order to ensure good contact between the absorber, the TEG module and the heat sink, different clamping mechanisms were tested. Initially, set of ceramic screws and spring washers were used to clamp the assembly of the absorber, module and heat sink (**Figure 46**). Holes were drilled in the heat sink to make the screw connection. The ends of the screws were covered with thermal epoxy at the heat sink end to ensure no water leak from the heat sink to the module. Unfortunately, the thermal expansion mismatch between the metal, epoxy and the screws caused enough stress and fatigue during heating cycle, the water leak was inevitable. Welding could have solved the water leak issue. However, the appropriate welding temperatures (50-90% of the metal melting temperature) are above the operating temperature for TEG modules which have to be in-between during the welding process.

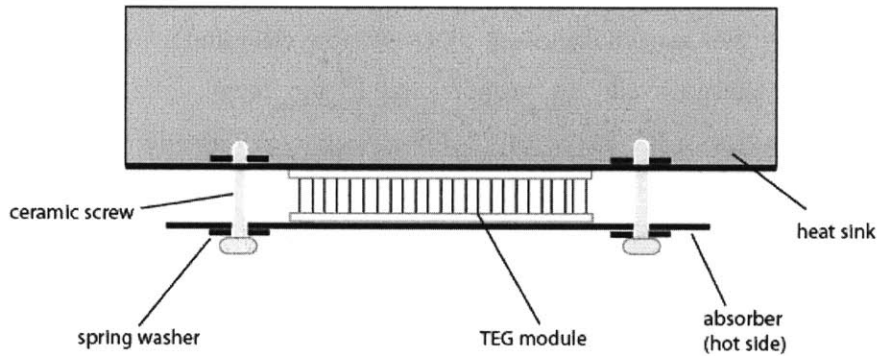


Figure 46: Clamping force for STEG assembly

Thermally conductive cement ($\kappa = 6.5 \text{ W/m.K}$) operating at moderately high temperature (315°C) was chosen for the assembly to ensure the attachment of the absorber, modules and heat sink. With no holes in the generator assembly for any screws, there was no water leak from the heat sink. However, the interface parasitic was worsened by the use of cement.

Since the generator will be operating during day, and at varying input power, it is necessary to use a battery for energy storage. Various batteries considered were lead-acid battery, nickel-cadmium, and lithium ion battery. In selecting a proper battery, both capacity and maximum charge current were considered. In this application of solar thermoelectrics, cost was the dominant factor for choosing the specific type of a battery. Sealed lead-acid battery had the most favorable characteristics for this application for storage capacity vs. cost. A 4.5 Ah sealed lead-acid battery was chosen, which was also commonly used with solar PV systems in many villages. At a nominal voltage of 12 V, the corresponding energy storage capacity was 54 Watt-hour. With a generator output power of 10 W, it would take less than 6 hours of daily charging time for a completely discharged battery.

Battery lifetime is influenced by the charging/discharging rate, the level of charge achieved when cycling and the level of discharge. Discharging a battery past its safe discharge voltage (10.2 V), will significantly degrade the battery. Also, leaving the battery at this low charge state will degrade the lifetime quickly. Thus, a charge controller is critical for systems when batteries are charged and discharged frequently. One of integral component of a charge controller is a DC-DC converter. With variable input voltage to the charge controller, a DC-DC converter is essential for charging a battery with steady voltage. In order to charge a 12 V battery, a DC-DC converter is generally used to boost the input voltage to 12.5-14.4 V. A controller circuit comes with indicators to show various states of battery charging. Once the battery is fully charged (13.8 V), the current is decreased significantly (< 50 mA) to protect it from overcharging. During the bulk phase of the charge cycle (initial charge stage), the voltage rises to bulk level (14.4V). The battery draws maximum current at this stage. A commercial charge controller was chosen with a DC-DC converter and a current limiting circuit (1.5 A), which provided a charging current proportional to the input voltage. Commercial DC-DC converters have efficiencies in the range of 85-90%. A charge controller also protects the battery during discharge cycle with a cutoff circuit that is designed to cut off the output power to a load for voltage lower than 10.5 V.

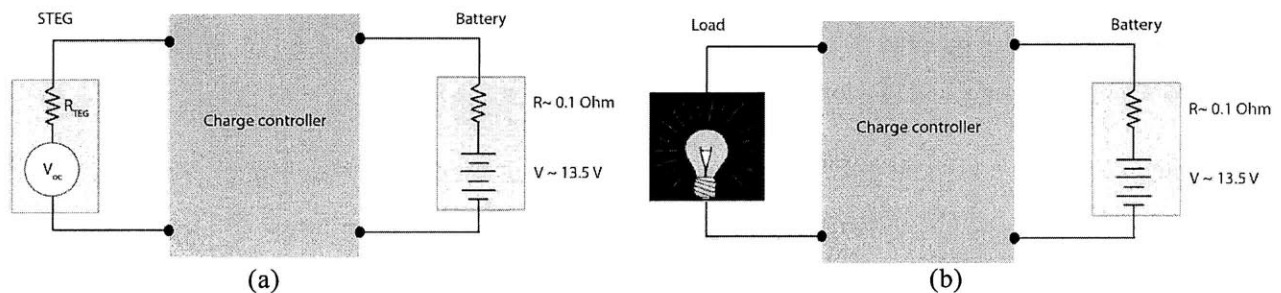


Figure 47: Circuit schematic for (a) battery charging with STEG using a charge controller; (b) battery discharging across a load

The output power from the generator was measured over time, along with water temperature. With water heating at the cold side, the time constant was set by the system thermal impedance and capacitance of water and absorber. Transient simulations were done to understand the system performance over time as discussed in the next section.

2.5 Transient simulation

The theoretical analysis and the experiments discussed in the previous sections were steady-state results, mostly with natural air convection based heat sink. Here we discuss the transient solution for the STEG. Transient simulations become important when looking at systems with considerable heat capacitance such as water convection heat sink. The total thermal resistance and thermal capacitance of the absorber and the heat sink determines the system time constant for the transient data. As mentioned in the previous section, natural water convection using water heating for the STEG can provide cogeneration of electricity and hot water. Expensive natural air convection based heat sinks used in the bench-top prototype gave the heat sink temperature of $\sim 70^{\circ}\text{C}$. The TEG module efficiency is lowered due to this increase in the cold side temperature. However, as mentioned before, the requirement for heat transfer coefficients to maintain the cold side closer to the ambient temperature is very high both in terms of cost and system complexity. With a large specific heat capacity (4186 J/kg.K), water can retain heat for a long time as its temperature increases. For the STEG operation, with a constant heat flux, the water temperature rises to reach the pasteurization temperature (65°C) (Figure 48 a). The measured output power is shown in Figure 48 b. After couple of minutes above pasteurization temperature, hot water at the heat sink side can be changed with cold water. The system performance for a STEG in such a scenario can be properly analyzed with a transient simulation.

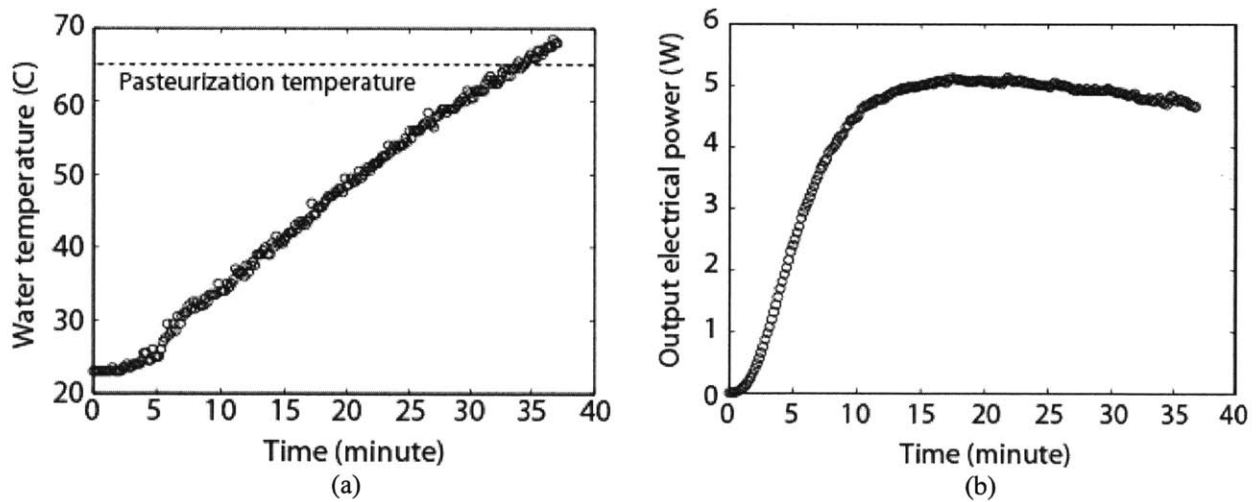


Figure 48: (a) cold side water temperature over time reaching pasteurization point (65°C); (b) output electrical power for STEG measured across a fixed load resistor with an input thermal power of 230 W

The transient simulation was done using SPICE modeling tool. A SPICE-compatible circuit equivalent model (Figure 49) for the thermoelectric generator was used along with the thermal impedances and capacitance of the absorber and the heat sink. In the electrical circuit within SPICE model the equivalent electrical-thermal parameters are listed in Table 13.

Electrical circuit	units	Thermal equivalent (SPICE)	units
Voltage	V	Temperature gradient	K
Current	A	Thermal power	W
Resistance	Ω	Thermal impedance	K/W
Capacitance	F	Thermal capacitance	J/K

Table 13: Electrical – thermal equivalent parameters for SPICE

The TE material properties as well as the heat transfer coefficients for convection losses at the heat sink side are represented as voltage dependent current sources to capture the temperature dependent properties.

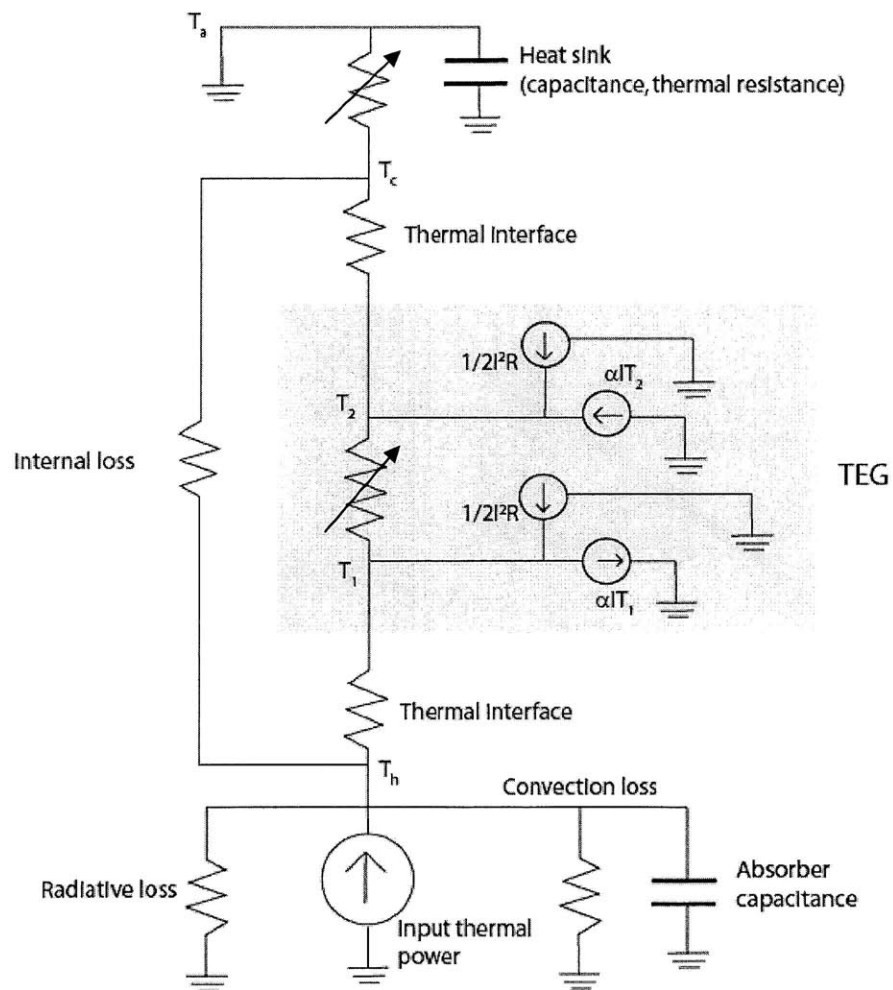


Figure 49: STEG system schematic used in SPICE to do transient modeling (all temperature dependent parameters: TE material parameters and heat transfer coefficients are represented by voltage controlled current sources inside the model: shown here as variable resistors)

The voltage resulting from the Seebeck effect is given by a temperature-controlled voltage source in series with the internal resistance of the TEG module (Figure 50).

The electrical output power from the generator is given by the following equation.

$$\text{Electrical output power} = I^2 R_{load} = \left(\frac{V_{oc}}{R_{TEG} + R_{load}} \right)^2 R_{load} = \frac{(S(T))^2}{(R_{par} + R_{TE}(T) + R_{load})^2} (T_1 - T_2)^2 R_{load} \quad (27)$$

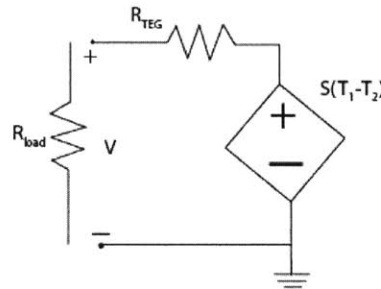


Figure 50: Seebeck voltage modeled as a temperature-controlled voltage source in series with the internal resistance of the module

The STEG system was tested in the laboratory setting with a radiative heat source. The input power to the STEG was characterized with a thermopile sensor. For the transient simulation, the volume of water during the experiment was assumed constant. Heat loss from the water surface/pot surface to the environment was also considered in the model. The output power was measured across a fixed load resistor ($\approx R_{TEG}$).

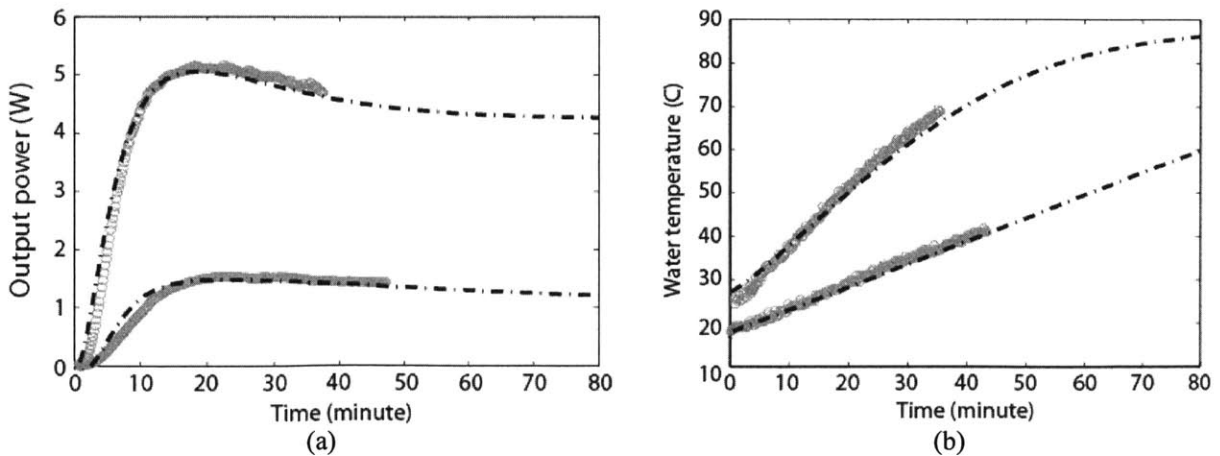


Figure 51: (a) Measured output electrical power and transient simulation results; (b) cold side water temperature measured by a thermocouple with SPICE model results (dark lines) for 130 W and 230 W thermal inputs

The transient simulation matches well for the measured output power and the water temperature (Figure 51). The thermal parasitic and the convective impedance due to heat transfer at the hot side were taken as the fitting parameters in the model. The total interface impedance of 0.55 K/W and the convective absorber impedance of 6.25 K/W were used in the above transient model. As expected, at low input power, the peak efficiency for the system was lower ($< 1.5\%$), due to smaller temperature gradient across the TEG. As the input thermal power is increased, the system efficiency also increased ($\sim 2.2\%$ at 230 W input thermal power). The achieved efficiency for this four module system with natural water convection was lower than the previous bench-top prototype (3%) due to increase in the convective loss around the hot-side absorber and the additional thermal interfaces.

2.6 Conclusion

We presented experiment and theory showing solar-to-electrical conversion using thermoelectrics. We can predict conversion efficiency for a STEG with various materials at different temperature ranges using a thermodynamic analysis based on energy balance and heat transfer. The model utilizes temperature dependent TE parameters to give a better picture of thermoelectrics. System parasitics (thermal and electrical) were included in the model to represent the module correctly. Instead of a fixed cold side temperature, heat transfer coefficients for different heat sinks were used. Experimentally, a system efficiency of 3% with a commercial Bi_2Te_3 module was achieved using a solar simulator with solar concentration of 66x suns.

The theoretical model was used to study the influence of various parameters on the system performance:

- **Selective surface:** For concentrated solar thermoelectrics, the emissivity change is less important when the concentration ratio is high. The radiative loss increases with temperature. However, for Bi_2Te_3 based modules, the material parameter degrades faster at high temperature to give lower performance than due to radiation loss.
- **Material properties:** The system performance increases with higher ZT . Even for similar Z values, if the operating temperature can be higher (in a non heat sink limited condition, i.e. temperature gradient also increases), the system efficiency will increase. In order to get to higher operating temperature, higher solar concentration is required. Commercial modules are limited in operating temperature of 230-250°C, which limits the thermal flux that can go through the module.

- **Heat sink:** The cold side temperature of the TEG module can determine its performance for a given heat flux. The conversion efficiency of the module decreases as the cold side temperature rises. High output power specifications of commercial modules are only achieved with aggressive heat sinking. For a small-scale distributed power generation application, such aggressive heat sinking mechanisms have more disadvantages in terms of cost, system complexity and additional energy requirement. System performance with different types of heat sinks were studied and evaluated. Natural water convection was the best option for the STEG system when considering performance vs. cost.
- **Hot side absorber (impedance):** The absorber was designed to provide thermal concentration to increase flux with solar cookers. An added interface and increased convection loss around the absorber will decrease the system performance. However, without the absorber, the optical concentration alone is low ($\sim 10\text{-}20\times$ suns) for solar cookers to expect high efficiency. A cylindrical enclosure was designed to suppress the convection loss near the hot surface.

A system prototype with four modules was built in lab to be used with local solar cookers. Transient simulations were done with SPICE to show time varying system performance. The prototype was tested with local cookers in Western China. Field trials and their results are discussed in the next chapter.

Chapter 3

Field Trial and Demonstration

The system level development of solar thermoelectrics discussed at the end of Chapter 2 was geared towards building an instrument for deployment into rural communities in developing countries. Successful demonstration of a high performance system that is manufacturable and inexpensive enough to be introduced into rural communities throughout the developing world will serve as an important proof-of-concept for further commercial development of this technology. Operational assessment in the field will be critical feedback for design optimization. Public demonstration projects and field trials have long been considered critical and have a vital role to play in the learning process for system design and for accelerating commercialization of sustainable technology in solar photovoltaics ^[118, 119]. For other renewable technologies such as wind power, the major benefit of the demonstration projects and field trials have been ‘learning by using’ for the wind farm operators, reducing operational costs ^[120]. A common theme for such demonstration projects or field trials has been the involvement of many stakeholders, with local authorities and individual operators taking the lead for system operation. Such field demonstrations help in understanding technology adoption by a community. Feasibility of the solar generator can only be evaluated through field testing and interaction with end-users. The study aims to demonstrate STEG as a viable source for distributed electricity by involving families from rural communities to test the system for their daily use. The field study gave feedback on the applicability, construction (robustness and durability) and intuitive understanding of the generator functionality with feedback on the usefulness of the generator technology.

For an application driven technology such as solar thermoelectrics, there are many aspects that can only be realized with field testing. In order to define system specifications, it was necessary to understand energy need and utilization in rural communities. We can test for *objective practical issues* in the lab such as if the generator works or not, what kind of conversion efficiency and output power we can get with the generator. But it is harder to test *subjective issues* without proper feedback from the end-user. These issues can range from: people’s desire to learn about a new technology (how open a community or a family is to incorporate a new appliance in their daily routine: social acceptance of a technology) to durability and maintenance of the system under different conditions (climatic variations: hot, humid, or cold; frequency of usage: high or low). We developed a platform to test STEGs with a goal of evaluating

the technology in developing countries. There were few outcomes from the field study that were not realized earlier, especially involving the use of the generator with other heat sources.

There were several primary objectives to the field testing of the generator. They are as follows:

1. To understand the energy need of a community such that system specifications could be drawn.
2. To gather data on user habits such as hours of solar cooker use and maximum input thermal power available, which could to be used in subsequent system modeling.
3. To demonstrate the technology and prove its feasibility with local solar cookers in the environment it was intended for.
4. To identify and understand any failure mechanisms of the generator system, maintenance issues and shortcomings.
5. To compare predicted output power generation and peak power values from lab testing to those realized in the field.
6. To gather user feedback on the generator performance, what they liked and disliked, and how it could be improved.
7. To study potential geographic effects on the use, performance or need of the generator.
8. To establish partnerships with local organizations that could be involved in any future scale up.

A brief outline for the methodology of field testing is discussed in Section 3.1. Communities where the STEG systems were tested are introduced in Section 3.2. Results from comprehensive household surveys, which covered household composition (family size and male/female ratio), economics (profession, income flow and fuel expenditure) and consumptions (electricity use hours, heating fuel source and lighting source) are discussed here. The outcomes of the field trials and experiments are discussed in Section 3.3.

3.1 Methodology for field testing

There were several methods used to gather data from the prototype units in the field. Technical objective data such as power, voltage and temperature were recorded with data loggers. A voltage meter was used to log and display the voltage across the load resistor and/or battery charge controller. Data loggers were used at the beginning of the trial (first week of installation) to characterize all prototypes and ensure that they were working properly. Thermocouple loggers were used to measure water temperature to indicate pasteurization point. Families participating in the

trials were given water pasteurization indicators (WAPI) – a small polycarbonate tube containing a wax that melts when water is heated enough to be pasteurized i.e. 65°C. The last method for gathering data was based on user feedback. Various tests and surveys were conducted throughout the period of August 2008-November 2011 that helped in system design and optimization. The field trial includes a lot of consideration of interaction between humans and the technology. In the case of the STEG, the families testing the generators did not have any prior knowledge of thermoelectrics or how electricity could be generated using solar cookers. Designing the generator as a part of the “water heating pot” structure was aimed such that anyone using the solar cooker could adopt and use the technology without educational background or prior technical knowledge.

A chronological order for field testing has involved following steps.

1. Initial field trials (2008-2009) in China and Nepal were conducted to characterize local solar cookers and assess their performance. The thermal output of a solar cooker varies depending on the size of the cooker, maintenance, and location. The output power was measured for different solar cookers by testing the water boiling time. Variable solar flux into the generator makes it a hard problem to optimize the STEG system.
2. Various prototypes with design iterations were tested in and around Xining area (Qinghai, Western China), with the help of a local organization - One Earth Designs (January 2009 – August 2010).
3. An agricultural and a nomadic village in Qinghai, Western China were selected to be test-beds for field trials (July 2011). The villagers were familiar with solar cookers as they were using locally made cookers for boiling water.
4. A baseline survey (Appendix 2 a) was conducted in each village. The survey was designed to increase understanding of what type of energy source was utilized for electricity/heat and to understand applications for electricity in order to determine generator specifications. Household socio-economic questions involving income, monthly electricity payments and total electrical appliances used in a home were included to learn about electricity cost for current options.
5. The generator was demonstrated with local solar cookers during a village meeting (August 2011).
6. Three families from each village were chosen based upon the village leader’s recommendation for testing STEGs.
 - a. Meetings with individual families were carried out to explain the system in detail and brief them about maintenance and handling.
 - b. After demonstration, the system was left with the family. The families were visited frequently within the first month, to check on the system. After the first two weeks, a mid-survey was

conducted to gather their feedback (Appendix 2 b). There is an ongoing continuous monitoring of the system with the help of OED.

7. Many villagers in China have PV modules for solar home lighting. For comparison, two of the families to test STEG were chosen who also used PV system. They were asked to rate the quality of the technology in terms of ease of use and reliability, and state their preference.

The main goal of the field trial was to demonstrate the technology as a viable option for distributed power generation. A small sample size (six families) was taken as an initial step towards this demonstration. The families involved in the trials were from both nomadic and agricultural communities representing the rural Western China. The nomadic village potentially best represents the most rural setting in Western China with no electricity access in the summer months. The outcome from the trials will help build a platform for a larger scale (100+families) and a long term (1-2 years) testing of the generator to study viability, market potential etc.

3.2 Trial locations

Most of the field work was carried out in Qinghai Province of Western China in collaboration with One Earth Designs. The organization is developing a cheap and portable solar cooker for local nomadic and agricultural communities. The solar thermoelectric generator as an added tool with the cooker could provide solution for the energy need of the community.

With an average net household income of less than \$1,300, the region is one of the poorest provinces in the country ^[8]. For comparison, the average annual household income in China is \$10,900 ^[121]. The western region of the country is rich in natural resources, both solar and water. There are 178 hydro power stations in Western China, which provide nearly 68% of the grid electricity. Even though China can boast exceptionally high (99.4%) grid electricity coverage, there are still roughly 8.5 million people without electricity, and most of them live in the rural parts of Western China. The rural population in Qinghai alone is ~ 2.5 million, with an estimated 495,000 people without electricity ^[7]. This accounts for nearly 20% of the total rural households. Among the rural population, nomadic communities lack basic essentials. There are estimated two million nomads within the nine provinces in Western China, mostly in the Tibetan plateau region. The average annual monetary income for a nomadic family is only \$100-\$300. The lifestyle of a herd's man (nomad) is such that it does not involve many monetary transactions as the community relies on their animal products for food (meat, milk, butter etc.) and clothes (sheep wool). Most agricultural villages have become grid connected in the past ten years, and the electricity cost is

heavily subsidized by the government (< 7 cents/kWh) [9]. Several NGOs are actively addressing the ‘power poverty’ issues in Qinghai with deployment of small scale solar photovoltaics for lighting as well as solar cookers. China’s renewable energy development project distributed nearly 400,000 PV systems (20 W panels for lighting and cell phone charging) in the country by the end of 2008. Even with the government subsidy, the total cost for the system (PV module, charge controller, battery, and light bulbs) was \$175 i.e. more than \$8/W [122]. In such a market scenario, STEG could be a viable competition to the PV system.

For STEG testing, a baseline survey was conducted in three remote villages to understand the energy requirement, use and cost. Results from the survey are discussed in Appendix 2 a. From these baseline surveys, comparisons were drawn between agricultural and nomadic villages in terms of electricity need and use. Electricity was only available to nomads for 5-7 months in a year. Apart from lighting, the most common appliances using electricity were cell phones and televisions (Figure 52). The total number of hours of electricity use was similar in both communities, as people felt electricity was an expensive commodity which cost 20-25% of their monthly income. After talking to individual families, it was found that there was a cultural notion that people did not prefer paying regularly for electricity. That was one of the reasons, few families in the agricultural village had bought PV systems even though there was grid connection, as it was considered a one-time payment and the electricity would be ‘free’ thereafter.

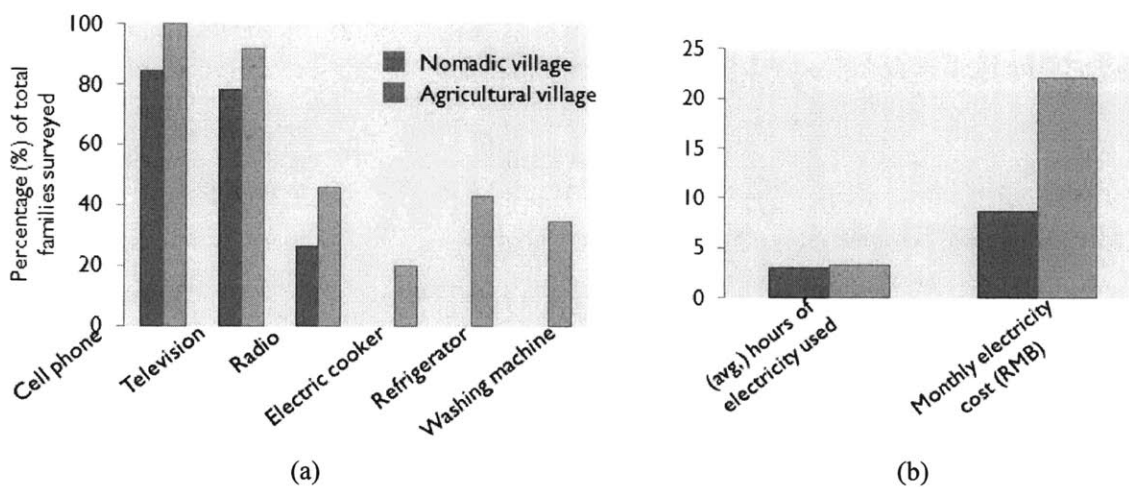


Figure 52: (a) Electrical appliances used by nomadic and agricultural communities; (b) average hour of electricity use and monthly electricity bill for different communities

During summer months, the need for electricity was highest for the nomadic community, which used inefficient sources such as candles and oil lamps (Figure 53).

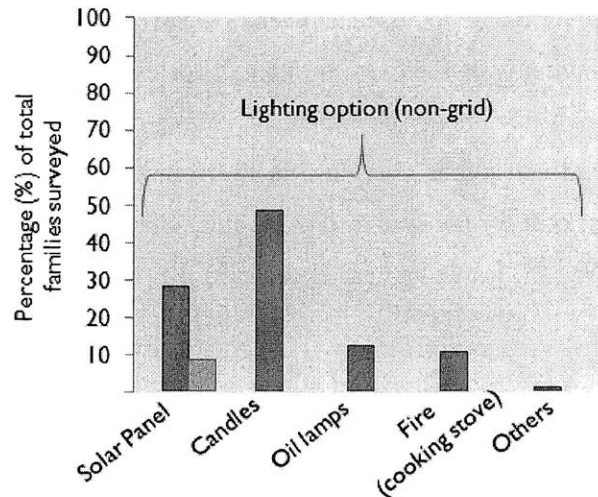


Figure 53: Lighting sources available in the summer settlement for nomadic community; a small percentage of families in the agricultural village (~10%) also used PV system for lighting

The list of available options for lighting in these rural communities is shown in **Table 14**.

Options	Monthly expenditure	Quality of light	Remarks
Grid electricity	50-60 RMB/3months (< \$4 per month)	Good (mostly incandescent light)	Not universally available; considered expensive
PV system	Onetime expense ~ \$175	Good (CFL)	Not robust system for easy transportation; bad charging practices causing battery failure
Battery operated flash lights	Expensive	Limited visibility	Portable source; Quick battery replacement required if used continuously
Wood burning (during cooking)	-	Very poor	Risk of fire; health issues due to smoke
Candles (Yak butter)	- (home-made)	Very poor	Risk of fire
Diesel lamp	5-10 RMB/month (< \$2 per month)	Poor	Risk of fire

Table 14: Current options for lighting in many rural communities

Solar thermoelectrics along with popular local solar cookers can be a useful power generator for the nomadic communities especially during summer for lighting and cell phone charging. A 10 W lamp (LED or CFL) to be used for 3 hours every day would require energy of 30 Watt-hour. Similarly, for cell phone charging, at less than 5V, with a battery capacity of 1150 mAh, the required energy for charging couple of cell phones is ~ 12 Watt-hour. Thus, the total energy requirement would be less than 45 Watt-hour. With

a peak output power of 10 W, and a battery capacity of 54 Watt-hour (4.5 Ah/12V), the generator can be useful for both of the necessary applications.

3.3 Field trials

Initially, we looked to establish the market opportunity for small-scale thermoelectric generators in China and Nepal. Local vendors in Nepal, China, and India were contacted for sourcing of various components such as solar cookers, thermoelectric modules, and selective surface (used commonly in solar water heaters). Solar thermoelectrics represent a compelling case for communities where large numbers of solar cookers have already been deployed. According to OED's market survey, in many villages of Western China, concrete solar cookers were distributed by the government as a part of renewable energy initiative in the late 90's and early 2000. Within Qinghai, the concrete solar cookers were most popular. The cookers in rural areas are heavily government subsidized. The concrete solar cooker cost about 350 RMB (~ \$55) (Figure 54 a). The metal reflector based lighter solar cookers cost slightly more (460 RMB ~ \$75) (Figure 54 b). Government organizations distribute these solar cookers with 50-60% subsidies.

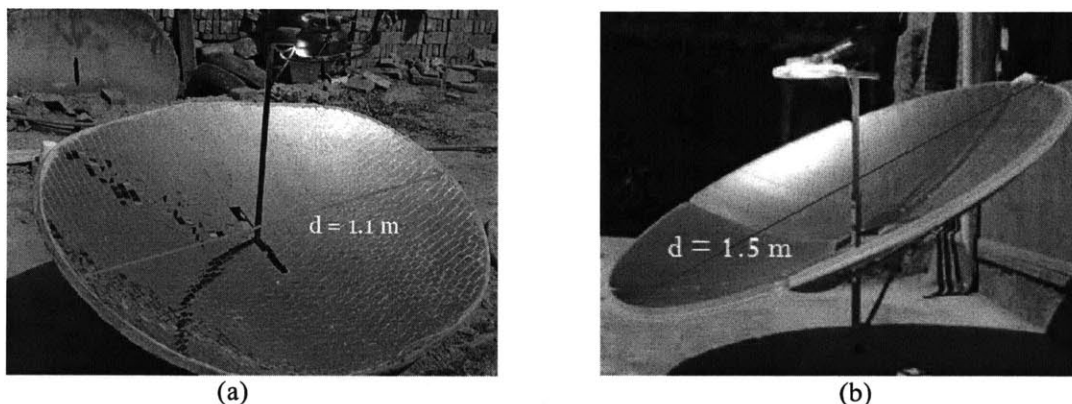


Figure 54: (a) concrete-based mirror reflector and (b) metal reflector solar cooker, locally available in China

Different local solar cookers were tested using water boiling experiment to evaluate the thermal performance (Table 15). On average, the input thermal power was measured to be ~ 350 W near Xining area. During the visit of August 2011, very high power solar cookers were tested (maximum power ~ 760 W). The increase in the power was attributed to higher altitudes (larger direct solar irradiance), larger reflector areas (metal solar cooker: diameter ~ 1.5 m) as well as good maintenance of the solar cookers in the villages of Gangta and Serjia.

Cooker type	Location	Altitude (m)	Volume of water (liter)	Boil time (minutes)	Thermal power ($\sim mc_p \Delta T/t$) max. (measured)	Date
Concrete (Area $\sim 0.75\text{m}^2$)	Ping'an, China (local concrete cooker manufacturer)	2,200	0.55	7.5	345 W	July 2010
	Xining, China	2,200	2	34	306 W	July 2010
	Gangta, China	4,000	3.5	30	670 W	Aug 2011
Metal reflector (SK-14) (area $\sim 0.95\text{m}^2$)	Kathmandu, Nepal	1,375	1.5	17.5	458 W	Aug 2010
	Cambridge, USA	2	2	41	268 W	May 2010
Metal reflector (area $\sim 1.76\text{m}^2$)	Gangta, China	4,000	p in24	24	760 W	Aug 2011
	Serjia, China	4,500	3.5	27	694 W	Aug 2011

Table 15: Thermal power available at the focal spot for local solar cookers in various locations

During the development phase from early 2009, each generator prototype was tested in China with the help of the volunteers from OED (Figure 55). Feedback from these field test, helped in design optimization to make the system more robust to the harsh conditions. Results from these preliminary tests are listed in Table 16.

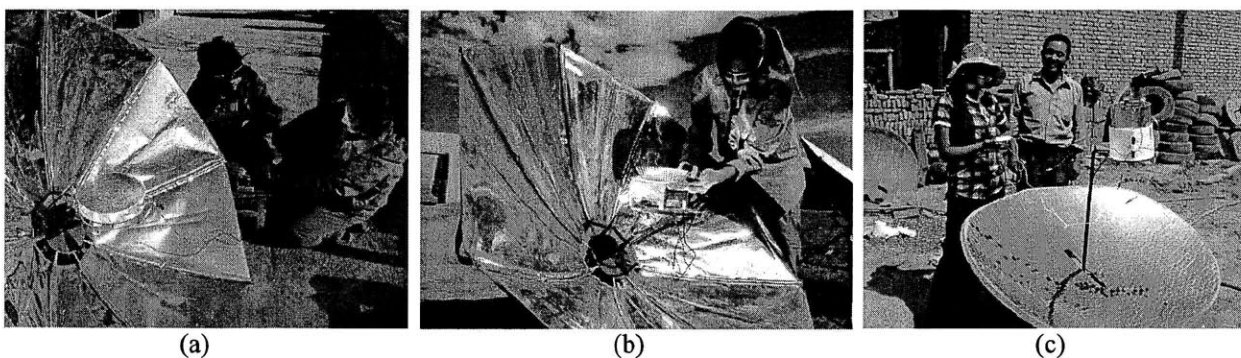


Figure 55: Testing for STEG in (a) Mairi, China; (b) Tianzhu, China; (c) Ping'an, China

Date	Location	Altitude (m)	Thermal power (boiling)	Output power (W)	Comment
Jan 2009	Mairi, China	2,709	140 W (Sol-Source: OED's cooker)	0.67	<ul style="list-style-type: none"> • Hi-Z module used (very inefficient) • Felt (insulator) burning issue even at hot side temperature < 180°C • Black paint used instead of selective surface
Aug 2009	Tianzhu, China	1,000	156 W (Sol-Source: OED's cooker)	0.96	<ul style="list-style-type: none"> • Natural air convection heat sink used • Single TG-12-4 module used without thermal absorber • Not robust (ceramic screws holding the assembly fell/broke during transportation)
July 2010	Ping 'an, China	2,200	345 W (Concrete cooker)	5.2	<ul style="list-style-type: none"> • Water leak from the heat sink through the screw holes used to hold the generator • Large area absorber (height ~ 13 cm) used – high convection loss • Enough power for successful cell phone charging ~ 2.5 hours

Table 16: Results from preliminary test conducted on STEG

The field trials involving villagers were conducted in Gangta and Serjia starting July 2011. The test plan was to install three STEG systems in each village. The generators were to be monitored for 3-4 months. The generator components were built at MIT and transported to China. A volunteer from OED, who was originally from Gangta, was instructed on how to install the generator, as well as how to diagnose the generators. For a baseline test, each generator was tested with a local solar cooker in the field. The solar cooker was used in a “typical” style with the generator installed at the focal spot. For power measurement, the module was connected to a resistor equal to the internal resistance of the module. The output voltage was measured with the voltage logger. Water temperature at the cold side was measured with a type T thermocouple data logger.

Due to high altitude and intense solar irradiance ($> 1030 \text{ W/m}^2$), the input thermal power for the solar cookers in the region was higher than previous measured values (Table 16). In these field trips, the solar irradiance was measured using a PV based digital solar meter (Daystar Inc.). Usual thermal power from the concrete solar cooker near Xining area was measured in the range of 350 W. However, in Gangta and Serjia, we measured high power ($> 650 \text{ W}$). The STEG was not designed for such high power as the hot side temperature was continuously measured above 350°C. With such

high temperature, the TE legs of the module separated at the hot side due to electrical contact failure. The thermal cement used for the generator assembly was also rated for lower temperature (315°C), which failed. On-site modification was needed to ensure the safe operation of rest of the generators. In order to decrease the direct power hitting the hot side absorber, a thin iron plate (5-10 mm) was placed at the focal spot before placing the generator. For these local cookers, heating at the focal spot was also not uniform. Without the additional iron plate, uneven intensity at the absorber caused partial burning of the metal at such hotspots (Figure 56). The thickness of the iron plates varied slightly for different houses involved in the testing. It primarily depended on the availability of metal with the local blacksmith.

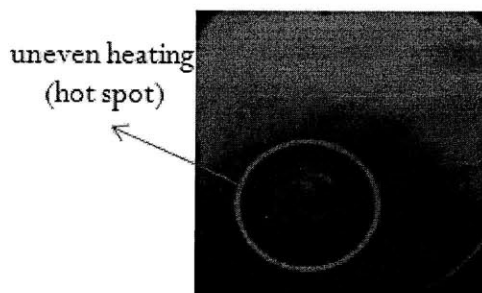


Figure 56: Uneven heating of the absorber at the focal spot of the local solar cooker causes burning at the hot spot

The thermal power measured from the boiling test was reduced to ~ 470 W (peak) after placing the iron plate at the focal spot. 35-40% of the thermal energy was lost at the iron plate interface due to convection, radiation and reflection from the plate.

3.3.1 STEG performance with the local cookers

The output electrical power from the generator depended on the solar irradiance and external environmental conditions. An average power of 8 W was measured consistently during multiple day trials, with the maximum power of 11 W. Early in the morning (~ 9 am), when the sun was low in the sky, electrical power in the range of 4-6 W was measured, with similar results in the afternoons (Figure 57).

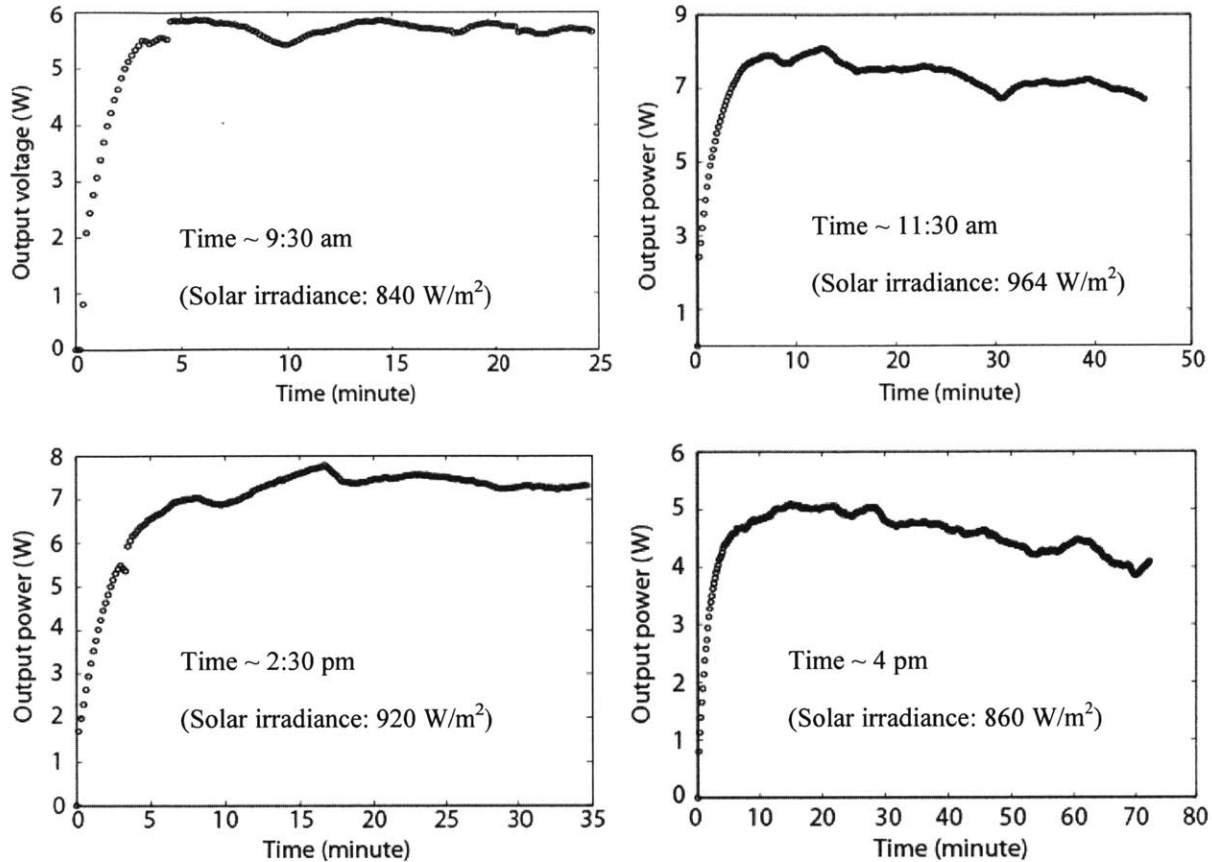


Figure 57: Output power for STEG measured across a load resistor (16Ω) for different hours of a day (solar irradiance measured at the beginning of the experiments with a flux meter)

Transient simulation (SPICE) described in Chapter 2 was used to compare the field results with the theoretical system analysis (Figure 58). The goodness of the fit would assure that all the major heat transfers and loss mechanisms inside the system are well understood.

There were major uncertainties and sources of discrepancies for the comparison of the field experiments and the simulation.

1. Input thermal power: the boiling test only gives a rough estimate of the input power but does not give an exact measure of the irradiance at the focal spot during the generation measurement.
2. Constant thermal power assumption: Within the SPICE modeling, constant input power is assumed at the hot side of the generator. Due to factors such as cloud, dust and tracking, the input power varies within a single measurement period.

3. Unknown optical properties of the iron plate used in between the focus and the generator: some iron pieces were rusty dark in appearance and some had black soot. The absorbance of 0.75 was assumed taking values similar to the oxidized dark surface ^[124].
4. Unlike the closed laboratory environment, air flow around the system varied during the day as well as even within the hour of a single experiment.

In the SPICE model, an input power of 632 W was used which was measured from a water boiling experiment right before the power generation measurement. With the use of an iron plate, there was an additional interface between the plate and the hot side absorber. Since the solar flux was not hitting the absorber directly, the selective surface painted on the absorber had no effect. Heat transfer was mainly through conduction between metals and inefficient convection path through air trapped between the absorber and the plate. The interfaces were represented with bulk thermal resistor within the model. For the fit shown below, the value of 0.36 K/W was used for the bulk resistor as a fitting parameter.

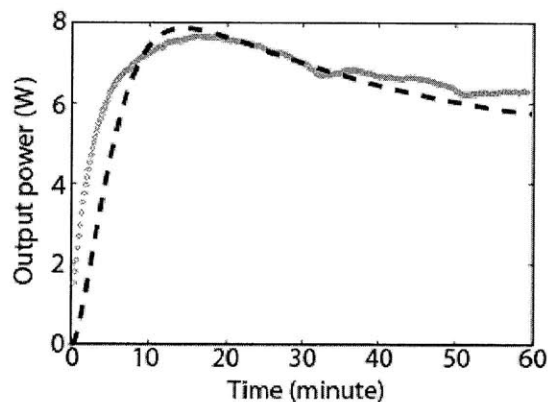


Figure 58: Comparison of the transient simulation with the measured field data

More prominent variation in the transient power data was observed due to climatic reasons such as cloud coverage (Figure 59). A peak power of 11 W was measured during sunny condition (irradiance $\sim 1030 \text{ W/m}^2$); an average of 6.5 W was measured over a period of 35 minutes even with the cloud. Due to thermal mass of the absorber, output power $> 1 \text{ W}$ was maintained with full cloud coverage. Such power generation capability can be a huge benefit compared to the solar panels where the output voltage would be zero during cloud coverage.

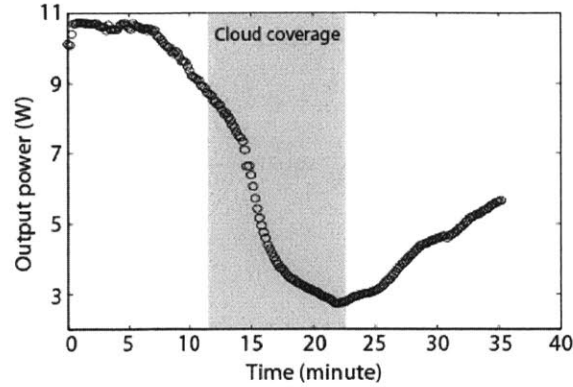


Figure 59: Effect of cloud coverage on the output power (average power of 6.5 W was measured even under such condition)

3.3.2 Tracking

Another reason for output power variation over time is due to tracking; an aspect of the concentrated solar engineering that has not been discussed earlier. For a solar PV panel, a dual axis tracking system can boost the output from anywhere between 30-40% compared to the stationary latitude tilted panels. For concentrated optics, tracking is even more critical. As described in Chapter 1, with smaller acceptance angle, the concentration ratio increases. However, smaller acceptance angle means continuous tracking is required. With an optical concentration ratio of 20x, the acceptance angle for a solar cooker is $\sim 6^\circ$ (Equation 4). In the northern hemisphere, the solar (azimuth) angle varies $+70^\circ/-70^\circ$ in winter and $+110^\circ/-110^\circ$ in summer (Figure 60). The rate of angle variation is roughly 15° per hour ^[125]. This gives an estimate of the tracking requirement for the cooker in one direction. Within 30 minutes, the focal point of the solar cooker will be completely off the pot stand if no tracking is observed. Solar cookers are based on manual tracking with two axis variation (azimuth-altitude).

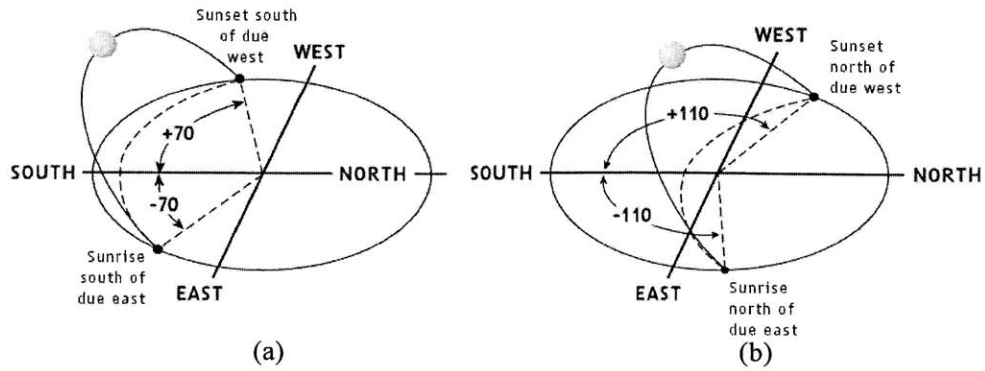


Figure 60: Azimuth angle variation in (a) winter and (b) summer at the northern hemisphere [www.solarplot.info]

During its typical use, people (generally women) put a water-pot on the focal spot and track for the highest solar intensity either by looking for the brightest spot under the pot (which is slightly dangerous and uncomfortable for eyes) or by looking at the shadow sun tracker which is build on the rim of some solar cookers. The cooker’s position is changed every 10-15 minutes before the water boils. The output power for the generator does vary as the solar intensity decreases due to tracking misalignment (Figure 61). An average power of 9.5 W was measured with the peak power of 11 W, where the dip in power was due to manual tracking alignment (Figure 61 a).

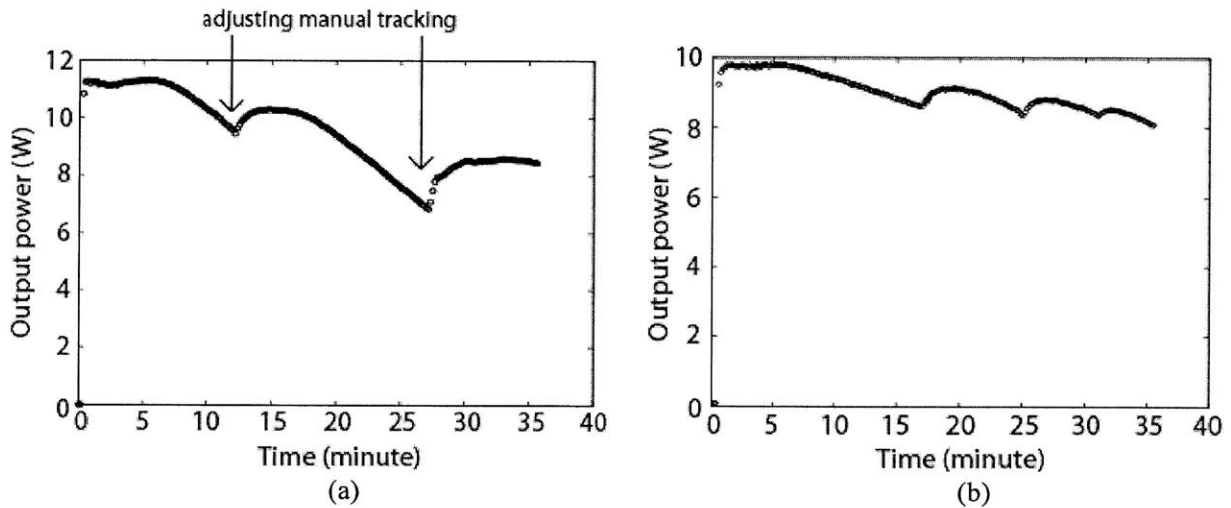


Figure 61: Decrease in power during manual tracking as the sun moves away from the focal spot causing decrease in the input intensity and temperatures; power level increases as the cooker’s position is changed every 10-15 minutes

Due to manual tracking adjustment, the average power during the generation cycle was 86-90% of the measured peak power. In Chapter 6, for the total power generation calculation in the economic analysis, the loss factor due to tracking is included to take into account the difference between the average power and the peak power.

3.3.3 STEG performance with cooking stoves

Even though most of the villagers had solar cookers, they used traditional cooking stoves for cooking in the mornings (7-9 am) and the evenings (7-9 pm). In agricultural villages, a traditional iron stove was used for cooking, which also worked as a heat source in winter (Figure 62). Apart from the cooking area for a pot directly on top of fire, there are flat surfaces around the stove which are unused and could be a good heat source for STEG (surface temperature $\sim 150-180^{\circ}\text{C}$).

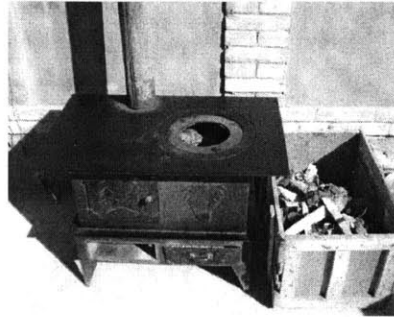


Figure 62: Traditional cooking stove used in Qinghai region (metal body)

The STEG was tested for power generation with these cooking stoves during regular use. Input thermal power was relatively low compared to the solar cookers ($< 220 \text{ W}$) as measured by the water heating experiment. Useful electrical power of 4-5 W was measured during this cycle (Figure 63). Although the water temperature did not go above pasteurization even after a long time (~ 1 hour), according to the villagers, warm water would be useful for daily chores such as washing utensils, especially after meals.

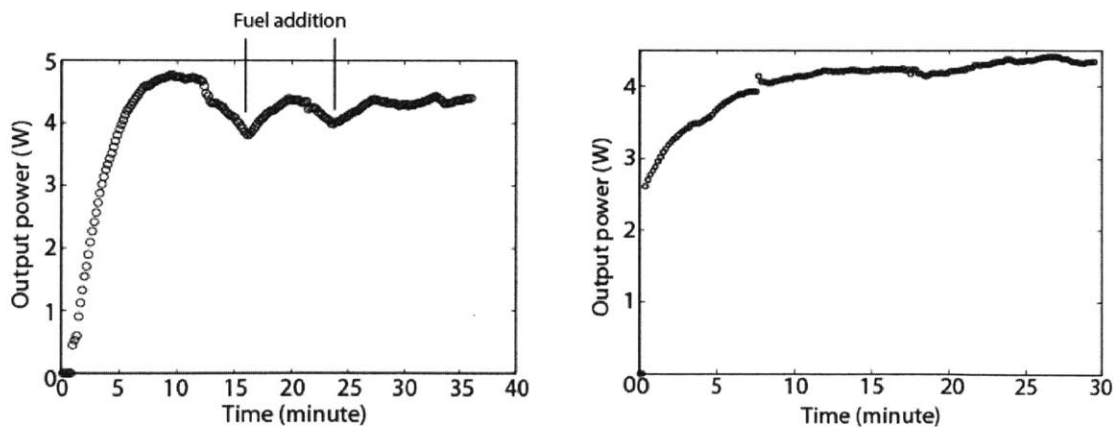


Figure 63: Output power from the STEG using waste heat from the cooking stove

During peak summer time, the stove is used only for 3.5 hours per day. However, it is used for longer period starting October till April. In winter, with shorter solar hours, villagers use cooking

stoves for over 5 hours daily, mainly for cooking and indoor heating. The STEG can use these additional hours for extra power generation.

Apart from heat during fuel burning, additional latent heat from the stove can also be used for power generation (Figure 64). The generator could be used for additional 10-15 minutes after every meal when the fire is out. Different transient times can be expected from different fuels as well as it varies over quantity and quality (water content) of the fuel (Table 17). The decrease in the output power will be relatively quicker for a larger area cooking stove (metal vs. mud) due to loss of heat from convection to the environment.

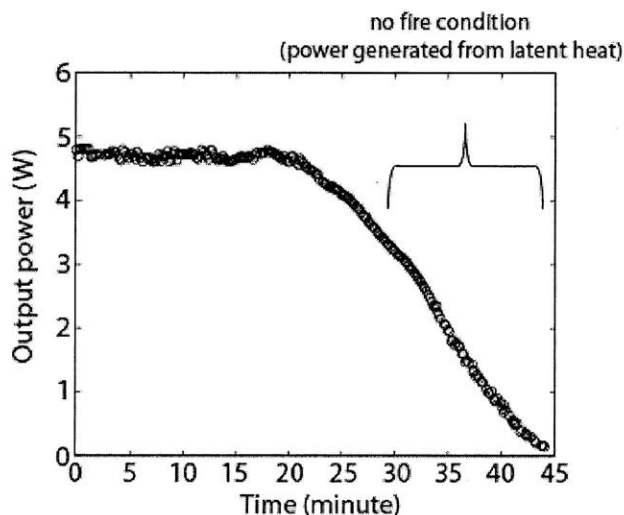


Figure 64: Using latent heat from the cooking stove to generate electricity even after the fire is out and no more fuel is added

Fuel	Burn energy (MJ/kg)	Specific heat (J/kg. K)	Remarks
Twigs	20	160	Fast burning (quick fire) ^[126]
Wood	22	250	High heat (frying, quick cooking) ^[126]
Dung	17	367	Low heat (slow cooking) ^[127]

Table 17: Energy and capacitance for different fuel source

The concept of potential dual use of the STEG with cooking stoves as well as solar cookers was very popular with the villagers as they felt the generator could be easily used even during cloudy or rainy conditions continuously unlike the solar panels (Figure 65). The additional benefit of this hybrid use is the longer generation time: 2 hours in the morning with the stove; 6 hours with the

solar cooker, and additional 2 hours in the evening with the stove. 67% more generation time could be available for battery charging with a STEG compared to a solar panel on a sunny day. From the average power generation data using the solar cooker (8 W) and the cooking stove (4 W), the total energy yield for a day can be 32% higher than with just using the solar energy.



Figure 65: STEG being tested with the cooking stove during a cloudy day as the stove was being used for meal preparation

3.3.4 Feedback from STEG users

The results from the field trials involving families are presented below. Three families were from an agricultural village (Gangta) and three were from a nomadic village (Serjia). Result from the monthly surveys summarizes the use pattern for STEG from July 2011-November 2011.

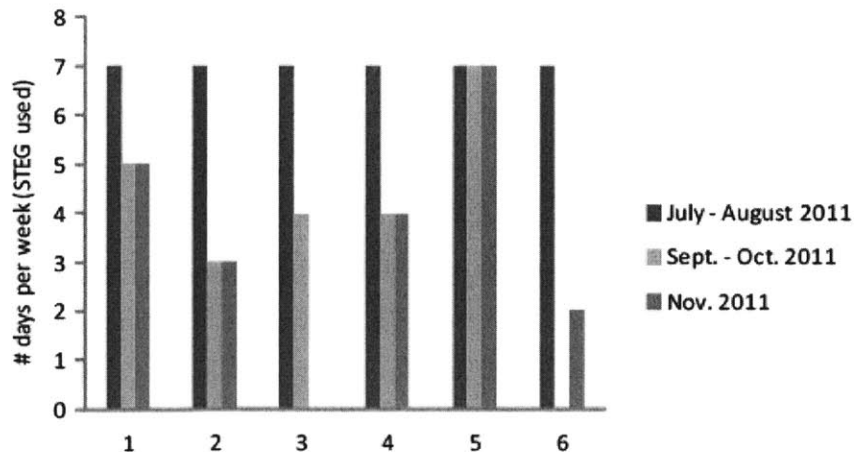


Figure 66: Frequency of use of STEG by six families surveyed over four months

Decrease in the generator use hour has been observed in all the homes compared to the first month of the installation (Figure 66). There are few reasons for this decline:

1. With colder outside temperature (November: $\sim 10^{\circ}\text{C}$), people were not using the solar cooker as much. It was uncomfortable to be outside to track and change water every 30-40 minutes for the generator in such weather.
2. Battery charging with the cooking stoves could only be done in alternate nights as the families had only one set of charge controller which could either be used for charging or discharging at any given time.
3. Nomadic villagers moved to their winter settlement which was grid connected. Basic lighting was connected to grid line in these homes. The convenience of grid connection was far more appealing than using STEG.
4. The system was complicated with too many wires (generator – charge controller – battery) to connect in a certain order for it to work properly. Only one or two people in the house knew how to operate the generator. When they were away, the generator was not used.

Interestingly, the families who used STEG the most (#1 and #5) were also the families who had PV systems, indicating the ease of adoption of a new technology to families who are more familiar with similar technologies (such as battery charging). The families used both PV and STEG over the duration of the trial. Feedback on STEG and PV performance is discussed at the end of this section.

The total hours of charging and use of STEG also saw decline over the period (**Figure 67**). Charging time difference for the cell phone was mentioned by the families as a reason they did not to use the STEG for cell phone charging. With 2-3 hours of charging, the cell phones would not be completely charged, whereas with grid connection, cell phones were charged under 2 hours. Trickle charging (low-current: 100 mA) may be happening through the charge controller for DC-cell phone charging, causing long charge time compared to direct AC-wall connection. For one of the families, only the husband could operate the generator (he was away from home for a month), wife found it too complicated to use. STEG for family #3 was broken, most likely due to high heat exposure (open flame) – failure at electrical contacts. For family #5, the solar cooker was broken due to strong wind, thus they could not use it to charge battery after October. There was no data directly suggesting any kind of degradation in the performance of the generator during the trial period. The water pasteurization time was slightly longer (40-50 minutes) compared to 30 minutes or less during noon time in the first month of installation. This could be due to lower solar irradiance in the winter months compared to the peak summer season.

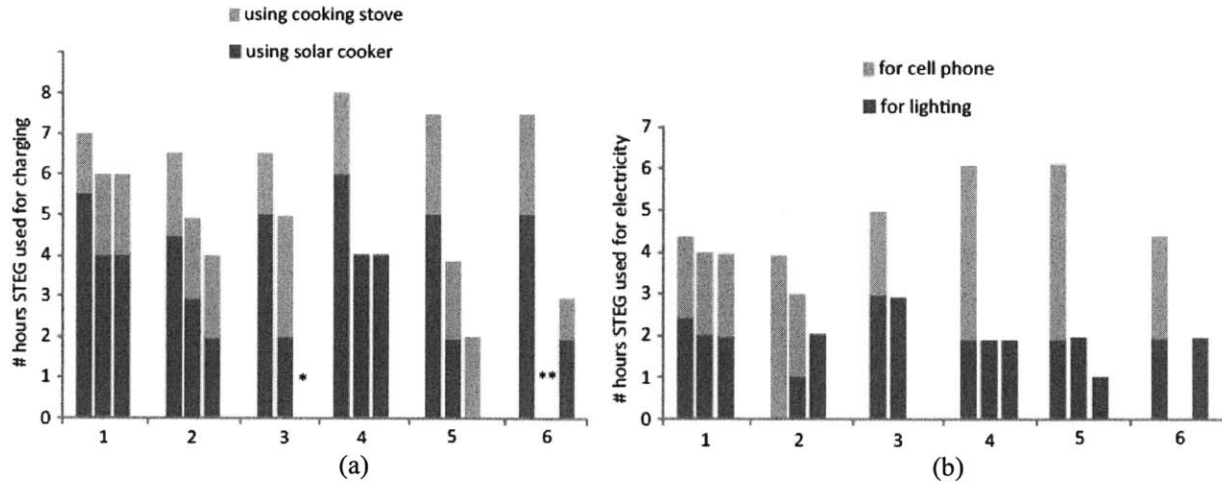


Figure 67: (a) # of hours STEG used to charge a battery; (b) # of hours STEG used for cell phone charging and lighting

* STEG broken due to electrical contact failure

** Family member who knew how to operate the STEG was away on business

Overall the generator performed well at house # 1. The family owned a 10 W solar panel, which they used for lighting a 7 W CFL in the evenings. Grid electricity was used for other appliances such as television, refrigerator and charging cell phones. Even though they had solar panels for more than 10 years, they were not satisfied with the battery charging. They needed to replace the battery within every six months -1 year. Intermittent cloud or rain did not allow for continuous charging sometimes for 3-4 days in a month, which left the battery in a completely discharged stage reducing its lifetime. With STEG, they saw the potential of maintaining good battery life with continuous charging using solar cooker during sunny days and with cooking stove in mornings, evenings and rainy days. The generator appeared to be in good condition when the volunteers from OED visited the family after 3 months. According to the family, they used the STEG nearly every day. It was used for additional lighting as well as cell phone charging along with PV and grid connection.

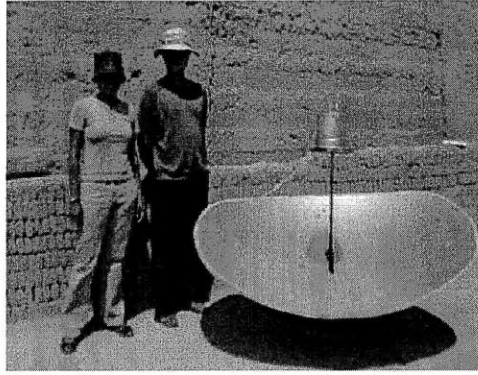


Figure 68: STEG being tested in one of the homes in an agricultural village of Gangta

The solar cooker belonging to the second family was not in the best condition from the beginning with few mirror pieces missing and dark spots of dirt all around (Figure 69). The family used the generator for cell phone charging at the beginning (July-August). Due to long charging hours for cell phones, they did not use the generator for cell phones later in the trial. They were using the generator for lighting a LED lamp in their common room. The generator was used with both the cooking stove and the solar cooker. One application that the family thought the STEG might be useful was for having a portable light source with a small rechargeable battery. The current irrigation system in the village was such that farmers had to work at night during harvest season (3-4 months in a year). There are no street lights or any permanent light source near the field. People use either fire as light or small flash lights, which were not very bright. The potential of carrying a small sealed lead acid battery and LED lamps or CFL would be useful. The battery could be charged during day time with solar cookers and used at night for such applications.

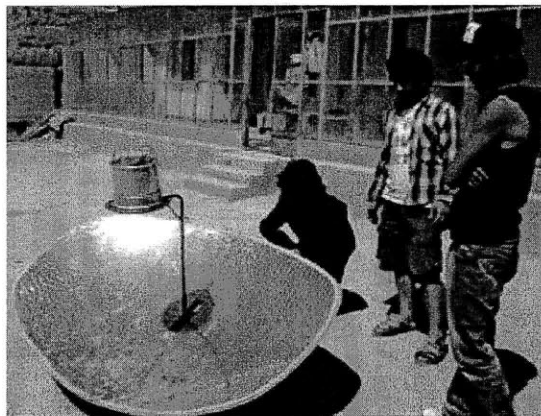


Figure 69: STEG being tested by family # 2 in Gangta

The third family used the generator with the solar cooker to charge the battery for 5 hours and used the (5 W) LED bulb in the kitchen for 3 hours every night during cooking and eating for the first

couple of months. However, during a visit in November 2011, the generator was found to be broken. One of the electrical leads of the generator had come off potentially due to high heat exposure near open flame of the cooking stove.

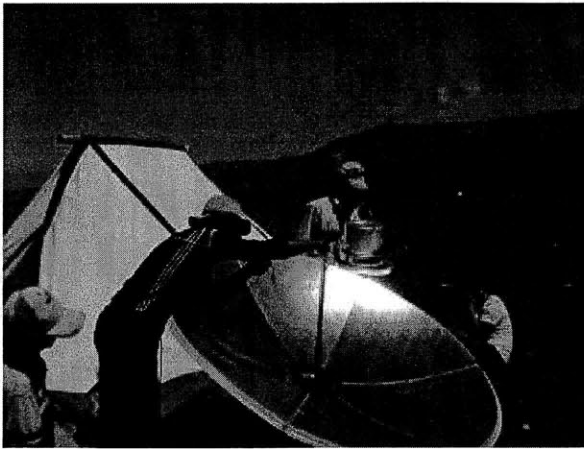
The next three families were from nomadic village of Serjia. The families lived in high grassland during summer, which was situated 15 km away from Gangta but due to unpaved road, the travel time was ~ 4 hours motorcycle ride and an hour of hike. Only few families had solar panels for electricity. The rest of the villagers relied heavily on candles and fire for lighting. For cell phone charging, one or two members from the village would hike back to the town and charge the cell phones and bring it back to the tents. Instead of heavy concrete base solar cookers, they used carbon-steel based solar cookers which were much lighter compared to the concrete cookers (15 kg vs. 90 kg).

The first family where the STEG was installed did not have any electricity source apart from a flash light for emergency. The STEG was used to charge battery for up to 6 hours and used daily for 2 hours of lighting and 4 hours of cell phone charging during summer. When they moved back to their winter settlements in late September, the generator was used primarily for lighting.



Figure 70: STEG being tested in high grassland village of Serjia using metal reflector cooker

The second family had owned a solar panel. However, even with daily charging, the battery was not supporting a small 2 W CFL for more than 1 hour of full lighting in the evening. With STEG, the battery was charged for 5 hours daily and used for 2 hours for lighting every evening and 3 hours for 2 cell phones charging. Unfortunately, the solar cooker broke due to high wind. However, the family is still using the generator with their cooking stove to charge battery for lighting.



(a)



(b)

Figure 71: STEG being tested with: (a) solar cooker and (b) mud cooking stove



Figure 72: A 5 W LED bulb lighting a tent in the nomadic village of Serjia in the evening (fire from the stove was used for lighting before the installation of the STEG)

Similarly, the third family also used STEG for battery charging to use for lighting. The family suggested a potential use of STEG in winter for ice melting. Due to relative high altitude, winter in these villages is harsh. Water freeze is a common problem where they have to heat ice to get water. With STEG, the cold side with ice can be used to generate even higher power (colder heat sink for longer time) and melt ice for daily use.



Figure 73: STEG being used by a family in the nomadic village (Serjia)

3.4 Conclusion

The solar thermoelectric generator was demonstrated to work as a power source with local parabolic solar cooker. Maximum output power of 11 W was measured during the field visit. On average, 6-8 W power was generated throughout the day using the solar cooker. The generator could also be used with mud/metal cooking stoves. This hybrid use gave the potential of long useful hours for the generator to charge battery. Of six prototypes, five are still being used either with solar cookers or cooking stoves by the families. The generators were being used on average for 4 hours every day to charge battery, which was used mostly for lighting.

Comparisons were drawn between solar panels and STEGs after talking to two families who owned PVs and also used STEGs during these trials (**Table 18**).

	PV	STEG	Remarks
Peak power	8-10 W	11 W	
Maintenance	√	√	Both PV and TEG require low maintenance, with main concerns towards battery charging and controller
Ease of use	√	X	<ul style="list-style-type: none"> - Solar panel left in the stationary latitude tilt position requiring no further attention - Tracking as well as water change at the cold side requires some attention
Cogeneration	X	√	Option of pasteurized water for drinking or warm water for daily cleaning chores
Hybrid use (non solar hours)	X	√	Using the thermoelectric generator with the cooking stove

Table 18: comparison between PV and STEG (input from families using both)

Even though the families thought STEGs were beneficial for them, when compared to PV, they talked about the ease of use for PV as no monitoring was required. Whereas, for STEG with solar cookers, they had to change water every 30-40 minutes for 5-6 times a day to utilize it fully. They did appreciate the fact that the generator could be used with cooking stoves as well. Suggestions for improvements ranged from having an electrical or a mechanical tracking system attached to the solar cooker to water loop system such that less attention could be given to the generator.

Overall, the STEGs were found to be a useful source for distributed power generation for families who did not have any electricity (i.e. nomadic community during summer months). Cost comparison of the generator with PV will be done in Chapter 6 for completeness. In the next chapter, we look at ways of improving the performance of the generator.

Chapter 4

Module Design and Optimization

From the previous analysis and experiments described in Chapter 2 and 3, it is clear that with Bi_2Te_3 modules, the system efficiency for solar thermoelectrics is limited (4%) even without any system parasitics, primarily due to material ZT limitation. In this and the next chapter, we explore potential ways of increasing the system efficiency for these generators. Apart from looking at new TE materials with high ZT (which will be discussed in Chapter 5), another way of optimizing the system performance is with module redesign. By optimizing the TE leg size (cross section area, and thickness), the fill factor (total area of TE legs/area of the ceramic substrate), and the number of TE legs, higher system performance could be obtained as shown here.

To increase the system efficiency, we can individually improve the absorber efficiency and the module efficiency. In Chapter 2, we discussed design rules for improving the absorber efficiency by suppressing radiative and convective losses. Here, we discuss parameters that affect module performance. One key parameter for improvement is the material itself which will be discussed briefly at the end of this chapter and then Chapter 5 is dedicated to new TE material discussion.

Key module variables and their effect on the system performance are discussed in Section 4.1. Results of varying the TE leg geometry and its effect on the system efficiency are shown in Section 4.2. Module design optimization and TE material volume limitations are discussed in Section 4.3.

4.1 Module variables

In order to achieve high efficiency from a TEG module, the effective module ZT has to be large. As shown in Chapter 2, there are various parameters that affect the module ZT . They are: material parameters (Seebeck coefficient, thermal conductivity and electrical conductivity), TE leg geometry (cross-section area and height), and electrical/thermal parasitics. The material properties and the potential enhancement in the system performance will be discussed in Chapter 5. As we know, lower electrical and thermal parasitics always improve the system. Most of the module parasitics arise due to the interfaces (i.e. TE material, electrical contact, metal and ceramic), and the connections between the TE legs. A type of

thermal parasitic impedance that is influenced by the geometry of the TE leg is the spreading resistance (R_{spread}), given by [128]:

$$R_{spread} = \frac{1}{2 \cdot \kappa_{ceramic} \sqrt{S_{ceramic}}} \left(1 - \sqrt{\frac{S_{element}}{S_{ceramic}}} \right)^{3/2} \left(\frac{\tanh(L_{ceramic} \cdot \delta) + \frac{\kappa_{ceramic} \cdot \delta}{h}}{1 + \frac{\kappa_{ceramic} \cdot \delta}{h} \tanh(L_{ceramic} \cdot \delta)} \right) \quad (28)$$

Here, $\delta = \sqrt{\pi^3 / S_{ceramic}} + \sqrt{1 / S_{element}}$, $S_{element}$ is the TE leg cross-section area, $S_{ceramic}$ is the ceramic plate area size per element, $\kappa_{ceramic}$ is the thermal conductivity of the ceramic layer, $L_{ceramic}$ is the thickness of the ceramic plate, and h is the heat transfer coefficient at the cold side. The spreading resistance accounts for the constraint in heat flow from one region to another of different cross sectional area. In a module, the spreading resistance is controlled by the fill factor which is defined as the ratio of the cross-section area of the TE leg to area of the ceramic per element.

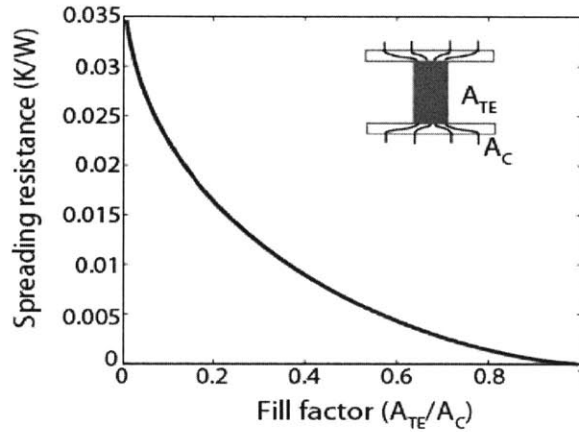


Figure 74: Spreading resistance increasing as the fill factor is decreased (in this case by decreasing the cross-section area of the TE leg) ($L_{ceramic} = 0.75$ mm, $\kappa_{ceramic} = 20$ W/m.K)

For a fixed number of TE couples, when the cross-section area of the TE leg is decreased (i.e. the fill factor is increased), the spreading resistance increases (Figure 74). In the case of the STEG system, at low fill factors, the spreading resistance can be nearly 10% of the total TE module thermal impedance (0.4 K/W).

The TE leg geometry affects both the thermal and the electrical resistance of the module (Equation 17/18). For a given generator system, a larger module thermal impedance indicates higher temperature gradient for a constant heat flux. This can improve the electrical output power and the system efficiency, unless the generator is limited by the operating temperature range such as maximum hot side temperature

or by material degradation at higher temperature. We will discuss the limitation of current commercial modules later in the chapter. Higher thermal impedance is usually accompanied by higher internal resistance which can lower the output electrical power. Smaller electrical resistance leads to higher module ZT and higher output power.

The key module parameters that are varied in this study (Figure 75) are categorized into two parts:

1. **Height of the TE leg:** Both the thermal and the electrical resistance of a module depends on the leg thickness. As a one-dimensional model, the thermal resistance as well as the electrical resistance of a TE leg increases when the thickness of the leg is increased. As the thermal resistance is increased, the temperature gradient across the module becomes larger for same input thermal power, which leads to larger open circuit voltage and higher power. With increased electrical resistance, the output power decreases as the current decreases. There would be an optimum height for maximum output power for a given system design (Figure 76 a).
2. **Fill factor** (= area of TE legs/area of the module): The fill factor can be changed by varying three different parameters: changing the total module area; changing the total number of TE couples, and changing the cross-section area of the TE legs.
 - a. By changing the total module area, the thermal parasitic resistance of the system can be changed which is equal to the ceramic resistance and the spreading resistance. Dependence of the spreading resistance on the fill factor is shown in Figure 74. The durability and the stress factor of the module (especially ceramic wafer) will be important in limiting the size of the total module area. In all the optimization processes, the total area of the module for the STEG is kept constant (similar to the commercial module used for the prototypes).
 - b. The fill factor can be changed by changing the total number of the TE couples. The number of TE couples is usually determined by the open circuit voltage requirement of the system. In the optimization process, the number of couples is equal to the commercial module.
 - c. By changing the cross-section area of the TE leg, both the electrical and the thermal resistances of the module can be changed, which affects the system performance (Figure 76 b).

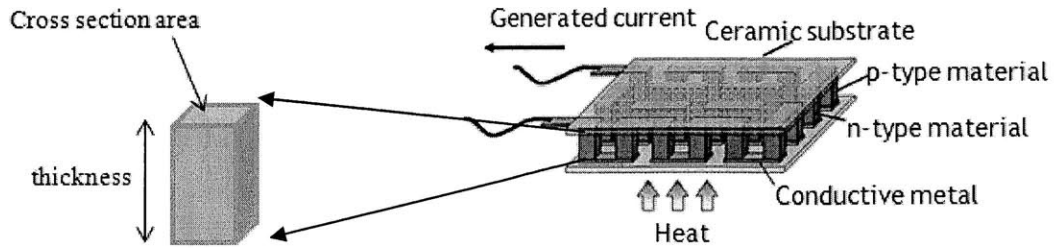


Figure 75: TEG module schematic showing n- and p-type legs with ceramic substrate at the top and bottom

The effects of these parameters (TE leg thickness and fill factor) on the system performance were studied. Once we understand the influence of the parameters, we can optimize the geometry for maximum output power. Here, we consider steady state simulation using the modeling tool discussed in Chapter 2. For this simulation, the hot side absorber with a commercial selective surface coating ($\alpha = 0.94$, $\epsilon = 0.22$) was considered. At the cold side, natural water heat transfer was utilized. For this simulation, similar system parameters as those used in the field trials were considered including all the interface impedance (absorber/module interface and module/heat sink interface). The number of TE couples (127 x 4) and the total area of the TE module (10 cm x 10 cm) in the STEG system were kept the same as the commercial TEG module.

At first, the dependence of both the leg thickness and the cross-section (fill factor) were explored independently. The following figures show system efficiency vs. TE leg thickness and fill factor for a constant input solar flux of 1000 W/m^2 with an optical concentration of $10x$.

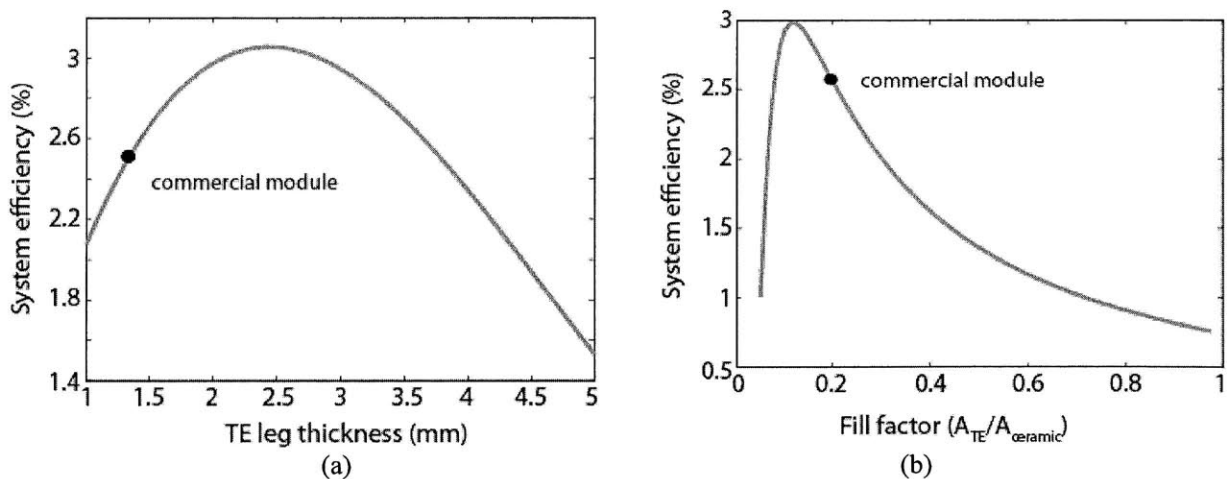


Figure 76: (a) STEG system efficiency vs. TE leg thickness; (b) efficiency vs. fill factor achieved here by changing the cross section area of the TE leg

For thinner modules, the overall thermal impedance is lower, which indicates that for the same amount of input power, the temperature gradient across the TE material will be smaller leading to lower output power. Similarly if the module is very thick, the thermal impedance will be very high and it can be comparable to other loss paths (convection) decreasing the total power flow through the TE material. The internal electrical resistance of the TE module will also be high when the thickness increases. Due to this tradeoff, there is an optimum thickness of the TE leg which gives maximum efficiency. Similarly, for the fill factor, by changing the cross-section area of the TE leg, both the thermal and the electrical resistance can be varied and there is an optimal point for maximum efficiency. In **Figure 76**, the thickness (1.4 mm) and the fill factor (20%) for a commercial Bi_2Te_3 module is shown for comparison. In both cases, either by using slightly taller leg geometry or a smaller fill factor, the system efficiency could be increased.

The experimental demonstration of the effect of the aspect ratio (i.e. cross-section area/thickness) variation in a commercial Bi_2Te_3 module is shown in **Figure 77**. In the bench-top prototype described in Chapter 2, the highest system efficiency of 3% was achieved by effectively stacking two TEG modules to give a smaller aspect ratio module compared to a single commercial module structure. Even with an increased thermal parasitic due to the inner ceramic layers, an overall increment of 31% was measured for the output electrical power for the smaller aspect ratio module prototype. Without any system parasitics, this aspect ratio in the bench-top setup can give 4% system efficiency as shown in Chapter 2.

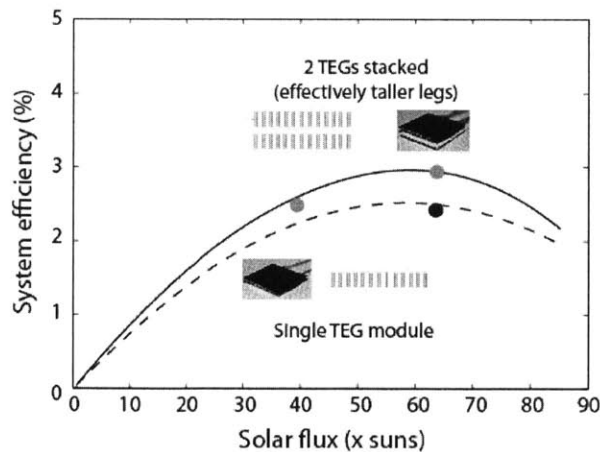


Figure 77: System efficiency for different aspect ratio modules achieved in the bench-top prototype design

In the remaining sections of this chapter, we look at optimization of the aspect ratio of the TE legs in a module to maximize the output power for the large-scale system prototype used in field trials.

4.2 Optimization of the aspect ratio

In order to optimize the leg geometry, both the fill factor and the leg thickness were varied to get the maximum system efficiency (Figure 78). The analysis is for non-ideal system including all thermal and electrical parasitics.

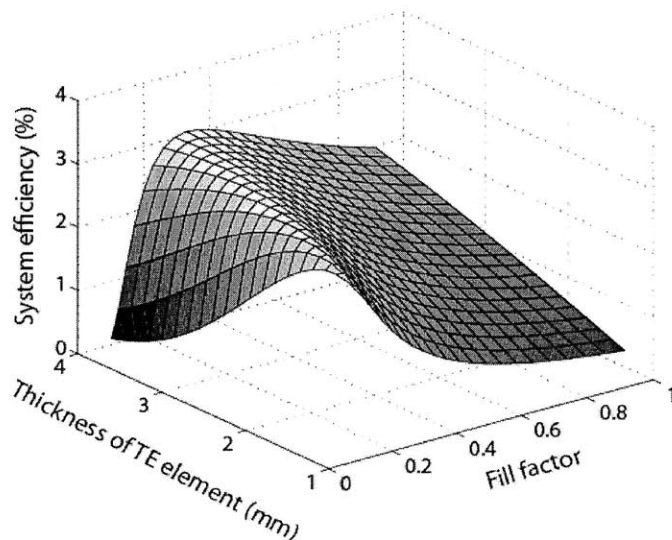


Figure 78: 3-dimensional plot showing maximum system efficiency for various leg thicknesses and module fill factors

From the matrix, there are various combinations of leg dimensions that can give system efficiency ~ 3%. If we consider the tallest TE leg (4 mm), the maximum system efficiency can be achieved with a module where the TE leg cross-section area is 2 mm x 2 mm. The system efficiency over a wider flux range for this new module compared to the commercial module is shown in the following figure.

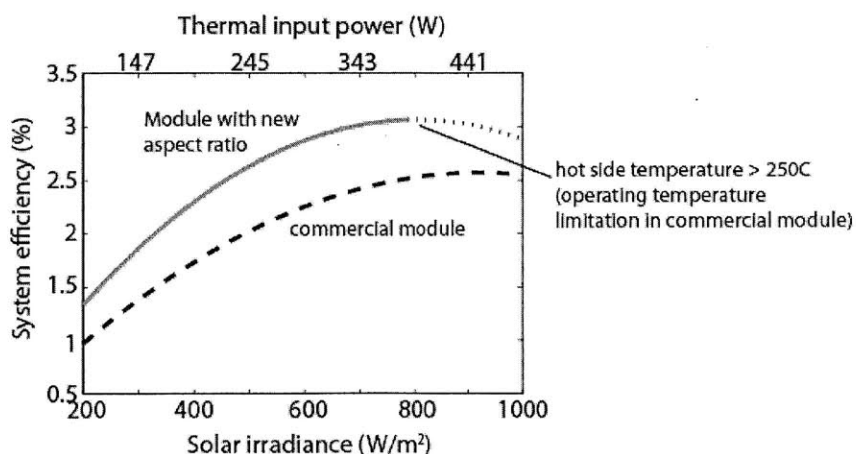


Figure 79: System efficiency at various solar irradiance with the optical concentration ~ 10x for the module with different TE leg geometry than the commercial Bi₂Te₃ module

Overall increase in the system efficiency is seen for various input fluxes. Modules with this new leg dimension will work better than the current commercial module for input thermal power ranging from 100-500 W. The point beyond which the hot side temperature of the module is above 250°C is indicated in the figure (light dash line) to show the point where a commercial Bi_2Te_3 module would be limited due to contact failure. More on this limitation will be discussed later on.

In the analysis till now, the TE material volume has not been considered. The commercial module used in the STEG system only uses TE material volume of 3.15 cm^3 per leg, where as the new module discussed above uses 16 cm^3 volume of TE material. For optimization, we considered the total volume of TE material used in a module to be a limiting factor. Overall, even though the system efficiency does improve due to taller TE legs, the cost of the system will also increases as more material is used. The material cost in a bulk module is $\sim 30\%$ of the total module cost. The issue of material use (especially rare elements) and the cost factor will be discussed in detail in Chapter 5 and 6.

In the next analysis, we restricted the total volume of the TE material to be same as that of the commercial module. By changing the dimensions of the TE leg, even with the same volume of material, higher efficiency can be obtained as shown in **Figure 80** and **Figure 81**. The optimized leg in this case is $1.2 \text{ mm} \times 1.2 \text{ mm} \times 2.25 \text{ mm}$. The commercial module performance is shown for comparison to the optimized system.

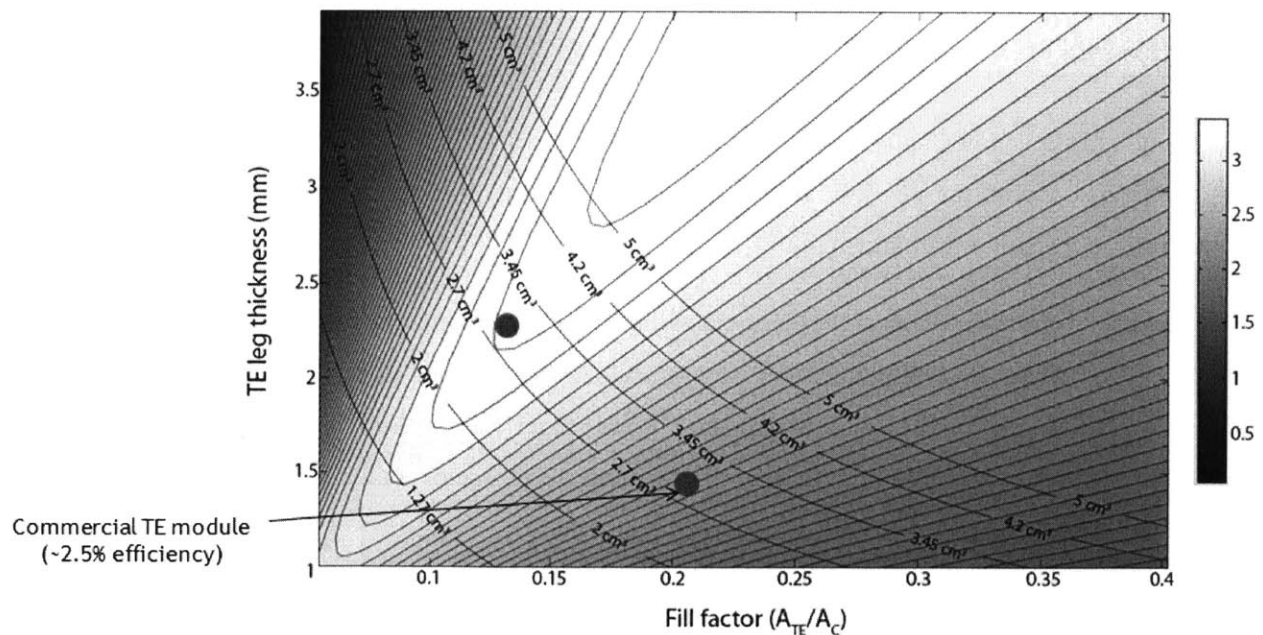


Figure 80: A top-down view of the system efficiency vs. TE leg thickness and the fill factor (shading: dark $\sim 0\%$ efficiency, lightest $\sim 3.3\%$ efficiency), with the total TE volume used for different thickness and fill factors

Under similar system conditions, the optimized module can perform better than the current commercial module for the STEG system over a wide range of input incidence (**Figure 81**).

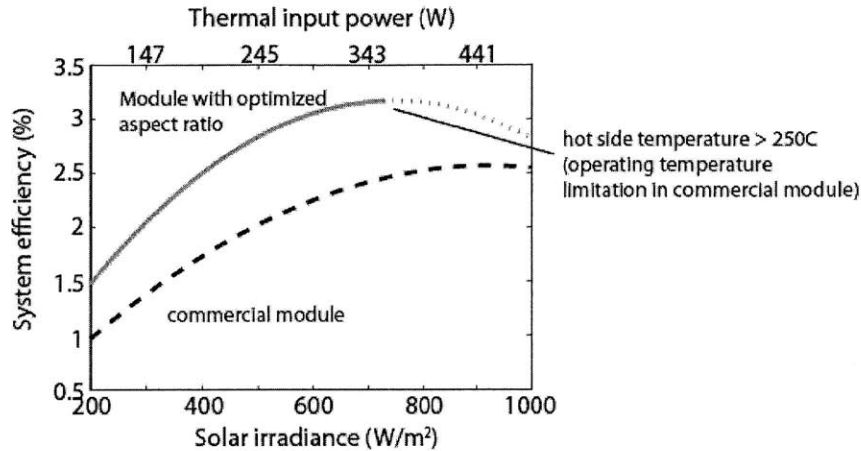


Figure 81: System efficiency for optimized module and commercial module using same amount of TE material

The issue of the hot side temperature limitation in the commercial module is due to use of common soft solder filler metal that have liquid temperature below 350°C. The melting point for most solder mixture of tin/lead is ~ 180-215°C. Most lead free solder based on tin-silver-copper have eutectic behavior at ~ 250°C. Apart from these low temperature soft solder metals, there are hard solders which are used for brazing and have higher melting temperatures. Alloys for copper with zinc or silver are the most common. Zn-Al hard solder used for aluminum welding can have high melting temperature ~ 380-400°C [129]. Contact metallurgy for high temperature thermoelectrics such as PbTe or SiGe can be used here to overcome the limitation of low operating temperature. Pure nickel based contact metallurgy was used in a PbTe generator developed at U.S Army Research Laboratory which worked at hot side temperature of 600°C [130]. Thus, with the new optimized system, the contacts have to be some form of hard solder to work with larger input power and at higher temperature beyond 250°C.

Next we look at the potential best performance with this optimized module redesigning by considering an ideal condition where we use the best research grade selective surface of $\alpha = 0.96$ and $\epsilon = 0.05$, and no module parasitics (**Figure 82**). System efficiency greater than 4% can be achieved for Bi₂Te₃ module in this case. However, it can be seen that the system performance quickly degrades as the overall temperature increases and the material ZT starts to degrade.

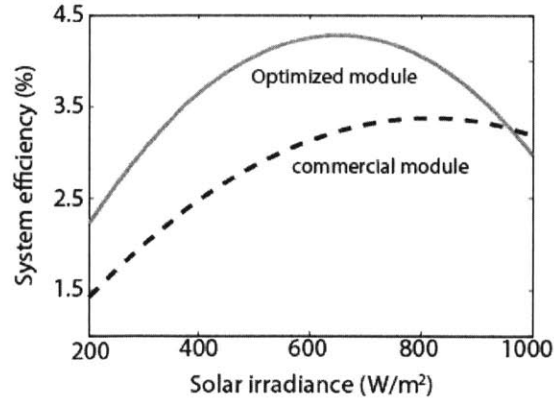


Figure 82: Improved system performance achieved with the best research grade selective surface and ideal conditions (no module parasitics)

With the field trial experience, we know that higher input power from solar cooker is possible (> 650 W). With Bi_2Te_3 , such input power will lead to average temperature > 500 K where the material $ZT < 0.3$ (Figure 20). Even if we optimize the geometry such that it works all the way to such high power by decreasing the thickness (i.e. the thermal impedance), it will quickly start to operate at the heat sink limited regime^[131]. Currently, with natural water heat transfer, the cold side temperature of the heat sink is at $\sim 70^\circ\text{C}$. As the input thermal power increases, it puts pressure on the heat sink to remove large heat flux to the environment. Thinner module will also have smaller temperature gradient, giving lower power. There is no benefit going to thinner module just to make it work at higher thermal fluxes. With the possibility of higher average temperature (500 K), material other than Bi_2Te_3 may provide higher efficiency.

4.3 Conclusion

Module optimization has been discussed as a way to improve the performance of the solar thermoelectric generator. By changing either the thickness of the TE leg or the fill-factor, the module performance can be improved by optimizing the electrical and the thermal resistances. Total material use (volume) was considered for cost reasons when choosing the aspect ratio for the TE leg. In this analysis, in order to keep the cost fixed (material cost), the same volume as the commercial module was used to optimize the leg geometry for maximum output electrical power. For Bi_2Te_3 , in an ideal condition, maximum system efficiency of 4.4% can be achieved with an optimized module, which is 33% more than the maximum efficiency achieved with the commercial modules used in the STEG. One limiting factor for taking the module to the maximum performance is the hot side operating temperature range. Currently, this

limitation is set by the electrical solder contact which melts beyond 250°C. Even at lower operating temperature, the optimized module does perform better than the commercial module. With the optimized module, the operating temperature of the material quickly reaches the maximum of 250°C at lower input power due to larger thermal impedance compared to the commercial module. The limit of the operating temperature can be changed by switching to higher melting solder. As seen from field trials, large flux is available with many of the local solar cookers at high altitude. New TE material may be more efficient than Bi_2Te_3 in this range for solar thermoelectrics.

For comparison, looking at new TE material such as silicides (MgSiSn-Sb doped) which shows $ZT \sim 1$ at higher temperature 700 K (Figure 83), the system efficiency can be larger at higher solar irradiance compared to the commercial module as well as the optimized Bi_2Te_3 modules (Figure 84).

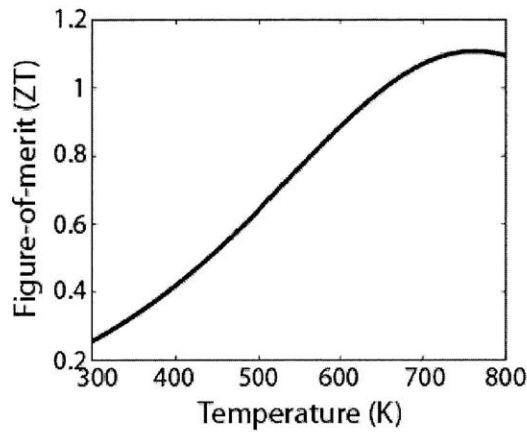


Figure 83: ZT for MgSiSn – Sb doped taken from Ref. [132]

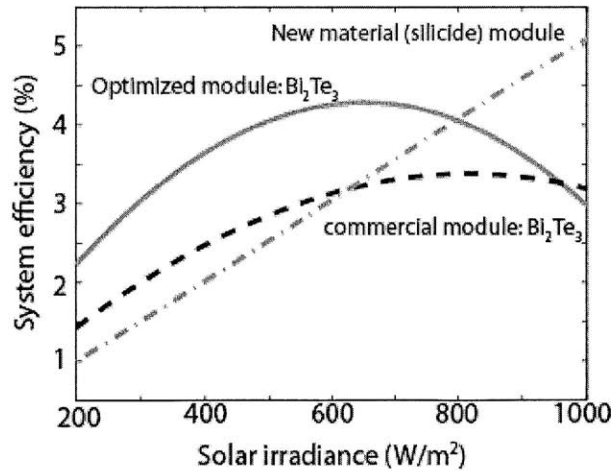


Figure 84: Performance of a new material (MgSiSn) module compared to Bi_2Te_3 -based modules

At input thermal power > 600 W, the system efficiency with the new material is greater than that for Bi_2Te_3 . In the next chapter, more new TE materials are explored and a high-temperature characterization tool is described which was developed during this research.

Chapter 5

Novel Thermoelectric Material Study

In the past two decades, there has been a surge in research of new thermoelectric materials, driven partly by the need for clean and sustainable power generation technology. Until the 1980s, the figure-of-merit of state-of-the-art thermoelectric material was approximately 1^[41], which limited the thermal-to-electrical conversion efficiency to below 5% with a temperature drop of ~ 200 K, at an average temperature of 350 K. Thus, application of thermoelectrics was only in niche markets such as power sources for deep-space probes and small thermoelectric coolers for electronics^[133, 134]. Recently, with the development of new materials and fabrication technologies, there have been continuous reports of materials with $ZT > 1$; some of the highest ZT materials are listed in Table 19. The advancement in material technology has helped grow the application space for thermoelectrics. Waste heat recovery in automobiles^[135], industrial waste heat recovery^[136], and solar thermoelectrics^[35, 99] are some of the applications that become feasible with high ZT materials as shown in Chapter 2.

As the scope of thermoelectrics increases, material usage and environmental conservation issues start to become of importance when choosing elements for thermoelectrics. Some of the key constituent elements in recent high- ZT materials are not abundant in the Earth's crust, such as tellurium (Te) (0.001 ppm by weight), antimony (Sb) (0.2 ppm), germanium (Ge) (1.4 ppm), ytterbium (2.8 ppm) and gallium (Ga) (19 ppm)^[77, 137]. The low crustal abundance of materials contributes to their price volatility as applications (competing with thermoelectrics) continue to grow, for example, cadmium telluride photovoltaics (PV), antimony-lead alloy for batteries, antimony-tin-oxide for display panels and capacitors, Ge for fiber optics and infrared optical technologies, and Ga for PV films and integrated circuits.

Previous consideration of material scarcity has focused primarily on Te-based thermoelectrics^[138], as Te is one of the most commonly used elements in thermoelectrics, and it also happens to be one of the rarest elements in the Earth's crust. The annual production of Te is ~ 200 metric tons, of which nearly 70% is used for industrial metallurgical applications^[139, 140]. The current demand from Te-thermoelectrics is less than 15%, due to small application range^[140]. However, with growth in emerging new technologies such as photovoltaics^[13], the supply/demand balance and eventually the price has been very volatile^[141, 142]. In such a scenario, increase in demand from thermoelectrics with Te will only add to the scarcity and rising cost of the element^[139]. For growing TE applications such as waste heat recovery in automobiles, annual

Te production could be exhausted fitting Te-based thermoelectrics in less than 15% of new passenger cars annually in the US with 5% fuel economy benefit. Similarly for solar thermoelectrics, the STEG can benefit more than 1 billion people around the world who do not have electricity. At the current rate of 0.55 watt per gram of Te usage, the annual Te production can supply 110 MW through STEG; whereas the demand for such application could be more than 5 GW. Such high demand would automatically spike the price of the material causing the system to be too expensive. For bulk material TEG, estimated 30-40% of the generator cost is the material cost. With volatility in material price, the system cost is going to be susceptible. One way to avoid such influences is to look at earth-abundant material for thermoelectric application.

In this research, we broaden the rare TE material analysis to include new materials such as skutterudites, Zintl phase compounds, and clathrates that employ Sb, Yb, and Ge. The insight from this research helps us to identify material characteristics for good thermoelectric performance. In the first section of this chapter, we will discuss recent TE materials, and ZT relation to earth-abundance of their constituent elements. In Section 5.1, the trend in ZT and the material abundance is analyzed for bulk thermoelectric materials. The crustal abundance of several important elements in today's thermoelectrics is explored in this section. Detailed discussion on some of the recent high ZT materials, namely skutterudites, clathrates and Zintl phase are presented in Section 5.2. Some new earth-abundant, benign bulk thermoelectrics (half-Heusler, oxides and silicides) are described in Section 5.3. Observations and guidelines for a good thermoelectric material are discussed in Section 5.4. Here, we have included only bulk thermoelectric materials in our discussion. Analysis of thermoelectric properties of other materials and technologies, namely, low dimensional materials and nano-structuring (nanocomposite) can be found elsewhere [22, 143, 144].

Material	ZT	Operating temperature	Weighted crustal abundance (metric tons)	Competing applications	Comments
Bi_2Te_3	(n-type): 1.1 (350K) (p-type): 1 (320K) ^[133]	300-450 K	2.8×10^{14}	Te – CdTe PV	Used in commercial modules
$\text{Si}_{(1-x)}\text{Ge}_x$	(p-type): 0.6 (1200K) (n-type): 1.1 (1200) ^[50]	> 800 K	2.6×10^{17}	Ge – fiber optics, infrared technologies	Used in deep space probes
PbTe ^[133]	(n-type): 0.9 (750K) (p-type): 0.9 (750K)	400-600 K	3.5×10^{14}	Te – CdTe PV	Concern: lead toxicity
$\text{AgPb}_{18}\text{SbTe}_{20}$ (LAST)	1.72 (800 K) ^[145]	700-800 K	3.4×10^{14}	Te – CdTe PV Sb – batteries, capacitors, displays	Natural nanostructure and grain boundaries suppress thermal conductivity
$(\text{GeTe})_{75}(\text{AgSbTe})_{25}$ (TAGS – 75)	1.75 (700 K) ^[146]	600-800 K	2.3×10^{14}	Ge – fiber optics and infrared technologies Te – CdTe PV Sb – batteries, capacitors, displays	Small features (~ 10nm) causes phonon scattering to suppress thermal conductivity
$\text{Sr}_{0.16}\text{Yb}_{0.03}\text{Co}_4\text{Sb}_{12}$ (Skutterudite)	1.32 (850 K) ^[147]	700-1000 K	3.2×10^{16}	Co – permanent magnet for wind turbines, hybrid automobiles Sb – batteries, capacitors, displays	p-type: $(\text{Ce}_y\text{Co}_{4-x}\text{Fe}_x\text{Sb}_{12})$ ZT ~ 1 ^[148]
$\text{Ba}_8\text{Ga}_{16}\text{Ge}_{30}$ (Clathrate)	1.35 (900 K) ^[149]	800-1000 K	3.8×10^{17}	Ge – fiber optics and infrared technologies	p-type: $(\text{Ba}_8\text{Ga}_{16}\text{Al}_3\text{Ge}_{27})$ ZT = 0.61 ^[150]
$\text{Yb}_{14}\text{Mn}_{1-x}\text{Al}_x\text{Sb}_{11}$ (Zintl phase)	1 (1200 K) ^[47]	>1000 K	7.7×10^{16}	Sb – batteries, capacitors, displays	
$\beta\text{-Zn}_4\text{Sb}_3$	1.3 (670 K) ^[151]	600-800 K	4.6×10^{16}	Sb – batteries, capacitors, displays	
$\text{Hf}_{0.75}\text{Zr}_{0.25}\text{NiSn}_{0.975}\text{Sb}_{0.025}$ (Half-Heusler)	0.8 (1025 K) ^[152]	>1000 K	3×10^{18}		(No Sb) $\text{Zr}_{0.5}\text{Hf}_{0.5}\text{NiSn}$ ZT = 0.5 ^[153, 154]

Material	ZT	Operating temperature	Weighted crustal abundance (metric tons)	Competing applications	Comments
NaCo ₂ O ₄ (Oxide)	0.8 (1050 K) ^[155]	>1000 K	7.1x10 ¹⁸		n-type material (SrTiO ₃) ZT ~ 0.37 ^[156]
Mg ₂ Si _{0.4-0.015} Sn _{0.6} Sb _{0.015} (Silicide)	1.1 (800 K) ^[132]		0.5x10 ¹⁸		(No Sb) Mg ₂ Si _{0.4} Sn _{0.6} ZT < 0.1 ^[132]
Nano structured TE material:					
Bi ₂ Te ₃ /Sb ₂ Te ₃ (superlattice)	(p-type) 2.4 (350K) (n-type) 1.2 (300K) ^[157]	300 – 400 K		Te – CdTe PV Sb – batteries, capacitors, displays	Enhancement due to reduction in thermal conductivity
PbSeTe/PbTe (quantum dots superlattice)	(n-type) 1.6 (300K) ^[158]	350 – 600 K		Te – CdTe PV	Enhancement due to reduction in thermal conductivity (Bulk alloy ZT ~ 0.34)
Bi-Sb-Te	1.4 (300K) ^[144]	300 – 500 K	□ Te – CdTe	Te – CdTe PV Sb – batteries, capacitors, displays	Nanostructured sites due to ball milling
Si nanowires	<1 (@ 1200 K)				Nanostructuring reduces thermal conductivity
ErAs/InGaAlAs (nano dots)	(n-type) 1.4 (800K) ^[159]	400 – 800 K		Ga – PV, integrated circuits	Arsenic toxicity

Table 19: High ZT thermoelectric material

Apart from material scarcity and abundance, another interesting aspect of material selection is the temperature. As mentioned in the previous chapters (1 and 2), the achievable temperature from a solar concentrator depends on its design and size. With available solar cookers, the hot side temperature ranges from 400-600 K. Today, the only commercial thermoelectric modules are made from Bi_2Te_3 and has $ZT_{\text{material}} \sim 0.9$, which gives module efficiency of 4-5% at low temperature range (< 400 K). Current commercial modules work at operating temperature of less than 530 K due to melting contact failure. Bi_2Te_3 performance also degrades beyond average temperature range of 350 K. From the conventional TE materials, high ZT (~ 0.8) PbTe can be a suitable candidate for the STEG. However, due to the presence of toxic and rare-earth elements such as lead and tellurium it is not the most suitable option. By understanding the material selection for good thermoelectrics, we look at other possibilities.

For a generator, not only high ZT is important, but a large temperature gradient across the generator and high average temperature also increase the maximum achievable thermal-to-electrical conversion efficiency (η_{max}) given by ^[160]:

$$\eta_{\text{max}} = \frac{T_h - T_c}{T_h} \cdot \frac{\sqrt{1 + ZT_M} - 1}{\sqrt{1 + ZT_M} + T_c / T_h} \quad (29)$$

Here, T_h is the hot side temperature, T_c is the cold side temperature, and T_M is the average temperature of the TE material. This is true for all heat engines such as Brayton, Stirling and Rankine engines (**Figure 85**) ^[161]. Even with the ZT value of 0.7, if the material can withstand high temperature above 1000 K, the optimum efficiency of 10-15% can be achieved (**Figure 85**). At this efficiency, TEG is significantly cheaper than photovoltaics and other distributed energy generation for low power electricity. As shown in **Figure 85**, thermoelectric materials with higher ZT can push the efficiency towards that of the large-scale heat/steam engines. Due to this proportional relationship between temperature, ZT and efficiency, researchers have focused on trying to find materials with high ZT that can work at large temperature. In this work, we have looked at novel thermoelectric materials (with earth-abundant constituent elements) that potentially have high ZT at temperature ranging from 400-1000 K. The material is introduced in Section 5.5.

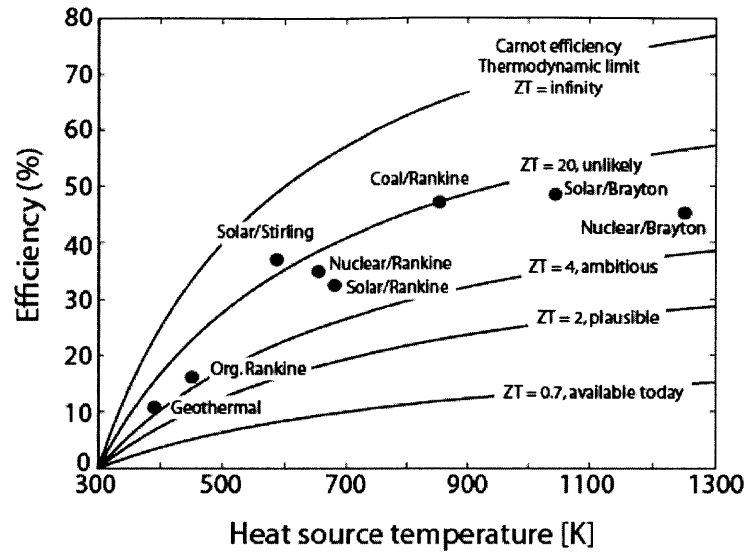


Figure 85: Comparison of various energy generation sources such as heat engines with thermoelectric efficiency at different ZT and temperature range [Adapted from [161]]

For TE material characterization, we have developed an experimental setup (Z -meter) to work at high temperature which is described in Section 5.6. For high temperature measurements, there are several considerations to ensure accurate measurement. They are described in detail in this section. The experimental system is described in Section 5.6.1. The principles of measurements of TE parameters are described in Section 5.6.2. One of the key improvements in the system for high temperature measurement, the thermal radiation suppression is discussed in Section 5.6.3. The system verification with TE parameter measurements for known samples is presented in Section 5.6.4. New material measurement results are discussed in Section 5.7.

5.1 ZT vs. crustal abundance

We begin our research by looking at the crustal abundance and understanding the reasons behind the material distribution on Earth. Figure 86 shows the solar (a) and the crustal (b) abundance of the elements with respect to their atomic number. There is a general trend of decreasing abundance for heavier elements. In the universe, all the elements after iron (Fe), which is the most stable nuclei, are formed by a slow neutron capture process called the S-process^[162]. This nucleosynthesis process occurs in stars where a stable isotope captures a neutron and forms a radioactive isotope, which decays to its stable daughter before the next neutron is captured to form a heavier isotope^[162, 163]. Bismuth is the last and the heaviest of the stable atoms created by the S-process^[163]. Atoms produced by such neutron capture are less stable

then Fe ^[163]. Another noticeable trend is that elements with even atomic numbers are slightly more abundant than the odd numbered elements. This has to do with the stability of neutrons and protons in the nuclei which forms “closed shells” configuration (similar to shells in atomic structure) in even atomic numbered elements (Oddo-Harkins rule) ^[164]. The crustal abundance (Figure 86 b) does not follow this simple trend with the atomic number. The rarest elements are not the heaviest stable atoms. Ruthenium (Ru), rhodium (Rh), palladium (Pa) and Te with atomic numbers between 40 and 55 are rarer than the heavier rare-earth elements. The crustal abundance is determined not only by the overall solar abundance (Figure 86 a) but also by the element’s affinity to ore forming chemicals such as oxygen (O), sulfur (S) and Fe. The oxides and the silicates form the lightest mineral ores which are found easily on the Earth’s crust. Elements which have higher affinity for Fe tend to be denser and closer to the core, thus limiting their distribution on the Earth’s crust. Crustal abundance of some of the thermoelectric elements is discussed in detail here.

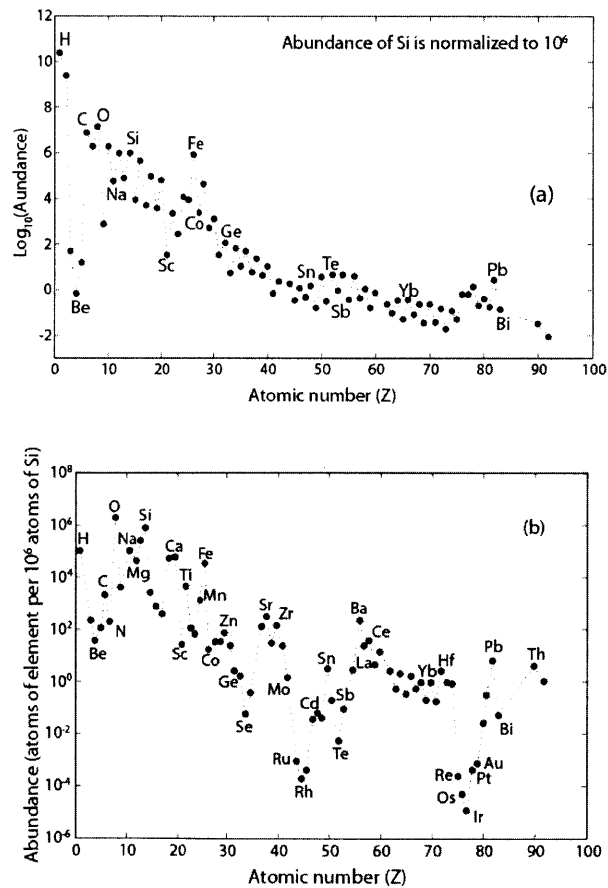


Figure 86: Solar (a) and crustal (b) abundance of elements according to their atomic number [Adapted from [165, 166]]

Even though the knowledge of the crustal abundance can give guidance in terms of environmental sustainability and scarcity of elements, the major factor influencing a material's usage for any technology is going to be its price. Determining an element's price for comparison can be a tricky topic as it is a dynamic function of economics (demand/supply chain), engineering, political and environmental factors. **Figure 87** shows the overall increasing price trend for some of the constituent elements used in thermoelectrics for the past decade.

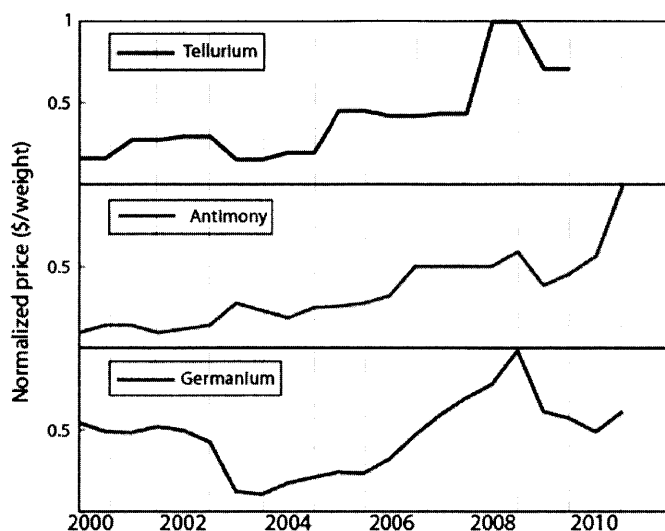


Figure 87: Price data collected from USGS and metalprice.com (*USGS report includes material purity for the price data; e.g. 99.6% purity for Antimony price)

Many economic geologists agree on a negatively sloped trend in price and crustal abundance for most of the elements (**Figure 88**), which shows that as the elements become rarer, they are generally more expensive ^[167-169]. There are few elements which deviate from this trend such as Ge, Ga, gold (Au) and platinum (Pt) are more expensive than other elements of similar crustal abundance ^[167]. Similarly, cadmium (Cd), arsenic (As), bismuth (Bi), and mercury (Hg) have lower market price relative to abundance ^[167]. These deviations could be due to difference in demand for these elements. For example, Ge has similar crustal abundance as molybdenum (Mo), Yb, lanthanum (La), and tungsten (W). As the demand for Ge is higher compared to these other elements, it is natural that Ge has higher market price. Another important factor in the market price of an element is the homogeneity and the concentration in which it is found in ores or minerals. This is important in determining which mines which are economical for extraction. Many sulfide ores have high concentrations of minable elements due to precipitation, compared to oxide or silicates, which can lower the price ^[168]. Elements such as Cd, Bi and Hg are extracted in high concentration from sulfide ores.

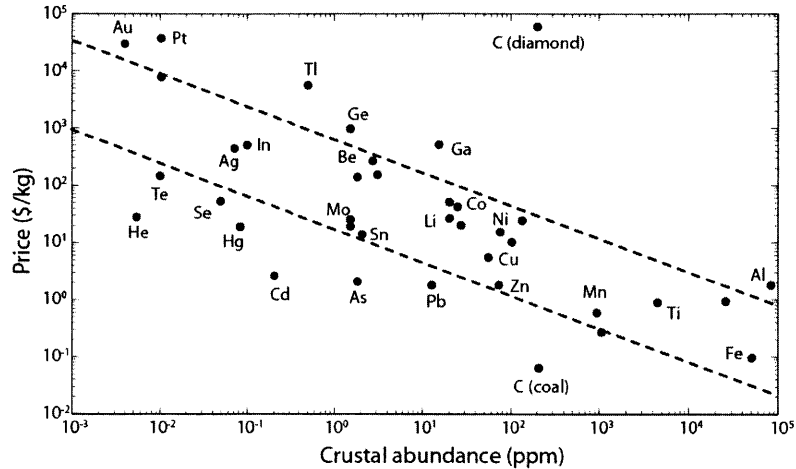


Figure 88: Price (\$/kg) vs. crustal abundance [Adapted from [167] (2009-2010 prices)]

As material demand increases with every new emerging technology competing with thermoelectrics, the price fluctuation will invariably affect the application scope of thermoelectrics. Many thermoelectric elements such as Sb, As, Bi, selenium (Se), and Te are mined as a by-product with primary metals like lead (Pb), zinc (Zn) or copper (Cu) ores ^[139]. The production capacity of these mines chiefly depends on market (demand and price) of the primary element. Looking at the high ZT thermoelectrics (Table 19) and the crustal abundance (Figure 86 b), some elements that may be critical in terms of cost and sustainability are Te, Sb, Ge, and Yb.

Even though Te is widely distributed in the solar system, having comparable solar abundance to tin (Sn), the low average abundance on the Earth's crust has to do with the fact that Te has low affinity for oxygen and prefers to bond with sulfur forming heavier minerals ^[170, 171]. These chalcophile (sulfur-loving) elements are much denser than the lithophile elements (silicate minerals), and they accumulated below the lithophiles at the time of the first crystallization of the Earth's crust, which lead to their depletion on the crust compared to the solar abundance ^[172]. Te does not occur in concentrations high enough to economically justify mining on its own ^{[139], [173]}. The surge of new technologies has driven the price of Te in the last decade from less than \$22/kg (2004) to nearly \$440/kg at the beginning of 2011 ^[139]. However, the global production of Te has only increased by less than 25% in the last decade ^[13], which may indicate to the limitation in the accessible quantity of this element.

Sb is also a chalcophile element mostly produced as a by-product from a sulfide ore mineral called stibnite ^[174, 175]. The primary use of Sb has been for flame retardants and lead-acid batteries. Increasing use in new technologies in the past decade has caused a sharp rise in the price for Sb. Recently, the price volatility has also been due to speculation of decline in mines in China, which is the world's largest Sb

producer (> 90%)^[173]. Herfindahl index defines the measure of the degree of competition in an industry. A normalized index value of 0 indicates highly competitive market with all involved firms/countries with equal share. The index of 1 indicates full concentration in a single firm/country. For Sb, the normalized Herfindahl index is 0.77; for comparison, the index value for copper is 0.16^[176].

As with Te, Ge is unevenly distributed on the Earth's crust, and it forms more than 100 minerals, but only few ores (usually chalcophiles) have enough concentration of Ge to allow for economic extraction^[177]. Ge also has the tendency to alloy with Fe which makes it denser and closer to the core^[177]. Due to small extractable quantities, there are many refining steps from mining to the actual element which adds to the cost. The current market price of Ge (~ \$1,000/kg) may make it prohibitive to be used for any large-scale thermoelectric application^{[139],[173]}. Another potential critical material used in thermoelectrics is Yb. The low annual production of Yb has more to do with few commercial applications rather than the production capability given by the crustal abundance. However the element is very expensive (\$14,000/kg) primarily due to difficulties in isolation of rare-earth elements from each other as their chemical properties are very similar^[173].

Figure 89 shows the plot of ZT vs. crustal abundance for some of the best, recent thermoelectric materials. The maximum demonstrated ZT for each particular compound exhibits an empirical dependence on the crustal abundance, A , such that $ZT \sim A^{-b}$ where b is in the range from 0.05-0.10, depending on inclusion of the Te-based materials. Here, A is the weighted crustal abundance of the rarest element in the composition of a thermoelectric material. In an alloy (M_xN_y), the variable A is given by:

$$A = \begin{cases} xC_M & \text{if } C_M < C_N \\ yC_N & \text{if } C_M > C_N \end{cases}, \text{ where } C_M \text{ and } C_N \text{ are the crustal abundance of the constituent elements}$$

(conversion from ppm to kg is done by estimating the crust's mass ($\sim 1.3 \times 10^{23}$ kg) from the rock density and the total volume of the crust); x and y are the percentage weights of the individual component.

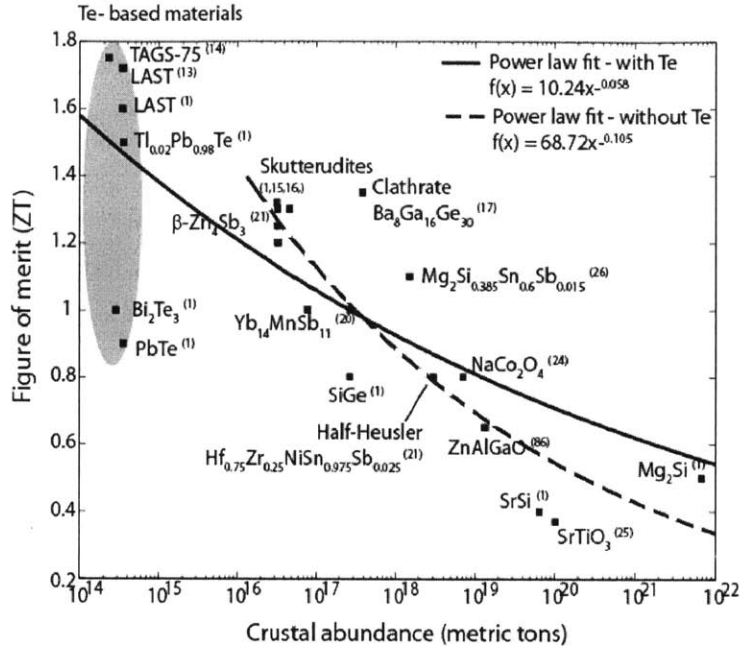


Figure 89: ZT vs. crustal abundance for bulk thermoelectric materials

Careful consideration has to be made when researching new thermoelectric materials, keeping in mind such factors as element scarcity, toxicity and price, especially if the end goal is high volume application of thermoelectrics. In the next section, individual thermoelectric elements utilizing these trace and rare elements will be analyzed to understand the role of rare elements in enhancing the thermoelectric properties.

5.2 High ZT material

5.2.1. Skutterudite

Based on Slack's phonon-glass-electron-crystal (PGEC) concept, skutterudites are one of the most researched thermoelectric materials of the last decade^[178]. Occurring naturally in CoAs_3 type structure (Figure 90), skutterudites are formed by transition metals (TM) (Co, Rh, iridium (Ir)) and group V elements (Phosphorus (P), As, Sb). Among the choices, Rh (0.0007 ppm) and Ir (0.0004 ppm) are two of the rarest elements on the earth's crust^[171], leaving Co and Sb as the pair with the smallest electronegativity difference (0.17). Small electronegativity difference (≤ 0.3) gives covalent bonds between elements, which improves the electrical transport properties, namely large electrical conductivity is possible due to high carrier mobility^[133]. Original skutterudite, CoSb_3 , has high power factor but also

relatively high thermal conductivity (10 W/m K) ^[179]. The conduction and valence bands near the Fermi level are derived from the hybridized combination of TM 3*d*-states and pnictogen (group V elements) *p*-states ^[180]. The interactions between *d* and *p*-orbitals lead to non-bonding orbitals ^[181, 182]. The non-bonding orbitals in molecular orbital theory are equivalent to lone pairs in Lewis structure. These states have little overlap with the *d*-orbitals of the neighboring TM sites, which results in low dispersion curve near the Fermi energy and a high effective mass ^[183, 184], thus giving a large Seebeck coefficient. The relatively large lattice thermal conductivity of the compound can be suppressed by partially filling the voids in the structure with heavy small ions that produce large disorder for phonon scattering. The filler element should satisfy the electronegativity (χ) relation to Sb ($\chi_{\text{Sb}} - \chi_{\text{filler}} > 0.8$) ^[185]. These filler atoms essentially form loose bonds with Sb atoms and their displacement parameter is responsible for the reduction of the lattice thermal conductivity. Yb has been shown to be a successful filler element, with thermal conductivity reduced to nearly 2 W/m.K ^[186]. Other substitutions can be La, cesium (Ce) or more abundant barium (Ba) ^[187, 188].

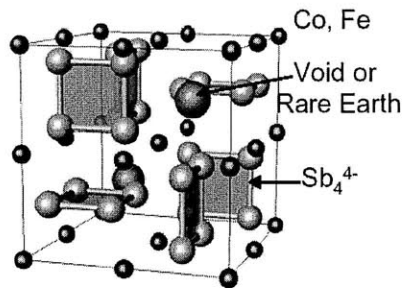


Figure 90: Yb₁₄MnSb₁₁ – crystal structure (www.thermoelectrics.caltech.edu/thermoelectrics/index.html)

Recent advances in the material development have been looking at multiple elements as filler in the voids. A combination of alkaline earth and rare-earth elements as fillers is better for thermal conductivity suppression as they have different masses and different vibrational frequencies to scatter wide range of phonons ^[147, 189, 190]. Skutterudite development is at the stage of research where it has a good potential of industrial production and application as both n- and p-type legs can be obtained with good *ZT* at high temperature by changing the filler ions and TM doping. In terms of the abundance of elements used in making common skutterudite, Sb (0.2 ppm) is the least abundant on the Earth's crust. Even though it is not a rare element such as Te, increased demand, usage in new emerging technology other than thermoelectrics, and a single country production monopoly (China) may limit the market size and its sustainability.

5.2.2. Clathrate

Clathrates are one of the best examples of phonon-glass materials in thermoelectrics, as they have shown thermal conductivity trend similar to that of glass (SiO_2), with measured values below 0.5 W/m K ^[191]. These compounds are open framework of tetrahedral coordinate (**Figure 91**) of group IV semiconductor/metalloids (Si, Ge, Sn) as host atoms with “guest” atoms from group I (sodium (Na), potassium (K)) and II (strontium (Sr), Ba) that are encapsulated in two different polyhedral cages of the host atoms ^[150, 191]. The loose bond between the guest atoms and the host lattice cage causes vibration of the guest atoms, which interacts with wide range of low frequency phonons causing a flattening of the phonon bands and lowering of the velocity of the phonons that leads to lower lattice thermal conductivity ^[133, 191]. Group IV elements form the host matrix, which contributes to most of the electronic transport properties of the thermoelectric material. The highest ZT for clathrate has been measured for Ge-based material. Instead of Ge, if more abundant Si is used, the thermoelectric properties have been slightly lower ^[192]. This could be primarily due to the fact that Ge is heavier than Si and could contribute to lower thermal conductivity. Sn compounds have slightly lower melting point compared to Ge and Si-based clathrates ^[150]. As mentioned earlier, the high cost of Ge may make these types of thermoelectrics cost prohibitive for any application in the current market scenario.

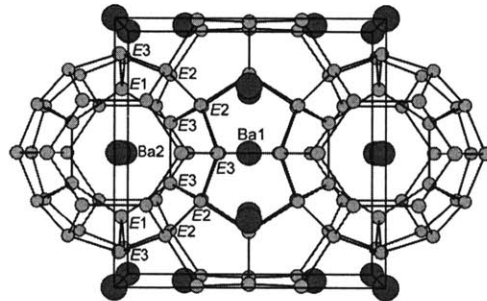


Figure 91: Clathrate structure showing open framework (dark dots), with guest atoms in between [150]

5.2.3. Zintl phase

Another PGEC thermoelectric material that has shown $ZT > 1$ is Zintl phase material ^[47]. It has low thermal conductivity most likely due to structure complexity (limiting the phonon mean-free path) and heavy constituent elements (reducing the fraction of atomic vibrational modes that carry heat efficiently) ^[193, 194]. Zintl phase have elements with relatively large electronegativity difference (0.40) to form anionic and cationic parts. The existence of polyanionic bonds (Sb-chain) is responsible for the complexity of the crystal structure ^[194, 195]. The exceptionally low thermal conductivity $\sim 1 \text{ W/m.K}$ is also due to this ionic nature of the bonds. The tradeoff is that the ionic bond formation leads to relatively poor electrical properties. However, Zintl phase complex structures often have cationic sites (alkaline/heavy elements)

that allow addition of disordered scattering and the tuning of carrier concentration by doping. This allows fine adjustment of the Fermi level, which can enhance the electrical transport properties^[196].

β -Zn₄Sb₃ is another thermoelectric compound with low thermal conductivity at room temperature (0.9-1.1 W/m.K)^[197, 198]. The low thermal conductivity is likely due to highly disordered Zn sites. In the crystalline structure, some Zn atoms occupy interstitial sites that give rise to significant local lattice disorientation to reduce the thermal conductivity^[199]. Sb pairs also form a linear chain in the structure which contributes to large vibration along the chain direction to suppress the thermal conductivity. Ordered Sb framework provides the electron-crystal component of PGEC with decent power factor^[194, 200]. Thermoelectric module level development has been hard due to phase transition around 670 K which changes the thermal and electrical properties, as well its brittle character is also problematic^[199]. Usage of trace Sb and expensive Yb in these Zintl phase compounds may also hinder their utilization in any large-scale thermoelectric systems.

5.2.4. TAGS/LAST

Both of these materials have shown some of the highest ZT s measured for a thermoelectric material (TAGS-75: $ZT = 1.75$ at 700K^[146], AgPb_mSbTe_{2+m}: $ZT = 1.72$ at 700K^[145]). Considerable number of nano-scale domains ~ 10 nm in the samples have been seen which reduces the lattice thermal conductivity due to enhanced grain boundary scattering^[146]. The boundary defects and nano-scale microstructures occur naturally when the material is grown as a bulk. LAST compound is roughly Sb and Ag co-doped PbTe^[145]. These compounds have shown difficulties in handling and stability at high temperatures, and the material properties are highly sensitive to the chemical composition. Due to toxicity of lead-based compounds, usage of TAGS/LAST may be limited for terrestrial applications.

Even though the above mentioned materials have been studied heavily for the past two decades and have consistently shown $ZT > 1$, module development and utilization has not yet been significant. There are challenges of stability and handling. However, the use of some critical elements like Te, Ge and Sb could prevent these materials from scaling. In the next section, we look at some of the more recent earth-abundant thermoelectrics which hold promising potentials.

5.3 Earth-abundant TE material

5.3.1. Half-Heusler

The interest in these inter-metallic compounds as potential thermoelectrics started because of their high melting point, chemical and thermal stability, mechanical sturdiness, non-toxicity and potential low-cost elements ^[152, 185, 201]. Half-Heusler structures are of MgAgAs format (**Figure 92**) and the most promising of all material combination is that of M(=Ti,Zr,Hf)NiSn ^[202-204]. The large Seebeck coefficient in these compounds is primarily due to the TM *d*-orbital, which can induce a large density-of-state (DOS) peak near the Fermi level ^[205]. The energy position of the *d*-orbital induced DOS peaks are element sensitive. The relatively flat band structure near the Fermi level is due to hybridization between *d*-band states of the primary TM (Co/nickel (Ni)) and *d*-band states of neighboring zirconium (Zr)/hafnium (Hf) atoms ^[205, 206]. TiCo(Sn,Sb), NiMn(Ga,Sb,Sn) and NiZrSn are few of the examples of the half-Heusler structures that are being investigated for their thermoelectric properties ^[153, 207]. Currently the limiting *ZT* values are mostly due to high thermal conductivity (5-10 W/m.K) ^[153]. Half-Heusler materials have voids in the crystal structures which can be engineered to decrease the thermal conductivity. The best *ZT* values are for Zr_{0.5}Hf_{0.5}NiSn with *ZT* = 0.5 at 700K ^[153, 154]. Substitution and doping of Ni and Sn with Pd and Sb has given *ZT* ~ 0.8 at 800 K ^[154]. The usage of Sb as dopant is relatively small quantity compared to that in skutterudites or Zintl phase compounds (**Figure 89**). The other constituent elements of half-Heusler compounds are moderately abundant on the Earth's crust.

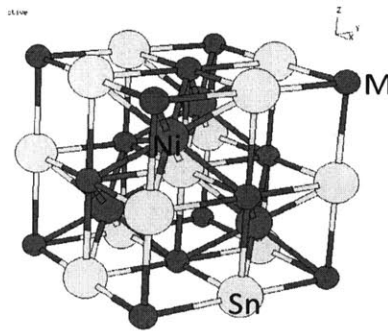


Figure 92: Half-Heusler crystal structure (http://cst-www.nrl.navy.mil/lattice/struck/c1_b.html)

5.3.2. Oxide

The recent discovery of high Seebeck coefficient (100 μ V/K) in NaCo₂O₄ has opened a new direction for search of thermoelectric materials ^[208]. Oxides are very promising thermoelectric materials due to their high temperature stability, high oxidation resistance, and usage of environmentally benign elements ^[209]. The origin of good thermoelectric properties in these TM oxides is due to a large peak in the DOS, which comes from the narrow 3*d*-orbital of the TM at the valence band ^[209]. The relatively large Seebeck value for NaCo₂O₄ is attributed to the spin-induced entropy from the possibility of large degeneracies in

different valence states of Co (i.e. Co^{4+} , Co^{3+})^[210]. These different valence states of Co in the low spin state carry large entropy which is transported by the charge carriers to increase the Seebeck coefficient^[210]. Co-O forms the metallic layer with high carrier mobility and electrical conductivity^[211]. This compound has very high carrier concentration (10^{21} - 10^{22} cm^{-3}). These oxides form a natural two-dimensional layered structure (**Figure 93**), and the reduction in the thermal conductivity (3-4 W/m K) is due to misfit structures of Na ion nanoblock layer between CoO_2 layers^[208, 209]. Substitution of Co with other transition metals (Rh, Ti, and Pd) can reduce thermal conductivity as they act as phonon scattering sites. Ni instead of Co has low electrical conductivity due to small charge carrier density^[212]. SrTiO_3 is another example of a potential good thermoelectric material which is found in layered structure^[156, 213]. High electrical conductivity and high Seebeck coefficient are due to high effective mass, where the band structure is mostly influenced by Ti 3d-orbitals^[214]. This compound has relatively high thermal conductivity of 8 W/m K at room temperature. At higher temperature, the conductivity goes down to 3 W/m K with doping^[215]. Zn-based oxides have good power factors (comparable effective mass to Bi_2Te_3 , PbTe) but very high thermal conductivity ~ 40 W/m.K at room temperature and 5 W/m K at 1000°C ^[216, 217]. Doping with heavier elements can decrease the thermal conductivity but it will also reduce the carrier mobility and the electrical conductivity. Nevertheless, $ZT \sim 0.8$ has been achieved for the oxides, which is comparable to the high-temperature state-of-art thermoelectric material (SiGe) but without using expensive and scarce materials. The constituent elements of the oxide-based thermoelectrics are some of the most abundant crustal elements such as Na, Zn, Ti and Sr.

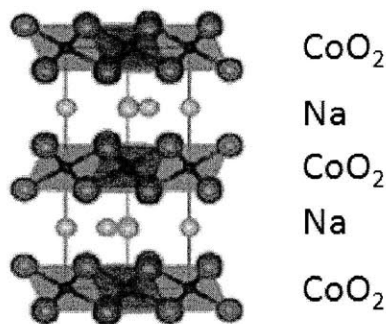


Figure 93: $\text{Na}_x\text{Co}_2\text{O}_4$ - crystal structure (<http://physicsworld.com/cws/article/news/17531>)

5.3.3. Silicide

Another interesting and benign compound as potential thermoelectric material is metal silicide, which was initially studied in the late 1950's^[218]. Most heavy metal silicides are mechanically and chemically stable Nowotny chimney-ladder compounds (**Figure 94**)^[218]. The good Seebeck coefficient (150-200 $\mu\text{V}/\text{K}$) can

be associated with the *d*-band states of TM in materials such as FeSi₂ and MnSi_x [181, 219, 220]. Other silicides: Ru₂Si₃, Ru₂Ge₃, and Os₂Si₃ are also semiconductors with narrow band gap and could potentially have good thermoelectric properties [221], especially Ru₂Si₃ can potentially be better than SiGe at high temperature but the main difficulty has been finding suitable dopants for optimum doping [221]. However, the material choices in these examples are few of the rarest elements in the Earth's crust. A potential problem with alkali/alkaline earth silicides (Mg₂Si, Ca₂Si, and Sr₂Si) is their chemical reactivity and low melting point. Tertiary compounds based on magnesium silicide have recently shown great promise as thermoelectric material with $ZT \sim 1$. Bi doped Mg₂Si_{0.6}Ge_{0.4} was reported with measured $ZT \sim 1$ at 800 K [222]. The most favorable system till now has been Mg₂Si_{0.4-x}Sn_{0.6}Sb_x with measured $ZT \sim 1.1$ at 800 K [132]. High ZT has been due to low thermal conductivity given by the maximum mass difference between components [132]. Utilization of Ge and Sb in both of these compounds limits the abundance of this material. However, the average weight percentage usage of these trace elements (as dopants) is lower than that in clathrates and skutterudites (Figure 89). Some of the metal silicides, even though they have small ZT s (FeSi₂: n-type ~ 0.4 ; p-type ~ 0.2 [218]), could be very useful as they make very inexpensive thermoelectric materials.

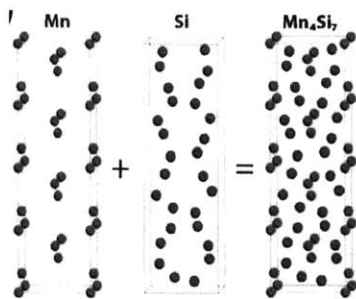


Figure 94: MnSi – crystal structure (Nowotny-chimney ladder) [223]

5.4 Guidelines for good thermoelectrics

There are some general observations that are used as guides for looking at elements and compounds, which could give good ZT . These “selection criteria” [224-226] lead to either lower thermal conductivity or higher power factor ($S^2\sigma$) necessary to increase ZT . The well known criteria to have good thermoelectric materials are listed below [224-226].

- Optimum carrier concentration in the range of 10^{19} - 10^{20} cm⁻³ is needed in order to maximize the power factor, leading to usage of mostly semiconductor based material for thermoelectrics.

- Most thermoelectric materials have covalent bonds (i.e. elements with low electronegativity difference) and high atomic co-ordination, which gives large electrical conductivity due to high carrier mobility ^[133].
- Heavy elements make good thermoelectric material as large atomic mass contributes to low lattice thermal conductivity ^[133, 224, 225]. Ge, Sn, Sb, Te, Pb, Bi, As, and Se are the heaviest stable elements that show semiconductor/semi-metal properties (i.e. group IV, V and VI) ^[224]. Within the above listed elements, many are toxic (Pb, As) and less abundant on the crust (Te, Sb, Ge). Elements such as tin, zinc, strontium, hafnium and zirconium are earth-abundant heavy elements (atomic weight > 50) which may be utilized to make good thermoelectrics.
- Alloys with atoms of similar electric potentials but different masses can scatter phonons more effectively, where scattering is due to difference in mass and/or bond stiffness.
- Large number of valleys in the band structure gives rise to a higher effective mass and a large change in the DOS near the Fermi level, giving high Seebeck coefficient ^[133].

On the basis of the materials discussed in this work, we can add several more observations in this guideline for good thermoelectrics:

- Complex/open cage structure can give very low lattice thermal conductivity. Structures with large empty cage where ‘fillers/guest’ atoms are introduced can scatter acoustic phonons as these atoms have large atomic displacement parameter (ADP), which is interpreted as the rattling effect causing decrease in the lattice thermal conductivity. ADP is the measure of the mean-square displacement amplitude of an atom about its equilibrium lattice site ^[133, 194]. In skutterudite, Sb is an important element in making this type of cage structure where as in clathrates; Ge or Si form the host matrix. In terms of abundance, Si will be an ideal choice for making earth-abundant thermoelectrics.
- Use of transition metals with partially-filled *d*-band states can give high Seebeck coefficient even for large carrier concentration ^[227], due to low dispersion curve near the Fermi energy and a high effective mass ^[184]. Earth-abundant transition metals such as manganese, iron, nickel, zirconium and scandium could provide benefits of partially filled *d*-band for high thermoelectric performance.

Most bulk thermoelectric materials discussed above have good TE properties, and they follow one or more of the guidelines mentioned above.

The primary material found in today’s commercial thermoelectric modules is Bi₂Te₃, which has the highest $ZT_{material} \sim 1$ at 350 K. As a generator, these modules can be used primarily with a low grade heat for waste heat recovery applications. The current limitation in the availability of other material options as

modules is mainly due to low module performance and low ZT . As the material ZT and the module performance are improved, and new applications are explored, the demand for the modules will also rise. If we look at the earth-abundant thermoelectric materials (i.e. lower right-hand side materials in **Figure 89**), they hold the promise of potential high thermoelectric performance without the risk of material scarcity. The annual production of some of the key elements such as Na (200 kilo tons), Co (17 kilo tons), Zn (12.5 mega tons), Al (30 mega tons), Zr (7 kilo tons), Ni (1.3 mega tons), Sn (165 kilo tons), Mg (350 kilo tons), Si (3.88 mega tons), Sr (137 kilo tons), and Ti (99 kilo tons) is very high ^[137]. The reserve base, which is the pre-determined/known economically viable concentration for mining, for these elements is also high, as these are mostly high crustal abundant elements ^[169]. Even though the current ZT for these material is low compared to most high ZT thermoelectrics (i.e. skutterudites, clathrates, LAST, and TAGS), new material development technology such as nanostructuring and nanocomposite synthesis can potentially enhance the performance without changing the key constituent elements ^[144, 228]. Such technological improvement will be a key factor in developing thermoelectric materials with earth-abundant constituents for high volume applications.

The research for high ZT thermoelectrics has been driven mostly by engineering the thermal properties of the materials. Both the lattice vibration and the electron movement contribute to the thermal conductivity for a material ^[36]. If we reduce electron movement to suppress thermal transfer, electrical conductivity goes down, which decreases ZT . In bulk (non-metal) material, the lattice contribution is dominant, and people have looked at various ways of suppressing phonon contribution to the thermal conductivity such as by using nano particles which would break the path of phonon transport ^[45, 229-232]. Using superlattice structures, the interface can be used to scatter phonons. These scattering structures can have very small effect on the mobility of high energy electrons mostly due to difference in mean free path for electrons and phonons ^[230]. Apart from decreasing thermal conductivity, many studies are being done to increase the Seebeck coefficient and the thermoelectric power factor using techniques such as electron filtering ^[42, 44]. For potential large volume applications such as solar thermoelectrics, can we engineer a TE material made from earth-abundant and non-toxic material to give good thermoelectric properties? In this research, we have looked at a novel TE material where the ZT could be enhanced by mechanisms such as electron filtering, and thermal conductivity suppression using interface scattering. They are metal-semiconductor superlattice structure of Hafnium (Hf)/Zirconium (Zr) nitride and Scandium nitride (ScN). The following section introduces the material and describes an experimental setup developed during this research to characterize new TE material with high temperature measurement capabilities. Measurement results of the thermoelectric properties are shown and discussed at the end.

5.5 Metal-Semiconductor superlattice

Alloyed metal-semiconductor superlattice structures have been studied as a candidate for thermoelectric material because of their potential to simultaneously reduce lattice thermal conductivity using interface scattering and enhance thermopower factor using energy-dependent electron filtering ^[44, 233, 234]. The material system of Hafnium/Zirconium nitride ((Hf, Zr) N) – Scandium nitride (ScN) has been studied in this research. These are both physically and chemically stable materials for a large temperature range with melting point > 2500°C. ScN is a rock-salt (face-centered cubic) structure transition metal nitride semiconductor with a direct bandgap of 2.15 eV and an indirect gap of 0.9 eV ^[235]. The conduction and the valance bands for ScN are based on mostly *d*-states of the transition metal. The overlap with the *p*-state of nitrogen determines the effective mass for the nitrides. Transition metal nitrides such as HfN and ZrN have conductivity similar to that of a bulk metal (15-50 $\mu\Omega$ -cm). They are well known for their outstanding physical properties including high hardness and mechanical strength. ZrN and HfN have similar band structures and both are metallic in nature ^[236]. ScN and HfN have same rock-salt crystal structure and similar lattice constants, allowing epitaxial growth. For ZrN, there is ~ 1.5% lattice mismatch with ScN ^[236]. All the constituent elements i.e. Hf, Zr and Sc are relatively heavy elements (atomic weight > 45) as well as earth-abundant. The crustal distribution of Zr is larger than that of zinc and both Sc and Hf are comparable to tin.

As mentioned in Chapter 1, metals are not considered good thermoelectrics because of low Seebeck coefficient, and this is due to the fact that the Fermi energy for a metal is deep inside the conduction band. The contribution of electrons of different energies to the conduction process is symmetric with respect to the Fermi energy ^[235]. By introducing a tall barrier inside a metal, the hot electrons (i.e. high-energy particles) can be filtered contributing to the conduction process and increasing the overall entropy transport and thus the Seebeck coefficient (**Figure 95**) through solid state thermionic transport. Relatively large electrical conductivity can still be maintained with high carrier density at the metal layers of the material. Utilizing this concept, a metal-semiconductor structure can have a potential of large thermopower. With a moderate band gap, ScN can be utilized for controlling the Schottky barrier height for electron filtering to tune the Seebeck coefficient. With superlattice structure, the interface can support phonon scattering to decrease the thermal conductivity as well, increasing the overall *ZT* value. The scattering of phonons could be due to acoustic mismatch or defect scattering of phonons at the interface. The lattice thermal conductivity of ScN is larger than the other two nitrides ^[236]. Since ScN is semiconducting in nature, its lattice thermal conductivity should be roughly equal to the total conductivity

as the electronic contribution will be very small. As we will see from the measurement results, at higher temperature, the electronic contribution mostly from the metallic nitride does come into play for these metal-semiconductor superlattice structures.

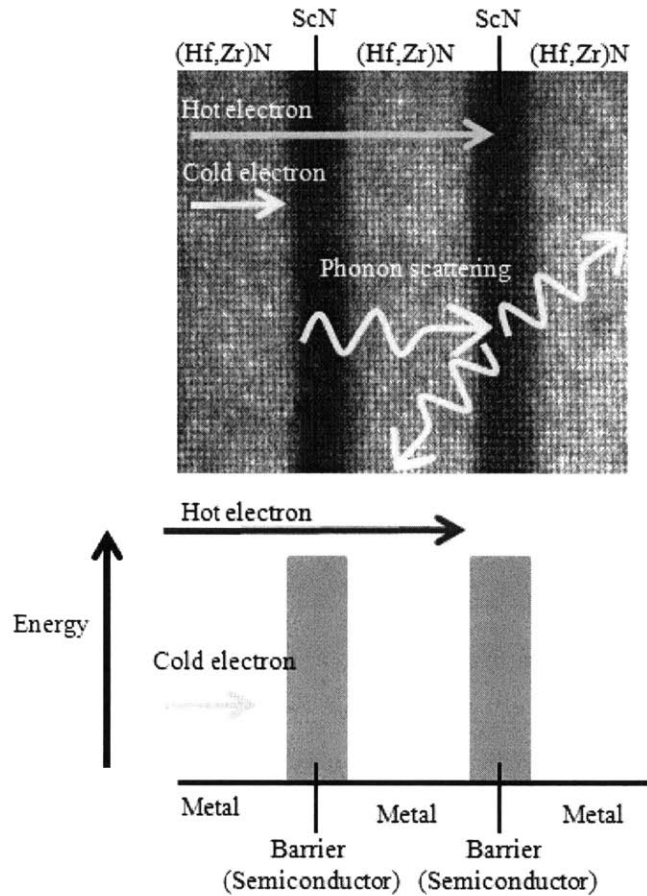


Figure 95: Pictorial depiction of electron filtering in metal-semiconductor superlattice structure with phonon scattering at the interface

The theoretical estimation using Boltzmann transport-based model for such a metal-semiconductor superlattice structure was presented in Ref. [233]. The potential of high ZT (> 2) (Figure 96) even at relatively moderate temperature such as 500 K makes this material very interesting for further development. The thermoelectric properties can be engineered to give high ZT by controlling factors such as the barrier height whose dependence is shown in the following plots.

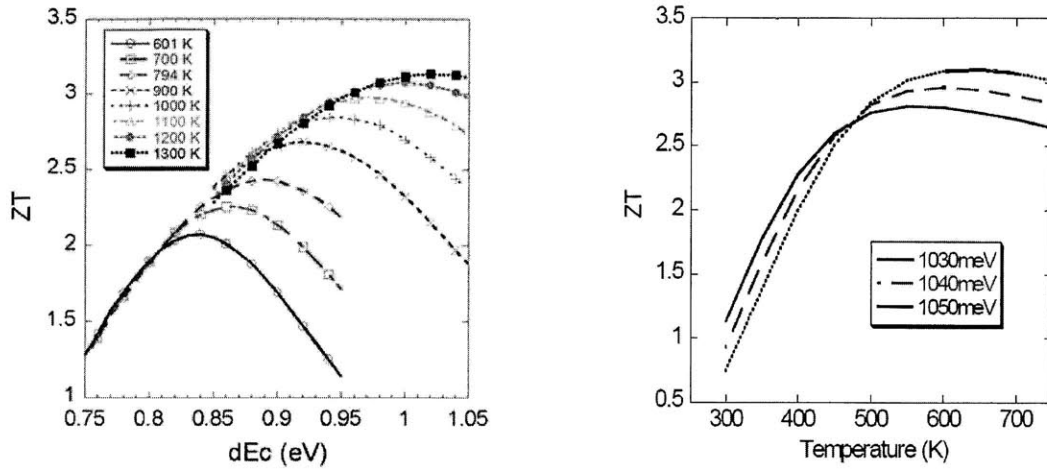


Figure 96: Theoretical estimation for ZT vs. conduction band edge for ZrN/ScN ^[233]; Theoretical estimation for ZT for 6 nm HfN/ 6 nm ScN multilayer structures with different conduction band offset

For a metal-semiconductor nitride superlattice structure of ZrN/ScN , a room temperature Seebeck coefficient of $820 \mu V/K$ has been extracted from a Seebeck voltage transient measurement and a thermal imaging technique ^[233]. The large Seebeck coefficient indicates enhancement due to electron filtering for these superlattice structures. The electrical resistance measurement using the four-wire method gave the electrical conductivity which was less than $0.25 (\Omega\text{-cm})^{-1}$. The theoretical fit for the electrical conductivity data resulted in an effective barrier height of 280 meV. A relatively small thermal conductivity of 5.25 W/m.K has been measured for the epitaxial superlattice multilayer of ZrN/ScN , which was $\sim 2.7x$ smaller than the mean of the thermal conductivities of the constituent materials ^[234]. Due to low electrical conductivity, the effective ZT at room temperature for this sample was ~ 0.001 . The low electrical conductivity was attributed to the barrier height being too large. The barrier height can be adjusted by alloying or by varying the concentration of nitrogen in the metal layer. Alloying ZrN with WN reduces the lattice mismatch which resulted in the reduced thermal conductivity of 2 W/m.K ^[234]. The thermal conductivity of the multilayer was measured using the time-domain thermoreflectance technique. In the samples studied in this research, combination of Zr and Hf were used to try and optimize for maximum thermopower.

Sample fabrication and processing was done at Purdue University. Ref. [237] describes the material and the fabrication technique in detail. Material optimization and TE properties characterizations are still in progress. Here we report the preliminary result for these novel materials using a measurement setup developed during this research. First experimental result for temperature dependent Seebeck coefficient

was obtained using the setup. Electrical conductivity measurements helped in understanding the effects of parasitics and provided an overall direction to get higher performance.

5.6 Z-meter

The TE parameters (σ , S and κ) are temperature dependent and are typically measured independently with a small temperature gradient ($\Delta T \sim 1$ or 2 K) ^[238]. However, to properly estimate a thermoelectric generator's performance, it is desirable to characterize the elements with a large temperature gradient. Conventionally, the TE parameters are measured using different measurement tools and different sample geometries. ZT values obtained from such characterization can have high uncertainty, not only due to measurement errors but also due to sample variability ^[239]. The van der Pauw's method is a common technique to measure the electrical conductivity of an arbitrarily shaped sample ^[240, 241]. This four-point probe technique requires that the sample be approximately two-dimensional to get accurate results ^[240]. The standard way of measuring the Seebeck coefficient is by fixing a small temperature gradient across a TE sample and varying the average temperature ^[239]. At each temperature, the ratio of the open circuit voltage to the temperature gradient gives the Seebeck coefficient. Thermal diffusivity measurement technique is widely used to measure material's thermal conductivity ^[239, 242]. Accurate specific heat data is required simultaneously with the thermal diffusivity value to obtain thermal conductivity from this method ^[239]. Apart from individual parameter measurement and ZT evaluation, another convectional method to extract ZT directly is the transient Harman technique ^[243, 244]. Adiabatic boundary conditions are required for this method, and only a small temperature difference across the sample can be applied during the measurement ^[243, 244]. Many variants of this technique have been used to measure properties of TE samples ^[157, 245].

In this work, we present an experimental DC measurement technique with a Z-meter to measure the TE properties of a material under practical working conditions of a generator i.e. with a large temperature gradient (~ 200 K), for a wide range of average sample temperatures. Simultaneous measurements are used to extract all three TE properties to determine the ZT values. Apart from ZT , the measurement also gives the power density for a single TE element, which can be crucial information for material optimization and generator design, especially for waste heat recovery application where power density is more important than maximizing efficiency. The advantage of this Z-meter measurement over other techniques is that it can give all three TE parameters from a single sample simultaneously as well as the power density and efficiency values. Some of the key aspects of previous work on the Z-meter are

summarized in **Table 20**. The systems described in previous work have mostly been for macroscopic sample (> 1 mm) characterization. When it comes to short-leg and thin-film samples, there are no Z-meter setups that can give accurate results with high temperature (> 500 K) measurement capabilities. We have adopted a variant of the Z-meter setup described in Ref. [246] and improved on its parasitic performance as well as worked on making it a flexible system for various temperature ranges. Here, we present a Z-meter system which is used to characterize thin-film TE samples ($\sim 100\text{s } \mu\text{m}$) as well as thick bulk materials. When measuring thin-film samples, the system parasitic become very important; they have been addressed in this setup to minimize errors. Even for a macroscopic TE sample (thickness ~ 1.5 mm) used in commercial modules, the internal resistance for a single leg can be as low as 10-15 m Ω . Any device characterization technique has to accurately measure such small resistances. Both intrinsic thermal and electrical resistances for TE samples decrease with thickness, and the system parasitics would become dominant in such measurements. The Z-meter described in Ref. [247] can measure the TE properties in the range of 100-600 $^{\circ}\text{C}$, but each parameter is measured under different temperature gradient conditions. Some Z-meters are limited in the lowest possible resistance measurement (30 m Ω), and thus limit the electrical conductivity measurements due to high system parasitic [248]. High temperature electrical resistivity and Seebeck coefficient measurement setup is described in Ref. [249], where the maximum temperature gradient is limited to 20 K. A commercial Z-meter from RMT Ltd. is used to characterize TE modules and is not meant for single TE element characterization [250]. The experimental setup described in Ref. [251] shows measurement under large temperature gradient (160 $^{\circ}\text{C}$) for hot side temperature up to 200 $^{\circ}\text{C}$. In that work, rather than characterizing the system parasitics to get actual material TE parameters, effective ZT values were measured with lumped parasitics.

5.6.1. Experimental setup

The Z-meter setup (**Figure 97**, **Figure 98**) includes a high temperature heater with a measure bar and a water-chilled cold plate inside a vacuum system. A 1" diameter ceramic 'button' style heater enclosed in a molybdenum radiation shield can heat the sample to a very high temperature of 1200 $^{\circ}\text{C}$. The heater is controlled with a proportional-integral-derivative (PID) temperature controller (Heat Wave Labs) to maintain the hot side temperature within an absolute accuracy of 1 $^{\circ}\text{C}$ of the set value. The measure bar stands on top of an aluminum-based cold plate connected to a water chiller outside the vacuum chamber through appropriate feed-through. The water was maintained at 20 $^{\circ}\text{C}$ during all experiments. A small conical shaped Cu metal piece is used between the heater and a TE sample to compensate for the area difference between the two pieces; it also acts as a holder for thermocouple and electrical contacts for the hot side. A copper measure bar embedded with type-K thermocouples sits below the sample. The

thermocouples are set in small holes drilled in the metal pieces with high temperature thermal cement to ensure good contact as well as to electrically insulate them from the metal and the sample. Two thermocouples are placed within 1 mm of the metal-thermoelectric interface to measure the hot and the cold side temperatures. The temperature is assumed to drop linearly in the sample so that the average sample temperature is the mean of the hot and the cold side temperature. In most cases of interest, particularly for thin-film samples, the linear temperature drop is a reasonable assumption ^[246]. Averaging the TE parameters for the mean temperature generates effective values which are reasonably close (< 3% error for the elements we tested) to the properties measured at absolute temperature.

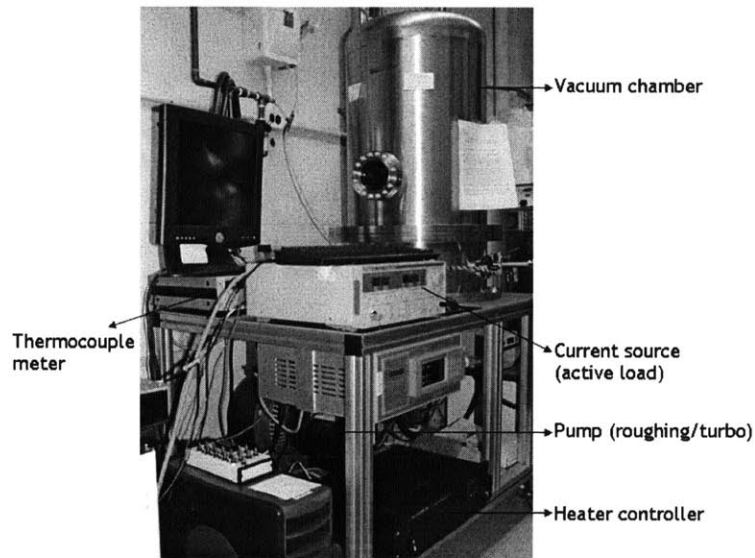


Figure 97: Z-meter schematic showing a picture of the vacuum chamber within which the measure bar setup is held for high temperature experiments

TE measurement approaches	Ref.	Heater temperature (max)	Hot side TE temperature	Temperature gradient	Thermal/electrical parasitic	Heat flux measurement technique	Electrical resistivity measurement
Classical arrangement	[247]	600°C	*600°C (close agreement till 350°C)	<ul style="list-style-type: none"> ▪ $\Delta T \sim 10^\circ\text{C}$ (thermal conductivity) ▪ $\Delta T \sim 100^\circ\text{C}$ (Seebeck coefficient) 	-	Pyrometer used to measure heat flux through the sample	Current/voltage measurement (at zero temperature gradient)
Transient Z-meter (no vacuum)	[252]		*700°C (good agreement till 300°C)		-	Heat flow meter used to measure thermal flux	Square wave current input, voltage measurement
Graded TE measurement setup	[248]	800-900°C		$\Delta T = 385^\circ\text{C}$ (TE couple)	Indium solder: <ul style="list-style-type: none"> ▪ $0.5 \text{ K cm}^2/\text{W}$ ▪ $\sim 30 \text{ m}\Omega$ (Contact resistance variability)	Reference material (Ni) measure bar setup	Variable load resistor circuit
Effective ZT measurement	[251]		200°C	$\Delta T = 160^\circ\text{C}$	-	Flux sensor used to measure thermal power	Current/voltage (4-wire) ac method
Commercial Z-meter (Module level testing)	[250]		110°C	$\Delta T = 65\text{-}75^\circ\text{C}$	-	No thermal conductivity measurement	AC resistance measurement
This work (Measurements done on both bulk and thin samples)		1200°C	440°C	$\Delta T = 255^\circ\text{C}$	Dry metal contact: <ul style="list-style-type: none"> ▪ $1.5 \text{ K cm}^2/\text{W}; 7 \text{ m}\Omega$ Bonded metal contact: <ul style="list-style-type: none"> ▪ $0.05 \text{ K cm}^2/\text{W}; 3 \text{ m}\Omega$ (Strain gauge used to maintain reliable contact)	Au-plated Cu measure bar	Current/voltage (4-wire) active load measurement (Maximum power detection)

Table 20: Summary of previous Z-meter measurement for TE characterization

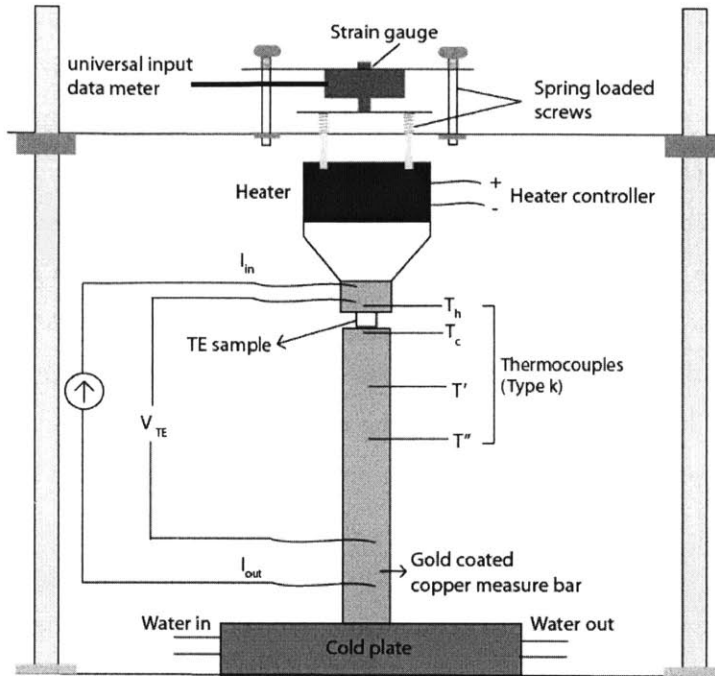


Figure 98: Schematic of a Z-meter setup inside a vacuum chamber

Once the TE sample is placed between the measure bar and the heater, a set of spring loaded screws are used to set and maintain high pressure (~ 800 psi) for good contact. In order to ensure repeatable contacts, a piezoelectric strain gauge (Omega Engineering Inc.) is used to measure the pressure on the sample (Figure 99).

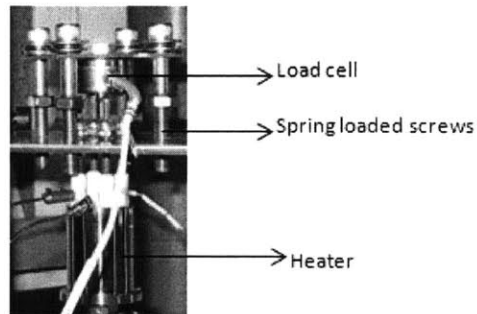


Figure 99: Strain gauge on top of the Z-meter ensures low and reproducible thermal and electrical contact parasitics

5.6.2. Measurement parameters

The measured parameters during the experiment are the open circuit voltage ($V_{oc} = V_{TE}$ at $I = 0$), the voltage across the TE sample (V_{TE}) for various input currents (I), and temperature at different points using type-K thermocouples. At each temperature setting, for each input current value, averaging the data points for voltage and thermocouple readings minimizes noise and quantization errors. A fully automated data collection system allows for a quick measurement even with long averaging.

For the thermal conductivity measurement of a single TE element, the thermal power (Q) through the measure bar is equal to the power through the sample (approximate one-dimensional heat flow). Two potential sources of errors in this measurement are due to convection and radiation. The experiment was performed in a vacuum environment (pressure $\sim 1 \mu\text{Torr}$) such that any convection loss through the side walls and air conduction can be neglected. The thermal conductivity for air at such low pressure is nearly four orders of magnitude lower than at room pressure ($3 \times 10^{-6} \text{ W/m.K}$). The error due to radiation at high temperature is suppressed with low emissivity gold plated measure bar. More details on radiation suppression are discussed in Section 5.3.3. The cross-section area of the measure bar is chosen such that the spreading resistance between the sample and the metal is negligible. The electrical wire contacts are held away from the thermocouples (**Figure 98**) to minimize any heat conduction loss from the wires. Long length wires and thermal shielding in thermocouples are used to minimize any heat loss through them. For each measurement, two values of thermal power are obtained by combination of three thermocouples in the measure bar. Less than a 3% difference in the input thermal power reading between the thermocouples in the measure bar ensures that the measurement is close to 1-D approximation. Another possible source of error in the measurement is due to the sample-metal interface in the setup, which causes a temperature difference between the thermocouple measuring the hot (T_h) (or cold (T_c)) side and the actual sample (T'_h/T'_c). Different interface thermal resistances ($R_{th,interface}$) have been studied in Ref. [246], these are used here as a correction factor to estimate the actual temperature gradient across the sample. The heat flow through the sample and the measure bar can be depicted with a thermal equivalent circuit as shown in **Figure 100**.

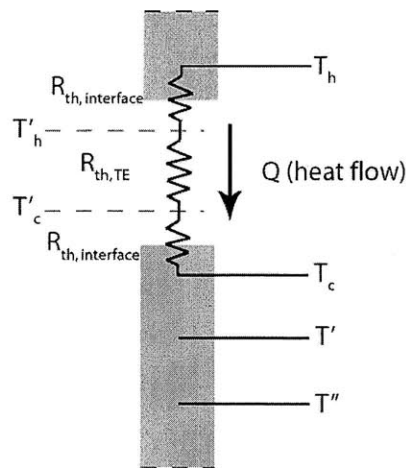


Figure 100: Thermal equivalent circuit showing interface resistances and heat flow through the sample to the measure bar

The thermal conductivity for a TE sample of cross-section area A_{TE} , and thickness l_{TE} , is given by:

$$\kappa_{TE} = \frac{Q}{T'_h - T'_c} \left(\frac{l_{TE}}{A_{TE}} \right) \quad (30)$$

Where,

$$T'_h = T_h - Q \times R_{th,interface} \quad (31)$$

$$T'_c = T_c + Q \times R_{th,interface} \quad (32)$$

$$Q = \left(\frac{A_{mb}}{l_{mb}} \right) \kappa_{mb} (T' - T'') \quad (33)$$

Here, A_{mb} is the cross-section area of the measure bar, l_{mb} is the distance between the adjacent thermocouples in the measure bar (2 cm), and κ_{mb} is the thermal conductivity of the measure bar (copper = 391 W/m K). T' and T'' are the temperatures recorded by type-K thermocouples in the measure bar.

The Seebeck coefficient is measured as the ratio of the open circuit voltage ($V_{oc} = V_{TE}$ at $I = 0$) and the temperature gradient ($T'_h - T'_c$) across the sample.

$$S = \frac{V_{oc}}{T'_h - T'_c} \quad (34)$$

A four-wire DC electrical measurement setup (**Figure 101 a**) is used to compute the resistance and the output electrical power of the sample. For a fixed temperature gradient, as the input current (I) through an external power supply is changed, the voltage (V_{TE}) across the TE sample is measured with the wire contacts. Sweeping the current across the sample and measuring the voltage provides us with the capability of having an active load equivalent across the sample. The advantage of this technique is simple circuitry and lower parasitic. The four-wire measurement eliminates the parasitic due to electric wires. Initially, an active load based on low resistance power FET transistor was used for electrical measurements (**Figure 101 b**), similar to the one described in Ref. [246]. The electrical parasitic resistances for both approaches were compared and the initial method has lower system parasitic, which is essential to measure very small resistances of short-leg or thin-film TE samples **Figure 102**.

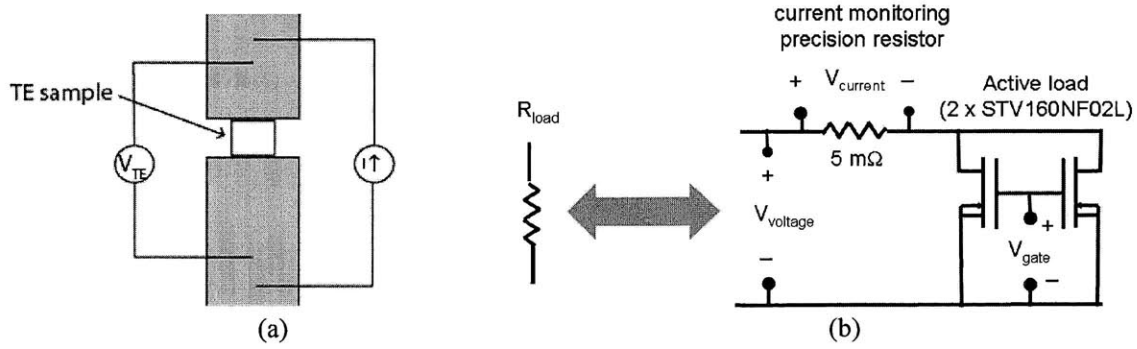


Figure 101: (a) Active load for electrical resistivity and power measurement with current input setup, (b) Active load using low resistance power FET circuitry

Dry metal-metal interface resistance between the sample and the measure bar was measured using TE samples of a same material but different thicknesses. Matched load resistance for different thickness samples with a linear fit shows the setup parasitic at zero length to be 7 mΩ for current source setup and 14 mΩ for the power FET circuit (Figure 102).

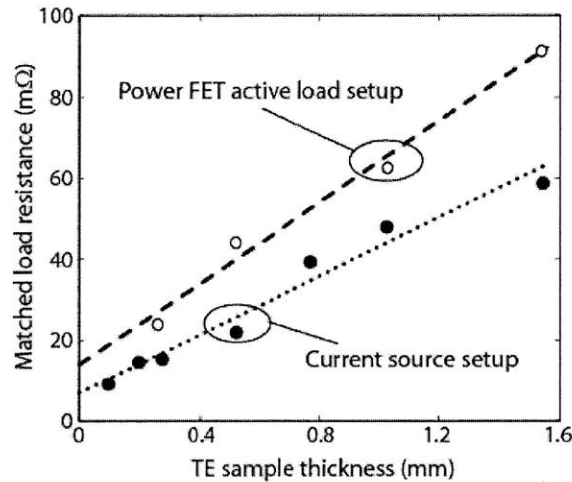


Figure 102: Matched load resistance (○, ●) vs. thickness of MAM-Bi₂Te₃ samples to evaluate dry metal-metal contact parasitic, with a linear fit (----,) for power FET active load system and current source setup

In the power generation mode, the maximum output power is measured when the load resistance is equal to the sum of the internal resistance of the TE sample and the electrical parasitics (Figure 103). From this matched load (R_{Load}), the electrical conductivity of the sample can be obtained using the following relation.

$$\sigma = \frac{1}{(R_{Load} - R_{parasitic})} \left(\frac{l_{TE}}{A_{TE}} \right) \quad (35)$$

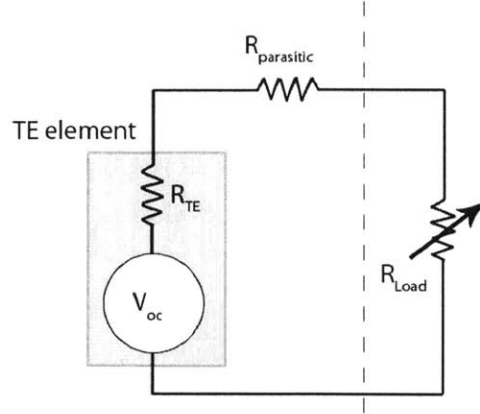


Figure 103: Equivalent electrical circuit depicting TE sample and system parasitics at maximum power condition with load matching

For all the measurements performed using this setup, the electrical resistance for a single TE leg is generally small. The input current density is within the limit such that any Joule heating term is negligible to have any observable effect on the overall average temperature of the sample. The temperature recorded during current sweep showed fluctuation of less than 0.5°C for the hot and the cold side thermocouple reading.

The power density and the efficiency (η) are given by:

$$PD = \frac{(IV_{TE})_{\max}}{A_{TE}} \quad (36)$$

$$\eta = \frac{(IV_{TE})_{\max}}{Q} \quad (37)$$

For the matched load condition, where the output power is maximized, the power density increases as the thickness of the TE leg is decreased, which is why thin-film TE generators are expected to have high power density.

5.6.3. Thermal radiation suppression

In this Z-meter setup, the results rely on the fact that the thermal power through the sample is transferred to the copper measure bar via conduction (i.e. 1-D heat flow). The overall output electrical power for a single TE leg is very small to be negligible for this purpose. As mentioned earlier, the convective heat loss through the sample and the measure bar is eliminated by performing the experiment in μ Torr pressure range inside a vacuum chamber. As the hot side temperature is raised, the radiative heat transfer

from the heater to the measure bar will decrease the measurement accuracy. In order to estimate the radiation error, a model for the parasitic radiative heat transfer from the heater to the measure bar is developed and experimentally validated. The radiated power is calculated from the Stefan-Boltzmann law using a geometrical setup as shown in **Figure 104** to represent the heater and the measure bar. Radiation from the side walls of the hot side is suppressed by thermal shielding. Thus only the bottom cross-section area of the heater is exposed for radiation loss.

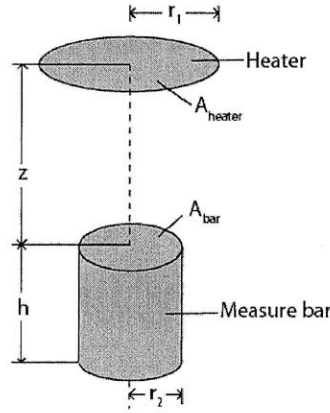


Figure 104: Schematic for radiation error calculation from the measure bar due to the heater

The total power radiated from the heater to the measure bar (q_1) is given by Equation 31, where A_{heater} is the cross-section area of the heater, ε_{heater} is the emissivity, T_{heater} is the temperature of the heater, σ_{sb} is the Stefan-Boltzmann constant, and F_{12} is view factor which depends on the geometry of the heater and the bar ^[253]:

$$q_1 = A_{heater} \varepsilon_{heater} T_{heater}^4 \sigma_{sb} F_{12} \quad (38)$$

Similarly, the power re-radiated by the top surface of the measure bar (q_2) is given by Equation 39, where A_{bar} is the cross-section area of the measure bar, ε_{bar} is the emissivity, and T_{bar} is the temperature of the measure bar.

$$q_2 = A_{bar} \varepsilon_{bar} T_{bar}^4 \sigma_{sb} F_{21} \quad (39)$$

The total power transferred from the heater to the measure bar (q_3) is:

$$q_3 = q_1 - q_2 \varepsilon_{heater} \quad (40)$$

And, the total power absorbed by the surface of the measure bar due to radiation from the heater (q_4) is:

$$q_4 = q_3 \varepsilon_{bar} \quad (41)$$

For this particular geometrical setup of a cylinder and a disk, the view factor (F_{12}) is given by ^[254]:

$$F_{12} = \frac{1}{2} \left(x - \sqrt{x^2 - 4 \left(\frac{R_2}{R_1} \right)^2} \right), \text{ where } R_i = \frac{r_i}{z} \text{ and } x = 1 + \frac{1 + R_2^2}{R_1^2} \quad (42)$$

$$F_{21} = \frac{A_{heater} \times F_{12}}{A_{bar}} \quad (43)$$

Here, r_1 and r_2 are the radii of the heater and the measure bar respectively.

This analysis is based on the grey body assumption, where the emissivity is independent of the wavelength of the thermal radiation. In vacuum condition, the radiative power was measured for different heater temperature at various gaps between the measure bar and the heater. The experimental data in **Figure 105** closely follows the theoretical estimation based on the above discussed relations. The parasitic radiative heat transfer is suppressed by gold coating the copper measure bar which reduces the emissivity from 0.54 for copper to 0.09 for gold. This modified apparatus suppresses radiative transfer 20-fold relative to the blackbody limit (**Figure 105**).

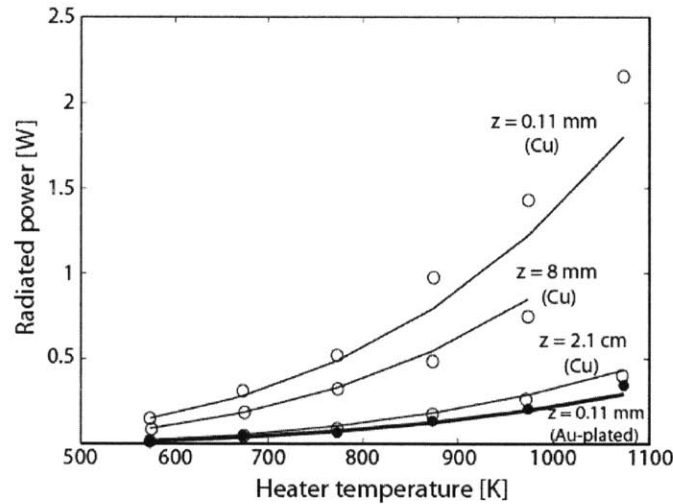


Figure 105: Radiated power measured for copper (o) and gold-plated (●) measure bars at different heater temperatures and under different gap (z) conditions follow close to the theoretical prediction (solid lines)

Using such radiation suppressed measure bar setup, high temperature accurate thermal measurements of TE samples can be done, as shown in the results in the next section.

5.6.4. System validation

Before testing novel TE materials, the system was validated by measuring three different samples which had been previously measured with other techniques mentioned at the beginning of this section. The samples were obtained from different research groups/collaborators, and measurements were done using the Z-meter setup (Table 21). Two of the samples were bulk material (Bi_2Te_3 , SiGe), where as the last one was a nanostructured thin-film sample. The operating temperature regime of the samples also varied widely ranging from room temperature (300 K - Bi_2Te_3) to high temperature (800 K – SiGe). The measurements with variety of samples demonstrated the flexibility of the measurement setup going from thick samples to thin samples, and working over wide temperature range.

TE samples	Measurement temperature	Dimensions	Collaborator
MAM – Bi_2Te_3	300 K	1 mm x 1 mm x 500 μm	Marlow Inc.
SiGe	500-800 K	6.5 mm x 2.75 mm x 17 mm	JPL
ErAs:InGaAlAs	300-650 K	1.4 mm x 1.4 mm x 120 μm	UCSB/UCSC

Table 21: Samples used for system validation

The first sample measured was the conventional bismuth telluride. At room temperature (311 K), we measured a ZT of 0.87 for a 1 mm x 1 mm x 500 μm , Micro-Alloyed-Material Bi_2Te_3 , with a thermal parasitic correction of 1.5 Kcm^2/W (dry metal-metal contact), and a system electrical parasitic resistance of 7 $\text{m}\Omega$. The value was within 3% of the measured data provided by Marlow Inc.

Silicon germanium (SiGe) from JPL was characterized using the Z-meter. The Seebeck coefficient and the thermal conductivity for the n-type SiGe were within 1-3% of the independently measured values (Figure 106). This sample did not have any metal contacts for good electrical measurement. The electrical conductivity, efficiency and power density measurements were dominated by the electrical parasitic resistance to get any meaningful data.

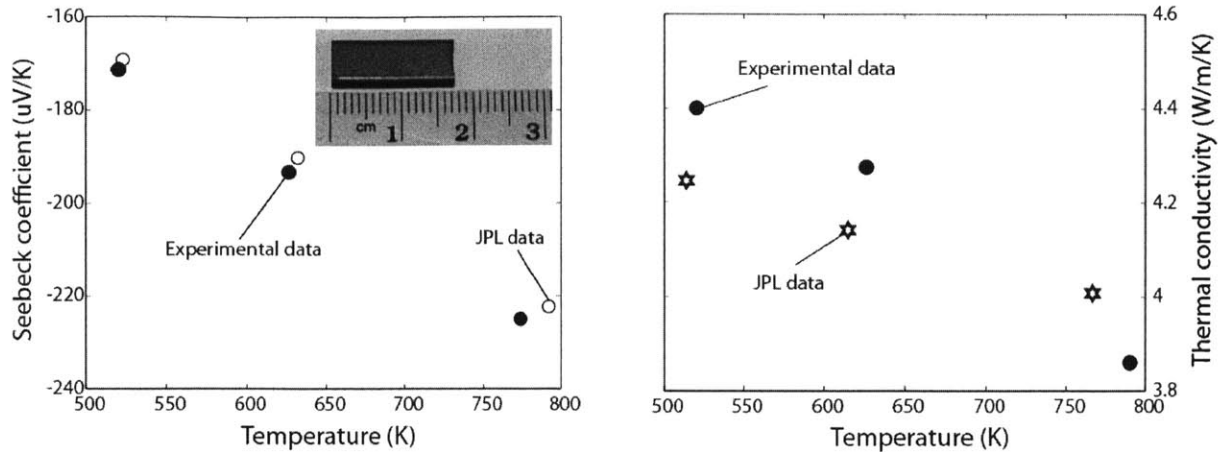


Figure 106: Seebeck coefficient and thermal conductivity measurement for n-type SiGe (JPL)

A semimetal/semiconductor nanocomposite thermoelectric material ($0.6\% \text{ErAs: InGaAlAs}$)^[43] was the next sample tested with the system. The n-type sample was approximately $1.4 \text{ mm} \times 1.4 \text{ mm} \times 60 \mu\text{m}$. Two samples were stacked on top of each other for a total thickness of $120 \mu\text{m}$. This relatively thin sample had gold contacts on both sides. The heater was set at a constant temperature using the heater controller and allowed to reach steady state before taking measurements. During several high temperature cross-plane measurements, it was realized that at such a high applied pressure ($\sim 800 \text{ psi}$) metal bonding was formed between the TE sample contacts and the gold-coated metal pieces as the temperature passed certain threshold ($\sim 500 \text{ K}$). This bonding lead to very low thermal contact ($0.05 \text{ K cm}^2/\text{W}$) and system electrical parasitic ($3 \text{ m}\Omega$) compared to the dry metal-metal contacts verified earlier (Section 5.6.2). The measurement results shown in **Figure 107-111** represent data taken after high temperature exposure ($> 500\text{K}$), such that the sample was bonded to the measurement setup, and a single thermal and electrical parasitic correction factor could be used to obtain the ZT values.

The ZT data (**Figure 107**) obtained from the Z-meter measurement matches with less than 7% average error compared to the published data^[43] for the same material. The sample was measured within an average temperature range of $300\text{-}620 \text{ K}$, with the highest temperature gradient of 200 K .

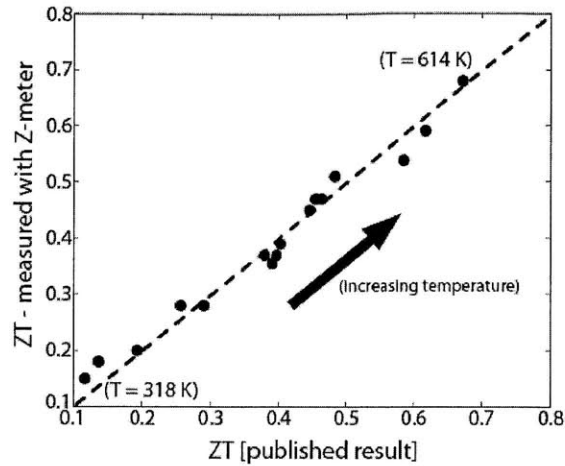


Figure 107: ZT measurement for the n-type ErAs: InGaAlAs using the Z-meter in comparison to published result ^[43]

Looking at individual TE parameters measured with the Z-meter, the thermal conductivity for the TE sample would have had an additional error of 6-7% if the measurement was done without addressing the radiation issue (Figure 108 a). The estimation for this erroneous thermal conductivity was done by adding radiative power, calculated using the theory based on Section 5.6.3, to the measured thermal power. The radiation error would have caused the measured thermal power to be higher, resulting in larger thermal conductivity than the true material value.

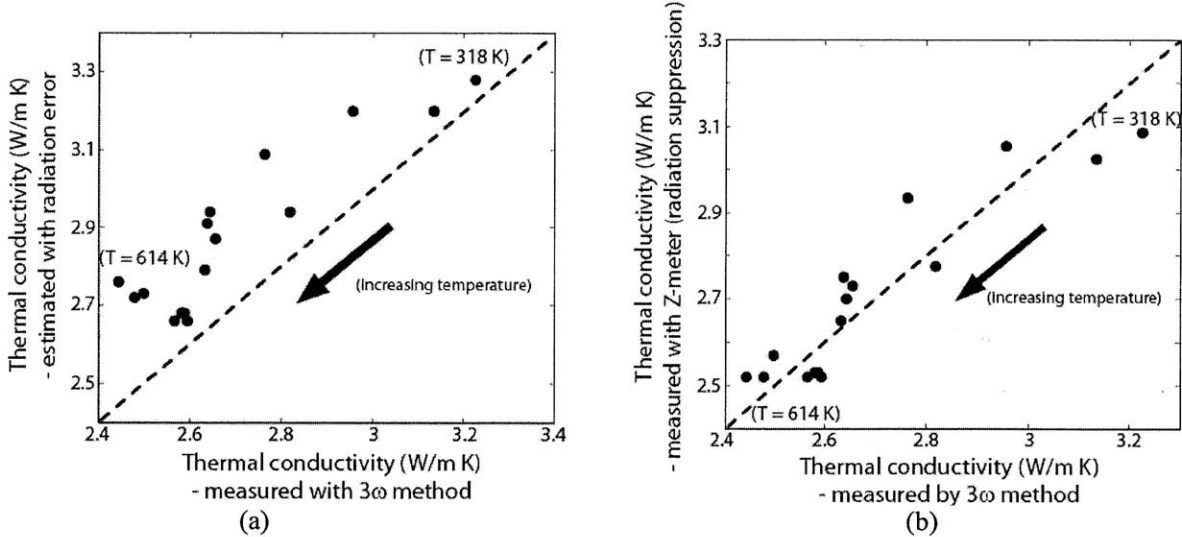


Figure 108: (a) Thermal conductivity estimation for the TE sample in the case of no radiation suppression, compared to thermal conductivity measured with 3ω method ^[43], (b) The measured thermal conductivity data vs. data from 3ω measurement ^[43]

The measured thermal conductivity with the gold-plated measure bar shows much better results (b) with a closer fit to the data from other measurement technique (3ω method) ($< 3\%$ error) ^[43]. Thus, without addressing the radiation issue, the Z-meter would overestimate the thermal conductivity and underestimate the overall ZT value with an additional 6-7% error.

The measured temperature dependence of the Seebeck coefficient and the electrical conductivity for the sample is shown in **Figure 109**.

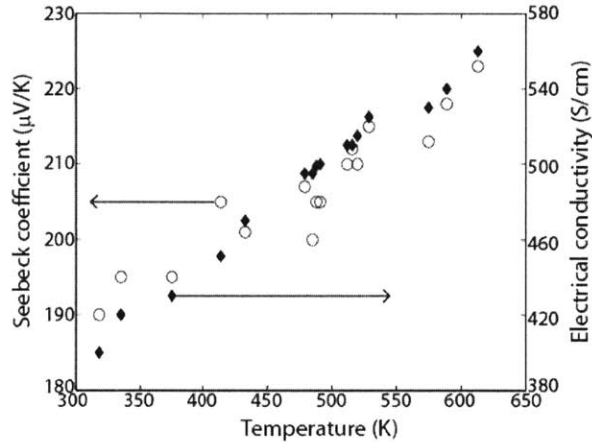


Figure 109: Seebeck coefficient (○) and electrical conductivity (◆) measurement for the n-type ErAs: InGaAlAs sample

The Z-meter also gives the efficiency and the electrical power density for a single TE element. The measurement result for different load resistance at an average sample temperature of 614 K, with a temperature gradient of 200 K is shown in **Figure 110**. Different load resistance across the TE sample is achieved by changing the current source. The maximum measured efficiency and the power density are limited by the system electrical parasitics. In **Figure 110**, the theoretical evaluation for efficiency and power density are shown with the electrical contact parasitics as the fitting parameter. The theoretical simulation with a system parasitic of $3\text{ m}\Omega$ fits the experimental data showing very low electrical contact resistance for metal-metal bonding.

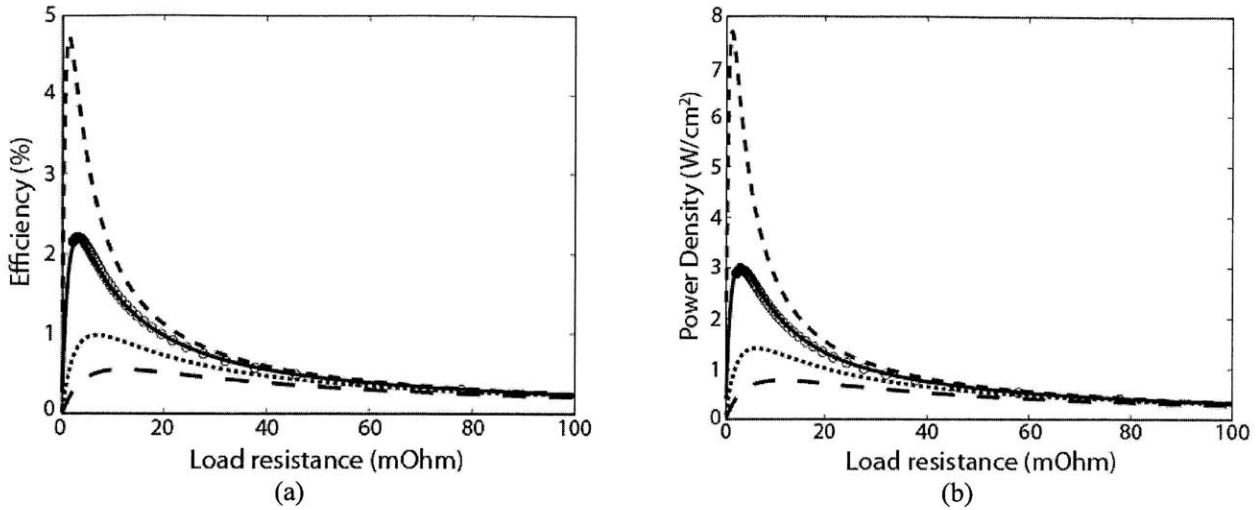


Figure 110: (a) Efficiency and (b) power density measurement data (o) with theoretical estimations for different system parasitics at an average temperature of 614 K (- - - $R_{\text{parasitic}} = 0 \Omega$, — $R_{\text{parasitic}} = 3 \text{ m}\Omega$, $\cdots R_{\text{parasitic}} = 5 \text{ m}\Omega$, — $R_{\text{parasitic}} = 10 \text{ m}\Omega$)

Irreversible degradation was noticed after the sample was kept at such high temperature gradient for considerable amount of time (> 24 hours). The open circuit voltage started to decrease even for the same temperature gradient that initially showed high open circuit voltage. The most likely cause for this degradation is the thermal stress at the metal-semiconductor contact which has different thermal expansion coefficient ($\text{InGaAlAs} \sim 5 \times 10^{-6} \text{ 1/}^\circ\text{C}$; $\text{Gold} - 14 \times 10^{-6} \text{ 1/}^\circ\text{C}$). The stress is directly proportional to the difference in thermal expansion coefficient for the two layers as well as the temperature gradient. This would point towards the need for a better diffusion barrier at high temperature for such a material to be used as a generator. Larger temperature gradient (> 250 K) was applied across the sample to achieve high power density measurement as shown in **Figure 111**, but at an overall lower average sample temperature and for less time. For a single TE leg, high generated electrical power density of 9.5 W/cm^2 was measured which was 5x large than the power density for $\text{MAM-Bi}_2\text{Te}_3$ material ^[246] with same the temperature gradient.

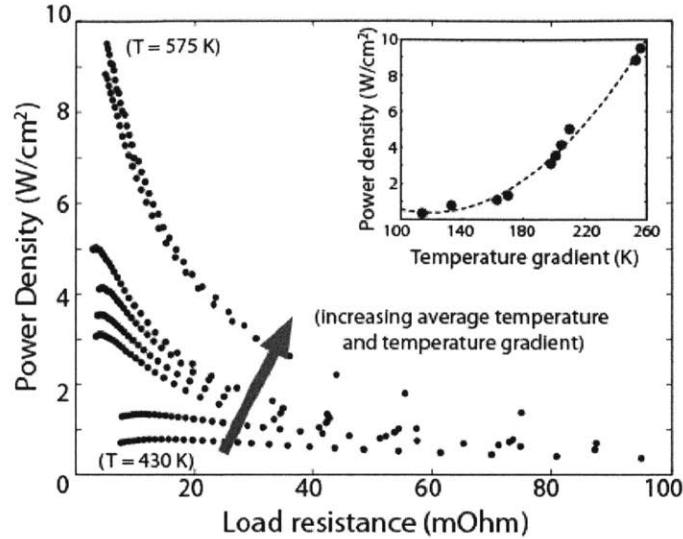


Figure 111: Generated power density for ErAs sample at different temperature gradient and average temperature increasing from 350 K to 575 K (Power density vs. temperature gradient is shown in the inset)

Such thin TE samples with large power density at higher temperature gradient can be useful for power generation.

5.7 New TE material measurement

The Z-meter was used to characterize a novel thermoelectric material: metal-semiconductor superlattice structure ((Hf, Zr) N/ScN) that was discussed earlier. These samples are bulk-laminate structures with stacks of 5-10 μm superlattice layers (SL). Pictorial representation of the sample preparation is shown in **Figure 112**. 5-10 μm superlattice layers with metal contacts are bonded to make taller bulk-like laminate structures. Initial samples were made with copper as bonding metal with thin layer of gold (**Figure 113**). Direct gold contacts were also tried in some of the samples. The pros and cons of different contact materials will be discussed later in this chapter.

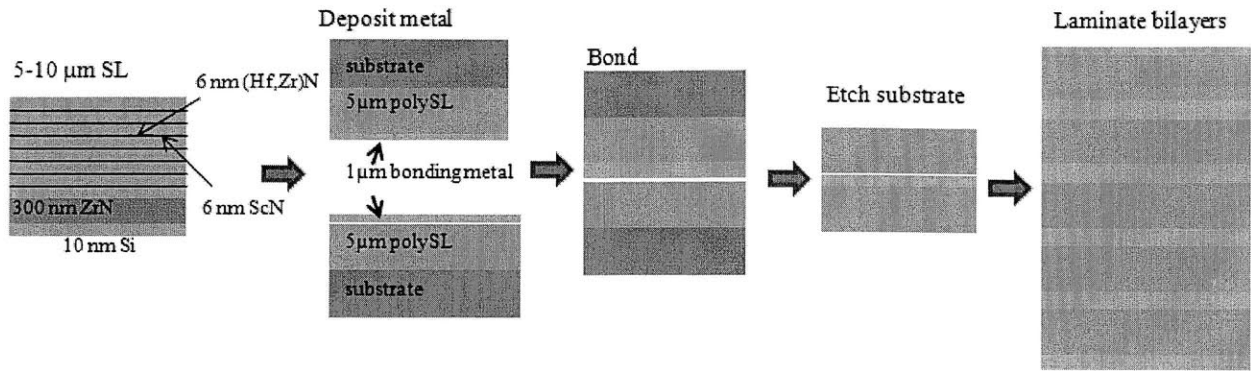


Figure 112: Bulk-laminate superlattice sample preparation order

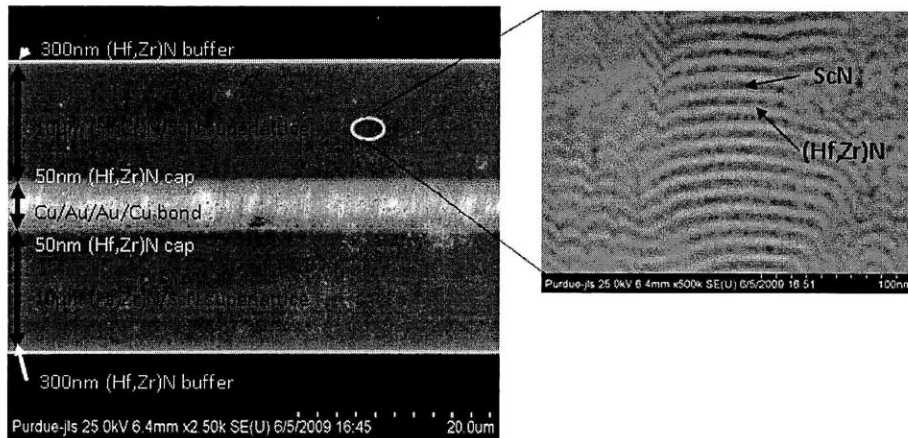


Figure 113: (Hf, Zr) N and ScN superlattice structure with 12 nm periodicity

*(Courtesy: Jeremy Schroeder; Purdue University)

Initial measurements on the sample (CuBond21) resulted in very low Seebeck coefficients ($\sim 5\text{-}10 \mu\text{V/K}$ - similar to a metal) (Figure 115), primarily due to metal shorts created during the dicing process (Figure 114). A metal film of 40 nm thickness across the cross-section of the sample would be sufficient to give such a low Seebeck coefficient. An independent electrical resistance measurement (four point probe method) of similar nitride sample also showed increasing resistance with temperature which implies a metallic type conduction [237]. During the Z-meter measurement, it was also noticed that the material degraded considerably at large temperature gradient ($> 300 \text{ K}$), due to thermal stress at the contact layers. The stress due to large temperature gradient can be huge at the interfaces because of the thermal expansion mismatch between the contact metal – copper and the nitride layer ($\text{Cu} - 17 \times 10^{-6} \text{ 1/}^\circ\text{C}$; $\text{HfN} \sim 7 \times 10^{-6} \text{ 1/}^\circ\text{C}$). In the next sample fabrication, instead of in-situ copper deposition, gold was directly deposited after diffusion layers on top of nitride to make the sample more stable. Gold ($14 \times 10^{-6} \text{ 1/}^\circ\text{C}$) has slightly less thermal expansion coefficient than copper.

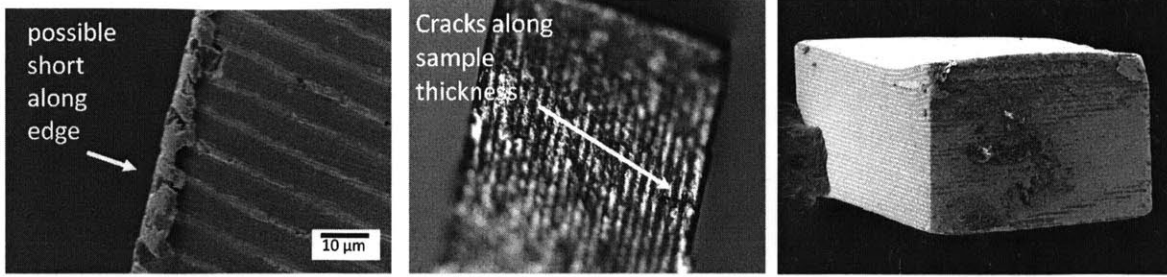


Figure 114: Samples (CuBond21) with gold shorts along the thickness of the superlattice structure

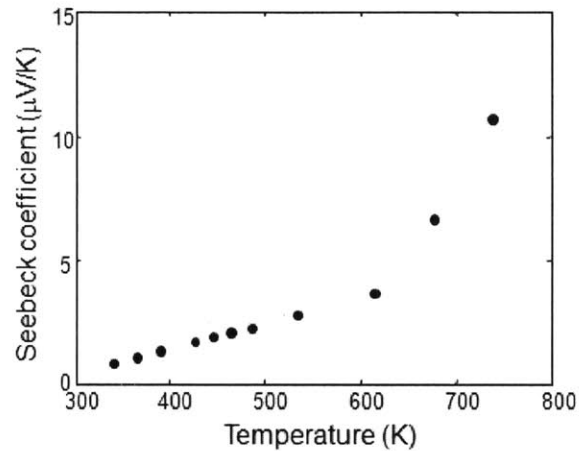


Figure 115: Seebeck coefficient measurement for CuBond21 sample

A second set of samples were polished with 3 μm diamond lapping disc to get rid of gold shorts on the edges (**Figure 116**). There were still few gold smears along the cross-section of the sample creating some parallel and series leakage path. The sample was 280 μm thick with 40 superlattice layers (5 μm each) and 80 gold layers (1 μm each). The cross section area was ~ 300 μm x 300 μm. The Z-meter setup was slightly modified to keep the temperature gradient below 200 K. A rope heater was wrapped around the measure bar to increase the cold side temperature as the heater temperature was increased (**Figure 117**). This modification allowed for higher temperature Seebeck and electrical conductivity measurements without any material degradation. However, the thermal conductivity measurement was impossible due to the rope heater which acted as a path for heat flow to and from the cold side, distorting the heat flux measurement.

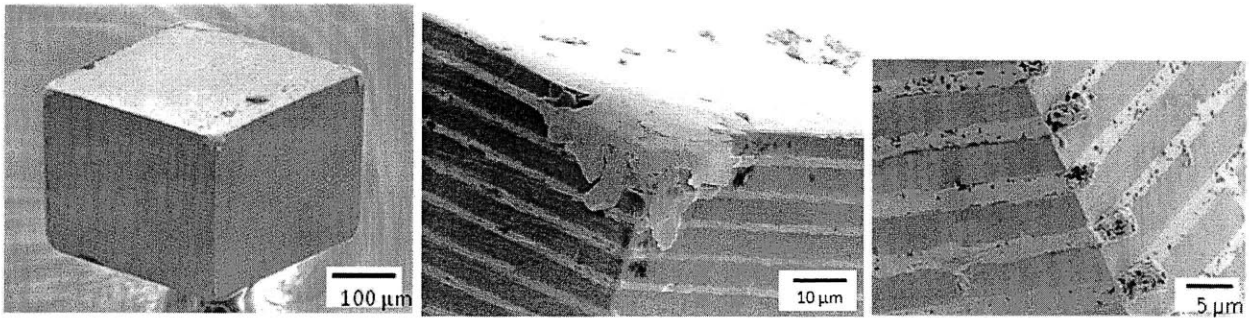


Figure 116: Polished nitride sample with visibly less gold shortenings between TE layers

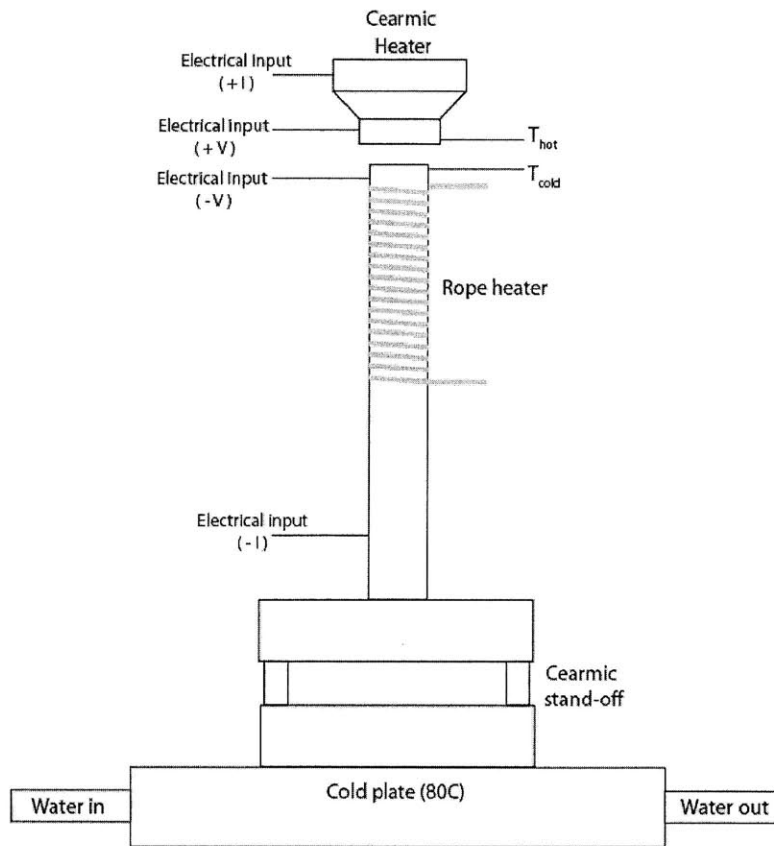


Figure 117: Modified Z-meter setup to decrease the temperature gradient across the TE sample

The temperature dependent Seebeck coefficient measurement for this sample is shown in **Figure 118**. A steady increase in the Seebeck coefficient was measured with the highest value of $132 \mu\text{V/K}$ at an average temperature of 830 K, which is comparable to high temperature conventional TE material such as p-type SiGe. Relatively low Seebeck coefficient at room temperature could still be dominated by the parasitic electrical shunts inside the superlattice. Theoretical estimates for the Seebeck of pure multiple layer structures show the Seebeck coefficient to decrease with temperature. We can model the TE sample as having the superlattice film in parallel with a current leakage path and both of them together in series with

an electrical resistance primarily from contacts. To measure such low Seebeck coefficient at lower temperature, the leakage resistance with metallic Seebeck must be much lower than the superlattice film, indicating that the leakage dominates the current flow. The measured increase in Seebeck can be explained by the relative increase of conductance through “active TE material” compared to the leakage path in parallel. As the temperature increases, at some point the sample conductivity becomes comparable to the shunt and we see the Seebeck of the sample. The increase of the Seebeck coefficient with temperature indicates potential increase in the electrical conductivity of the superlattice.

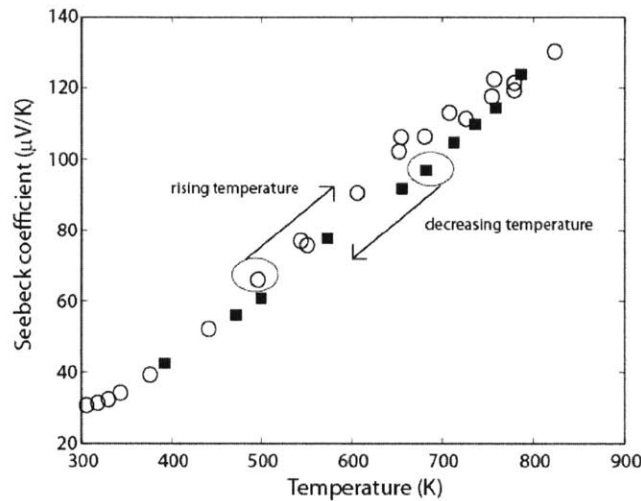


Figure 118: Seebeck coefficient measured for the nitride superlattice structure

On the other hand, the electrical conductivity measurement seemed dominated by the interface parasitic. The matched load resistance showed no dependence on temperature (**Figure 119**). From a literature research, we can find that the contact resistance in order of $1e-5 \Omega\text{cm}^2$ can easily occur between a nitride and metal interfaces ^[255]. For our measurements, an Ohmic contact of $1.1e-5 \Omega\text{cm}^2$ is enough to give a resistance of 1Ω for 80 gold layered TE sample, indicating that the interface contact resistance could easily dominate the measurement. For this polished sample, the superlattice growth and contact metal deposition were done in different chambers. During the transfer process, any kind of oxide or organic layer between the metallic nitride and the metal can easily cause such large resistivity. Also, while processing and handling, gold de-lamination was observed in many of the samples indicating weaker bonding at the interfaces.

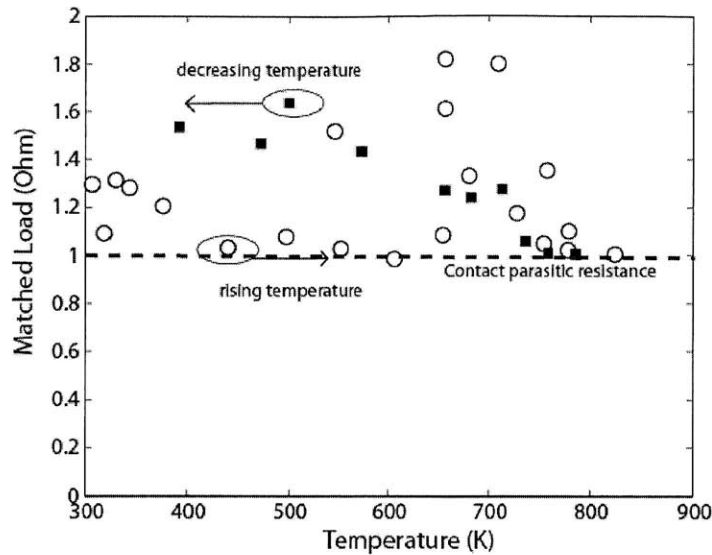


Figure 119: Measured matched load resistance at various average temperatures

The next generation of samples measured were CuBond36 (HfN/ScN) metal-semiconductor superlattice structure (Figure 120). These samples had 85 μm of active TE superlattices (17 layers - each 5 μm thick). The total contact layer was 35 μm . The sample was 120 μm x 300 μm x 377 μm .

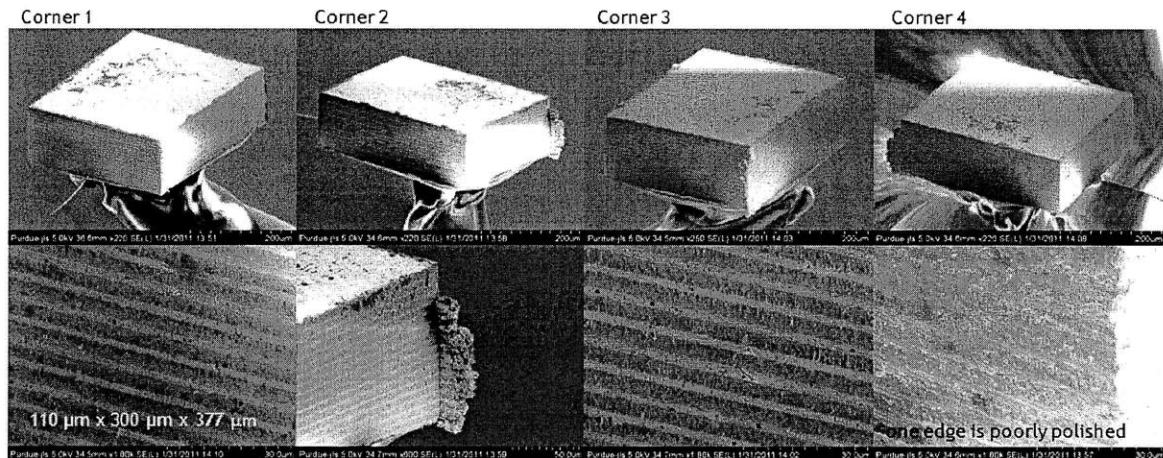


Figure 120: HfN/ScN superlattice structure (120 μm thick sample)

The measurements were done in the original Z-meter setup with the intent of getting all three TE parameters and extracting ZT values. The temperature gradient and material degradation were watched closely during the experiment. The sample did fail after being exposed to temperature gradient > 215 K. The thermal conductivity for the sample was measured to be between 2.4-4.4 W/m K (Figure 121 b). The conductivity value for the metal-semiconductor superlattice structure was lower than the individual value (ZrN ~ 47 W/m K and ScN ~ 10 W/m K). The rise in thermal conductivity with increase in temperature

could be mostly due to electronic contribution at higher temperature. The thermal conductivity increases as the electron contribution increases at higher temperature. These values for thermal conductivity are similar to the independent measurements done on similar nitride samples (HfN 8nm/ScN 4nm) with 3- ω technique where it ranges from 2.7-4.5 W/m K. The increase in thermal conductivity also points to increasing electrical conductivity for the material based on the Wiedemann-Franz law. The Seebeck coefficient was 20-65 $\mu\text{V}/\text{K}$, similar to the previously measured values for the polished sample within the measured temperature range. Slight variation can be attributed to final polished quality of the sample.

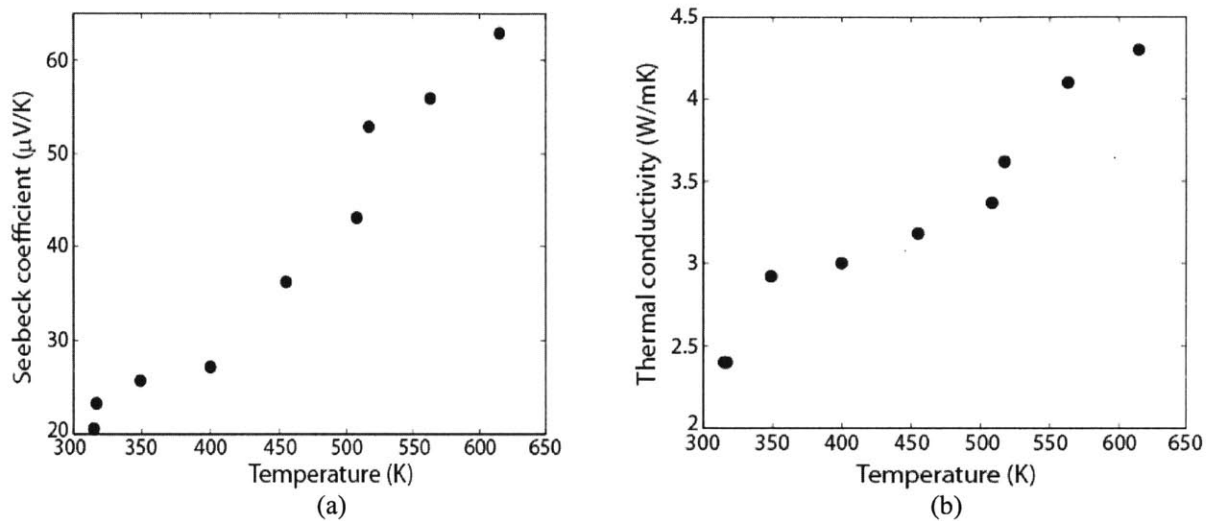


Figure 121: Measured Seebeck coefficient (a) and thermal conductivity (b) for CuBond36 sample

The electrical conductivity measurement was again dominated by the interface resistance with load resistance not having any temperature dependence. Interface resistivity of $5\text{e-}6 \Omega\text{cm}^2$ was estimated from the Z-meter measurements for this sample. This interface resistivity was 50% lower than the resistivity compared to previous samples. The decrease in parasitic was achieved primarily by going back to in-situ copper deposition on metallic nitride before depositing titanium (Ti)/gold (Au) contacts. Similar interface resistivity was also measured independently at Purdue University using the transmission line model (TLM) measurement ^[237], proving that the high electrical conductivity potential for the TE material is currently limited by the large interface parasitics. The TLM measurement was done on two samples: HfN – Ti/Au contact and HfN – Cr/Au contact. The initial contact resistivity was very high (on the order of $1\text{e-}3 \Omega\text{cm}^2$). After annealing the sample at 300°C for 4 hours, the contact resistance for Ti/Au contact was measured to be in the range of $4\text{e-}6 \Omega\text{cm}^2$. There was no improvement for Cr/Au contact even after annealing, indicating Cr not to be a good adhesive layer for gold contact with the metallic nitride. For a single layer nitride superlattice structure, independent electrical conductivity measurements from UC-

Santa Cruz have shown conductivity in the order of $100 (\Omega\text{cm})^{-1}$, which is still an order of magnitude lower than standard TE materials. With the theoretical estimation for the electrical conductivity for such nitride samples to be $> 3,000 (\Omega\text{cm})^{-1}$ at temperature range of 500 K, the interface resistance seemed to be dominant even for a single layer superlattice structure. The leakage path is a significant error source in determining the material conductivity and the potential barrier. Lower contact resistances in the order of $1\text{e-}7 \Omega\text{cm}^2$ have been made possible in other TE materials (ErAs: InGaAlAs). Considering most interfaces are between metallic nitride, barriers and metals, low parasitics of such order should be achievable. With low parasitics, true electrical conductivity for the material will be possible to measure. Work is being done currently to address the interface parasitic issues by looking at suitable diffusion barrier, adhesive layer material and contact metal choices. Investigation on potential oxide formation between the metallic nitride and contacts are also being carried out which could cause such high resistance. Optimization of the constituent materials in the sample is also an ongoing process, where the barrier height greatly affects the thermoelectric properties (**Figure 96**). The effective barrier height for HfN-ScN is lower than that for ZrN-ScN ^[237]. Determination of exact barrier height for different doping levels of Hf/Zr has not been done yet. **Table 22** summarizes the results for the metal-semiconductor superlattice samples using Z-meter.

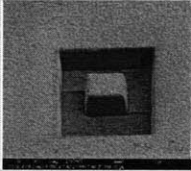
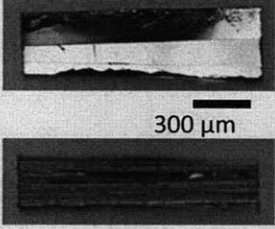
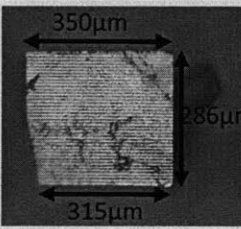
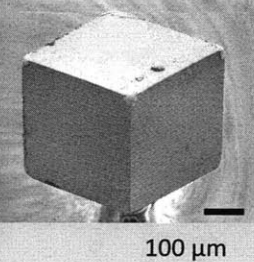
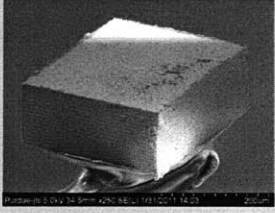
	Theoretical estimates	Electrical conductivity measurement (FIB)	Thermal conductivity measurement (3 ϕ @ 300 K)	1 st Z-meter measurement (@ 340 K)	2 nd Z-meter measurement (@ 380 K)	3 rd Z-meter measurement (@ 305 K)	4 th Z-meter measurement (@ 300 K)
		* (Purdue, UCSC)	* UC-Berkeley	CuBond21-6	CuBond21 (polished #1)		
							
Composition	HfN (8 nm) / ScN (4 nm)	HfN (6 nm) / ScN (6 nm) (pillar structure)	HfN (8nm) / ScN (4nm)	(Hf,Zr)N (6nm) / ScN (6nm)	(Hf,Zr)N (6nm) / ScN (6nm)	(Hf,Zr)N (6nm) / ScN (6nm)	HfN (6nm) / ScN (6nm)
Seebeck Coefficient (μ V/K)	360 (Calculated from ZT at 300 K = 0.7)			2.25 (dominated by metallic short)	19	30 (132 @ 830 K)	21 (65 @ 625 K)
Thermal conductivity (W/m K)	2.8		2.9	2.7	4.6	2.35	2.4
Electrical conductivity ($1/\Omega$ cm)	500 (6 nm HfN/ 6 nm ScN) with $\Delta E_c = 1040$ meV	300 100-400		—	—	Interface parasitic: $1e-5 \Omega\text{cm}^2$	Interface parasitic: $5e-6 \Omega\text{cm}^2$

Table 22: Z-meter measurement showing progressive improvement for metal-semiconductor sample

5.8 Conclusion

In this work, we have looked at thermoelectric material from the perspective of earth-abundance to understand the characteristics of a good thermoelectrics. With 20-30% of the price of a thermoelectric generator being material cost, abundance and material scarcity due to high demand can be very important for large volume applications. We presented ZT vs. crustal abundance for many state-of-art and new researched materials looking at the issue of earth-abundant elements and its usage in thermoelectrics. We looked at a novel thermoelectric material utilizing metal-semiconductor superlattice, which has a potential of high ZT over a large temperature range. Large ZT could be possible in such a material due to low thermal conductivity (phonon scattering at superlattice interface) and high thermopower (electron filtering with energy barriers). We presented an experimental technique to measure the TE parameters of a single sample with a large temperature gradient (~ 200 K), similar to real-life conditions for a generator. The measurement setup was used for a wide range of temperature (300-800 K), as well as for both bulk and thin-film samples (~ 100 μm). Both thermal and electrical parasitics for the setup were carefully studied and minimized for the measurements. More than 50% reduction in the electrical parasitic compared to the lowest literature value was obtained by using a four-wire measurement. We developed theory for radiation loss factors and verified it experimentally at high temperature for measure bars with different emissivity. Using a gold-plated measure bar, radiation loss error in the order of 6-7% can be suppressed in the thermal measurements with the hot side temperature ranging from 330-718 K. TE parameters and ZT for different samples (Bi_2Te_3 , SiGe and ErAs:InGaAlAs) were measured and were in good agreement with the published results measured with conventional techniques. High power density of 9.5 W/cm^2 was measured for the thin-film sample using the Z-meter under a large temperature gradient of 255 K. Such a system can provide a good platform for verification and measurement of TE parameters in conjunction with conventional techniques to assure correct measurement and reduce uncertainties by measuring all TE parameters in a single sample.

The TE parameters for novel metal-semiconductor superlattice were measured with the Z-meter. Great reduction in the thermal conductivity was measured for the superlattice sample compared to the bulk nitrides (at room temperature: ZrN $\sim 16 \text{ W/m.K}$, ScN $\sim 6 \text{ W/m.K}$). **Figure 122** shows the TE parameters for the nitride sample in comparison to some of the earth-abundant materials discussed at the beginning of the chapter. At low temperatures (> 600 K), the nitrides have comparable thermal conductivity of 2-4 W/m.K to other earth-abundant TE materials. At high temperature (800 K), the rise in the thermal conductivity $\sim 5.5 \text{ W/m.K}$ is most likely due to electronic contribution.

Acceptable high temperature Seebeck coefficient ($132 \mu\text{V/K}$) was measured for a finely polished nitride sample at 830 K. The Seebeck coefficient for the superlattice sample at 800 K is twice that for the semiconductor nitride (ScN) and an order of magnitude larger compared to the metallic nitride (ZrN). However, at low temperature the Seebeck is still small and closer to the metallic values indicating dominance of the metallic shunts. The electronic transport may be dominated by metallic type conduction in these samples.

The one parameter that is suppressing the current material performance is the electrical conductivity which has been dominated by the interface parasitic. Improvements were made to lower the electrical resistivity at the interface, but it is still too large and dominates any electrical measurement of the sample. In order to make a useful thermoelectric material out of the metal-semiconductor superlattice, the interface electrical resistivity issue has to be lowered by nearly 2 orders of magnitude.

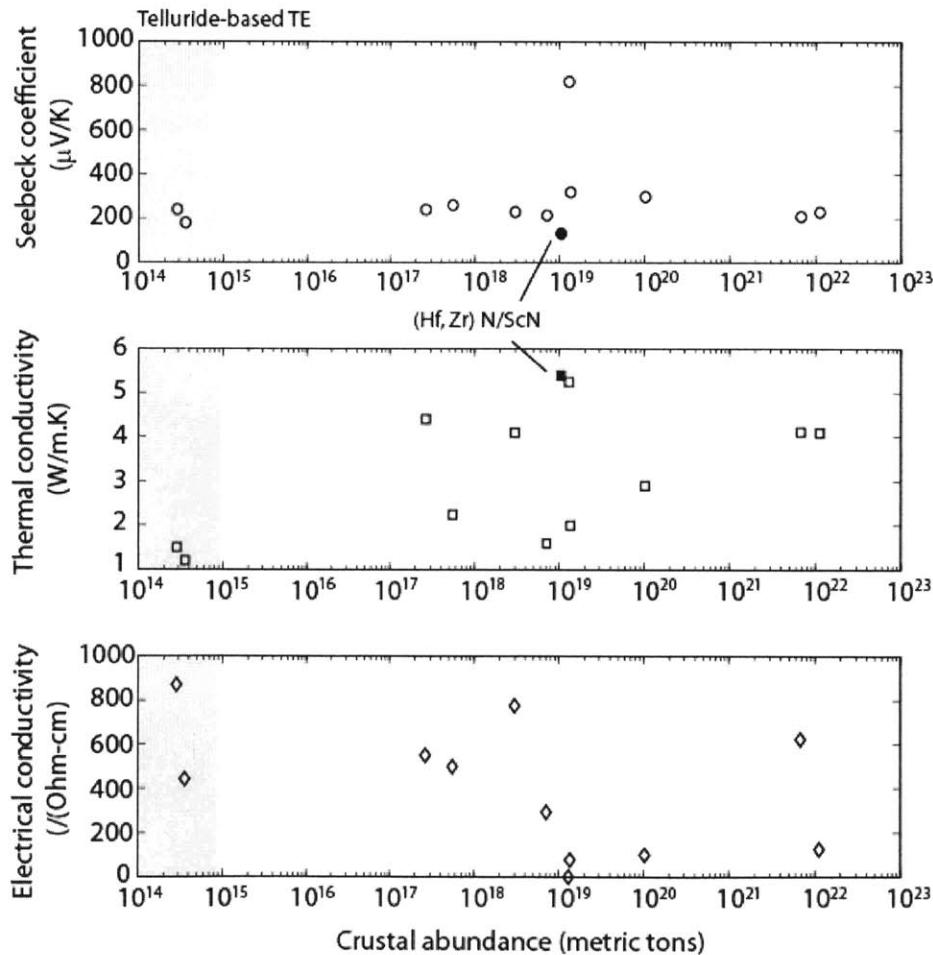


Figure 122: Thermoelectric parameters for different earth-abundant TE materials in comparison to nitride samples measured in this research

Due to very low electrical conductivity measured for ZrN/ScN superlattice ($2/(\Omega\text{cm})$ at 450 K), Hf was added to the metal to adjust the barrier height. However, for the superlattice structures (both bulk laminate sample and focused-ion-beam (FIB) etched pillar structure) the measured electrical conductivities have been dominated by parasitics. The effective measured conductivity for the nitride sample with the parasitic is in the order of $30/(\Omega\text{cm})$, giving a small $ZT \sim 0.007$. Even though the individual TE parameters for different nitrides show promising TE material prospect with high Seebeck coefficient and low thermal conductivity, much higher electrical conductivity is required for enhancement of ZT .

Chapter 6

Economic Model

As described in Chapter 1, solar photovoltaics are the leading technology for distributed power generation in developing countries. However, if we look at the cost of power generation, photovoltaics cost can be as high as \$10/W in these regions (2011, LUTW Foundation). The high cost for generation is primarily due to the economic structure of micro-credit and financing which relies on high interest rates, as people cannot pay the high upfront cost for the PV system. The size of the installed system also dictates the total cost due to advantages of volume purchase. As shown from this research, the solar thermoelectric generator can provide electricity utilizing the solar energy as well as waste heat. Using local solar cookers, relatively high thermal fluxes can reach the thermoelectric generator to raise its temperature. Using different heat sinks, a moderate temperature gradient can be maintained across the module to generate electricity. As seen from the previous chapters, the system efficiency for STEGs is lower than that for the conventional PV systems, but we look at the cost for the electricity generation to compare STEG with PV in developing countries.

For a commercial silicon PV, the highest efficiency (19%) in the field is achieved for the electronic-grade silicon (single-crystalline)^[256], used mostly in integrated chips and optoelectronic devices. It has less than few parts per billion of impurities^[256]. As the quality of silicon degrades and impurity level rises to hundreds of parts per million, the efficiency decreases drastically (7%). This is due to the recombination losses in PV due to impurities. One advantage of thermoelectric modules compared to photovoltaics maybe that the TEG module can be made from 'dirtier' materials compared to photovoltaics without much effect on the efficiency and the system performance. For many thermoelectric materials, the ZT does not vary much for different metallurgical grade materials. This has been true in the case of SiGe, where the ZT value decreases from 0.7 to 0.56 for electronic vs. metallurgical grade silicon^[257]. Thus, the material for thermoelectrics could be relatively cheaper. The bulk cost for a commercial thermoelectric module ranges from \$1.5 - \$3/W_p (2011, BSST Inc./Marlow Inc). The retail peak power price for a silicon based PV module is \$2-4/W_p (2011)^[256]. Thin-film CdTe modules are cheaper with a single module price at \$1.18/W_p^[256]. The output capacities of the modules considered in Ref. [256] are in the range of 110-125 W. With a larger output system capacity (utility scale > 1 MW), the module price is less than \$1/W_p. The module cost is typically 35-40% of the total installed cost of a solar PV system^[256]. Both TEG and

PV have similar lifetime (15-20 years) and low maintenance cost. The electronic circuit requirements are also similar for PV and TEG, as both require batteries, charge controllers, inverters etc. The critical difference is the conversion efficiency which is between 7-12% for a low-cost thin-film PV module. Commercial TEG modules are rated for 4-5% optimum conversion efficiency for a large temperature gradient ($T_h = 230^\circ\text{C}$, $T_c = 50^\circ\text{C}$). With solar thermoelectrics, as shown in the previous chapters, the system efficiency is below 3%. Improvements in efficiency can be made as discussed in Chapter 4. With a low-cost parabolic concentrator providing a solar flux of $\sim 10\text{-}20\times$ suns, and with thermal concentration, a system efficiency of 2.5% has been achieved with the unoptimized commercial TEG modules. In this Chapter, we will discuss the system cost as well as the cost of electricity generation which takes into account both the system efficiency as well as the bulk component (capital) costs.

The prototype cost breakdown is given in Section 6.1. A simple cost model was developed for the STEG to get the levelized cost of electricity (LCOE). The model is described in Section 6.2. The influences of different parameters such as module design and TE material choice on the price are discussed here.

6.1 System cost

A summary of the component cost for the STEG system is presented in **Table 23**. The costs are based on quotes from the current component manufacturers for quantities of 250 units or less. The final cost for the 11 W (peak) solar thermoelectric system was \$105, which results in a per watt cost of $\$9.5/W_p$. The current cost for a solar thermoelectric generator is higher than the complete solar home PV system ($\$7\text{-}8/W$)^[122] which is currently available in China.

Component	#	Specifications	Cost (US \$)(@ 250 units)	Cost (US \$) (total)
Absorber (metal)	1	Aluminum	5 (US vendor)	5
Heat sink (pot)	1	Aluminum	5 (US vendor)	5
TEG module	4	TG-6-12 (Marlow Inc.)	20 (US vendor)	80 ($\sim \$4/W_p$)
Battery	1	Sealed lead-acid (12V, 4.5 Ah)	8 (Chinese vendor)	8
Charge controller	1	Over charge protection: 14.8 V Over discharge protection: 11.5 V Current rating: 1.5 A	5 (Chinese vendor)	5
LED light	1	5 W	2 (Chinese vendor)	2
			Total:	\$105

Table 23: Cost break down for solar thermoelectric generator

The highest cost component of the system is the thermoelectric generator module. After market research, we found a lower module cost for higher volume consumption. The bulk (10,000+) retail price for a 15 W thermoelectric generator was \$25 (Thermonamic Electronics Xiamen Co. Ltd.); giving the peak power price of \$1.67/W_p. With the module price coming down by more than 60%, the total system cost can be reduced to \$58, resulting in per watt cost of \$5/W_p which is lower than the current PV system cost.

For further price breakdown, basic material pricing was considered for the system to look at the absolute minimum system price (Table 24). The major components of the generator i.e. absorber, TEG module, heat sink and battery charging setup were included in the system. By using a simple absorber design and a pot-like structure for a heat sink, the cost can be kept low. Only the metal (aluminum) cost is considered here, with an assumption that for a simple manufacturing design, the material cost would be the dominant factor. The material price for thermoelectric is \$250/kg^[35]. The price for a TEG module is estimated by taking the material cost to be 20% of the total module cost. A fixed price for the additional electronics for battery charging is considered similar to the current market value (Table 23). With this analysis, the cost for the generator can be ~ \$ 4/W_p.

Material	\$/kg	Requirement for STEG (kg)	Cost for STEG
Aluminum (heat sink/absorber)	2	0.98	1.96
Bi ₂ Te ₃	250 ^[35]	0.025	31.25
Peripherals (wires, battery, charge controller, light etc.)			15
		Total:	48.21

Table 24: Material cost for STEG

When the upfront system cost is lower, the technology is more likely to be adopted in developing countries as proven by the case of amorphous silicon versus crystalline silicon PV^[8, 12]. With lower TEG module cost, the overall system cost for solar thermoelectrics can be lower than that for photovoltaics. In the next section, we look at the cost for electricity generation which will incorporate the system efficiency to get the levelized cost of electricity (LCOE).

6.2 LCOE cost model

In developing countries, the initial system cost is an important consideration as many people cannot pay a large upfront price for power generation options such as diesel generators and photovoltaics. The micro-finance system has been somewhat successful in covering these large system cost by breaking it down to monthly payments. Even though the system cost is important to the end-user, it does not tell the complete story of the economics of the technology. The important parameter in the cost analysis is the levelized electricity cost (LCOE), which includes lifetime cost analysis for the power generation system. The LCOE analysis includes operational/maintenance cost as well. The electricity price given by the LCOE analysis would be a fair comparative parameter between different electricity generation options. In such economic cost analyses different levels of complexities can be introduced such as market size, government subsidies, financing interest, taxes, material recycling etc. For common off-grid power generation technologies such as PV, wind turbine, and diesel generators, there are many commercial modeling tools (HOMER: NREL's Micropower Optimization Modeling software) which can be used to extract the LCOE for different output power systems. For this research, a simple economic model was developed to take into account the system efficiency and the cost for solar thermoelectrics which is described below.

For the levelized cost analysis, the electricity price for the STEG was calculated by using the total amount of the electrical power generated within the lifetime of a generator (20 years) and the system cost along with the operational charges. The annual maintenance cost was taken as 5% of the capital cost. An initial battery cost (\$8) with a lifetime of 5 years and replacement costs for 20 years have been considered in the model along with the cost for the charge controller and the lighting system. The peripheral costs are similar to the one used in the PV cost modeling [HOMER analysis]. The solar thermoelectric generator efficiency ($\eta(q_i)$) depends on the incident solar flux (q_i) as shown in Chapter 2 and 4 (**Figure 18**, **Figure 84**). The yearly solar irradiance for this analysis was taken to be for Xining, Western China. The hourly solar radiation data (**Figure 123**) was taken from HOMER simulation data set (NREL/NASA's energy database).

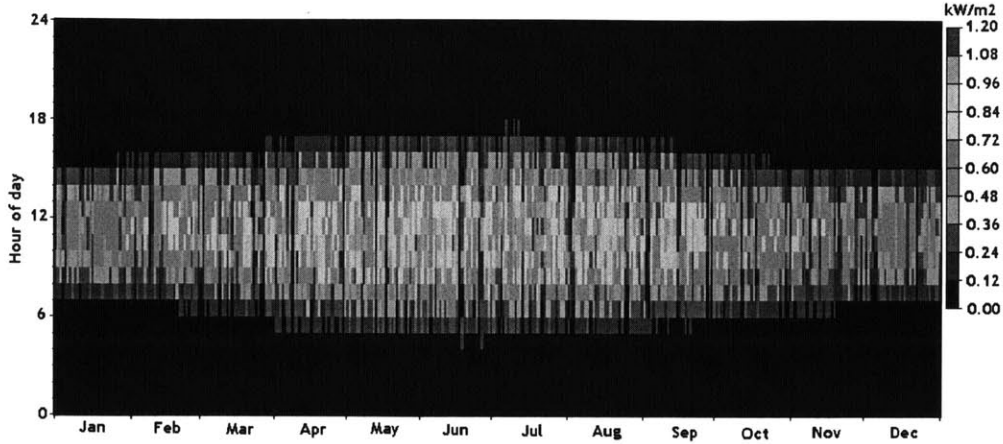


Figure 123: Solar irradiation for different hours in a day over a year (location: Xining, China) [Ref. HOMER simulation: solar radiation data set provided by US NREL and NASA's Surface Solar Energy database]

The output power for the STEG at any given instant is equal to the system efficiency multiplied by the total thermal power incident on the generator. The thermal power into the generator depends on the incident solar flux (W/m^2), the optical concentration, and the generator area (A).

In an ideal condition, the total output power within the lifetime of a generator is given by the sum of the output power for each hour of the day as shown in Equation 44.

$$\langle P_{electrical} \rangle = \left(\sum_i \eta(q_i) \times q_i \times C_{opt} \times A \times P_{q_i} \right) \quad (44)$$

Here, P_{q_i} is the total number of hours in a year the solar radiation of certain intensity (q_i) hits the earth's surface. The histogram showing the total number of hours of solar irradiance is shown in **Figure 124** along with the system efficiencies for a commercial Bi_2Te_3 module, an optimized Bi_2Te_3 module and a new TE material module (using silicide). The histogram is achieved by considering the hourly solar data from **Figure 123** and binning them according to the solar irradiance.

$$LCOE = \frac{\text{Capital Cost} + \text{O\&M}}{\left(\langle P_{electrical} \rangle \times \text{lifetime} \right)} \quad (45)$$

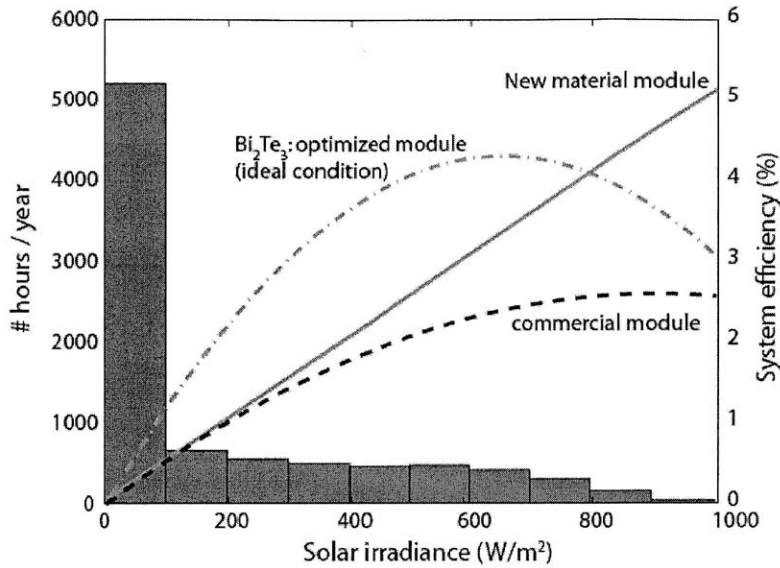


Figure 124: Solar flux dependence for the system efficiency for Bi_2Te_3 and silicide material is shown. The total number of hours within a year for certain flux radiation is also shown as a histogram

The cost of generated electricity was calculated according to Equation 45 and is based on the values for the capital cost and the operation/maintenance cost (O&M). The calculation assumes a 20-year lifetime for the generator. The cost for the generator is shown in Table 25 along with the PV and the grid extension prices for comparison. Commodity prices (volume purchase) for the solar concentrator (\$30 – OED pricing), TEG modules (\$1.67/ W_p) and electronics were used for the system’s capital cost. Inefficiencies and power loss due to manual tracking was included in the total power calculation for the STEG by taking a loss factor as 0.25 for conservative estimate. As shown in Chapter 3, an average output power during the electricity generation cycle was 85% of the peak power due to manual tracking. The PV cost is shown for US and developing countries. The difference in the electricity prices for the residential (2 kW), commercial (50 kW) and industrial (500 kW) use in the US is due to the discount on the retail prices on the volume purchases. For the STEG, a bulk volume price for the thermoelectric module was considered (10,000+ pieces \approx 150 kW). Thus, the correct comparison will be with the electricity price for commercial and industrial use in the US. The electricity price in the developing countries varies, depending on the location (solar radiation) and the financial structure for distributing solar PV. Involvement of the government and subsidies also greatly affect the cost of electricity for the distributed power. For example, the cost of electricity with a solar home system (SHS) in Zimbabwe is \$1.51 /kWh^[258], where as the cost in Nigeria is \$0.70/kWh [2008, Solar Electric Light Fund (SELF)].

In order to check the accuracy of our economic model, the electricity price for PV was calculated using Equation 44/45. The LCOE cost for PV was 26 cents/kWh, which is similar to the commercial electricity

cost for PV using HOMER simulation (\$0.28/kWh) and published data ^[256]. The peak conversion efficiency for the module under consideration was 12.5%. The current generator system with commercial TEG modules was the most expensive option with the generated electricity cost of 66 cents/kWh due to the low system efficiency. Improvement in efficiency is directly related to lowering the electricity cost as seen by the LCOE for the optimized modules with higher efficiencies. Even for Bi₂Te₃, with module optimization, discussed in Chapter 4, lower LCOE (37 cents/kWh) can be achieved for solar thermoelectrics. During module optimization, the volume of the TE material was considered to be constant and kept same as the commercial module. The total area of the module and the number of the TE legs were also kept equal to the commercial module. The improvement in the system efficiency was achieved by varying the aspect ratio. Since the material volume is similar, we expect the material cost and the system cost to remain same for this analysis.

Material	Max. System efficiency	Electricity price (\$/kWh)
Bi ₂ Te ₃	2.5%	0.66 (current commercial modules)
Bi ₂ Te ₃	4.4%	0.37 (optimized module/ideal condition)
Si (PV)	12.5%	0.26 (our analysis)
Si (PV)	18%	0.20 – Industrial (500 kW) ^[256]
US data		0.25 – Commercial (50 kW) ^[256] 0.35 – Residential (2 kW) ^[256]
Si (PV) Developing countries	11%	0.50 - 2 (varies for different countries)
Grid extension in rural locations		0.70 - 1 (World Bank 1996)
Grid electricity cost (China)		0.07 (Government subsidy)

Table 25: Price of electricity for an STEG using various thermoelectric materials compared to PV

From the current economic analysis, the electricity cost from a Bi₂Te₃ commercial module seems to be too expensive compared to PV. However if we consider developing countries, where the PV price and the grid extension cost to remote locations are also very expensive (> \$0.50/kWh), the solar thermoelectric generators can be a cost competitive solution in that market.

6.2.1 Cost analysis using new TE material

There are many other parameters in the module design that can be varied to achieve lower cost and higher performance for the STEG. One such aspect of module redesigning that was considered at the end of Chapter 4 and in Chapter 5 was the new TE material. Using novel high *ZT* materials (efficiency ~ 5%), the electricity cost can be lowered to make it comparable to the US residential electricity price. The cost

for generated electricity was calculated to be 30 cents/kWh using the efficiency curve for MgSiSn-based TE material module (Figure 81). In this preliminary analysis, we assumed the TEG module price to be similar to that of Bi₂Te₃ material system (\$1.67/W_p). Since the raw materials for MgSiSn composition are earth-abundant elements, the base material prices are not as expensive as that for Bi₂Te₃ (Table 27). The high *ZT* performance for this silicide material was achieved for a sample which was prepared by ball milling and hot pressing^[132]. Such process is considered to be a low-cost material development technique. Thus, we can expect the actual cost of a generator module made from silicide material to be lower than that for Bi₂Te₃ material, leading to a lower electricity cost.

Material	Price (\$/kg)	Purity
Bi ₂ Te ₃ :	250 ^[35]	
Bi	13.40	99.99%
Te	188.25	99.99%
MgSiSn (Sb-doped):		
Mg	2.45	99.95%
Si	1.80	98.5%
Sn	8.5	
Sb	4.50	99.91%

Table 26: Price of raw material for thermoelectrics [Ref. www.metalprices.com, April 2009]

With novel materials working at a higher temperature range, the electricity from STEG can be comparable to the current PV prices. The results from this simple economic model will give a lower bound on the electricity price as many factors such as material and system degradation over the lifetime have not been considered.

6.2.2 Impact of dual (hybrid) use of STEG on cost

Another advantage of the solar thermoelectrics that can bring down the generated electricity cost is the potential of dual-use of the generator. As mentioned in Chapter 3, the hybrid generation capability of the solar thermoelectric generator with a solar cooker and a cooking stove was well appreciated by the villagers who tested the generator. The potential of longer use hours for the generator also helps in reducing the electricity cost. The total amount of the output power generated by the STEG is increased due to the additional use of the generator in the early mornings and in the evenings. The total electricity generated is calculated according to Equation 46, where apart from the power generated by using the solar cooker, there is a second term that represents the power generated by heat from the cooking stove. During

field trials, the input thermal power for the cooking stove was measured to be ~ 230-250 W with the boiling water experiment. This input thermal power is lower than the input power for a solar cooker. Thus, the output electrical power was also lower compared to that for the daytime generation (4 W vs. 8 W average output power). Nevertheless the additional power generation for extra 3-4 hours can boost the total energy generation and help in cost reduction.

$$\langle P_{electrical} \rangle = \left(\sum_i \eta(q_i) \times q_i \times C_{opt} \times A \times P_{q_i} \right) + \langle P_{cookstove} \rangle \quad (46)$$

From the field trial results, it was estimated that an additional 32% of extra electrical energy could be generated from the STEG by using the generator with the cooking stove along with the solar cooker. This estimation was done on the basis for 4 hour cooking time and an average output electrical power of 4 W as measured during the field trials. Using Equation 46, where $\langle P_{cookstove} \rangle$ is considered to be 32% of $\langle P_{electrical} \rangle$, the cost analysis for a Bi₂Te₃ optimized module in an ideal condition was performed. The generated electricity cost was 27 cents/kWh which is 27% lower than the cost for the optimized module using just the solar cooker.

6.3 Conclusion

The system costs as well as the levelized cost for electricity were discussed in the chapter for comparison with other off-grid electricity options, namely photovoltaics. The upfront system cost is an important consideration for adoption of a technology in developing countries as often times high capital cost is the barrier for penetration. Due to cheaper module cost, the solar thermoelectric generators can be a viable option for rural off-grid electricity with a total system cost below \$ 4/W. The levelized cost of electricity was also calculated for STEG as well as PV. The cost for the current prototype system is relatively high compared to the levelized cost in developed countries. However, when we take into consideration the cost of PV in the developing world market and the cost of grid extension in rural and remote communities, the STEG cost can be comparable and many times cheaper than other options. With higher efficiencies that can be achieved with module optimization or new TE material use, the cost of electricity will go down. An advantage that the solar thermoelectric generator has over PV is the potential of hybrid use where the STEG can be used at nighttimes or during cloudy/rainy conditions with the cooking stoves. With this added benefit, the generated electricity cost can be further reduced to make the STEG price comparable to residential PV cost.

Chapter 7

Conclusions and Future work

7.1 Summary

With nearly 1.6 billion people living without electricity, the demand for small-scale distributed power generation is high. In developing countries, especially in rural communities, residential electricity consumption is less than 0.5 kWh per day which is used for lighting and powering household appliances such as television, radio, and satellite receiver ^[259]. Till now, solar photovoltaics (PV) have been the prominent source for rural electrification, but the penetration has been slow, primarily due to large upfront system cost for the panels. Historically, thermoelectrics have been used mostly for limited applications such as deep-space exploration and waste heat recovery due to limited thermal-to-electrical conversion efficiency. Developments in new thermoelectric materials over the last two decades have shown a promise of higher material ZT and thus higher conversion efficiency, opening doors for new applications. This thesis investigated the potential of thermoelectrics with solar energy for electricity generation. Direct solar to electrical energy conversion is possible with a solar thermoelectric generator (STEG). STEG using inexpensive parabolic concentrators with high ZT modules can be a cost-effective alternative to solar photovoltaics for distributed power generation. We have designed and demonstrated a solar thermoelectric generator using concentrated sunlight (66x suns) incident on a Micro Alloyed Material Bi_2TE_3 thermoelectric module with a selective surface coating achieving 3% system efficiency in laboratory. This approach is shown to be cost competitive with small-scale solar PV that is currently available in developing countries. We demonstrated that a STEG can be integrated into solar cookers that are widely deployed in the developing world for electrical output power (11 W_p) while sterilizing drinking water.

A solar thermoelectric generator designed and built at MIT produced a useful power of 11 W to directly charge small appliances such as cell phones and was used to charge a small sealed lead-acid battery. The thermal power dissipated at the cold side of the generator was used to heat water to 70°C sufficient for sterilization. The generator can also be used at night with the waste heat from cooking stoves in the rural household providing useful electricity for lighting and small electrical appliances. In collaboration with a

non-profit organization, One Earth Designs, the generator was tested in rural Western China's Qinghai Province utilizing existing concrete/glass hybrid solar cookers and a portable metal solar cooker as the light concentrator. Data gathered from field test installations have been used for design improvements. The STEG as a part of a portable solar cooker called Sol-Source has won numerous design awards including Clinton Global Initiative Award, St. Andrews Prize for the Environment, and First place in National Sustainable Design competition. Collaboration with the organization has been an ongoing process to deploy thermoelectric generators as a part of Sol-Source 3-1 for solar cooking, heating and electricity generation for remote villages in rural Western China.

Modeling and optimization tools have been developed in order to understand the limitations and to enhance the system performance. A thermodynamic model based on energy balance and heat transfer was developed and tested against experiments for verification. The theoretical analysis had been used to explore various system parameters and advanced TE materials for solar thermoelectric applications. Unlike previous published theoretical models for solar thermoelectrics, our model utilized temperature dependent TE parameters and heat transfer coefficients to give a more accurate result for solar thermoelectrics. System parasitics (thermal and electrical) had been included in the model to represent the TEG module correctly. Ideal conditions (i.e. no parasitics) were also considered to explore the potential best performance and limitations of the generator. Instead of a fixed cold side module temperature, as considered in many theoretical models, the heat transfer coefficients for different heat sinks were used to analyze a more realistic system. The system efficiency for the generator is a product of the efficiency for the absorber and the thermoelectric module efficiency. The former is limited by the thermal losses (convection and radiation), while the latter is mostly limited by the TE material parameters.

One important advantage of using a concentrated solar thermoelectric in comparison to a flat-plate solar thermoelectric system is the suppression of the influence of the emissivity of the selective surface for the radiative loss at the hot-side absorber. For a flat-plate solar thermoelectric generator with thermal concentration, having a small long-wavelength emittance ($\epsilon < 0.1$) is critical for high system efficiency, whereas for the concentrated solar thermoelectrics, more than emittance, a large solar absorptance gives high system performance. For the STEG using solar cookers, the convective loss factor was contributing nearly 75% to the absorber inefficiency. Thus, higher emphasis was placed on convective loss suppression with absorber design that would restrain air flow around the hot side. An inexpensive selective surface coating with an emissivity of 0.22 was used to suppress the radiative loss.

Apart from the TE material parameters, the module efficiency can also be limited by the heat sink, as we saw in the prototype testing. In this research, a critical system component i.e. the heat sink for solar

thermoelectrics was analyzed which has often been neglected in other solar thermoelectric studies. In the literature, the highest system efficiency for solar thermoelectrics has been achieved by using an actively cooled heat sink. For a system level generator where high input thermal power (400-600 W) is considered, maintaining the heat sink temperature near ambient is a challenge. Different heat sink options with varying heat transfer coefficients were studied and characterized to be used with the STEG. Even though the forced water convection mechanism could keep the heat sink temperature near ambient, there were significant disadvantages in terms of cost, system complexity and additional energy requirement from a low-power generation system. Natural water convection was chosen as the heat sink mechanism for solar thermoelectrics to take advantage of the cogeneration aspect with water pasteurization, and to incorporate the system easily into the daily use of a solar cooker. The current commercial Bi_2Te_3 modules are limited in performance by the cold side module temperature of 80-90°C. With an actively cooled heat sink, higher output power (36% increase) can be expected for the current input thermal conditions, but this may not be enough to run the heat sink efficiently to make the system self-powered.

As a part of understanding the generator's limits, module optimization was discussed in Chapter 4. By changing the electrical and the thermal resistances of the TEG module, system efficiency can be varied to find an optimum aspect ratio that maximizes the output power. One issue with the current prototype design is the low thermal impedance of the module that does not allow for a large temperature gradient across the module ($\Delta T \sim 150\text{-}160\text{ K}$). The cold side temperature also limits the total input thermal power into the module because of the fixed operating temperature regime of 250°C. The issue of the operating temperature regime (250°C at the hot side) has been discussed in the thesis as it is an important limitation to the current system design to be used with high power solar concentrators. During module manufacturing, solders with higher melting points have to be used in order to take advantage of the optimized modules at higher thermal input power. As mentioned in Chapter 4, one of the options for such hard solders is Zn-Al solder used in aluminum welding, which has high melting temperature ($\sim 400^\circ\text{C}$). Pure metal (e.g. Ni) based metallurgy used in high temperature thermoelectrics can also be used to overcome this problem. The system efficiency could be improved by nearly 20% for the commercial modules by changing the aspect ratio slightly such that higher output power was possible for the same input thermal conditions.

During field trials, powerful solar concentrators were tested at greater altitudes that could give higher operating temperature than the regime where Bi_2Te_3 is most effective. At low temperature ($< 450\text{K}$), with commercial Bi_2Te_3 modules ($ZT_{\text{module}} = 0.4\text{-}0.6$), the system efficiency for solar thermoelectrics is limited to 3%. With the increase in temperature, the efficiency in this material system only degrades as the

material properties degrade. It has been shown here that, with the currently existing novel thermoelectric materials, which work better at slightly elevated temperatures, the system efficiency of STEGs can theoretically exceed 5% using inexpensive parabolic reflectors. For a higher ZT material (silicide $ZT \sim 1.1$) with an average temperature of 520 K, the system efficiency of 5.1% can be achieved for solar thermoelectrics with the input power range that is currently available with the local solar cookers. Thus, new TE material could be more efficient than Bi_2Te_3 for solar thermoelectrics.

During module redesign and optimization, the total TE material volume was considered to be the limiting parameter. Since, the cost of the material is a big factor for bulk TEG modules covering 20-40% of the module price; we tried to use the fixed volume to keep the cost similar in all our analysis. The issue of the cost, the material use and the potential material scarcity are important when considering application driven technology such as solar thermoelectrics. In this work, new thermoelectric materials were analyzed from a slightly different perspective of earth-abundance due to the potential of a large-scale application scope for solar thermoelectrics. As mentioned, the cost of the TE material is a large fraction of the module price, and the issues of abundance and material scarcity and their influence on material price become important. The current bulk high ZT materials largely have rare and toxic elements such as tellurium, lead, germanium and antimony whose limited crustal abundance could limit the scale of thermoelectric applications. Some of the more recent earth-abundant TE materials had been discussed which included oxides, silicides, and half-Heusler as prospect for new solar thermoelectric material. Even though the ZT for most earth-abundant thermoelectric materials are low compared to the traditional bulk TE materials, utilizing new material development technologies such as nanostructuring or nanocomposite synthesis, higher ZT could be achieved without changing the constituent elements. One such potential for a large ZT has been shown by metal-semiconductor superlattice structure. A large ZT could be possible in such a structure due to low thermal conductivity (phonon scattering at superlattice interface) and high thermopower (electron filtering with energy barriers).

We designed and tested a high-temperature Z -meter setup for thermoelectric generator device testing under large temperature gradients. The need for this setup was motivated by the limitations of current thermoelectric characterization tools especially at high temperatures. Using the Z -meter tool, a novel thermoelectric material utilizing metal-semiconductor superlattice ((Hf,Zr)N/ScN) was tested.

The measurement tool was used for a wide range of temperature (300-800 K), as well as for both bulk and thin-film samples ($\sim 100 \mu\text{m}$). One of the key improvements for this setup compared to other Z -meters was made in terms of the system parasitics. Both thermal and electrical parasitics for the setup were carefully studied and minimized for the measurements. More than 50% reduction in the electrical

parasitic compared to the lowest literature value was achieved by using a four-wire measurement. The parasitic was even further reduced by using metal-metal bonding in the setup for high temperature measurements. For accurate high temperature measurement, theory for radiation loss factor was developed and verified experimentally. Radiation influence was suppressed from the thermal conductivity measurement by using low emissivity gold coated metals in the setup. For system verification, ZT for different samples (Bi_2Te_3 , SiGe and ErAs : InGaAlAs) were measured and they were in good agreement with the published results measured with conventional techniques. One of the advantages of the Z -meter developed in this work was the ability to measure power density and efficiency along with the TE material parameters. High power density of 9.5 W/cm^2 was measured for the thin-film sample of ErAs : InGaAlAs using the Z -meter under a large temperature gradient of 255 K. Such a measurement tool will provide a good platform for verification and measurement of TE parameters in conjunction with conventional techniques to assure correct measurement and reduce uncertainties by measuring all TE parameters in a single sample.

First measurements of the TE parameters for a novel metal-semiconductor superlattice ($(\text{Hf,Zr})\text{N}/\text{ScN}$) were performed using the Z -meter setup. A reduction of 58% in the thermal conductivity was measured for the superlattice sample (2.5 W/m.K) compared to the semiconductor nitride ($\text{ScN} \sim 6 \text{ W/m.K}$) at room temperature. An increase in the thermal conductivity with respect to the rise in temperature was measured which was consistent with the $3-\omega$ measurement of the sample and it is most likely due to electronic contribution at higher temperatures. An acceptable high temperature Seebeck coefficient of $132 \mu\text{V/K}$ was measured for a finely polished nitride sample at 830 K. The relatively low Seebeck coefficient ($20\text{-}30 \mu\text{V/K}$) at lower temperature was most likely due to parallel electric shunts and parasitics which formed during sample preparation (dicing process). The superlattice interface parasitics also dominated all the electrical conductivity measurements. Improvements were made to lower the electrical resistivity at the interface, but it is still too large and dominates any electrical measurements of the sample. The individual TE parameters for the nitride samples show the promise with high Seebeck and low thermal conductivity. If the electrical conductivity for this sample is in the order of $5000 \text{ /}\Omega\text{cm}$ as suggested by the theory, the ZT value for the material would be ~ 1.3 at 830 K. This result indicates that the nitrides are potentially good TE materials but more work is needed to improve the electrical conductivity to enhance the ZT .

One of the inheriting challenges for a superlattice sample is the tradeoff between electron filtering/phonon scattering and the interface resistance of the superlattice. The decrease in thermal conductivity has been widely measured in many superlattice structures primarily due to the phonon scattering at the superlattice interfaces ^[157, 158], which has also been measured with the nitride samples in this work. However, increase

in the power factor has not been very prominent. One of the reasons could potentially be the decline in the electrical conductivity due to the contact interface parasitic resistance as was measured here. The idea behind preparing a bulk-laminate sample was to try and make thicker samples ($> 300 \mu\text{m}$) than the usual thin-film samples ($5\text{-}10 \mu\text{m}$) to measure power generation characteristics. The added interfaces during laminate processing further degraded the electrical conductivity of the sample. Even for the FIB pillar structures, the electrical conductivities in the range of $50\text{-}100 \text{ } \Omega\text{cm}$ were measured. As discussed above, in order to reach a reasonable ZT value > 1 , nearly two orders of magnitude higher electrical conductivity is needed. The multilayer and interfaces may limit the true electrical conductivity for a useful generator sample in the case of superlattice structures. Instead of nanostructuring with superlattices, utilizing nanodots or nano-composites could reduce or eliminate the issue of interface resistance problem, while still giving low thermal conductivity due to phonon scattering and maintaining high power factors.

In order to present a complete argument for the solar thermoelectric generator as a viable distributed power generation source, a system level model had been developed to understand the cost-benefit trade-offs for the technology and to compare it with other electricity sources. Due to cheaper module cost ($< \$2/W_p$), the solar thermoelectric generators can be an attractive alternative for rural off-grid electricity with a total system cost below $\$ 4/W$. Even though, the levelized cost of electricity for the current prototype system was relatively high compared to the levelized cost for grid and PV in developed countries, it was comparable to the cost of grid extension and PV in rural communities. With higher efficiencies brought by module redesign or by using better TE material, the electricity cost will go down. There can be a 44% cost reduction in the LCOE for the Bi_2Te_3 material by using optimized TE geometry compared to the current commercial modules. By taking advantage of the possibility of the hybrid use of the STEG with the solar cookers and the cooking stoves, larger total output power can be achieved which helps in decreasing the cost by another 27%.

In summary, this work has demonstrated that a solar thermoelectric generator is a technically and economically feasible method for distributed power generation. The technology has been tested and demonstrated in the lab, as well as in multiple field test locations in Western China. **Table 27** summarizes the options for basic lighting that are available in many rural communities which are not connected to grid. STEGs can provide useful power for such needs while being relatively inexpensive.

Category	Wood fire	Candles	PV system (5-10 W)	STEG
<i>Amount of light</i>	Insufficient	Insufficient	Sufficient	Sufficient
<i>Maintenance required</i>	High	High	low	low
<i>Initial investment to the user</i>	50 RMB (for stove)	-	* 280 RMB for 6 W (\$7.3/W _p) * 500 RMB for 10 W (\$7.85/W _p)	\$4-5/W _p
<i>Monthly expense</i>	-	(animal products)	-	-
<i>Reliable service</i>	No	No	Partial	Yes (dual use with cooking stove during cloudy rainy days)
<i>Comfort</i>	Low	Low	High	Medium (need to track the solar cooker and change water)

Table 27: Lighting options for a rural community not connected to grid

PV system price was gathered during the trip to China (2010-2011) by talking to vendors and customers

7.2 Future work

We concluded the previous section by stating that STEGs are a viable option for distributed power generation. Next, we explored the possibility of solar thermoelectrics for grid-parity in US to look at the prospect of the technology for future. The estimated module ZT to achieve grid parity (10 cents/kWh) with solar thermoelectrics is greater than 2 (Figure 125). This analysis was done by varying the material parameter, namely the thermal conductivity (0.1-2 W/m.K) to change the module ZT and hence the system efficiency. The current commercial TEG modules using Bi_2Te_3 have module $ZT < 1$. As discussed in Chapter 4 and 6, even with the same TE material, there are potential approaches of lowering the cost with new module designs. Similarly, the approach of utilizing earth-abundant TE material was discussed in Chapter 5 and 6 as another possibility to bring down the cost. Currently, there are few earth-abundant thermoelectric materials (silicide, half-Heusler) which have shown promise of material ZT closer to 1, which suggests that material $ZT \sim 2$ is plausible. At $ZT \sim 2$, the system efficiency that is larger than 15% can be expected for solar thermoelectrics in the temperature range of 500-600 K. The mindset during this research was thinking about solar thermoelectrics as a viable option for distributed power generation for remote access. With potential grid-parity, new wide spread applications for solar thermoelectrics can be

possible. With cheaper yet efficient TE materials, the STEG could overtake the concentrated PV technology that is currently being deployed in US which is limited due to high cost of III-V semiconductor materials used in photovoltaics.

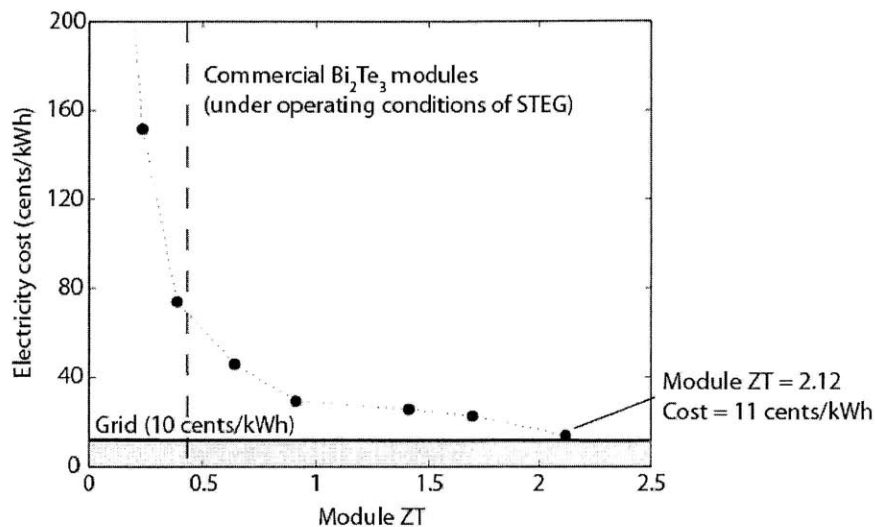


Figure 125: Electricity cost variation for STEG using different module ZT ; as the module ZT increases, the system efficiency also increases which leads to lower electricity price; in order to achieve grid parity, the required module ZT for thermoelectrics is > 2

Few reported nanostructured TE materials containing tellurium and lead have shown $ZT > 2$ [157, 158]. However, measurement reproducibility, material stability and module manufacturability have been issues for these high ZT materials [146]. These are few of the reasons why even after a decade of the published high ZT measurements; there are no modules available with such high material ZT . As discussed in Chapter 1, the system scaling is an important factor when deciding the generation technology. Looking at the current trend in material development, solar thermoelectrics can be much more competitive in smaller generation scale for remote and rural application than grid or utility scale.

One important aspect of this analysis that has also been focused in this thesis from early on is the concept of the module ZT and the material ZT . The requirement of $ZT > 2$ is for the TEG module that includes all the electrical and thermal parasitics. In the current commercial modules, the decline in ZT due to the parasitics ranges from 30-50%. For solar thermoelectrics, by eliminating the module parasitics, efficiencies closer to 4.5% can be achieved for Bi_2Te_3 material in an optimized module, which is 33% higher than that with current commercial modules. Completely eliminating electrical or thermal parasitics would be impossible during module making. However, potential new module designs have to be explored that can minimize the effect of the parasitics. Instead of the traditional rectangular TE leg assembly over a

ceramic wafer (Figure 3), innovative module designs such as the Y-form generator (Figure 126) from BSST Inc. could give module ZT s that are closer to the material ZT . These module designs from BSST Inc. are for high power density such that they utilize less TE material than the traditional thermoelectric design; thus offering opportunities for substantial cost reduction.

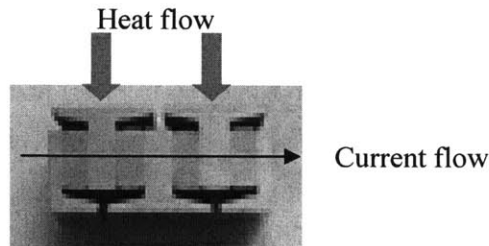


Figure 126: Y-form generator design from BSST Inc. that has lower

In this thesis, all the work for module design and material choice have been done by taking a single TE material type into consideration. Cascade thermoelectric material can be utilized to take advantage of higher temperature available with large input thermal powers^[260]. As we found out during the field trials, the hot side temperature of the module can easily reach beyond the operating temperature regime for the Bi_2Te_3 modules. Potential aspect ratio optimization and hard solder solutions were discussed in Chapter 4. One concept that could be beneficial in such a scenario is the use of cascade or segmented TE materials i.e. using two different materials which work at different temperature ranges. Material which performs better at higher temperature could be placed near the hot side, and lower temperature TE material could be placed underneath the first TE material and closer to the cold side. Concepts of such cascade TE modules can be found in literature that have shown higher theoretical efficiency than individual bulk materials^[261]. The main challenge for such a graded TE composition will be ensuring a good contact between the dissimilar materials without affecting the overall performance. The cost for the segmented TE also needs to be taken into consideration, as the fabrication cost will be higher than the usual single material TEG. Such cascade or segmented TE module designing, optimization and implementation for solar thermoelectrics will be an interesting path for research.

Near-Term plans for STEG implementation:

For the current generator system, the future work will involve further endurance testing in a potential large scale (100+ families) field trial such that statistically relevant data on user preference, performance and failure can be gathered. In collaboration with One Earth Designs, the test will be conducted in Gajia village, a nomadic village where the initial baseline survey has already been conducted. The trial will take

place for a period of one year starting May/June 2012 with a periodic survey every 1-2 months to keep an update on the generator use. A longer term test will help in understanding any time dependent interface deterioration or TE material degradation in the system. Design changes will be incorporated in the prototype to eliminate hot spot damages and thermal interface degradation as mentioned in Chapter 3. As a part of the system improvement, theoretical analysis for module redesigning was done. As the next step, we started a dialogue with a module manufacturing company (Marlow Inc.) with the intent of preparing modules with the optimized aspect ratio. The optimized leg dimensions have been given to the company and it is currently being considered for batch manufacturing. With the optimized design, we expect higher output power from the generator. Since the material volume is constant, we do not expect increase in the module cost for the optimized design.

With this thesis, a new application scope for thermoelectrics has been explored. In the past, due to low material ZT , the application for thermoelectrics was only in niche markets. The recent advancement in material technology has helped grow the application space for thermoelectrics. Even though the concept of solar thermoelectrics is an old one, with this work, we have reignited the interest within the thermoelectrics community by showing the potential of the system as a viable distributed power generation source. We have contributed to the solar thermoelectrics application by developing a complete system analysis model and by looking at the system level design constraints for improvements. With the system field trials, we have shown that moving the technology from research laboratory into real world is not very far. With the work in thermoelectric device design and new TE material characterization, the potential of solar thermoelectrics as a successful application is inevitable. The growing interest within the community partly driven by the need for clean energy and a potentially large market for such an application will keep the research on solar thermoelectrics going in the future.

Appendix 1: Properties of fluids

Temperature dependent properties of air and water were used for the calculations of the heat transfer coefficients for the system analysis ^[109].

<i>Temperature</i>								
K	°C	ρ (kg/m ³)	c_p (J/kg·K)	k (W/m·K)	α (m ² /s)	ν (m ² /s)	Pr	β (K ⁻¹)
Water								
273.16	0.01	999.8	4220	0.5610	1.330×10^{-7}	17.91×10^{-7}	13.47	-6.80×10^{-5}
275	2	999.9	4214	0.5645	1.340	16.82	12.55	-3.55×10^{-5}
280	7	999.9	4201	0.5740	1.366	14.34	10.63	4.36×10^{-5}
285	12	999.5	4193	0.5835	1.392	12.40	8.91	0.000112
290	17	998.8	4187	0.5927	1.417	10.85	7.66	0.000172
295	22	997.8	4183	0.6017	1.442	9.600	6.66	0.000226
300	27	996.5	4181	0.6103	1.465	8.568	5.85	0.000275
305	32	995.0	4180	0.6184	1.487	7.708	5.18	0.000319
310	37	993.3	4179	0.6260	1.508	6.982	4.63	0.000361
320	47	989.3	4181	0.6396	1.546	5.832	3.77	0.000436
340	67	979.5	4189	0.6605	1.610	4.308	2.68	0.000565
360	87	967.4	4202	0.6737	1.657	3.371	2.03	0.000679
373.15	100.0	958.3	4216	0.6791	1.681	2.940	1.75	0.000751
400	127	937.5	4256	0.6836	1.713	2.332	1.36	0.000895
420	147	919.9	4299	0.6825	1.726	2.030	1.18	0.001008
440	167	900.5	4357	0.6780	1.728	1.808	1.05	0.001132
460	187	879.5	4433	0.6702	1.719	1.641	0.955	0.001273
480	207	856.5	4533	0.6590	1.697	1.514	0.892	0.001440
500	227	831.3	4664	0.6439	1.660	1.416	0.853	0.001645
520	247	803.6	4838	0.6246	1.607	1.339	0.833	0.001909
540	267	772.8	5077	0.6001	1.530	1.278	0.835	0.002266
560	287	738.0	5423	0.5701	1.425	1.231	0.864	0.002783
580	307	697.6	5969	0.5346	1.284	1.195	0.931	0.003607
600	327	649.4	6953	0.4953	1.097	1.166	1.06	0.005141
620	347	586.9	9354	0.4541	0.8272	1.146	1.39	0.009092
640	367	481.5	25,940	0.4149	0.3322	1.148	3.46	0.03971
642	369	463.7	34,930	0.4180	0.2581	1.151	4.46	0.05679
644	371	440.7	58,910	0.4357	0.1678	1.156	6.89	0.1030
646	373	403.0	204,600	0.5280	0.06404	1.192	18.6	0.3952
647.0	374	357.3	3,905,000	1.323	0.00948	1.313	138.	7.735

T (K)	ρ (kg/m ³)	c_p (J/kg·K)	μ (kg/m·s)	ν (m ² /s)	k (W/m·K)	α (m ² /s)	Pr
Air							
100	3.605	1039	0.711×10^{-5}	0.197×10^{-5}	0.00941	0.251×10^{-5}	0.784
150	2.368	1012	1.035	0.437	0.01406	0.587	0.745
200	1.769	1007	1.333	0.754	0.01836	1.031	0.731
250	1.412	1006	1.606	1.137	0.02241	1.578	0.721
260	1.358	1006	1.649	1.214	0.02329	1.705	0.712
270	1.308	1006	1.699	1.299	0.02400	1.824	0.712
280	1.261	1006	1.747	1.385	0.02473	1.879	0.711
290	1.217	1006	1.795	1.475	0.02544	2.078	0.710
300	1.177	1007	1.857	1.578	0.02623	2.213	0.713
310	1.139	1007	1.889	1.659	0.02684	2.340	0.709
320	1.103	1008	1.935	1.754	0.02753	2.476	0.708
330	1.070	1008	1.981	1.851	0.02821	2.616	0.708
340	1.038	1009	2.025	1.951	0.02888	2.821	0.707
350	1.008	1009	2.090	2.073	0.02984	2.931	0.707
400	0.8821	1014	2.310	2.619	0.03328	3.721	0.704
450	0.7840	1021	2.517	3.210	0.03656	4.567	0.703
500	0.7056	1030	2.713	3.845	0.03971	5.464	0.704
550	0.6414	1040	2.902	4.524	0.04277	6.412	0.706
600	0.5880	1051	3.082	5.242	0.04573	7.400	0.708
650	0.5427	1063	3.257	6.001	0.04863	8.430	0.712
700	0.5040	1075	3.425	6.796	0.05146	9.498	0.715
750	0.4704	1087	3.588	7.623	0.05425	10.61	0.719
800	0.4410	1099	3.747	8.497	0.05699	11.76	0.723
850	0.4150	1110	3.901	9.400	0.05969	12.96	0.725
900	0.3920	1121	4.052	10.34	0.06237	14.19	0.728
950	0.3716	1131	4.199	11.30	0.06501	15.47	0.731
1000	0.3528	1142	4.343	12.31	0.06763	16.79	0.733
1100	0.3207	1159	4.622	14.41	0.07281	19.59	0.736
1200	0.2940	1175	4.891	16.64	0.07792	22.56	0.738
1300	0.2714	1189	5.151	18.98	0.08297	25.71	0.738
1400	0.2520	1201	5.403	21.44	0.08798	29.05	0.738
1500	0.2352	1211	5.648	23.99	0.09296	32.64	0.735

Appendix 2a: Survey Questionnaire I

GENERAL (Background)		
1.	How many people live in the house (family size)?	
2.	How many female, children are in the house?	Female Children (in school) Children (not in school)
3.	What is the primary occupation of the head of the house?	Nomad Farmer Businessman Teacher Other
ENERGY SOURCES:		
4.	What is your family's main fuel for cooking in winter?	Dung Wood Crops Coal Biogas Kerosene/Diesel Solar energy (cooker) Electricity Other
5.	What is your family's main fuel for cooking in summer?	Dung Wood Crops Coal Biogas Kerosene/Diesel Solar energy (cooker) Electricity Other
6.	What type of cooking stove do you have? <i>[If different for winter and summer, please mention by writing the season on the side]</i>	Mud (using wood, coal, dung, and crop) Electric stove Kerosene stove Solar cooker Biogas stove
7.	Which fuel do you use for lighting in your home? <i>[If different for winter and summer, please mention by writing the season on the side]</i>	Dung Wood Crops Coal Biogas Kerosene/Diesel Electricity (grid) Electricity (solar panel) Other
8.	Do you have any of these items in your house? <i>[If you have it, please mention the number of item and type]</i>	Solar panel Inverter Solar cooker Diesel generator Battery (rechargeable) (How do you recharge?)

		Battery (non-rechargeable)
		Charge controller
LIGHTING:		
9.	What do you use to light your home in the evening and night? Please also put the number of items used for lighting.	Candle Incandescent bulb Florescent light LED Kerosene lamp Other
10.	How many hours each night do you have light at your house?	
11.	What do you use the light for?	Reading..... Craft (knitting etc.)..... Preparing dinner..... Other
ELECTRICITY USE (Apart from lighting):		
11.	How many of each of these items do you own?	Television Radio Telephone Cell phone Digital watch/clock VCD player Water pump
12.	For what other immediate use would you want electricity? (Any job related machinery?)	
GRID ELECTRICITY:		
13.	What is the monthly electricity bill (cost)?	
14.	How many days do you have electricity supply in one year?	
15.	How many hours in a day do you have electricity?	

Survey results:

Gajia: A nomadic village of 100 families is located 200 km south of Xining (capital of Qinghai province). The villagers live in summer dwellings (tents) for 4-6 months in a year when they move around in high grasslands for herding purposes. There is no electricity in their summer housings. For winter, they move closer to towns and settle in adobe houses, which are grid connected. Animal dung is used for cooking and home heating by 86% of the families in winter as well as summer.

On average, the grid electricity during winter is used for less than 3 hours per day and the monthly electricity payment is ~ 9 RMB (< \$2). The overwhelming answer to why the electricity was used for such limited hours was the notion that electricity was expensive. The monthly electricity payment was nearly 20-25% of a household's total monetary income. During summer time, candles were used primarily for lighting inside tents (**Figure 127**). A few families did have working PV lighting systems. The

government had distributed subsidized PV systems in 2005 when 38 families bought them. In August 2010, when this survey was conducted, only 26 of the families had PV working in their summer dwellings. Lighting for summer was primarily the main electricity use that people needed in this village. The electricity source had to be portable as the villagers moved around 2-3 times during summer.

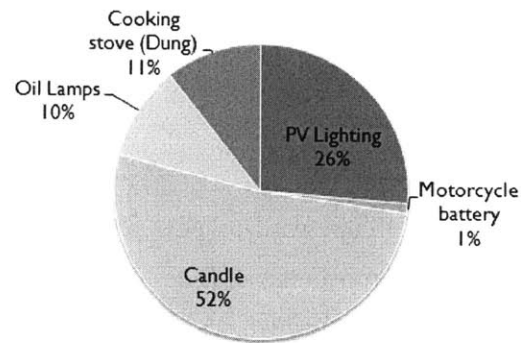


Figure 127: Survey result for lighting option during summer in Gajia village

Serjia: Another nomadic village of 27 families was visited for testing the STEG. The villagers spend 5-6 months during summer in high grasslands. Similar to Gajia, there was no electricity in the summer houses (**Figure 128**). The government had distributed PV system to the entire village in 2006. However, only 9 of them were functioning properly when we visited them in 2011. PV panel breakage during transportation, and battery failure (need to replace batteries every 6 months – 1 year due to bad charging practices) were the most common reasons for decline of PV system use in this village. In winter, like all nomadic communities, they move closer to bigger towns. Their winter settlement was grid connected at the beginning of 2011. They used electricity for basic lighting and television, with an average use for 3.2 hours. Their monthly electricity bill was also heavily government subsidized (8.5 Yuan ~ \$1.5). The information about electricity cost without subsidy is harder to obtain. According to Ref. [123], grid extension in many rural parts of China are extensively supported by the central government. In Tibet, the central government covered 100% of the cost incurred for electrification efforts, where as in Qinghai, 80% of the grid extension cost was covered by the central government ^[123].

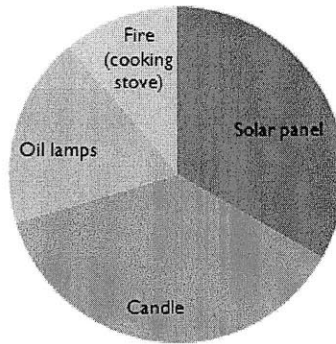


Figure 128: Survey result for lighting option during summer in Serjia village

Gangta: This was the only agricultural village where STEG was tested with local cookers. This small village of 35 households was located 160 km southeast from Xining, at a high altitude of 4,000 m. Each household had a solar cooker, which they received from a government program in 2006. The village was connected to grid in 1991. With limited power supply, the electricity was only used for lighting application till 2001, when larger capacity transformers were installed as a part of government’s rural electrification development initiative. As common in most rural households, animal dung was used extensively as cooking and heating fuel. Solar cookers were used for boiling water. On average, the villagers paid ~ 22 Yuan (< \$4) monthly electricity bill (Figure 129 a). The daily average electricity use was only for 3.2 hours (Figure 129). One of the main reasons for limited electricity use was the relative high cost (25% of monthly income) and also the fact that the families worked in the fields most of the day. Since the village was connected to the grid, there were more electrical appliances compared to nomadic villages. Affluent families had larger electrical appliances such as washing machines and refrigerators.

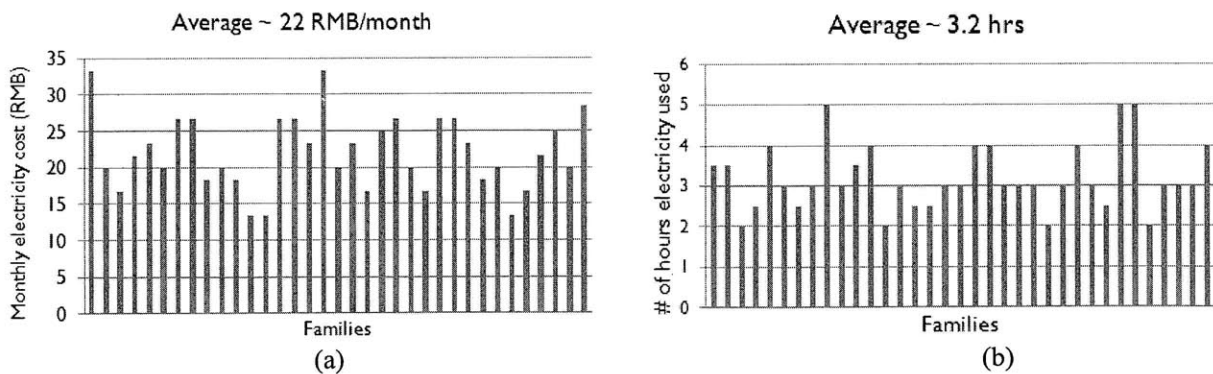


Figure 129: Survey result for (a) average monthly electricity bill; and (b) average electricity use (hours)

Survey size = 95 (nomadic) + 27 (nomadic) +35 (agricultural) = 157 families

		Nomadic	Agricultural	Nomadic (%)	Agricultural (%)
Fuel (cooking/heating)	Dung fuel (cooking)	122	35	100.00	100.00
	Petroleum product (kerosene, diesel)	13	0	10.66	0.00
	Wood fuel	7	30	5.74	85.71
	Coal fuel	1	11	0.82	31.43
Electricity for lighting	Grid (nomadic: winter)	122	35	100	100
	Grid availability			58	96
	Solar panel (*broken panel 20)	34	3	28	9
	Candles	59	0	48	0
	Oil lamps	15	0	12	0
	Usage of cooking stove for indoor lighting	13	0	11	0
	Other (motorcycle battery)	1	0	1	0
Electrical appliances	Cell phone	103	35	84	100
	TV	95	32	78	91
	Radio	32	16	26	46
	Electric cooker	0	7	0	20
	Refrigerator	0	15	0	43
	Washing machine	0	12	0	34
Fuel source	Dung fuel (cooking)	122	35	100.00	
	Petroleum product usage (kerosene, diesel)	13	0	8.28	
	Wood fuel	7	30	23.57	
	Coal fuel	1	11	7.64	
	# of hours electricity used	3	3.2		
	Cost of electricity (monthly)	8.6	22		

Appendix 2b: Survey Questionnaire II

LONG TRIAL (2-3 weeks):		
	How long does it take to boil water with the solar cooker using the generator?	
	How often did you use the generator over a week?	1 2 3 4 5 6 7 Never
	If you did not use the generator for more than twice, what is the reason?	Bad weather Generator broke Long time to boil water..... Hard to use Other
	If the generator failed, what broke? <i>[Field staff to evaluate the system and record the failure mechanism]</i>	Electrical connection Thermal contact (hot side) Thermal contact (cold side) Charge controller Battery Other
	How many days do you have electricity? (from the lead-acid battery provided)	
	How many hours in the evening do you have electricity for lighting? (from the lead-acid battery provided)	

Survey result:

frequency of use: #of days

house	1 survey (Aug.)	2 survey (Sept.)	3 survey (Nov.)
1	7	5	5
2	7	3	3
3	7	4	
4	7	4	4
5	7	7	7
6	7		2

total hours of charging:

house	1 survey (Aug.)		2 survey (Sept.)		3 survey (Nov.)	
	Solar cooker	Cooking stove	Solar cooker	Cooking stove	Solar cooker	Cooking stove
1	5.5	1.5	4	2	4	2
2	4.5	2	3	2	2	1.5
3	5	1.5	2	3		
4	6	2	3		3	
5	5	2.5	2	2		2
6	5	2.5			2	1

total hours for battery use:

house	1 survey (Aug.)		2 survey (Sept.)		3 survey (Nov.)	
	Lighting	Cell phone	Lighting	Cell phone	Lighting	Cell phone
1	2.5	2	2	2	2	2
2		4	1	2	2	
3	3	2	3			
4	2	4	2		2	
5	2	4	2		1	
6	2	2.5			2	

Appendix 3: MATLAB codes

I. STEG model: Bi_2Te_3 (steady-state)

```
function F = TEGBiTemaxeff(x,Is)
%%% TEG efficiency
%%% Concentrator:
A = (6.27e-2)^2;% area of the TE (hiZ module - 14W)
no = 0.875;      % optical efficiency
k1 = 0.5;        % reduced convection loss after using glass cover [W/m^2 K]
k2 = 2.83e-09;  % radiation loss [W/m^2 K^4]=emissivity (0.05)*Stefan
constant(5.67e-8) - selective surface properties
%%%TE module
As = 75e-6;      % aspect ratio for TE element (cross-section area/length) [m]
%%%System
kc = A/1.5e-4;  % thermal conductance(cold junction and heat sink - CuCu
interface (1.5 K cm^2/W) [W/K]
kh = A/1.5e-4;  % thermal conductance(hot junction and absorber - CuCu
interface (1.5 K cm^2/W) [W/K]
Tair = 293;     % atmosphere temperature [K]
% p-type element (temperature variation data not found)
ap = 2.3e-4;    % Seebeck coefficient (p-type) [V/K]
Rp = 1.75e-5;  % electrical resistivity (p-type) [Ohm m]
lp = 1.2;      % thermal conductivity (p-type) [W/m K]
%%% polynomial curve fit parameters for n-type element
p1 = 7.409e-012;
p2 = -3.947e-009;
p3 = 1.635e-007;
p4 = -0.0001326;
%an = p1*T^3 + p2*T^2 + p3*T + p4;    % Seebeck coefficient [V/K]
p5 = -2.739e-013;
p6 = 2.378e-010;
p7 = -1.043e-008;
p8 = 2.213e-006;
%rho = p1*T^3 + p2*T^2 + p3*T + p4;   % electrical resistivity [Ohm m]
p9 = -4.129e-008;
p10 = 6.759e-005;
p11 = -0.02962;
p12 = 5.393;
%k = p1*T^3 + p2*T^2 + p3*T + p4;     % thermal conductivity (p-type) [W/m K]
N = 49;                                % number of couples in a TE module (HiZ)
%Th = x(1); solar collector temperature [K]
%qh = x(2); net thermal power into the TE module [W]
%T1 = x(3); hot side temperature [K]
%T2 = x(4); cold side temperature [K]
%qc = x(5); net thermal power rejected from TE module [W]
%I = x(6); current [A]
%a = x(7)*N; Seebeck coefficient [V/K] - TE module
%Rn = x(8); n-type electrical resistivity [Ohm m]
%ln = x(9); n-type thermal conductivity [W/m K]
%R = x(10)*N; internal resistor [Ohm] - TE module
%k = x(11)*N; thermal conductance [W/K] - TE module
%Tc = x(12); heat sink temperature [K]
%Tavg = x(13); average temperature of TE [K]
```

```

%h = x(14); natural heat transfer coefficient [W/m2. K]
%Rl = x(15); load resistance [Ohm]
F = [no*Is*A-(k1*(x(1)-Tair)+k2*(x(1)^4-Tair^4))*A-x(2);
      x(1)-x(2)/kh-x(3);
      -x(4)+x(5)/kc+x(12);
      x(6)*x(7)*N*x(3)+x(11)*N*(x(3)-x(4))-x(6)^2*x(10)*N/2-x(2);
      x(7)*N*x(4)*x(6)+x(11)*N*(x(3)-x(4))+x(6)^2*x(10)*N/2-x(5);
      x(7)*N*(x(3)-x(4))/(x(10)*N+x(15))-x(6);
      -(p1*x(13)^3+p2*x(13)^2+p3*x(13)+p4)+ap-x(7);
      p5*x(13)^3+p6*x(13)^2+p7*x(13)+p8-x(8);
      p9*x(13)^3+p10*x(13)^2+p11*x(13)+p12-x(9);
      (1/As)*(x(8)+sqrt(lp*x(8)*Rp/x(9)))-x(10);
      As*(x(9)+sqrt(x(9)*lp*Rp/x(8)))-x(11)
      -x(5)+x(14)*(x(12)-Tair)*A;
      -x(13)+((x(3)+x(4))/2);
      -x(15) + N*x(10)*sqrt(1+x(13)*x(7)^2/(x(10)*x(11)))
      -x(14) - 4.079e-015*x(12)^5 + 2.125e-011*x(12)^4 - 4.282e-008*x(12)^3 +
      3.897e-005*x(12)^2 - 0.01556*x(12) + 29.99];

```

%%%

```

%% Melting point for BiTe = 858K
clear;
clc;
%% TEG efficiency
S_radiation = [100:100:3000]; % solar radiation [W/m2] for forced
convection
z = size(S_radiation);
m = 1;
%Th = x(1); solar collector temperature [K]
%qh = x(2); net thermal power into the TE module [W]
%T1 = x(3); hot side temperature [K]
%T2 = x(4); cold side temperature [K]
%qc = x(5); net thermal power rejected from TE module [W]
%I = x(6); current [A]
%a = x(7); Seebeck coefficient [V/K]
%Rn = x(8); n-type electrical resistivity [Ohm m]
%ln = x(9); n-type thermal conductivity [W/m K]
%R = x(10); internal resistor [Ohm]
%k = x(11); thermal conductance [W/K]
%Tc = x(12); heat sink temperature [K]
%Tavg = x(13); average temperature of TE [K]
%h = x(14); natural heat transfer coefficient [W/m2. K] initial value = 1 for
nc, 20 for fc
y = [300; 20; 300; 300; 1; 0.1; 4.25e-4; 1e-5; 1.5; 0.003; 0.0288; 300; 350;
20; 0.003];
for m =1:z(1,2);
    Is = S_radiation(m);
    x0 = y;
    x=fsolve(@TEGBiTemaxeff(x,Is),x0);
    T_hot(m) = real(x(1,1)); % (absorber) hot side temperature
    q_hot(m) = real(x(2,1)); % thermal power into TE hot side
    T_1(m) = real(x(3,1)); % TE hot side temp
    T_2(m) = real(x(4,1)); % TE cold side temp
    q_cold(m) = real(x(5,1)); % thermal power rejected from TE

```

```

    current(m) = real(x(6,1));           % current to the load
    Res(m) = real(x(10,1));             % electrical resistance of TE
    alpha(m) = real(x(7,1));           % Seebeck coefficient
    rn(m) = real(x(8,1));              % n-type electrical resistivity
    Ln(m) = real(x(9,1));              % n-type thermal conductivity
    k(m) = real(x(11,1));              % thermal conductance
    Tc(m) = real(x(12,1));            % heat sink temperature [K]
    Rl(m) = real(x(15,1));            % load resistance [Ohm]
    y = x;
    m = m+1;
end
A = (6.27e-2)^2;
no = 0.875;           % optical efficiency
k1 = 0.5;           % reduced convection loss after using glass cover [W/m^2 K]
k2 = 2.83e-09;     % radiation loss [W/m^2 K^4]=emissivity (0.05)*Stefan
constant(5.67e-8) - selective surface properties
Tair = 293;        % atmosphere temperature [K]
N = 49;           % no. of couples
qconv = ((T_hot-Tair).*k1).*A;           % convection loss [W]
qrad = ((T_hot.^4-Tair^4).*k2).*A;      % radiation loss [W]
ql = qconv + qrad;           % total concentrator loss [W]
deltaT = T_1-T_2;           % temperature difference across TE module
nsys = (current.^2).*Rl./(S_radiation.*A);
nTE = (current.^2).*Rl./(q_hot);
T = (T_1+T_2)./2;
Z = alpha.^2./(k.*Res);
nSC = (q_hot)./(S_radiation.*A);
nTE1 = ((T_1-T_2)./T_1).*((sqrt(1+Z.*T)-1)./(sqrt(1+Z.*T)+(T_2./T_1))); % TE
efficiency from ZT values

figure
subplot(3,1,1)
plot(T_hot,nsys*100,'r')
xlabel('Absorber Temperature [K]')
ylabel('System efficiency [%]')
subplot(3,1,2)
plot(T_hot,nTE1*100,'r')
xlabel('Absorber Temperature [K]')
ylabel('Solar concentrator efficiency [%]')
subplot(3,1,3)
plot(T_hot,nTE*100,'r')
xlabel('Absorber Temperature [K]')
ylabel('TE efficiency [%]')

figure
hold
plot(T_hot,S_radiation.*A, 'r')
plot(T_hot,ql, 'b')
plot(T_hot,qconv, '--b')
plot(T_hot,qrad, '+b')
plot(T_hot,q_hot, 'g')
plot(T_hot,q_cold, 'm')
plot(T_hot, (current.^2).*Rl, '--r')
xlabel('Absorber temperature [K]')
ylabel('Thermal power [W]')

```

```

figure
hold
plot(S_radiation,T_hot, 'r')
plot(S_radiation,T_1, 'b')
plot(S_radiation,T_2, 'g')
plot(S_radiation,Tc, 'm')
plot(S_radiation,deltaT, '+r')
xlabel('Incident radiation [W/m2]')
ylabel('Temperature [K]')

```

```

figure
plot(T_hot,Z.*T)

```

```

%%%%%%%%%%%%%%%%%%%%%%%%%%%%%%%%%%%%%%%%%%%%%%%%%%%%%%%%%%%%%%%%%%%%%%%%
%%%%%%%%%%%%%%%%%%%%%%%%%%%%%%%%%%%%%%%%%%%%%%%%%%%%%%%%%%%%%%%%%%%%%%%%

```

II. Heat transfer coefficient relations:

```

% heat transfer rate from heat sink side wall (natural air convection):
Tamb = 20+273; % [K] ambient temperature
Tsurf = [293:350]; % [K] water temperature (heat sink)
Ta = (Tamb+Tsurf)/2; % [K] average temperature of air near
sink surface
g = 9.8; % [m/s2] acc. due to gravity
B = 1/Tamb;
h = 13e-2; % [m] side wall height
% temperature dependent air kinematic viscosity [m2/s]
%t = [280,290,300,310,320,330,340,350];
%v = [1.385,1.475,1.578,1.659,1.754,1.851,1.951,2.073]*1e-5;
v = 9.7e-8.*Ta-1.3e-5; % [m2/s] air kinematic viscosity
%mean Pr for air over temperature range 280-350K
%Pr = [0.711,0.710,0.713,0.709,0.708,0.708,0.707,0.707];
Pr = 0.7091; % Prandtl number
% temperature dependent air thermal conductivity [W/m.K]
%k = [280,290,300,310,320,330,340,350];
%k = [0.02473,0.02544,0.02623,0.02684,0.02753,0.02821,0.02888,0.02984];
k = 7.1e-5.*Ta+0.0049; % [W/m.K] air thermal conductivity
%t = [280,290,300,310,320,330,340,350,400,450,500,550];
%l =
[1.879,2.078,2.213,2.340,2.476,2.616,2.821,2.931,3.721,4.567,5.464,6.421]*1e-
5;
l = 1.036e-010.*Ta.^2 + 8.07e-008.*Ta - 1.158e-005; % [m2/s] alpha
Ra = g.*B.*(Tsurf-Tamb).*h.^3/(v.*l);
Nu = 0.678.*Ra.^(1/4).*(Pr/(0.952+Pr)).^(1/4);
h_air = Nu.*k./h; % [W/m2 K] water temperature
dependent (air) heat transfer coefficient (cold side)
figure
plot(Tsurf,h_air)

```

```

% heat transfer rate from absorber side wall (natural air convection):
Tamb = 20+273; % [K] ambient temperature
Tsurf = [293:500]; % [K] heat sink

```

```

Ta = (Tamb+Tsurf)/2; % [K] average temperature of air near
sink surface
g = 9.8; % [m/s2] acc. due to gravity
B = 1/Tamb;
h = 6e-2; % [m] side wall height
% temperature dependent air kinematic viscosity [m2/s]
%t = [280,290,300,310,320,330,340,350];
%v = [1.385,1.475,1.578,1.659,1.754,1.851,1.951,2.073]*1e-5;
v = 9.7e-8.*Ta-1.3e-5; % [m2/s] air kinematic viscosity
%mean Pr for air over temperature range 280-350K
%Pr = [0.711,0.710,0.713,0.709,0.708,0.708,0.707,0.707];
Pr = 0.7091; % Prandtl number
% temperature dependent air thermal conductivity [W/m.K]
%t = [280,290,300,310,320,330,340,350];
%k = [0.02473,0.02544,0.02623,0.02684,0.02753,0.02821,0.02888,0.02984];
k = 7.1e-5.*Ta+0.0049; % [W/m.K] air thermal conductivity
%t = [280,290,300,310,320,330,340,350,400,450,500,550];
%l =
[1.879,2.078,2.213,2.340,2.476,2.616,2.821,2.931,3.721,4.567,5.464,6.421]*1e-
5;
l = 1.036e-010.*Ta.^2 + 8.07e-008.*Ta - 1.158e-005; % [m2/s] alpha
Ra = g.*B.*(Tsurf-Tamb).*h.^3/(v.*1);
Nu = 0.678.*Ra.^(1/4).*(Pr/(0.952+Pr)).^1/4;
h_air = Nu.*k./h; % [W/m2 K] water temperature
dependent (air) heat transfer coefficient (cold side)
figure
plot(Tsurf,h_air)

% evaporation loss (W/m2)
Pe = (9.675.*Tw.^2-5793.*Tw+8.678e+005); % 6m/s = 13.4 mph air
speed
%Pe = (8.1*Tw^2-4962*Tw+7.614e5); % 3m/s = 6.7 mph air speed
%Pe = (6.469*Tw^2-4005*Tw+6.211e+005); % 1.5m/s = 3.3 mph air
speed
%Pe = 0.04249*Tw^3-4.351*Tw^2+165.7*Tw-1980; % 0 m/s

```

```

%%%%%%%%%%%%%%%%%%%%%%%%%%%%%%%%%%%%%%%%%%%%%%%%%%%%%%%%%%%%%%%%%%%%%%%%
%%%%%%%%%%%%%%%%%%%%%%%%%%%%%%%%%%%%%%%%%%%%%%%%%%%%%%%%%%%%%%%%%%%%%%%%

```

III. STEG model: Bi₂Te₃ (optimization)

```

function F = TEGBiTe1_temp_depend_water_conv_parasitic1(x,Is)
% Simple analysis - Assumption: temperature dependent properties
% water convection heat sink

% variables: solar irradiance (Is), thickness of TE leg (t), area of TE leg
(Ate)
%Is = 900; % solar irradiance (W/m2)
%t = 2.25e-3; % thickness of a TE element [m]
%t = 4e-3;
t = 1.4e-3;
%Ate = 1.2e-3*1.2e-3;% area of TE element [m^2]
%Ate = 2.0e-3*2.0e-3;
Ate = 1.4e-3*1.4e-3;

```

```

% Thermal concentrator:
Aab = 2*pi*10e-2*2e-2; % surface area of absorber [m^2] -- small absorber
for concrete
Al = pi*(10e-2)^2; % cross section area of the heat sink [m^2] - pot
with water
A = pi*(12.5e-2)^2; % area of focal point in concentrator [m^2]
%no = 0.94; % optical absorption from hot side absorber
(selective surface)
no = 0.855;
%no = 0.96;
k1 = 5.0; % natural convection loss at the absorber side
[W/m^2.K]
k2 = 1.40e-8; % radiation loss = emissivity (0.25)*Stefan
constant(5.67e-8) - selective surface [W/m^2.K^4]
%k2 = 2.80e-9; % radiation loss = emissivity (0.05)*Stefan
constant(5.67e-8) - selective surface [W/m^2.K^4]
C = 10; % solar concentration
%%% TE module
Ac = 10e-2*10e-2; % area of TEG ceramic (same as 4 Marlow TEGS) [m^2]
n = 127*4;
% Thermal parasitic: Assumption: Same area n- and p-type element
kc = 20; % ceramic thermal conductivity [W/m.K]
Lc = 0.75e-3; % thickness of ceramic [m]
d = sqrt(pi^3*n^2/Ac)+sqrt(1/(Ate));
h = 5;
% total spreading resistance
Rspread = ((1/(2*kc*sqrt(Ac/(n^2)))))*((1-
sqrt(Ate*n^2/Ac))^(3/2))* (tanh(Lc*d)+kc*d/h)/(1+(kc*d/h)*tanh(Lc*d)))/(n^2);
% total contact resistance (dry metal-metal)
Rcont = 1e-4/Ac;
% ceramic thermal resistance
Rc = Lc/(Ac*kc);
Rthc = Rspread + Rcont + Rc; % total thermal impedance - cold side [K/W]
% same thermal parasitic on the hot side
Rthh = Rthc; % total thermal impedance - hot side [K/W]
% TEG module characteristic p-type element
ap = 2.3e-4; % Seebeck coefficient (p-type) [V/K]
Rp = 1.5e-5; % electrical resistivity (p-type) [Ohm m]
lp = 1.2; % thermal conductivity (p-type) [W/m K]
%%% polynomial curve fit parameters for n-type element
p1 = 7.409e-012;
p2 = -3.947e-009;
p3 = 1.635e-007;
p4 = -0.0001326;
%an = p1*T^3 + p2*T^2 + p3*T + p4; % Seebeck coefficient [V/K]
p5 = -2.739e-013;
p6 = 2.378e-010;
p7 = -1.043e-008;
p8 = 2.213e-006;
%rho = p1*T^3 + p2*T^2 + p3*T + p4; % electrical resistivity [Ohm m]
p9 = -4.129e-008;
p10 = 6.759e-005;
p11 = -0.02962;
p12 = 5.393;
%k = p1*T^3 + p2*T^2 + p3*T + p4; % thermal conductivity [W/m K]

```

```

%Lp = t = Ln      % assumption: same height legs
An = Ate;        % area of n-type TE element [m^2]
%R = (t/Ate)*(Rn+sqrt(Rn*Rp))*n; % electrical resistance of all TE elements
Rparasitic = 2*n*2*(1e-9/An);      % rough estimate

```

```
Tair = 298;
```

```
% cold side heat transfer
```

```

D = 20e-2;
u = 1.5;      % velocity of air flow ~ 3 mph [m/s]
L = 20e-2;    % diameter of the pot top ~ focal spot size [m]
Pr = 0.7091;

```

```

F = [no*Is*C*A-(k1*(x(2)-Tair)+k2*(x(2)^4-Tair^4))*Aab-x(1);
     x(2)-x(3)-x(1)*Rthh;
     -x(1)+(x(3)-x(4))/x(11)+n*(ap-x(9))*x(7)*x(3)-
     (x(7)^2*(x(13)+Rparasitic))/2;
     -x(8)+(x(3)-x(4))/x(11)+n*(ap-
x(9))*x(7)*x(4)+(x(7)^2*(x(13)+Rparasitic))/2;
     x(4)-x(6)-x(8)*Rthc;
     (x(3)+x(4))/2-x(5);
     -x(6)+x(8)/(x(15)*A1)+x(14);
     -x(7)+n*(ap-x(9))*(x(3)-x(4))/(2*(x(13)+Rparasitic));
     -x(9)+p1*x(5)^3+p2*x(5)^2+p3*x(5)+p4;
     -x(10)+p9*x(5)^3+p10*x(5)^2+p11*x(5)+p12;
     -x(11)+1/(((An/t)*(lp*sqrt((Rp)/(x(12))))+x(10)))*n);
     -x(12)+p5*x(5)^3+p6*x(5)^2+p7*x(5)+p8;
     -x(13)+(t/Ate)*(x(12)+sqrt(x(12)*Rp))*n;
     -x(8)+x(17)*A1+x(16)*A1*(x(14)-Tair);
     -x(15)+((-0.0038*x(14)^2+2*x(14)-1.6e2)*((1.7e-7*x(14)^2-
0.00012*x(14)+0.022)/(1.7e-7*x(6)^2-0.00012*x(6)+0.022))^0.14)*(-1e-
5*x(14)^2+0.0076*x(14)-0.79)/D;
     -x(16)+((0.023.*((u*L)./(9.7e-8.*((x(14)+Tair)/2)-1.3e-
5)).^0.8.*0.7091.^(1/3)).*((4.7e-8.*((x(14)+Tair)/2)+4.3e-6)./(4.7e-
8.*x(14)+4.3e-6)).^0.14).*(7.1e-5.*((x(14)+Tair)/2)+0.0049)./L;
     -x(17)+(8.1*x(14)^2-4962*x(14)+7.614e5)];

```

```
%%%%%%%%%%%%%%%%%%%%%%%%%%%%%%%%%%%%%%%%%%%%%%%%%%%%%%%%%%%%%%%%%%%%%%%%%
```

```
clear;
```

```
clc;
```

```
%%% TEG efficiency
```

```
l = 1.4e-3;      % length of a TE element [m]- for cross-section
```

```
Ate = l^2;
```

```
Is = 200:10:900;
```

```
a = size(Is);
```

```
Ac = 10e-2*10e-2; % area of TEG ceramic (same as 4 Marlow TEGS) [m^2]
```

```
n = 127*4;
```

```
As = Ate*n*2/Ac; % Area ratio: TE element area/ceramic area
```

```
% Thermal parasitic: Assumption: Same area n- and p-type element
```

```
kc = 20;        % ceramic thermal conductivity [W/m.K]
```

```
Lc = 0.75e-3;   % thickness of ceramic [m]
```

```
d = sqrt(pi^3*n*2/Ac)+sqrt(1/(Ate));
```

```

h = 5; % natural convection
% total spreading resistance
Rspread = ((1/(2*kc*sqrt(Ac/(n*2))))*((1-
sqrt(Ate*n*2/Ac))^(3/2))*(tanh(Lc*d)+kc*d/h)/(1+(kc*d/h)*tanh(Lc*d)))/(n*2);
% total contact resistance (dry metal-metal)
Rcont = 1e-4/Ac;
% ceramic thermal resistance
Rc = Lc/(Ac*kc);
Rthc = Rspread + Rcont + Rc; % total thermal impedance - cold side [K/W]
% same thermal parasitic on the hot side
Rthh = Rthc; % total thermal impedance - hot side [K/W]

y = [70; %qh = x(1) thermal power into hot side of TE [W]
365; %Th = x(2) solar absorber temperature [K]
365; %Th' = x(3) hot side temperature [K]
310; %Tc' = x(4) cold side temperature [K]
335; %Tavg = x(5) average TE element temperature
320; %Tc = x(6) heat sink temperature [K]
0.3; %I = x(7) current [A]
70; %qc = x(8) thermal power out to cold side of TE [W]
-2.4e-4; %an = x(9) n-type Seebeck coefficient [V/K]
1.5; %ln = x(10) n-type thermal conductivity [W/m.K]
1.0; %Rteg = x(11) thermal resistance of all TE elements [K/W]
1.5e-5; %Rn = x(12) n-type electrical resistivity [Ohm m]
17; %R = x(13) electrical resistance of all TE elements [Ohm]
307; %Tl = x(14) liquid temperature [K]
720; %hfw = x(15) forced water convection coefficient [W/m2.K]
17; %hna = x(16) natural air convection coefficient [W/m2.K]
1400]; %hl = x(17) heat loss from water surface -
evaporation/radiation [W/m2]

m = 1;
for m = 1:a(1,2)
x0 = y;
Isc = Is(m);
options = optimset('MaxFunEvals',1e8,'MaxIter',1e6,'TolFun',1e-6);
[x,exitflag] = fsolve(@(x)TEGBiTel_diff_intensity(x,Isc),x0,options);
qh(m) = x(1,1); % input thermal power
Th1(m) = x(2,1); % solar absorber temperature
Th2(m) = x(3,1); % hot side temperature
Tc2(m) = x(4,1); % cold side temperature
Tavg(m) = x(5,1); % average TE element temperature
Tc1(m) = x(6,1); % heat sink temperature
I(m) = x(7,1); % current
qc(m) = x(8,1); % output thermal power
an(m) = x(9,1);
ln(m) = x(10,1);
Rteg(m) = x(11,1);
Rn(m) = x(12,1);
R(m) = x(13,1);
Tl(m) = x(14,1);
hfw(m) = x(15,1);
hna(m) = x(16,1);
hl(m) = x(17,1);

```

```

    Y = x;
    m = 1 + m;
end
exitflag

% TEG module characteristic
ap = 2.3e-4;    % Seebeck coefficient (p-type) [V/K]
Rp = 1.5e-5;    % electrical resistivity (p-type) [Ohm m]
lp = 1.2;      % thermal conductivity (p-type) [W/m K]

An = Ate;      % area of n-type TE element [m^2]
Ap = An.*sqrt(Rp./Rn); % area of p-type TE element for maximum power density

%~Total thermal impedance of the module
Rth = Rthh+Rteg+Rthc;

Rparasitic = 2*n*2*(1e-9/An); % rough estimate
%~Total resistance of the module
Rmod = R+Rparasitic;

P = (I.^2).*Rmod; % output electrical power [W]
eff = (P./(Is.*10*pi*(12.5e-2)^2)).*100; % system efficiency
effab = (qh./(Is.*10*pi*(12.5e-2)^2)).*100; % absorber efficiency

%Check
s = n.*(ap-an);
effTE = ((I.^2).*Rmod./qh).*100;
effTE2 = ((Th2-
Tc2).^2.*s.^2)./(3.*Th2.*s.^2+8.*(1./Rteg).*Rmod+Tc2.*s.^2).*100;
Zmat = (((ap-an)*n).^2.*(Rteg)./R; % material Z
Zmod = (((ap-an)*n).^2.*(Rteg)./Rmod; % module Z
ZTmat = Zmat.*Tavg;
ZTmod = Zmod.*Tavg;
effTE3 = (Th2-Tc2)./(Th2.*2-(Th2-Tc2)./2 + 4./Zmod).*100; % TE efficiency
from ZT value for module

%[AX,H1,H2] = plotyy(Is,P,Is,eff);
%xlabel('Solar irradiance [W/m2]')
%set(get(AX(1),'Ylabel'),'String','Output electrical power [W]')
%set(get(AX(2),'Ylabel'),'String','System efficiency [%]')

x = Is.*10*pi*(12.5e-2)^2;
hold
plot(Is,eff,'g')

% thermal circuit equivalent:
Rhs = (Tc1-298)./qc;
Rabsorber = (Th1-298)./((1000*10*pi*(12.5e-2)^2)-qh);

%%%%%%%%%%%%%%%%%%%%%%%%%%%%%%%%%%%%%%%%%%%%%%%%%%%%%%%%%%%%%%%%%%%%%%%%
%%%%%%%%%%%%%%%%%%%%%%%%%%%%%%%%%%%%%%%%%%%%%%%%%%%%%%%%%%%%%%%%%%%%%%%%

```

IV. STEG model: MgSiSn (optimization)

```

function F = silicide_temp_depend_water_conv_parasitic1(x,Is)
% Simple analysis - Assumption: % temperature dependent properties
% water convection heat sink

% variables: solar irradiance (Is), thickness of TE leg (t), area of TE leg
(Ate)
%Is = 900;           % solar irradiance (W/m2)
t = 2.25e-3;        % thickness of a TE element [m]
%t = 1.4e-3;
Ate = 1.2e-3*1.2e-3;% area of TE element [m^2]
%Ate = 1.4e-3*1.4e-3;

% Thermal concentrator:
Aab = 2*pi*10e-2*2e-2; % surface area of absorber [m^2] -- small absorber
for concrete
Al = pi*(10e-2)^2;     % cross section area of the heat sink [m^2] - pot
with water
A = pi*(12.5e-2)^2;    % area of focal point in concentrator [m^2]
%no = 0.855;          % optical absorption from hot side absorber
(selective surface)
no = 0.96;
k1 = 5.0;              % natural convection loss at the absorber side
[W/m^2.K]
%k2 = 1.40e-8;        % radiation loss = emissivity (0.25)*Stefan
constant(5.67e-8) - selective surface [W/m^2.K^4]
k2 = 2.80e-9;         % radiation loss = emissivity (0.05)*Stefan
constant(5.67e-8) - selective surface [W/m^2.K^4]
C = 10;                % solar concentration
%%% TE module
Ac = 10e-2*10e-2;     % area of TEG ceramic (same as 4 Marlow TEGS) [m^2]
n = 127*4;
% Thermal parasitic: Assumption: Same area n- and p-type element
kc = 20;               % ceramic thermal conductivity [W/m.K]
Lc = 0.75e-3;         % thickness of ceramic [m]
d = sqrt(pi^3*n*2/Ac)+sqrt(1/(Ate));
h = 5;
% total spreading resistance
Rspread = ((1/(2*kc*sqrt(Ac/(n*2)))))*((1-
sqrt(Ate*n*2/Ac))^(3/2))*(tanh(Lc*d)+kc*d/h)/(1+(kc*d/h)*tanh(Lc*d)))/(n*2);
% total contact resistance (dry metal-metal)
Rcont = 1e-4/Ac;
% ceramic thermal resistance
Rc = Lc/(Ac*kc);
Rthc = Rspread + Rcont + Rc; % total thermal impedance - cold side [K/W]
% same thermal parasitic on the hot side
Rthh = Rthc;           % total thermal impedance - hot side [K/W]
% TEG module characteristic
% p-type element
ap = 2.0e-4;          % Seebeck coefficient (p-type) [V/K]
Rp = 1.0e-5;          % electrical resistivity (p-type) [Ohm m]
lp = 2.25;            % thermal conductivity (p-type) [W/m K]

%%% polynomial curve fit parameters for n-type element
%Seebeck = - 6.16e-007*T^3 + 0.000804*T^2 - 0.0687*T + 109;
p1 = 6.16e-007*1e-6;

```

```

p2 = -0.000804*1e-6;
p3 = 0.0687*1e-6;
p4 = -109*1e-6;
%an = p1*T^3 + p2*T^2 + p3*T + p4;          % Seebeck coefficient [V/K]

%rho = 4.76e-012*T^2 + 1.68e-008*T + 3.07e-006
p5 = 0;
p6 = 4.76e-12;
p7 = 1.68e-8;
p8 = 3.07e-6;
%rho = p1*T^3 + p2*T^2 + p3*T + p4;          % electrical resistivity [Ohm m]

%k = 1.55e-8*T^3-2.14e-5*T^2+0.00779*T+1.97;
p9 = 1.55e-8;
p10 = -2.14e-5;
p11 = 0.00779;
p12 = 1.97;
%k = p1*T^3 + p2*T^2 + p3*T + p4;          % thermal conductivity [W/m K]

%Lp = t = Ln      % assumption: same height legs
An = Ate;         % area of n-type TE element [m^2]

%R = (t/Ate)*(Rn+sqrt(Rn*Rp))*n; % electrical resistance of all TE elements
Rparasitic = 2*n*2*(1e-9/An);      % rough estimate

Tair = 298;

% cold side heat transfer
D = 15e-2;          % diameter of the stirrer [m]

u = 1.5;           % velocity of air flow ~ 3 mph [m/s]
L = 20e-2;         % diameter of the pot top ~ focal spot size [m]
Pr = 0.7091;

F = [no*Is*C*A-(k1*(x(2)-Tair)+k2*(x(2)^4-Tair^4))*Aab-x(1);
      x(2)-x(3)-x(1)*Rthh;
      -x(1)+(x(3)-x(4))/x(11)+n*(ap-x(9))*x(7)*x(3)-
      (x(7)^2*(x(13)+Rparasitic))/2;
      -x(8)+(x(3)-x(4))/x(11)+n*(ap-
x(9))*x(7)*x(4)+(x(7)^2*(x(13)+Rparasitic))/2;
      x(4)-x(6)-x(8)*Rthc;
      (x(3)+x(4))/2-x(5);
      -x(6)+x(8)/(x(15)*A1)+x(14);
      -x(7)+n*(ap-x(9))*(x(3)-x(4))/(2*(x(13)+Rparasitic));
      -x(9)+p1*x(5)^3+p2*x(5)^2+p3*x(5)+p4;
      -x(10)+p9*x(5)^3+p10*x(5)^2+p11*x(5)+p12;
      -x(11)+1/(((An/t)*(lp*sqrt((Rp)/(x(12))))+x(10)))*n);
      -x(12)+p5*x(5)^3+p6*x(5)^2+p7*x(5)+p8;
      -x(13)+(t/Ate)*(x(12)+sqrt(x(12)*Rp))*n;
      -x(8)+x(17)*A1;
      -x(15)+((-0.0038*x(14)^2+2*x(14)-1.6e2)*((1.7e-7*x(14)^2-
0.00012*x(14)+0.022)/(1.7e-7*x(6)^2-0.00012*x(6)+0.022))^0.14)*(-1e-
5*x(14)^2+0.0076*x(14)-0.79)/D;

```

```

-x(16)+((0.023.*((u*L)./(9.7e-8.*((x(14)+Tair)/2)-1.3e-
5)).^0.8.*0.7091.^(1/3)).*((4.7e-8.*((x(14)+Tair)/2)+4.3e-6)./(4.7e-
8.*x(14)+4.3e-6)).^0.14).*(7.1e-5.*((x(14)+Tair)/2)+0.0049)./L;
-x(17)+(8.1*x(14)^2-4962*x(14)+7.614e5)];

%%%%%%%%%%%%%%%%%%%%%%%%%%%%%%%%%%%%%%%%%%%%%%%%%%%%%%%%%%%%%%%%%%%%%%%%

clear;
clc;

% variables: solar irradiance (Is), thickness of TE leg (t), area of TE leg
(Ate)
%Is = 900;          % solar irradiance (W/m2)
Is = 200:10:1000;

%t = [1:0.1:5]*1e-3; % thickness of a TE element [m]
%t = 1.4e-3;
t = 2.25e-3;

%l = 1.4e-3;          % length of a TE element [m]- for cross-section
%l = [0.7:0.05:3.1]*1e-3;
l = 1.2e-3;

Ate = l.^2;
a = size(Is);

%%% TEG efficiency
C = 10;
Ac = 10e-2*10e-2;    % area of TEG ceramic (same as 4 Marlow TEGS) [m^2]
n = 127*4;
As = Ate.*n*2./Ac;  % Area ratio: TE element area/ceramic area

% Thermal parasitic: Assumption: Same area n- and p-type element
kc = 20;             % ceramic thermal conductivity [W/m.K]
Lc = 0.75e-3;       % thickness of ceramic [m]
d = sqrt(pi^3*n*2./Ac)+sqrt(1./(Ate));
h = 5;              % natural convection
% total spreading resistance
Rspread = ((1/(2*kc*sqrt(Ac/(n*2))))*((1-
sqrt(Ate.*n*2./Ac)).^(3/2)).*(tanh(Lc.*d)+kc.*d./h)./(1+(kc.*d./h).*tanh(Lc.*
d)))./(n*2);
% total contact resistance (dry metal-metal)
Rcont = 1e-4/Ac;
% ceramic thermal resistance
Rc = Lc/(Ac*kc);
Rthc = Rspread + Rcont + Rc; % total thermal impedance - cold side [K/W]
% same thermal parasitic on the hot side
Rthh = Rthc;           % total thermal impedance - hot side [K/W]

y = [130;           %qh = x(1)      thermal power into hot side of TE [W]
     670;           %Th = x(2)      solar absorber temperature [K]
     650;           %Th' = x(3)     hot side temperature [K]
     360;           %Tc' = x(4)     cold side temperature [K]
     500;           %Tavg = x(5)    average TE element temperature
     350;           %Tc = x(6)      heat sink temperature [K]

```

```

0.2;      %I = x(7)      current [A]
120;     %qc = x(8)     thermal power out to cold side of TE [W]
-8.0e-5; %an = x(9)     n-type Seebeck coefficient [V/K]
2.4;     %ln = x(10)    n-type thermal conductivity [W/m.K]
2;       %Rteg = x(11)  thermal resistance of all TE elements [K/W]
1.75e-5; %Rn = x(12)   n-type electrical resistivity [Ohm m]
100;     %R = x(13)    electrical resistance of all TE elements [Ohm]
350;     %Tl = x(14)   liquid temperature [K]
600;     %hfw = x(15)  forced water convection coefficient [W/m2.K]
20;      %hfa = x(16)  natural air convection coefficient [W/m2.K]
1000];   %hl = x(17)   heat loss from water surface -
evaporation/radiation [W/m2]

```

```

m = 1;
for m = 1:a(1,2)
    x0 = y;
    Is1 = Is(m);
    %At = Ate(m);
    %t = th(m);
    options = optimset('MaxFunEvals',1e8,'MaxIter',1e6,'TolFun',1e-6);
    [x,exitflag] =
    fsolve(@(x)silicide_temp_depend_water_conv_parasitic1(x,Is1),x0,'options');
    qh(m) = x(1,1);      % input thermal power
    Th1(m) = x(2,1);    % solar absorber temperature
    Th2(m) = x(3,1);    % hot side temperature
    Tc2(m) = x(4,1);    % cold side temperature
    Tavg(m) = x(5,1);   % average TE element temperature
    Tc1(m) = x(6,1);    % heat sink temperature
    I(m) = x(7,1);      % current
    qc(m) = x(8,1);     % output thermal power
    an(m) = x(9,1);
    ln(m) = x(10,1);
    Rteg(m) = x(11,1);
    Rn(m) = x(12,1);
    R(m) = x(13,1);
    Tl(m) = x(14,1);
    hfw(m) = x(15,1);
    hna(m) = x(16,1);
    hl(m) = x(17,1);

    y = x;
    m = 1 + m;
end
exitflag

```

```

% TEG module characteristic
ap = 2.0e-4; % Seebeck coefficient (p-type) [V/K]
Rp = 1.0e-5; % electrical resistivity (p-type) [Ohm m]
lp = 2.25; % thermal conductivity (p-type) [W/m K]

An = Ate; % area of n-type TE element [m^2]
Ap = An.*sqrt(Rp./Rn); % area of p-type TE element for maximum power density

%~Total thermal impedance of the module
Rth = Rthh+Rteg+Rthc;

```

```

%Rparasitic = 2.*n.*2.*(1e-9./An); % rough estimate
Rparasitic = 2.*(n.*(1e-9./An)+n.*(1e-9./Ap)); % parasitic contact
resistance between TE pellet and solder
%-Total resistance of the module
Rmod = R+Rparasitic;

P = (I.^2).*Rmod; % output electrical power [W]
eff = (P./(Is*C*pi*(12.5e-2)^2)).*100; % system efficiency
effab = (qh./(Is*C*pi*(12.5e-2)^2)).*100; % absorber efficiency

%Check
s = n.*(ap-an);
%qh1 = s*I.*Th2+K.*(Th2-Tc2)-(I.^2).*R./2;
%P1 = s^2.*(Th2-Tc2).^2./(4*R);
effTE = ((I.^2).*Rmod./qh).*100;
effTE2 = ((Th2-
Tc2).^2.*s.^2)/(3.*Th2.*s.^2+8.*(1./Rteg).*Rmod+Tc2.*s.^2).*100;
Zmat = (((ap-an)*n).^2.*(Rteg)./R; % material Z
Zmod = (((ap-an)*n).^2.*(Rteg)./Rmod; % module Z
ZTmat = Zmat.*Tavg;
ZTmod = Zmod.*Tavg;
effTE3 = (Th2-Tc2)/(Th2.*2-(Th2-Tc2)./2 + 4./Zmod).*100; % TE efficiency
from ZT value for module

x = Is.*10*pi*(12.5e-2)^2;

plot(Is, eff, '--r')
%plot(As, eff, 'r')
%plot(th.*1e3, eff, 'r')

```

```

%%%%%%%%%%%%%%%%%%%%%%%%%%%%%%%%%%%%%%%%%%%%%%%%%%%%%%%%%%%%%%%%%%%%%%%%
%%%%%%%%%%%%%%%%%%%%%%%%%%%%%%%%%%%%%%%%%%%%%%%%%%%%%%%%%%%%%%%%%%%%%%%%

```

V. Module optimization (constant TE volume):

```

clear;
clc;
% variables: solar irradiance (Is), thickness of TE leg (t), area of TE leg
(Ate)
Is = 900; % solar irradiance (W/m2)
%Is = 500:100:900;
%th = 2e-3; % thickness of a TE element [m]
th = [1:0.12:4]*1e-3;
%l = 1.2e-3; % length of a TE element [m]- for cross-section
l = [1.3:0.06:2.8]*1e-3;
Ate = l.^2;
a = size(th);
b = size(l);
%%% TEG efficiency
Ac = 10e-2*10e-2; % area of TEG ceramic (same as 4 Marlow TEGS) [m^2]
n = 440; % number of couples
As = Ate.*n*2./Ac; % Area ratio: TE element area/ceramic area
% Thermal parasitic: Assumption: Same area n- and p-type element

```

```

kc = 20;           % ceramic thermal conductivity [W/m.K]
Lc = 0.75e-3;     % thickness of ceramic [m]
d = sqrt(pi^3*n*2/Ac)+sqrt(1./(Ate));
h = 5;           % natural convection
% total spreading resistance
Rspread = ((1/(2*kc*sqrt(Ac/(n*2))))).*((1-
sqrt(Ate.*n*2./Ac)).^(3/2)).*(tanh(Lc.*d)+kc.*d./h)./(1+(kc.*d./h).*tanh(Lc.*
d))./(n*2);
% total contact resistance (dry metal-metal)
Rcont = 1e-4/Ac;
% ceramic thermal resistance
Rc = Lc/(Ac*kc);
Rthc = Rspread + Rcont + Rc;   % total thermal impedance - cold side [K/W]
% same thermal parasitic on the hot side
Rthh = Rthc;                 % total thermal impedance - hot side [K/W]
% TEG module characteristic
ap = 2.3e-4;   % Seebeck coefficient (p-type) [V/K]
Rp = 1.5e-5;   % electrical resistivity (p-type) [Ohm m]
lp = 1.2;      % thermal conductivity (p-type) [W/m K]
An = Ate;      % area of n-type TE element [m^2]
z = [70;       %qh = x(1)      thermal power into hot side of TE [W]
     365;      %Th = x(2)      solar absorber temperature [K]
     365;      %Th' = x(3)     hot side temperature [K]
     310;      %Tc' = x(4)     cold side temperature [K]
     335;      %Tavg = x(5)    average TE element temperature
     320;      %Tc = x(6)      heat sink temperature [K]
     0.3;      %I = x(7)       current [A]
     70;       %qc = x(8)      thermal power out to cold side of TE [W]
     -2.4e-4;  %an = x(9)      n-type Seebeck coefficient [V/K]
     1.5;      %ln = x(10)     n-type thermal conductivity [W/m.K]
     1.0;      %Rteg = x(11)    thermal resistance of all TE elements [K/W]
     1.5e-5;   %Rn = x(12)     n-type electrical resistivity [Ohm m]
     17;       %R = x(13)      electrical resistance of all TE elements [Ohm]
     307;      %Tl = x(14)     liquid temperature [K]
     720;      %hfw = x(15)    forced water convection coefficient [W/m2.K]
     17;       %hna = x(16)    natural air convection coefficient [W/m2.K]
     1400];    %hl = x(17)     heat loss from water surface -
evaporation/radiation [W/m2]
m = 1;
for m = 1:a(1,2)
    %Isc = Is(m);
    t = th(m);
    o = 1;
    for o = 1:b(1,2)
        y = z;
        x0 = y;
        At = Ate(o);
        options = optimset('MaxFunEvals',1e8,'MaxIter',1e6,'TolFun',1e-6);
        [x,exitflag] =
fsolve(@(x)TEGBiTe_ideal_hotside_final(x,At,t),x0,options);
        qh(m,o) = (x(1,1));   % input thermal power
        Th1(m,o) = (x(2,1));  % solar absorber temperature
        Th2(m,o) = (x(3,1));  % hot side temperature
        Tc2(m,o) = (x(4,1));  % cold side temperature
        Tavg(m,o) = (x(5,1)); % average TE element temperature

```

```

    Tc1(m,o) = (x(6,1));           % heat sink temperature
    I(m,o) = (x(7,1));             % current
    qc(m,o) = (x(8,1));           % output thermal power
    an(m,o) = (x(9,1));
    ln(m,o) = (x(10,1));
    Rteg(m,o) = (x(11,1));
    Rn(m,o) = (x(12,1));
    R(m,o) = (x(13,1));
    Tl(m,o) = (x(14,1));
    hfw(m,o) = (x(15,1));
    hna(m,o) = (x(16,1));
    hl(m,o) = (x(17,1));
    hla(m,o) = hl(m)/(Tl(m)-298);

    y = x;
    o = 1 + o;

end
    Ap = Ate(m)*sqrt(Rp./Rn);      % area of p-type TE element for maximum
power density
    Rth(m,:) = Rthh+Rteg(m,:)+Rthc; % Total thermal impedance of the module
    Rparasitic = 2.*(n.*(1e-9./Ate(m))+n.*(1e-9./Ap)); % parasitic contact
resistance between TE pellet and solder

    x0 = z;
    m = 1 + m;
end

%~Total resistance of the module
Rmod = R+Rparasitic;
P = (I.^2).*Rmod;                % output electrical power [W]
eff = (P./(Is.*10*pi*(12.5e-2)^2)).*100; % system efficiency
effab = (qh./(Is.*10*pi*(12.5e-2)^2)).*100; % absorber efficiency

%Check
s = n.*(ap-an);
P1 = s^2.*(Th2-Tc2).^2./(4*R);
effTE = ((I.^2).*Rmod./qh).*100;
effTE2 = ((Th2-
Tc2).^2.*s.^2)/(3.*Th2.*s.^2+8.*(1./Rteg).*Rmod+Tc2.*s.^2).*100;
Zmat = (((ap-an)*n).^2.*(Rteg)./R; % material Z
Zmod = (((ap-an)*n).^2.*(Rteg)./Rmod; % module Z
ZTmat = Zmat.*Tavg;
ZTmod = Zmod.*Tavg;
effTE3 = (Th2-Tc2)./(Th2.*2-(Th2-Tc2)./2 + 4./Zmod).*100; % TE efficiency
from ZT value for module

% thermal circuit equivalent:
Rhs = (Tc1-298)./qc;
Rabsorber = (Th1-298)./((1000*10*pi*(12.5e-2)^2)-qh);

[F,t]=meshgrid(As,th);
surf(F,t.*1000,real(eff))
xlabel('Fill factor (Area of TE/Area of ceramic)');
ylabel('Thickness of TE element (mm)');

```

```

xlabel('System efficiency (%)');

figure
contour(F,t.*1000,real(eff))
TH = transpose(th);
TH1 = repmat(TH,1,26);
ATE = repmat(Ate,26,1);
vol = TH1.*ATE;
hold
% unit wrong to get color contrast for contour lines
contour(F,t.*1000,vol.*100*100*2*440)

%%%%%%%%%%%%%%%%%%%%%%%%%%%%%%%%%%%%%%%%%%%%%%%%%%%%%%%%%%%%%%%%%%%%%%%%
%%%%%%%%%%%%%%%%%%%%%%%%%%%%%%%%%%%%%%%%%%%%%%%%%%%%%%%%%%%%%%%%%%%%%%%%

```

VI. Cost Model (LCOE):

```

clear;
clc;
% solar radiation on earth (Location: Xining, China)
A = load('solar_radiation1.txt');
x = A(:,3);
[n,xout]=hist(x,101);
a = ones(1,101)*8760;
% probability of getting certain solar radiation in a year
c = n./a;
x = xout.*1000;      % [W/m2]

af = pi*(25e-2/2)^2; % area of focus (25 cm diameter)
am = (10e-2)^2;      % area of the module [m^2]

% 15W TEG module from Taihuaxing: bulk quantity price $25 for 15 W module -
% $1.67 /Wp (20 W module used)
Price = 20*1.67;

% from thermodynamic analysis:
% Assumption: temperature dependent module parameter
% quadratic fit for efficiency vs. incident flux

% BiTe temperature dependent properties
% efficiency of the TEG module (using optimized aspect ratio/ideal condition)
eff = - 1.03e-005*x.^2 + 0.0134*x - 0.0392;
P = eff./100.*x.*af*10;
figure
plot(x,eff)
hold
% average output electrical power from TEG in a year [W]
avg_P = sum(((eff./100).*x.*c.*af*10));
% batterly + inverter + charge controller cost + bulb:
excess = 0.2*20*5 + 0.7*20 + 5 + 2;
% capital cost for one module and pot for generator with concentrator cost
CC = Price + 15 + 15 + excess;
% maintenance cost (5% of capital cost each year)
MC = 5/100*CC;

```

```

% loss due to tracking, total power in 20 years [W hr]
P = 0.85*(avg_P)*8760*20;
COE1 = ((CC+MC*20)/(P*1e-3))           % $/kW hr adding

% BiTe temperature dependent properties
% efficiency of the TEG module (using optimized aspect ratio/ideal condition)
+ power with cooking stove
eff = - 1.03e-005*x.^2 + 0.0134*x - 0.0392;
P = eff./100.*x.*af*10;
plot(x,eff)
% average output electrical power from TEG in a year [W]
avg_P = sum(((eff./100).*x.*c.*af*10));
% battery + inverter + charge controller cost + bulb:
excess = 0.2*20*5 + 0.7*20 + 5 + 2;
% capital cost for one module and pot for generator with concentrator cost
CC = Price + 15 + 15 + excess;
% maintenance cost (5% of capital cost each year)
MC = 5/100*CC;
% loss due to tracking, total power in 20 years [W hr]
P = 0.85*(avg_P*1.47)*8760*20;
COE1 = ((CC+MC*20)/(P*1e-3))           % $/kW hr adding

% BiTe - Marlow module (commercial module performance/ideal condition)
eff = - 5.1e-006*x.^2 + 0.0084*x - 0.056;
P = eff./100.*x.*af*10;
plot(x,eff,'r')
% average output electrical power from TEG in a year [W]
avg_P = sum(((eff./100).*x.*c.*af*10));
% battery + inverter + charge controller cost:
excess = 0.2*20*5 + 0.7*20 + 5 + 2;
% capital cost for one module and pot for generator with concentrator cost
CC = Price + 15 + 15 + excess;
% maintenance cost (5% of capital cost each year)
MC = 5/100*CC;
% total power in 20 years [W hr]
P = 0.85*(avg_P)*8760*20;
COE1 = ((CC+MC*20)/(P*1e-3))           % $/KW hr adding

% BiTe temperature dependent properties
% efficiency of the TEG module (current condition) excluding solar
concentrator efficiency
eff = - 3.2e-006*x.^2 + 0.0058*x - 0.035;
P = eff./100.*x.*af*10;
plot(x,eff,'g')
% average output electrical power from TEG in a year [W]
avg_P = sum(((eff./100).*x.*c.*af*10));
% battery + inverter + charge controller cost:
excess = 0.2*20*5 + 0.7*20 + 5 + 2;
% capital cost for one module and pot for generator with concentrator cost
CC = Price + 15 + 15 + excess;
% maintenance cost (5% of capital cost each year)
MC = 5/100*CC;
% total power in 20 years [W hr]
P = 0.85*(avg_P)*8760*20;
COE1 = ((CC+MC*20)/(P*1e-3))           % $/KW hr adding

```

```

% BiTe temperature dependent properties
% efficiency of the TEG module (current condition) + power with cooking stove
eff = - 3.2e-006*x.^2 + 0.0058*x - 0.035;
P = eff./100.*x.*af*10;
plot(x,eff,'g')
% average output electrical power from TEG in a year [W]
avg_P = sum(((eff./100).*x.*c.*af*10));
% battery + inverter + charge controller cost:
excess = 0.2*20*5 + 0.7*20 + 5 + 2;
% capital cost for one module and pot for generator with concentrator cost
CC = Price + 15 + 15 + excess;
% maintenance cost (5% of capital cost each year)
MC = 5/100*CC;
% total power in 20 years [W hr]
P = 0.85*(avg_P*1.47)*8760*20;
COE1 = ((CC+MC*20)/(P*1e-3))           % $/KW hr adding

% novel TE temperature dependent properties
% efficiency of the TEG module (ideal condition) excluding solar concentrator
efficiency
% higher concentration to take advantage of higher flux
eff = 0.0051*x - 0.032;
P = eff./100.*x.*af*15;
plot(x,eff,'m')
% average output electrical power from TEG in a year [W]
avg_P = sum(((eff./100).*x.*c.*af*15));
% battery + inverter + charge controller cost:
excess = 0.2*20*5 + 0.7*20 + 5 + 2;
% capital cost for one module and pot for generator with concentrator cost
CC = Price + 15 + 15 + excess;
% maintenance cost (5% of capital cost each year)
MC = 5/100*CC;
% total power in 20 years [W hr]
P = 0.85*(avg_P)*8760*20;
COE1 = ((CC+MC*20)/(P*1e-3))           % $/KW hr adding

% novel TE temperature dependent properties
% efficiency of the TEG module (ideal condition) excluding solar concentrator
efficiency
% higher concentration to take advantage of higher flux
Price = 20*0.20;
eff = 0.0051*x - 0.032;
P = eff./100.*x.*af*15;
plot(x,eff,'m')
% average output electrical power from TEG in a year [W]
avg_P = sum(((eff./100).*x.*c.*af*15));
% battery + inverter + charge controller cost:
excess = 0.2*20*5 + 0.7*20 + 5 + 2;
% capital cost for one module and pot for generator with concentrator cost
CC = Price + 15 + 15 + excess;
% maintenance cost (5% of capital cost each year)
MC = 5/100*CC;
% total power in 20 years [W hr]
P = 0.85*(avg_P)*8760*20;

```

```

COE1 = ((CC+MC*20)/(P*1e-3)) % $/KW hr adding

% For Si PV %
aS = 0.31*0.35; % area of PV panel ~ lutw org. (11 W panel)
PriceS = 2*11; % price for Si-based PV
e = 1.6e-19; % electron charge [C]
n = 3.4; % Si refractive index
h = 6.57e-16; % hbar [eV-s]
C = 3e8; % speed of light [m/s]
A = e*(n^2+1)*0.026/(4*pi^2*h^3*C^2)/100/100; % [A/cm^2]
Vm = 1.1-log((A*1.1^2*844)./(38e-3.*x)).*0.026-0.095; % [V]
eVm = 1.1-log((A*1.1^2*844)./(38e-3.*x)).*0.026-0.095; % [eV]
Jm = ((38e-3.*x)./844)./(1+0.026./eVm); % [A/cm^2]
effS = (Jm.*Vm)./(x).*100*100;
figure
plot(x,effS./2.5*100)
% average output electrical power from PV in a year [W]
avg_PS = sum((effS./2.5).*x.*c.*aS);
% capital cost for one module (no other cost included: installation etc,
electrical equipment)
CCS = PriceS+excess;
% maintenance cost (5% of capital cost each year)
MCS = 5/100*CCS;
COES = (CCS+MCS*20)/((avg_PS)*1e-3*8760*20) % $/KW hr

%%%%%%%%%%%%%%%%%%%%%%%%%%%%%%%%%%%%%%%%%%%%%%%%%%%%%%%%%%%%%%%%%%%%%%%%
%%%%%%%%%%%%%%%%%%%%%%%%%%%%%%%%%%%%%%%%%%%%%%%%%%%%%%%%%%%%%%%%%%%%%%%%

```

VII. Shrek (measurement code): TE material characterization

```

clear;
clc;
%%% This program will read the thermocouple readings from SRS 630
% and electrical measurements from the agilent multimeter%
% Author: Reja Amaty
% Creation Date: Jan 28, 2011 (version 5)
%%% OPEN Connection to the SRS630 & agilent multimeter

SRS = instrfind('Type', 'gpib', 'BoardIndex', 0, 'PrimaryAddress', 19, 'Tag',
'');
% Create the GPIB object if it does not exist
% otherwise use the object that was found.
if isempty(SRS)
    SRS = gpib('NI', 0, 19);
else
    fclose(SRS);
    SRS = SRS(1);
end
% Connect to instrument, SRS630.
fopen(SRS);

AGL = instrfind('Type', 'gpib', 'BoardIndex', 0, 'PrimaryAddress', 24, 'Tag',
'');
% Create the GPIB object if it does not exist

```

```

% otherwise use the object that was found.
if isempty(AGL)
    AGL = gpib('NI', 0, 24);
else
    fclose(AGL);
    AGL = AGL(1);
end
% Connect to instrument, Agilent 34401A.
fopen(AGL);
handles.AGL = AGL;

AGL2 = instrfind('Type', 'gpib', 'BoardIndex', 0, 'PrimaryAddress', 4, 'Tag',
'');
% Create the GPIB object if it does not exist
% otherwise use the object that was found.
if isempty(AGL2)
    AGL2 = gpib('NI', 0, 4);
else
    fclose(AGL2);
    AGL2 = AGL2(1);
end
% Connect to instrument, Agilent E3633A.
fopen(AGL2);

% Collect Data
n = 50;
A = 0.0:(0.10-0.0)/n:0.10;    % modulation voltage [V]
x = size(A);
n = x(1,2);
i = 1;
while i < (n+1)
    m = 1;
    for m = 1:10
        % take 1 points for a given bias current
        a = 'VOLT ';
        b = num2str(A(i));
        fprintf(AGL2, [a b]);
        fprintf(AGL2, 'MEAS:VOLT?');
        vin(m) = str2num(fscanf(AGL2));    %#ok<AGROW,ST2NM,SAGROW>
        il(m) = 1500*vin(m);    %#ok<AGROW>

        fprintf(AGL, 'MEAS:VOLT:DC?');
        vl(m) = str2num(fscanf(AGL));    %#ok<AGROW,ST2NM>

        fprintf(SRS, 'CHAN 5');
        fprintf(SRS, 'MEAS? 5');
        t5(m) = str2num(fscanf(SRS));    %#ok<AGROW,SAGROW,ST2NM>
        fprintf(SRS, 'CHAN 4');
        fprintf(SRS, 'MEAS? 4');
        t4(m) = str2num(fscanf(SRS));    %#ok<AGROW,SAGROW,ST2NM>
        fprintf(SRS, 'CHAN 3');
        fprintf(SRS, 'MEAS? 3');
        t3(m) = str2num(fscanf(SRS));    %#ok<AGROW,SAGROW,ST2NM>
        fprintf(SRS, 'CHAN 2');
        fprintf(SRS, 'MEAS? 2');
    end
    i = i + 1;
end

```

```

        t2(m) = str2num(fscanf(SRS));    %#ok<AGROW,SAGROW,ST2NM>
        %fprintf(SRS, 'CHAN 1');
        %fprintf(SRS, 'MEAS? 1');
        %t1(m) = str2num(fscanf(SRS));    %#ok<ST2NM,AGROW>
        m = m + 1;                        %#ok<FXSET>
    end
    Vin(i) = mean(vin);    %#ok<AGROW>
    V1(i) = mean(v1);     %#ok<AGROW,SAGROW>
    I1(i) = mean(i1);     %#ok<AGROW,SAGROW>
    %T1(i) = mean(t1);    %#ok<AGROW,SAGROW>
    T2(i) = mean(t2);    %#ok<AGROW,SAGROW>
    T3(i) = mean(t3);    %#ok<AGROW,SAGROW>
    T4(i) = mean(t4);    %#ok<AGROW,SAGROW>
    T5(i) = mean(t5);    %#ok<AGROW,SAGROW>
    i = i + 1;
end
fprintf(AGL2, 'VOLT 0');
%%% CLOSE Connection to the AGL2
% Disconnect all objects.
fclose(AGL2)
% Clean up all objects.
delete(AGL2);
clear AGL2
%%% CLOSE Connection to the SRS 630
% Disconnect all objects.
fclose(SRS);
% Clean up all objects.
delete(SRS);
clear SRS
%%% CLOSE Connection to the multimeter
% Disconnect all objects.
fclose(AGL);
% Clean up all objects.
delete(AGL);
clear AGL
Power = I1.*V1*1e-3;
R = V1./(I1.*1e-3);
figure
plot(R,Power.*1000,'r')
xlabel('Resistance (Ohm)')
ylabel('Power (mW)')
save 11_may_11_nitride_900_2 T2 T3 T4 T5 V1 I1 Power R

%%%%%%%%%%%%%%%%%%%%%%%%%%%%%%%%%%%%%%%%%%%%%%%%%%%%%%%%%%%%%%%%%%%%%%%%
%%%%%%%%%%%%%%%%%%%%%%%%%%%%%%%%%%%%%%%%%%%%%%%%%%%%%%%%%%%%%%%%%%%%%%%%

```

Bibliography

1. Prahalad, C.K. and A. Hammond, *Serving the World's Poor, Profitably*. Harvard Business Review, 2002. **80**(9): p. 48-58.
2. Gueymard, C.A., *The sun's total and spectral irradiance for solar energy applications and solar radiation models*. Solar Energy, 2004. **76**(4): p. 423-453.
3. Martins, J., *The impact of the use of energy sources on the quality of life of poor communities*. Social Indicators Research, 2005. **72**: p. 373-402.
4. Steigerwald, D.A., et al., *Illumination with Solid State Lighting Technology*. IEEE Journal on selected topics in quantum electronics, 2002. **8**(2): p. 310-320.
5. Mills, E., *The Specter of Fuel-Based Lighting*. Science, 2005. **308**: p. 1263-1264.
6. *PV for rural electrification in developing countries - programme design, planning and implementation*. 2003, International Energy Agency.
7. Ling, S., J. Twidell, and B. Boardman, *Household photovoltaic market in Xining, Qinghai Province, China: The role of local PV business*. Solar Energy, 2002. **73**(4): p. 227-240.
8. Byrne, J., et al., *Evaluating the potential of small-scale renewable energy options to meet rural livelihoods needs: A GIS- and lifecycle cost-based assessment of Western China's options*. Energy Policy, 2007. **35**: p. 4391-4401.
9. Zhao, H., N. Chi, and C. Li. *Study on Mechanism of Electric Universal Service Income Compensation - Lifeline Electricity Price*. in *The 2008 International Conference on Risk Management & Engineering Management*. 2008.
10. Hiranvarodom, S., R. Hill, and P.O. Keefe, *A strategic model for PV dissemination in Thailand*. Progress in Photovoltaics: Research and Applications, 1999. **7**: p. 409-419.
11. Philips, M. and B.H. Browne, *Accelerating PV markets in developing countries*, REPP.
12. Macias, E. and A. Ponce, *Photovoltaic solar energy in developing countries*. IEEE Xplore, 2006: p. 2323-2326.
13. Ullal, H.S. and B. Von-Roedern. *Thin film CIGS and CdTe photovoltaic technologies: commercialization, critical issues and applications*. in *22nd European Photovoltaic Solar Energy Conference and Exhibition*. 2007. Milan.
14. Pletka, R., *Renewable Energy Transmission Initiative - RETI Phase 2B*. 2010, Black & Veatch Corporation: San Francisco.
15. Kolodziej, A., *Staebler-Wronski effect in amorphous silicon and its alloys*. Opto-electronics Review, 2004. **12**(1): p. 21-32.
16. Faiman, D., S. Biryukov, and K.K. Pearlmuter. *PETAL: A research pathway to fossil-competitive solar electricity*. in *29th IEEE PVSC*. 2002. New Orleans.
17. Sinke, W.C., *A Strategic Research Agenda for Photovoltaic Solar Energy Technology*, in *PhotoVoltaic Technology Platform*. 2007, EU PV Technology Platform.
18. Yonghong, S., et al. *Experimental Investigation on Thermoelectric Generator for Micro Hybrid Power Source*. in *3rd International Symposium of Advanced Optical Manufacturing and Testing Technologies*. 2007: Proceedings of SPIE.
19. Andreev, V.M., et al. *Solar Thermophotovoltaic Converters: Efficiency Potentialities*. in *6th Conference on Thermophotovoltaic Generation of Electricity*. 2004. Freiburg.
20. Andreev, V., V.P. Khvostikov, and A.S. Vlasov, *Solar Thermophotovoltaics*, in *Concentrator Photovoltaics*. 2007, Springer Berlin/Heidelberg. p. 175-197.
21. Badescu, V., *Upper bounds for solar thermophotovoltaic efficiency*. Renewable Energy, 2004. **30**(2): p. 211-225.
22. Baxter, J., et al., *Nanoscale design to enable the revolution in renewable energy*. Energy and Environmental Science, 2009. **2**: p. 559-588.

23. Rephaeli, E. and S. Fan, *Absorber and emitter for solar thermo-photovoltaic systems to achieve efficiency exceeding the Shockley-Queisser limit*. Optics Express, 2009. **17**(17): p. 15145-15159.
24. Andreev, V.M., et al. *Solar thermophotovoltaic system with high temperature tungsten emitter*. in *31st IEEE PVSC*. 2005. Coronado Springs Resort, USA.
25. Kribus, A., *Thermal Integral Micro-Generation Systems for Solar and Conventional Use*. Journal of Solar Energy Engineering, 2002. **124**: p. 189-197.
26. Nakajima, N., K. Ogawa, and I. Fujimasa, *Study on microengines: miniaturizing Stirling engines for actuators*. Sensor Actuator, 1989. **20**: p. 75-82.
27. Kongtragool, B. and S. Wongwises, *A review of solar-powered Stirling engines and low temperature differential Stirling engines*. Renewable and Sustainable Energy Reviews, 2003. **7**: p. 131-154.
28. Stine, W.B. and R.B. Diver, *A Compendium of Solar Dish/Stirling Technology*. 1994, Sandia National Laboratories: Albuquerque.
29. Williams, A., *Pico hydro for cost-effective lighting*. Boiling point, 2007. **53**: p. 14-16.
30. *Renewable Energy Technologies and Poverty Alleviation: Overcoming Barriers and Unlocking Potentials*. 2007, Global Network on Energy for Sustainable Development (GNESD).
31. Telkes, M., *Solar Thermoelectric Generators*. Journal of Applied Physics, 1954. **25**(6): p. 765-777.
32. Green, M.A., et al., *Solar Cell Efficiency Tables*. Progress in Photovoltaics: Research and Applications, 2006. **14**(1): p. 45-51.
33. Poullikkas, A., *Economic analysis of power generation from parabolic trough solar thermal plants for the Mediterranean region - A case study for the island of Cyprus*. Renewable and Sustainable Energy Reviews, 2009. **13**(9): p. 2474-2484.
34. Taggart, S., *CSP: dish projects inch forward*. Renewable Energy Focus, 2008. **9**(4): p. 52-54.
35. Kraemer, D., et al., *High-performance flat-panel solar thermoelectric generators with high thermal concentration*. Nature Materials, 2011. **10**: p. 532-538.
36. Rowe, D.M., ed. *CRC Handbook of Thermoelectrics*. Conversion Efficient and Figure-of-Merit, ed. H.J. Goldsmid. 1995, CRC Press.
37. Rockwood, A.L., *Relationship of thermoelectricity to electronic entropy*. Phys. Rev. A, 1984. **30**(5): p. 2843-4.
38. Fleurial, J.-P. *Selection and evaluation of materials for thermoelectric applications*. in *Short Course on Thermoelectrics (SCT-93)*. 1993. Japan.
39. Mayer, P.M., *High-density thermoelectric power generation and nanoscale thermal metrology*, in *Electrical Engineering and Computer Science*. 2007, Massachusetts Institute of Technology: Cambridge.
40. Nuwayhid, R.Y., D.M. Rowe, and G. Min, *Low cost stove-top thermoelectric generator for regions with unreliable electricity supply*. Renewable Energy, 2003. **28**: p. 205-222.
41. Majumdar, A., *Thermoelectricity in Semiconductor Nanostructures*. Science, 2004. **303**(5659): p. 777-778.
42. Zide, J.M.O., et al., *Demonstration of electron filtering to increase the Seebeck coefficient in $In_{0.53}Ga_{0.47}As/In_{0.53}Ga_{0.28}Al_{0.19}As$ superlattices*. Phys. Rev. B, 2006. **74**.
43. Zeng, G., et al., *ErAs :($InGaAs$) $1-x$ ($InAlAs$) x alloy power generator modules*. Applied Physics Letters, 2007. **91**(263510).
44. Vashaee, D. and A. Shakouri, *Improved Thermoelectric Power Factor in Metal-Based Superlattices*. Physics Review Letter, 2004. **92**(106103).
45. Feldman, J.L., et al., *Lattice dynamics and reduced thermal conductivity of filled skutterudites*. Phys. Rev. B, 2000. **61**.
46. Kosuga, A., et al., *Thermoelectric properties of p-type ($AgSbTe_2$) x ($Pb_{0.5}Sn_{0.5}Te$) $1-x$ ($x = 0.05, 0.09, 0.2$)*. Journal of Alloys and Compounds, 2006. **416**: p. 218-221.

47. Brown, S.R., et al., *Yb₁₄MnSb₁₁: New high efficiency thermoelectric material for power generation*. Chemistry of Materials, 2006. **18**(7): p. 1873-1877.
48. Harman, T.C., et al., *Nanostructured Thermoelectric Materials*. Journal of Electronic Materials, 2005. **34**(5): p. 19-22.
49. Stabler, F., *Benefits of thermoelectric technology for the automobile*, in *DOE Thermoelectric Workshop*. 2011: San Diego, CA.
50. Bell, L.E., *Cooling, Heating, Generating Power, and Recovering Waste Heat with Thermoelectric Systems*. Science, 2008. **321**(5895): p. 1457-1461.
51. Leonov, V. and R.J.M. Vullers, *Wearable Thermoelectric Generators for Body-Powered Devices*. Journal of Electronic Materials, 2009. **38**(7): p. 1491.
52. Marlow Inc.
53. Snyder, G.J. and E.S. Toberer, *Complex thermoelectric materials*. Nature Materials, 2008. **7**: p. 105-114.
54. Fthenakis, V. and K. Zweibel, *The National Center for Photovoltaics and Solar Program Review Meeting*. 2003, National Renewable Energy Laboratory: Denver, Colorado.
55. Hendricks, T. and W.T. Choate, *Industrial Technologies Program*. 2006, U.S. Department of Energy.
56. Weidenkaff, A., et al., *Development of thermoelectric oxides for renewable energy conversion technologies*. Renewable Energy, 2008. **33**: p. 342-347.
57. Maensiri, S. and W. Nuansing, *Thermoelectric oxide NaCo₂O₄ nanofibers fabricated by electrospinning*. Materials Chemistry and Physics, 2006. **99**(1): p. 104-108.
58. Wang, S. and N. Mingo, *Improved thermoelectric properties of Mg₂Si_xGe_{1-x}Sn_{1-x-y} nanoparticle-in-alloy materials*. Applied Physics Letters, 2009. **94**(203109).
59. Itoh, T. and M. Yamada, *Synthesis of Thermoelectric Manganese Silicide by Mechanical Alloying and Pulse Discharge Sintering*. Journal of Electronic Materials, 2009. **38**(7): p. 925-929.
60. Ozturk, H.H., *Comparison of Energy and Exergy Efficiency for Solar Box and Parabolic Cookers*. Journal of Energy Engineering, 2007. **133**(1): p. 53-62.
61. Habeebullah, M.B., A.M. Khalifa, and I. Olwi, *The oven receiver: An approach toward the revival of concentrating solar cookers*. Solar Energy, 1995. **54**(4): p. 227-237.
62. Schwarzer, K. and M.E.V.d. Silva, *Characterization and design methods of solar cookers*. Solar Energy, 2008. **82**: p. 157-163.
63. Parretta, A., et al., *Optical efficiency of solar concentrators by a reverse optical path method*. Optics Letters, 2008. **33**(18): p. 2044-2046.
64. Price, H., E. Lupfert, and D. Kearney, *Advances in Parabolic Trough Solar Power Technology*. Journal of Solar Energy Engineering, 2002. **124**(2): p. 109.
65. Horne, S., et al. *A solid 500 compound concentrator PV design*. in *IEEE 4th World Conference on Photovoltaic Energy Conversion*. 2006.
66. Kalogirou, S.A., *Solar thermal collectors and applications*. Progress in Energy and Combustion Science, 2004. **30**(3): p. 231-295.
67. Winston, R. and H. Hinterberger, *Principles of cylindrical concentrators for solar energy*. Solar Energy, 1975. **17**(4): p. 255-258.
68. Stine, W.B. and R.W. Harrigan, *Power From The Sun*. 1985: John Wiley and Sons Inc.
69. Rabl, A., *Comparison of Solar Collectors*. Solar Energy, 1975. **18**: p. 93-111.
70. Rabl, A., *Active Solar Collectors and Their Applications*. 1985: Oxford University Press.
71. Kolb, G.J., et al., *Heliostat Cost Reduction Study*. 2007, Sandia National Laboratories: Albuquerque.
72. Segal, A. and M. Epstein, *The Optics of the Solar Tower Reflector*. Solar Energy, 2000. **69**: p. 229-241.
73. Brooks, M.J., I. Mills, and T.M. Harms, *Performance of a parabolic trough solar collector*. Journal of Energy in Southern Africa, 2006. **17**(3).

74. Shuai, Y., X. Xia, and H. Tan, *Radiation performance of dish solar concentrator/cavity receiver systems*. Solar Energy, 2007. **82**: p. 13-21.
75. Sodano, H.A., et al., *Recharging batteries using energy harvested from thermal gradients*. Journal of Intelligent Material Systems and Structures, 2007. **18**: p. 3-10.
76. *Solkote: HI/Sorb-II - Selective Solar Coating*, Solec Inc.: New Jersey, USA.
77. Rybicki, G.B. and A.P. Lightman, *Radiative Processes in Astrophysics*. 1979, New York: John Wiley & Sons.
78. Yin, Y., et al., *Direct current reactive sputtering Cr-Cr₂O₃ cermet solar selective surface for solar hot water applications*. Thin Solids Film, 2009. **517**(5): p. 1601-1606.
79. Zhang, Q., *Metal-AlN cermet solar selective coatings deposited by direct current magnetron sputtering technology*. Journal of Physics D: Applied Physics, 1998.
80. Bermel, P., et al., *Improving thin-film crystalline silicon solar cell efficiencies with photonic crystals*. Optics Express, 2007. **15**(25).
81. Heinzl, A., et al., *Radiation filters and emitters for the NIR based on periodically structured metal surfaces*. Journal of Modern Optics, 2000. **47**(13): p. 2399-2419.
82. Lin, S.Y., J. Moreno, and J.G. Fleming, *Three-dimensional photonic-crystal emitter for thermal photovoltaic power generation*. Applied Physics Letters, 2003. **83**(2).
83. Kennedy, C.E. *Progress to develop an advanced solar-selective coating*. in *14th Biennial CSP Solar PACES (Solar Power and Chemical Energy Systems) Symposium*. 2008. Las Vegas.
84. Yin, Y., et al., *Thermal oxidation properties of titanium nitride and titanium-aluminium nitride materials - A perspective for high temperature air-stable solar selective absorber applications*. Thin Solid Films, 2007. **515**: p. 2829-2832.
85. Harding, G.L. and B. Window, *Graded metal carbide solar selective surfaces coated onto glass tubes by a magnetron sputtering system*. Journal of Vacuum Science Technology, 1979. **16**(6): p. 2101-2104.
86. Adsten, M., et al., *Optical characterization of industrially sputtered nickel-nickel oxide solar selective surface*. Solar Energy, 2000. **68**(4): p. 325-328.
87. Chen, R., et al., *Nanowires for Enhanced Boiling Heat Transfer*. Nano Letters, 2008. **9**: p. 548-553.
88. Truong, B., et al., *Modification of sandblasted plate heaters using nanofluids to enhance pool boiling critical heat flux*. International Journal of Heat and Mass Transfer, 2010. **53**(1-3): p. 85-94.
89. Vatcharasanthien, N., et al., *Design and analysis of solar thermoelectric power generation system*. International Journal of Sustainable Energy, 2005. **24**(3): p. 115-127.
90. Omer, S.A. and D.G. Infield, *Design optimization of thermoelectric devices for solar power generation*. Solar Energy Materials and Solar Cells, 1998. **53**: p. 67-82.
91. Xi, H., L. Luo, and G. Fraisse, *Development and applications of solar-based thermoelectric technologies*. Renewable and Sustainable Energy Reviews, 2005. **11**: p. 923-936.
92. Goldsmid, H.J., J.E. Giutronich, and M.M. Kaila, *Solar Thermoelectric Generator Using Bismuth Telluride Alloys*. Solar Energy, 1980. **24**: p. 435-440.
93. Khattab, N.M. and E.T.E. Shenawy, *Optimal operation of thermoelectric cooler driven by solar thermoelectric generator*. Energy Conversion and Management, 2006. **47**: p. 407-426.
94. Maneewan, S., et al., *Investigation on generated power of thermoelectric roof solar collector*. Renewable Energy, 2004. **29**(5): p. 743-752.
95. Fan, H., R. Singh, and A. Akbarzadeh, *Electric power generation from thermoelectric cells using a solar dish concentrator*. Journal of Electronic Materials, 2011. **40**(5): p. 1311-1320.
96. Movsumov, E.A. and A.M. Bairamov, *Regime characteristics of a solar thermoelectric generator and comparison of experimental and calculated data*. Geliotekhnika, 1980. **16**(6): p. 69-70.
97. Fuschillo, N., et al., *Solar Thermoelectric Generator for Near-Earth Space Applications*. IEEE Transactions on Electron Devices, 1966. **13**(4): p. 426-432.

98. Riffat, S.B. and X. Ma, *Thermoelectrics: a review of present and potential applications*. Applied Thermal Engineering, 2003. **23**: p. 913-935.
99. Amatya, R. and R.J. Ram, *Solar thermoelectric generator for micropower applications*. Journal of Electronic Materials, 2010. **39**(9): p. 1735-1740.
100. Rowe, D.M., *A high performance solar powered thermoelectric generator*. Applied Energy, 1981. **8**(4): p. 269-273.
101. Chen, J., *Thermodynamic analysis of a solar-driven thermoelectric generator*. Journal of Applied Physics, 1996. **79**(5).
102. Dent, C.L. and M.H. Cobble. *A solar thermoelectric generator and analysis*. in *International Conference on Thermoelectric Energy Conversion*. 1982. Arlington, TX.
103. A.S. Roberts (Jr.), K.E.S., *Hybrid thermoelectric solar collector design and analysis*. Journal of Solar Energy Engineering, 1982. **104**(4): p. 373-377.
104. Shanmugam, S., M. Eswaramoorthy, and A.R. Veerappan, *Mathematical modeling of thermoelectric generator by solar parabolic dish collector*. Applied Solar Energy, 2011. **47**(1): p. 31-35.
105. Atik, K., *Numerical simulation of a solar thermoelectric generator*. Energy Sources, Part A: Recovery, Utilization, and Environmental Effects, 2011. **33**(8): p. 760-767.
106. Cai, Y., et al., *A general model for the electric power and energy efficiency of a solar thermoelectric generator*. Journal of Electronic Materials, 2011. **40**(5): p. 1238-1243.
107. Chen, G., *Theoretical efficiency of solar thermoelectric energy generators*. Journal of Applied Physics, 2011. **109**: p. 104908.
108. Thomas, L.C., *Heat Transfer - Professional Version*. 2nd ed. 1999, Tulsa: Capstone PC.
109. Lienhard, J.H., *A Heat Transfer*. 4 ed. 2011, Mineola: Dover Publications Inc.
110. *TG-4-12 (Specification)*, Marlow Inc.
111. Mayer, P.M., *High-density Thermoelectric Power Generation and Nanoscale Thermal Metrology*, in *Department of Electrical Engineering and Computer Science*. 2007, MIT: Cambridge.
112. Ritzer, T.M., M.J. Nagy, and R.J. Buist. *Evaluation of thermal junction quality in thermoelectric assemblies using transient analysis technology*. in *Fifteenth International Conference on Thermoelectrics*. 1996. Pasadena, CA.
113. Ishigai, S. and E. Nishikawa, *Experimental study of structure of gas flow in tube banks with tube axes normal to flow Part II; on the structure of gas flow in single column, single-row, and double-rows tube banks*. JSME, 1975. **18**: p. 528-535.
114. Burch, J., et al. *Modeling and Test-and-Rate Methods for Innovative Thermosiphon Solar Water Heaters*. in *Solar 2006*. 2006. Denver, Colorado.
115. Backer, H., *Water Disinfection for International and Wilderness Travelers*. Travel Medicine, 2002. **34**(3).
116. Li, Q., *Numerical calculation of the cooling rate in the J-Quenching technique*. Metallurgical and Materials Transactions B, 2008. **40**(3): p. 405-410.
117. Milkjkovicm, N. and E.N. Wang, *Modeling and optimization of hybrid solar thermoelectric systems with thermosyphons*. Solar Energy, 2011. **85**: p. 2843-2855.
118. Brown, J. and C. Hendry, *Public demonstration projects and field trials: Accelerating commercialization of sustainable technology in solar photovoltaics*. Energy Policy, 2009. **37**(7): p. 2560-2573.
119. Krebs, F.C., et al., *Manufacture, integration and demonstration of polymer solar cells in a lamp for the "Lighting Africa" initiative*. Energy and Environmental Science, 2010. **3**: p. 512-525.
120. Harborne, P. and C. Hendry, *Pathways to commercial wind power in the US, Europe and Japan: The role of demonstration projects and field trials in the innovation process*. Energy Policy, 2009. **37**(9): p. 3580-3595.
121. Farrell, D., U.A. Gersch, and E. Stephenson, *The value of China's emerging middle class*, in *The McKinsey Quarterly*. 2006.

122. Zhang, L., et al., *Rural energy in China: Pattern and policy*. Renewable Energy, 2009. **34**: p. 2813-2823.
123. Niez, A., *Comparative study on rural electrification policies in emerging economies: Keys to successful policies*. 2010, International Energy Agency.
124. *Infrared Thermography*.
125. *ASHRAE Handbook: HVAC Applications*. 1999, Amer Society of Heating.
126. Kelsey, R.G., F. Shafizadeh, and D.P. Lowery, *Heat content of bark, twigs, and foliage of nice species of western conifers*. 1979, U.S. Department of Agriculture: Ogden.
127. Witt, M., K. Weyer, and D. Manning, *Designing a clean-burning, high-efficiency, dung-burning stove: lessons in cooking with cow patties*. 2006, Aprovecho Research Center: Creswell.
128. Zeng, G., et al., *Power Generator Modules of Segmented Bi₂Te₃ and ErAs:(InGaAs)_{1-x}(InAlAs)_x*. Journal of Electronic Materials, 2008. **37**(12): p. 1786-1892.
129. Manko, H.H., *Solders and soldering: materials, design, production and analysis for reliable bonding*. 2001: McGraw-Hill Professional. 396.
130. Morgan, B., I. Lee, and P. Taylor, *Scalable Catalytic Burner with Integrated PbTe Thermoelectric Generator*, in *Army Science Conference*.
131. Mayer, P.M. and R.J. Ram, *Optimization of Heat Sink-Limited Thermoelectric Generators*. Nanoscale and Microscale Thermophysical Engineering, 2006. **10**(2): p. 143-155.
132. Zhang, Q., et al., *High figures of merit and natural nanostructures in Mg₂Si_{0.4}Sn_{0.6} based thermoelectric materials*. Applied Physics Letters, 2008: p. 102109-1.
133. Rowe, D.M., *CRC Handbook of Thermoelectrics*. 1995: CRC Press.
134. Rowe, D.M., *Applications of Nuclear-Powered Thermoelectric Generators in Space*. Applied Energy, 1991. **40**(4): p. 241-271.
135. Morelli, D.T. *Potential applications of advanced thermoelectrics in the automobile industry*. in *15th International conference on thermoelectrics*. 1996. Pasadena.
136. Rowe, D.M., *Thermoelectric waste heat recovery as a renewable energy source*. International journal of innovations in energy systems and power, 2006: p. 13-23.
137. *Abundance in Earth's Crust*. 1993-2010, The University of Sheffield.
138. Sharp, J. *Thermoelectric cooling and power generation as green technologies - Invited Talk*. in *International conference on Thermoelectrics*. 2009. Freiburg, Germany.
139. Muller, E., *Thermoelectric materials: Maturity for technological application (Short survey)*. 2009, German Aerospace Center (DLR).
140. George, M.W., *Selenium and Tellurium*. U.S. Geological Survey Minerals Yearbook. 2004.
141. Guilinger, J.G., *Assessment of critical thin film resources - Tellurium*. World Industrial Minerals, 1999.
142. Andersson, B., *Materials Availability for Large-Scale Thin-Film Photovoltaics*. Progress in Photovoltaics: Research and Applications, 2000. **8**: p. 61-76.
143. Dresselhaus, M.S., et al., *New directions for low-dimensional thermoelectric materials*. Advanced Materials, 2007. **19**(27): p. 1043-1053.
144. Lan, Y., et al., *Enhancement of thermoelectric figure-of-merit by a bulk nanostructuring approach*. Advanced Functional Materials, 2010. **20**: p. 357-376.
145. Hsu, K.F., et al., *Cubic AgPbmSbTe_{2+m}: bulk thermoelectric materials with high figure of merit*. Science, 2004: p. 818-821.
146. Yang, S.H., et al., *Nanostructures in high-performance (GeTe)_x(AgSbTe₂)_{100-x} thermoelectric materials*. Nanotechnology, 2008.
147. Bai, S.Q., et al., *Thermoelectric properties of n-type Sr_xMyCo₄Sb₁₂ (M = Yb, Ba) double-filler skutterudites*. Applied Physics A, 2010: p. 1109-1114.
148. Sales, B.C., D. Mandrus, and R.K. Williams, *Filler skutterudite antimonides: A new class of thermoelectric materials*. Science, 1996. **272**: p. 5266.

149. Saramat, A., et al., *Large thermoelectric figure of merit at high temperature in Czochralski-grown clathrate Ba₈Ga₁₆Ge₃₀*. Journal of Applied Physics, 2006: p. 023708-1.
150. Kleinke, H., *New bulk materials for thermoelectric power generation: Clathrates and complex antimonides*. Chemistry of Materials, 2010. **22**: p. 604-611.
151. Caillat, T., J.-P. Fleurial, and A. Borshchevsky, *Preparation and thermoelectric properties of semiconducting Zn₄Sb₃*. Journal of Physics and Chemistry of Solids, 1997: p. 1119-1125.
152. Sootsman, J.R., D.Y. Chung, and M.G. Kanatzidis, *New and old concepts in thermoelectric materials*. Angewandte Chemie International Edition, 2009: p. 8616-8639.
153. Muta, H., et al. *Thermoelectric properties of ZrNiSn based half-Heusler compounds*. in *International Conference on Thermoelectrics*. 2005.
154. Shen, Q., et al., *Effects of partial substitution of Ni by Pd on the thermoelectric properties of ZrNiSn-based half-Heusler compounds*. Applied Physics Letters, 2001. **79**(25): p. 4165-4167.
155. Fujita, K., T. Mochida, and K. Nakamura, *High-temperature thermoelectric properties of Na_xCo_{2-d} single crystals*. Japanese Journal of Applied Physics, 2001. **40**: p. 4644-4647.
156. Koumoto, K., I. Terasaki, and R. Funahashi, *Complex oxide materials for potential thermoelectric applications*. MRS Bulletin, 2006: p. 206-210.
157. Venkatasubramanian, R., et al., *Thin-film Thermoelectric Devices with High Room-temperature Figures of Merit*. Nature, 2001. **413**: p. 597-602.
158. Harman, T.C., et al., *Quantum dot superlattice thermoelectric materials and devices*. Science, 2002. **297**(5590): p. 2229-2232.
159. Zeng, G., et al., *Thermoelectric Power Generator Module of 16x16 Bi₂Te₃ and 0.6%ErAs:(InGaAs)_{1-x}(InAlAs)_x Segmented Elements*. Applied Physics Letters, 2009. **95**(083503-1).
160. Goldsmid, H.J., *Conversion Efficiency and Figure-of-Merit*, in *Handbook of Thermoelectrics*, D.M. Rowe, Editor. 1995, CRC Press. p. 19-25.
161. Vining, C.B., *An inconvenient truth about thermoelectrics*. Nature Materials, 2009. **8**: p. 83-85.
162. Burbidge, E.M., et al., *Synthesis of the Elements in Stars*. Reviews of Modern Physics, 1957. **29**(4): p. 547-650.
163. Clayton, D.D., et al., *Neutron capture chains in heavy elements synthesis*. Annals of Physics, 1961. **12**(3): p. 331-408.
164. Palme, H. and A. Jones, *Solar System Abundances of the Elements*. Treatise On Geochemistry, 2003: p. 41-61.
165. Lodders, K., *Solar system abundances and condensation temperatures of the elements*. The Astrophysical Journal. **591**: p. 1220-1247.
166. Haxel, G.B., S. Boore, and S. Mayfield, *Relative abundance of elements in the Earth's upper crust*. 2003, USGS.
167. Price, J.G., *The World is Changing*. The Society of Economic Geologists Newsletter, 2010. **82**.(54).
168. Magee, C., *Lounge of the Lab Lemming*. 2008.
169. Kesler, S.E., *Mineral Resources, Economics and the Environment*. 1994: Macmillan College Publishing Company.
170. Berger, L.I., *Tellurium. Semiconductor materials*. 1997: p. 89-91.
171. Suess, H.E. and H.C. Urey, *Abundances of the elements*. Review of Modern Physics, 1956. **28**: p. 53-74.
172. Liu, L.G., *Distribution of the chemical elements in the earth with some implications*. Geochemical Journal, 1982. **16**: p. 179-197.
173. Jaffe, R., et al. *Energy Critical Elements: securing materials for emerging technologies*. in *APS Physics, MRS*. 2010. Cambridge.
174. Williams, R.S., *Principles of Metallography*. 2007: McGraw-Hill Book Company, Inc.
175. Godfrey, S.M., et al., *Chemistry of arsenic, antimony and bismuth*. 1998: Springer.

176. Long, K.R., et al., *The Principal Rare Earth Elements Deposits of the United States - A Summary of Domestic Deposits and a Global Perspective*, in *U.S. Geological Survey Scientific Investigation Report 2010-5220*. 2010: Virginia.
177. Bernstein, L.R., *Germanium geochemistry and mineralogy*. *Geochimica et Cosmochimica Acta*, 1985. **49**(11): p. 2409-2422.
178. Nolas, G.S., D.T. Morelli, and T.M. Tritt, *Skutterudites: A phonon-glass-electron-crystal approach to advanced thermoelectric energy conversion applications*. *Annual Review Material Science*, 1999. **29**: p. 89-116.
179. Toprak, M.S., et al., *The impact of nanostructuring on the thermal conductivity of thermoelectric CoSb₃*. *Advanced Functional Materials*, 2004. **14**(12): p. 1189-1196.
180. Sofo, J.O. and G.D. Mahan, *Electronic structure of CoSb₃: A narrow-band-gap semiconductor*. *Physical Review B*, 1998. **58**(23): p. 620-623.
181. Sakai, A., et al., *Thermoelectric power in transition-metal monosilicides*. *Journal of the Physical Society of Japan*, 2007. **76**(9): p. 093601-1.
182. Singh, D.J. and I.I. Mazin, *Calculated thermoelectric properties of La-filled Skutterudites*. *Physical Review B*, 1997. **56**(4): p. 1650-1653.
183. Goodenough, J.B., *Band structure of transition metal and their alloys*. *Physical Review B*, 1960. **120**(1): p. 67-83.
184. Parel, D.v.d., et al., *Spin, charge, and bonding in transition metal mono-silicides*. *Physica B*, 1998. **244**: p. 138-147.
185. Li, J., et al., *High-performance nanostructured thermoelectric materials*. *NPG Asia Materials*, 2010. **2**(4): p. 152-158.
186. Nolas, G.S., et al., *High figure of merit in partially filled ytterbium skutterudite materials*. *Applied Physics Letters*, 2000. **77**(12): p. 1855-1857.
187. Shi, X., et al., *Low thermal conductivity and high thermoelectric figure of merit in n-type BaxYbyCo4Sb12 double-filled skutterudites*. *Applied Physics Letters*, 2008. **92**: p. 182101-1.
188. Qiu, P.F., et al., *High-temperature electrical and thermal transport properties of fully filled skutterudites RFe4Sb12 (R = Ca, Sr, Ba, La, Ce, Pr, Nd, Eu, and Yb)*. *Journal of Applied Physics*, 2011. **109**: p. 063713-1.
189. Ballikaya, S., et al., *Thermoelectric properties of triple-filled BaxYbyInzCo4Sb12 skutterudites*. *Journal of Electronic Materials*, 2010.
190. Zhang, L., et al., *Thermoelectric performance of mischmetal skutterudites MnyFe4-xCoxSv12 at elevated temperature*. *Journal of Alloys and Compounds*, 2010: p. 19-25.
191. Nolas, G.S., *Structure, Thermal Conductivity, and Thermoelectric Properties of Clathrate Compounds*, in *Thermoelectrics Handbook: Macro to nano*, D.M. Rowe, Editor. 2006, CRC Press.
192. Kuznetsov, V.L., et al., *Preparation and thermoelectric properties of A8IIB16IIIB30IV clathrate compounds*. *Journal of Applied Physics*, 2000. **87**(11): p. 7871-7875.
193. Kaulzarich, S.M., S.R. Brown, and G.J. Snyder, *Zintl phase for thermoelectric devices*. *Royal Society of Chemistry: Dalton Transactions*, 2007: p. 2099-2017.
194. Snyder, G.J. and E.S. Toberer, *Complex thermoelectric materials*. *Nature materials*, 2008. **7**(81): p. 105-113.
195. Saporov, B., et al., *Synthesis, crystallographic and theoretical studies of the new Zintl phases Ba2Cd2Pn3 (Pn = As, Sb), and the solid solutions (Ba1-xSrx)2Cd2Sb3 and Ba2Cd2(Sb1-xAsx)3*. *The Royal Society of Chemistry: Dalton Transactions*, 2009: p. 1063-1070.
196. Gascoin, F., et al., *Zintl phase as thermoelectric materials: Tuned transport properties of the compounds CaxYb10xZn2Sb2*. *Advanced Functional Materials*, 2005. **15**: p. 1860-1864.
197. Toberer, E.S., et al., *Composition and the thermoelectric performance of b-Zn4Sb3*. *Journal of Materials Chemistry*, 2010. **20**: p. 9877-9885.

198. Qiu, A.N., L.T. Zhang, and J.S. Wu, *Crystal structure, electronic structure, and thermoelectric properties of b-Zn₄Sb₃ from first principles*. Physical Review B, 2010. **81**: p. 035203-1.
199. Snyder, G.J., et al., *Disordered since in Zn₄Sb₃ with phonon-glass and electron-crystal thermoelectric properties*. Nature, 2004. **3**: p. 458-463.
200. Haussermann, U. and A.S. Mikhaylushkin, *Electron-poor antimonides: complex framework structure with narrow band gaps and low thermal conductivity*. The Royal Society of Chemistry: Dalton Transactions, 2009. **39**: p. 1036-1045.
201. Mastronardi, K., et al., *Antimonides with the half-Heusler structure: New thermoelectric materials*. Applied Physics Letters, 1999. **74**(10): p. 1415-1417.
202. Romaka, L.P., et al. *MgAgAs structure type solid solutions as a new thermoelectric material*. in *Proceedings ICT'97 (International Conference on Thermoelectrics)*. 1997. Dresden.
203. Kimura, Y., et al. *High-performance of half-Heusler MNiSn (M = Hf, Zr) single phase thermoelectric alloys fabricated using optical floating zone melting*. in *Material Research Society Symposium Proceedings*. 2006.
204. Shutoh, N. and S. Sakurada, *Thermoelectric properties of the Tix(Zr_{0.5}Hf_{0.5})_{1-x}NiSn half-Heusler compounds*. Journal of Alloys and Compounds, 2005. **389**(1-2): p. 204-208.
205. Lee, M., F.P. Poudeu, and S.D. Mahanti, *Electronic structure and thermoelectric properties of Sb-based semiconducting half-Heusler compounds*. Physical review B, 2011. **83**: p. 085204-1.
206. Yang, J., et al., *Evaluation of Half-Heusler compounds as thermoelectric materials based on the calculated electrical transport properties*. Advanced Functional Materials, 2008. **18**: p. 2880-2888.
207. Kawaharada, Y., et al., *High temperature thermoelectric properties of CoTiSb half-Heusler compounds*. Journal of Alloys and Compounds, 2004. **384**(1-2): p. 308-311.
208. Kurosaki, K., et al., *Thermoelectric properties of NaCo₂O₄*. Journal of Alloys and Compounds, 2000. **315**: p. 234-236.
209. Koumoto, K., et al., *Oxide Thermoelectrics*, in *Thermoelectrics Handbook: Macro to nano*, D.M. Rowe, Editor. 2006, CRC Press.
210. Wang, Y., et al., *Spin entropy as the likely source of enhanced thermopower in NaxCo₂O₄*. Nature Materials, 2003. **423**: p. 425-428.
211. Terasaki, I., et al., *Novel thermoelectric properties of complex transition-metal oxides*. The Royal Society of Chemistry; Dalton Transactions, 2009. **39**: p. 1005-1011.
212. Murayama, W. and N. Shin, *High performance p-type thermoelectric oxide based on NiO*. Materials Letters, 2000. **45**: p. 302-306.
213. Cui, Y., et al., *Thermoelectric properties of n-type double substituted SrTiO₃ bulk materials*. The Royal Society of Chemistry: Dalton Transactions, 2009. **39**: p. 1031-1035.
214. Wang, Y., et al., *Thermoelectric properties of electron doped SrO(SrTiO₃)_n (n = 1,2) ceramics*. Journal of Applied Physics, 2009. **105**(10): p. 103701-1.
215. Tinh, N.T. and T. Tsuji, *Thermoelectric properties of heavily doped polycrystalline SrTiO₃*. *Physics and Engineering of New Materials*. Vol. 127. 2009: Springer. 209-217.
216. Ohtaki, M., et al., *High-temperature thermoelectric properties of (Zn_{1-x}Al_x)O*. Journal of Applied Physics, 1996. **79**(3): p. 1816-1818.
217. Ohtaki, M., K. Araki, and K. Yamamoto, *High thermoelectric performance of dually doped ZnO ceramics*. Journal of Electronic Materials, 2009. **38**(7): p. 1234-1238.
218. Fedorov, M.I. and V.K. Zaitsev, *Thermoelectrics of Transition Metal Silicides*, in *Thermoelectrics Handbook: Macro to nano*, D.M. Rowe, Editor. 2006, CRC Press.
219. Heinrich, A., et al., *Thermoelectric properties of b-FeSi₂ single crystal and polycrystalline b-FeSi_{2+x} thin films*. Think Solid Films, 2001. **381**(2): p. 287-295.
220. Cheng, J.-F., et al., *Enhanced thermoelectric power near the quantum phase transition in the itinerant-electron ferromagnet MnSi*. Physical Review B, 2010. **82**: p. 214402-1.

221. Vining, C.B., *Thermoelectric Properties of silicides*, in *CRC Handbook of Thermoelectrics*, D.M. Rowe, Editor. 1995, CRC Press.
222. Mars, K., et al., *Thermoelectric properties and electronic structure of Bi- and Ag- doped Mg₂Si_{1-x}Gex compounds*. *Journal of Electronic Materials*, 2009. **38**(7): p. 1360-1364.
223. Szczech, J.R., J.M. Higgins, and S. Jin, *Enhancement of the Thermoelectric Properties in Nanoscale and Nanostructured Materials*. *Journal of Materials Chemistry*, 2011. **21**: p. 4037-4055.
224. Nolas, G.S., J. Sharp, and H.J. Goldsmid, *Thermoelectrics: Basic principles and new materials developments*. 2001: Springer.
225. Tritt, T.M., *Recent trends in thermoelectric materials research I*. Vol. 69. 2001: Academic Press.
226. Sharp, J.W. *Selection and evaluation of materials for thermoelectric applications II*. in *Material Research Society Symposium Proceedings*. 1997.
227. Tsymbal, E.Y., et al., *Sign of thermoelectric power in Co/Cu and Fe/Cr multilayers*. *Physical Review B*, 1999. **59**(13): p. 8371-8374.
228. Yan, X., et al., *Enhanced thermoelectric figure of merit of p-type Half-Heuslers*. *Nano Letters*, 2010. **11**: p. 556-560.
229. Balandin, A. and K.L. Wang, *Significant decrease of the lattice thermal conductivity due to phonon confinement in a free-standing semiconductor quantum well*. *Phys. Rev. B*, 1998. **58**: p. 1544-1549.
230. Cahill, D.G., W.K. Ford, and K.E. Goodson, *Nanoscale thermal transport*. *Journal of Applied Physics*, 2003. **93**(793).
231. Lee, S.M., D.G. Cahill, and R. Venkatasubramanian, *Thermal conductivity of Si-Ge superlattices*. *Applied Physics Letters*, 1997. **70**(22): p. 2957-2959.
232. Cahill, D.G., K. Goodson, and A. Majumdar, *Thermometry and Thermal Transport in Micro/Nanoscale Solid-State Devices and Structures*. *Journal of Heat Transfer*, 2002. **124**(2): p. 223-241.
233. Zebarjadi, M., et al., *Thermoelectric Transport in a ZrN/ScN Superlattice*. *Journal of Electronic Materials*, 2009. **38**(7): p. 960-963.
234. Rawat, V., et al., *Thermal conductivity of (Zr,W)N/ScN metal/semiconductor multilayers and superlattices*. *Journal of Applied Physics*, 2009. **105**: p. 024909-1.
235. Vashaee, D. and A. Shakouri, *Electronic and thermoelectric transport in semiconductor and metallic superlattices*. *Journal of Applied Physics*, 2004. **95**(3): p. 1233-1245.
236. Saha, B., et al., *Electronic structure, phonons, and thermal properties of ScN, ZrN, and HfN: A first-principles study*. *Journal of Applied Physics*, 2010. **107**: p. 033715.
237. Wortman, R.D., *Nitride metal-semiconductor superlattices for solid state thermionic energy conversion*. 2011, Purdue University: West Lafayette.
238. Goldsmid, H.J., *Electronic Refrigeration*. 1986, London: Pion.
239. Tritt, T.M., *Electrical and Thermal Transport Measurement Techniques for Evaluation of the Figure-of-Merit of Bulk Thermoelectric Materials*, in *Thermoelectrics Handbook - Macro to Nano*, D.M. Rowe, Editor. 2006, CRC Press.
240. Pauw, L.J.v.d., *A Method of Measuring Specific Resistivity and Hall Effect of Discs of Arbitrary Shape*, in *Phillips Research Reports*. 1958.
241. Pauw, L.J.v.d., *Determination of Resistivity Tensor and Hall Tensor of Anisotropic Conductors*. *Phillips Research Reports*, 1961. **16**.
242. Parker, W.J., et al., *Flash Method of Determining Thermal Diffusivity, Heat Capacity, and Thermal Conductivity*. *Journal of Applied Physics*, 1961. **32**(9): p. 1679-1685.
243. Harman, T.C., J.H. Cahn, and M.J. Logan, *Measurement of Thermal Conductivity by Utilization of the Peltier Effect*. *Journal of Applied Physics*, 1959. **30**(9): p. 1351.
244. Harman, T.C., *Special Techniques for Measurement of TE Properties*. *Journal of Applied Physics*, 1959. **30**: p. 1373.

245. Bowley, A.E., et al., *Measurement of the Figure-of-Merit of a TE Material*. Journal of Scientific Instruments, 1961. **38**: p. 433.
246. Mayer, P., *High-density thermoelectric power generation and nanoscale thermal metrology*, in *EECS*. 2007, MIT: Cambridge.
247. Phillips, L.S., *The Measurement of Thermoelectric Properties at High Temperatures*. Journal of Scientific Instruments, 1965. **42**: p. 209-211.
248. Muller, E., J.U. Bruch, and J. Schilz. *TE generator test facility for low resistance single elements*. in *17th International Conference on Thermoelectrics*. 1998: IEEE.
249. Burkoy, A.T., et al., *Experimental Set-up for Thermopower and Resistivity Measurements at 100-1300 K*. Measurement Science and Technology, 2001. **12**: p. 264-271.
250. *Z-meters*, RMT Ltd.
251. Muto, A., et al., *Thermoelectric Properties and Efficiency Measurements Under Large Temperature Differences*. Review of Scientific Instruments, 2009. **80**: p. 093901-1.
252. Woodbury, H.H., L.M. Levinson, and R.S. Lewandowski, *Z-meters*, in *CRC Handbook of Thermoelectrics*, D.M. Rowe, Editor. 1995, CRC Press LLC.
253. Menon, M.K.S.V.K.S.V.G., *Analytical Axial View Factors and Thermal Radiation Distribution Inside a Cylindrical Hohlräum*. Physics of Plasmas, 2000. **7**: p. 2616-2621.
254. Shukla, K.N. and D. Ghosh, *Radiation Configuration Factors for Concentric Cylinder Bodies*. Indian Journal of Technology, 1985. **23**: p. 244-246.
255. Suzuki, M., et al., *Low-resistance Ta/Ti Ohmic contacts for p-type GaN*. Applied Physics Letters, 1999. **74**(275): p. 123279.
256. *Solarbuzz LLC*.
257. Cook, B.A., et al., *Parasitic effects of oxygen on the thermoelectric properties of Si₈₀Ge₂₀ doped with GaP and P*. Journal of Applied Physics, 1992. **72**(4): p. 1423-1428.
258. Wamukonya, N., *Solar home system electrification as a viable technology option for Africa's development*. Energy Policy, 2005. **35**: p. 6-14.
259. Zhang, X. and A. Kumar, *Evaluating renewable energy-based rural electrification program in western China: Emerging problems and possible scenarios*. Renewable and Sustainable Energy Reviews, 2011. **15**(1).
260. McEnaney, K., et al., *Modeling of concentration solar thermometric generators*. Journal of Applied Physics, 2011. **110**.
261. McEnaney, K., *Modeling of solar thermal selective surfaces and thermoelectric generators*, in *Department of Mechanical Engineering*. 2010, MIT: Cambridge.